Geometrical Vision Measurement in Mechanical Engineering

Guest Editors: Fuqiang Zhou, Emanuele Zappa, and Liang-Chia Chen
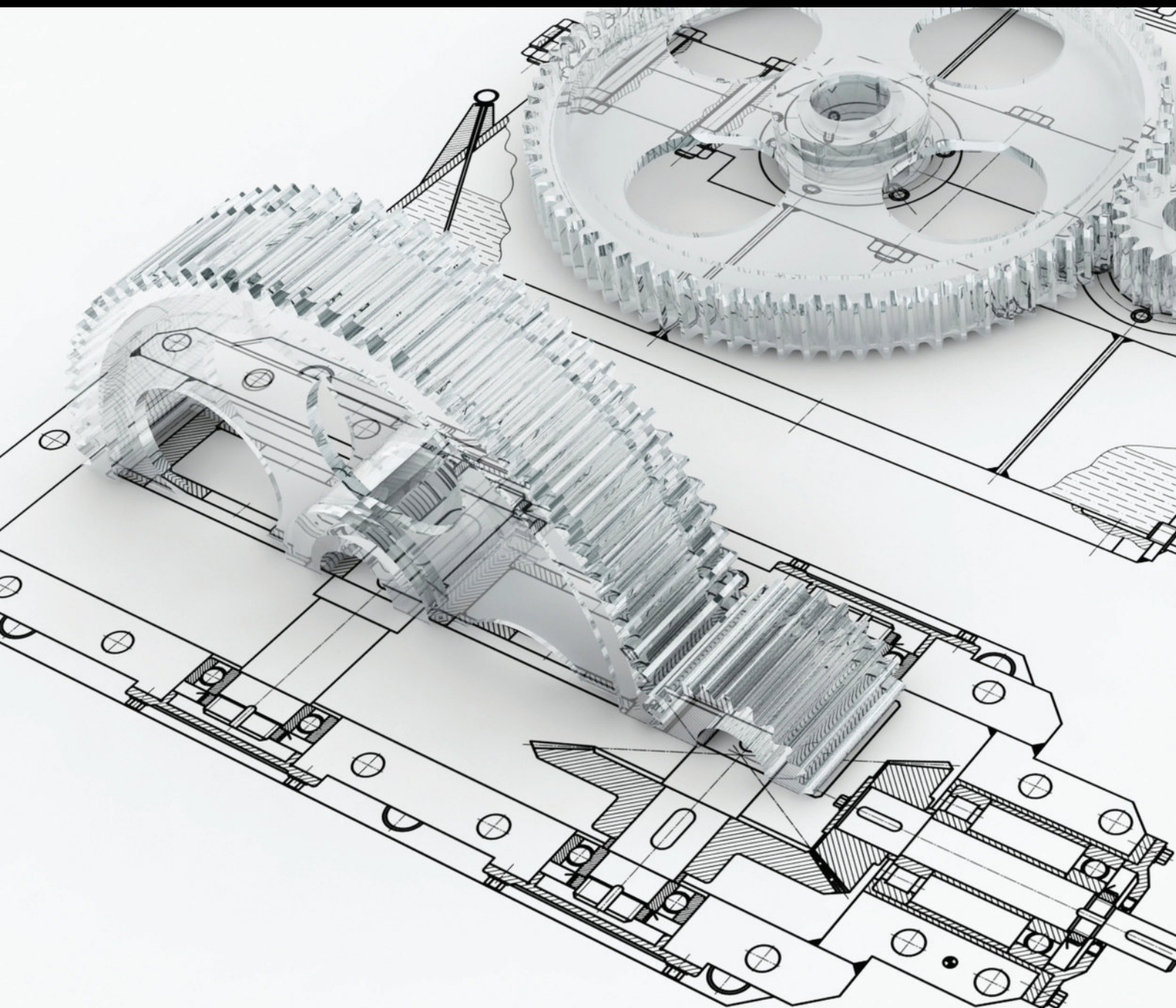
Geometrical Vision Measurement
in Mechanical Engineering

Geometrical Vision Measurement in Mechanical Engineering

Guest Editors: Fuqiang Zhou, Emanuele Zappa, and Liang-Chia Chen

Editorial Board

Contents

Editorial

Geometrical Vision Measurement in Mechanical Engineering

Fuqiang Zhou,[1] Emanuele Zappa,[2] and Liang-Chia Chen[3]

[1] *School of Instrumentation Science and Optoelectronics Engineering, Beihang University, Beijing 100191, China*
[2] *Department of Mechanical Engineering, Politecnico di Milano, 20156 Milan, Italy*
[3] *Department of Mechanical Engineering, National Taiwan University, Taipei, Taiwan*

Correspondence should be addressed to Fuqiang Zhou; zfq@buaa.edu.cn

In the past decades, advances in mechanical engineering have resulted in greater use of vision measurement methods in optical metrology, such as time-of-flight, stereo vision, structured light vision, fringe projection technique, depth from focus, photometric stereo, and digital image correlation. Since the advantages are noncontact, nondestructive, high-precision, automatic, and fast, the vision measurement methods have played an important role in the fields of reverse engineering, online inspection, dimensional analysis, quality assurance, sorting, material handling, and optical gauging. With the rapid development of computer technology and digital image processing technology, more and more vision measurement methods will be applied in many areas of engineering and science. This special issue aims to collect basic theory, key technology, and application articles on the most recent achievements in geometrical vision measurement, for the purpose to show the latest development and provide guidelines of future research directions. There are five papers about the structured light vision technology: B. Wu and B. Wang established a mathematical model of the reference sphere positioning measurement based on the measuring principle of the line-structured light vision sensor; H. Gao et al. developed a novel 3D wide FOV scanning measurement system which adopted two multiline-structured light sensors; Z. Wei et al. proposed a sphere-based calibration method for line-structured light vision sensor; Y. Wang et al. discussed the pipe defect detection method based on inside 3D points acquired by circle structured light vision system; R. Marani et al. presented a high-resolution laser scanning vision system for the inspection of drilling tools. Apart from the structured light vision method, there are also four papers

dealing with the problems in the stereo/multiple vision: J. Lin et al. presented a novel 3D profile automated reconstruction technique based on stereo vision for objects with complex free-form surface or step surface; Y. Guo et al. presented a real-time measurement method for the 2-DOF swing angles of rocket nozzle by the use of multivision and rocket nozzle rotation axes; C.-C. Ho et al. presented a real-time image capturing system that uses four cameras at 30 fps and stitches their views together to create a panoramic video; T. Xue et al. provided a segmentation method for multibubbles in gas-liquid two-phase flow based on virtual stereo vision and the characteristics of three-dimensional trajectory of bubbles are measured accurately. In addition, there are three papers related to the image processing and pattern recognition: M. Dong et al. derived a general algorithm for grayscale-weighted centroiding method; X. Chen et al. described a direction-guided method for real-time processing of light stripe images in practical active vision application; Z. Wang et al. proposed a manifold adaptive kernel semisupervised discriminant analysis algorithm for gait recognition. The rest of the five papers discussed other issues related to the vision measurement: A. B. Abdullah et al. aimed to evaluate the quality of a cold embossed hole based on profile deviation gathered from 3D surface measurement; W. L. Liu et al. developed a dynamic weighting model that describes not only the dynamic uncertainty but also the geometric variations of laser tracking system; Y. Wang et al. presented a new method to calibrate the robot visual measurement system; H. Wang presented a technique for noncontact optical measurement of in-plane displacement based on correlation analysis; B. Wu and B. Wang presented a novel automatic measurement

method for large-scale space and large workpieces (equipment) combined with the laser theodolite measuring and vision guiding technologies. We hope that this special issue would provide the readers with the latest trends of geometrical vision measurement in mechanical engineering.

Acknowledgment

Fuqiang Zhou
Emanuele Zappa
Liang-Chia Chen

Research Article

3D Wide FOV Scanning Measurement System Based on Multiline Structured-Light Sensors

He Gao,[1] **Fuqiang Zhou,**[1] **Bin Peng,**[1] **Yexin Wang,**[1] **and Haishu Tan**[2]

[1] *Key Laboratory of Precision Opto-Mechatronics Technology, Ministry of Education, Beihang University, Beijing 100191, China*
[2] *Department of Electronic Information Engineering, Foshan University, Foshan 528000, China*

Correspondence should be addressed to Fuqiang Zhou; zfq@buaa.edu.cn

Structured-light three-dimensional (3D) vision measurement is currently one of the most common approaches to obtain 3D surface data. However, the existing structured-light scanning measurement systems are primarily constructed on the basis of single sensor, which inevitably generates three obvious problems: limited measurement range, blind measurement area, and low scanning efficiency. To solve these problems, we developed a novel 3D wide FOV scanning measurement system which adopted two multiline structured-light sensors. Each sensor is composed of a digital CCD camera and three line-structured-light projectors. During the measurement process, the measured object is scanned by the two sensors from two different angles at a certain speed. Consequently, the measurement range is expanded and the blind measurement area is reduced. More importantly, since six light stripes are simultaneously projected on the object surface, the scanning efficiency is greatly improved. The Multiline Structured-light Sensors Scanning Measurement System (MSSS) is calibrated on site by a 2D pattern. The experimental results show that the RMS errors of the system for calibration and measurement are less than 0.092 mm and 0.168 mm, respectively, which proves that the MSSS is applicable for obtaining 3D object surface with high efficiency and accuracy.

1. Introduction

Structured-light 3D vision measurement is becoming increasingly important owing to its noncontact, high precision, and good system flexibility. A basic structured-light sensor is usually composed of one camera and one laser projector together forming an active stereo pair. The laser projector projects a light plane onto an object. When the light plane reaches the target surface, it forms a distorted stripe of illuminated points due to the irregular surface. Then the camera records the illuminated target. If the sensor is properly calibrated, the 3D coordinates of the illuminated points can be calculated by the well-known triangulation method.

According to the number of structured-light sensors, the existing structured-light 3D surface capturing system can be currently classified into two categories. One is single structured-light 3D surface capturing system which means that it contains only one structured-light sensor and projects a single light stripe on the object surface. This kind of system is easy to implement due to its simple structure, but its major defects are quite obvious: measurement range is limited and there are blind measurement areas for complicated objects. As a result, the single structured-light 3D surface capturing system is only applied to measure objects with simple structure and no hiding surface [1–4]. The other category is the double structured-light 3D surface capturing system, which is composed of two structured-light sensors. For such a system, the measured object is scanned from two different angels, so the measurement range is expanded and the dead zone is reduced relatively. However, the scanning efficiency of the double structured-light 3D surface capturing system is low, because the number of light stripes is small and it only covers a small area on the object surface.

Some vision measurement systems based on structured-light have already been successfully applied to industrial inspection. For example, Alippi et al. developed a detection system for track profiles of railways based on laser scanning

and image analysis [5]; Loh and Lu presented a solder joint inspection system using structured-light [6]; Haug and Pritschow proposed a robust laser-stripe sensor system for automated weld-seam-tracking in shipbuilding industry [7].

All the preceding inspection systems have a common point that they are all constructed on the basis of a single structured light sensor, as single structured-light system is low cost and easy to implement due to the simple structure. However, if the single structured-light sensor is adopted in the 3D surface measurement system, three obvious problems are inevitable: limited measurement range, blind measurement area, and low scanning efficiency. As a result, the single structured-light 3D surface measurement system is only applicable to the object with simple structure and no hidden surface [8].

Aiming at overcoming these problems, we design a 3D wide FOV scanning measurement system, which adopts two multiline structured-light sensors to construct the system. Each sensor is composed of one digital CCD camera and three line-structured-light projectors. While the object is moving at a certain speed, the system projects six parallel light stripes onto the object surface and scans from the two sides of the measured object. Therefore the FOV and measurement range had been expanded, dead zone is effectively reduced, and, most importantly, the scanning efficiency is greatly improved.

To design and use a MSSS system, three main aspects need to be made efforts on: the measurement model, the extraction and arrangement of light stripes, and system calibration.

Firstly, establishing a reasonable measurement model is the first requirement to construct a structured-light 3D surface measurement system. Because, in the scanning process, all the measurement data is calculated according to the measurement model, many existing measurement models have limitations. The model described in [9] requires the camera optical axis to be parallel to the datum axis, while, in the model established in [10], the structured-light plane should be perpendicular to the measurement platform. Both of the two models have restrictions due to the spatial arrangement limitations of their system components, which increased the difficulty of system implementation.

Secondly, subpixel image coordinates of the light stripes need to be localized in order to guarantee the sensor calibration accuracy and the measurement accuracy. A larger number of extraction methods at subpixel level have been presented in previous works, and all of these methods require certain conditions [11–14]. However, most of them are not robust enough to prevent suffering from considerable noise and the blaze of light stripe. Meanwhile, the arrangement of light stripes is also important as each light stripe is required to be matched to the corresponded projector, so that the 3D coordinates of the illuminated points can be calculated.

Thirdly, the structured-light sensor calibration, which directly affects the measurement accuracy, is the key to the 3D measurement results. The structured-light sensor calibration includes camera calibration and projector calibration. The camera calibration is to estimate the world-to-image perspective transformation matrix and the distortion coefficients of the camera lens. The projector calibration is to determine the coefficients of the light plane equation in space. There are many calibration algorithms for reference: Dewar [15] proposed a calibration method based on self-generated targets; Duan et al. [16] used a toothed target and 1-D mobile stage to locate the projecting light plane of the sensor in the camera coordinate and calculated the parameters with a restrained penalty function method; Huynh et al. [17] proposed the cross-ratio invariance calibration method. However, in our case, the data fusion and the spacial relationship between the two sensors should also be considered, making those methods inconvenient. In addition, the calibration methods described in [18, 19] require stringent standard calibration patterns with high positioning accuracy, which make the calibration process costly and difficult to implement.

In this paper, the potential of a MSSS is assessed. Emphases are put on the three main aspects mentioned above. Moreover, the following three aspects should be noted. First, the mathematical model of the MSSS should fit the structure which is fabricated and assembled without particular spatial constrains. Second, the light stripes should be extracted at subpixel level and arranged in an appropriate order. Third, the system calibration should be simple and easy to implement without requiring complex calibration patterns or high-precision auxiliary equipment. The rest of contents of this paper are organized as follows. In Section 2, the structure of the MSSS is introduced. The measurement model of the system is built and explained in Section 3. In Section 4, the extraction and arrangement methods of light stripes are given. In Section 5, the system calibration approach for the MSSS is described in detail. Calibration experiments and the experimental measurement results are presented in Section 6. And the paper ends with conclusions in Section 7.

2. Construct of the MSSS

The MSSS shown in Figure 1 mainly consists of two multiline structured-light sensors, a glass platform, a motorized linear motion stage, a stepping motor and its controller, a grating ruler, and a computer. Each sensor is composed of one digital CCD camera and three line-structured-light projectors. The block diagram of the system is shown in Figure 2.

The measured object is placed on the glass platform, and the six laser projectors generate six distorted light stripes on the object surface, which contain the 3D characteristics information of the object surface since the stripes are modulated by the depth changing. Two CCD cameras capture the images of the distorted light stripes in two different angles. After calculating the 3D coordinates of points on the light stripes from the 2D images on the basis of parameters of cameras and light plane equations, the profiles of the six light plane sections can be obtained. During the measurement process, two sensors are driven by the stepping motor along one direction to scan the object at a certain speed; thus, a series of profiles can be acquired. At the same time, the separation distances between the profiles are read from the grating ruler. By building up the profiles according to the
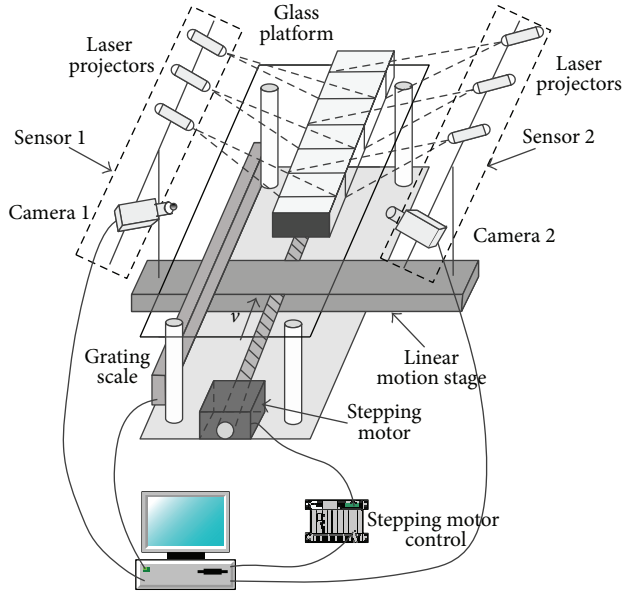
FIGURE 1: Schematic diagram of the MSSS scanning measurement system.
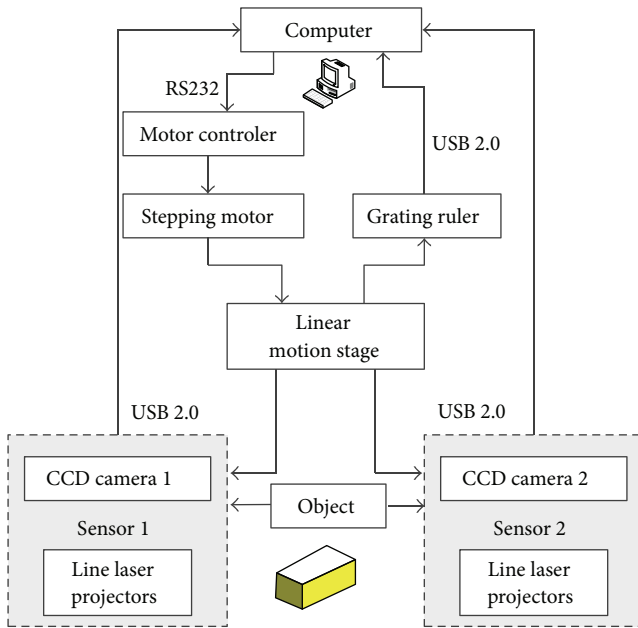
FIGURE 2: Block diagram of the system.

separation distances, the entire 3D surface of the measured object can be obtained.

3. Measurement Model

The measurement model of the MSSS is shown in Figure 3. The coordinate systems in Figure 3 are defined as follows: $o_{c1} - x_{c1}y_{c1}z_{c1}$ is camera 1 coordinate system, $o_{c2} - x_{c2}y_{c2}z_{c2}$ is camera 2 coordinate system, $o_{u1} - x_{u1}y_{u1}$ is nondistortion image coordinate system of camera 1, $o_{u2} - x_{u2}y_{u2}$ is
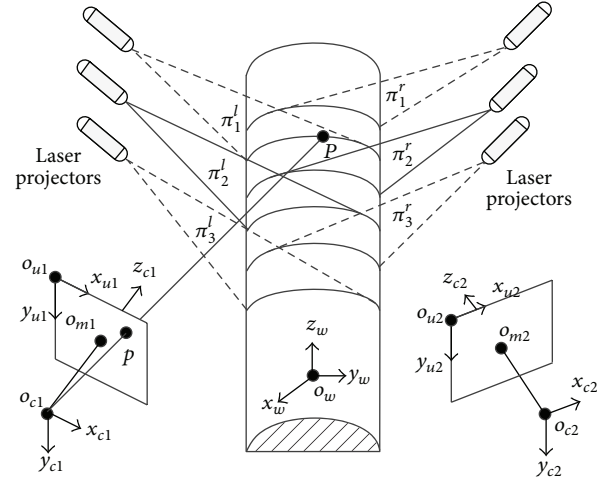
FIGURE 3: The model of the MSSS scanning measurement system.

nondistortion image coordinate system of camera 2, and $o_w - x_w y_w z_w$ is world coordinate system. Those coordinate systems are relatively static during the scanning process. In addition, O_{m1} and O_{m2} are the principal points of the two cameras, π_s^l is the sth light plane in sensor 1, and π_s^r is the sth light plane in sensor 2. The following description only takes the light plane π_1^l in sensor 1 as an example because the model of either sensor is similar.

For any illuminated point P on the light stripe formed by light plane π_1^l and the object surface, its coordinate in $o_w - x_w y_w z_w$ is denoted by $\mathbf{P}_w = (x_w, y_w, z_w)^T$ and its coordinate in $o_{c1} - x_{c1}y_{c1}z_{c1}$ is denoted by $\mathbf{P}_c = (x_c, y_c, z_c)^T$. The Euclidian transformation between $o_w - x_w y_w z_w$ and $o_{c1} - x_{c1}y_{c1}z_{c1}$ is specified by a rotation matrix and a translation vector as follows:

$$\mathbf{P}_c = \mathbf{R}\mathbf{P}_w + \mathbf{T}, \qquad (1)$$

where $\mathbf{R}$ is the 3×3 rotation matrix and $\mathbf{T}$ is the 3×1 translation vector. $\mathbf{R}$ and $\mathbf{T}$ are called the external parameters.

Point p on the image plane is the projection of P. The homogeneous coordinate of p in $o_{u1} - x_{u1}y_{u1}$ is denoted by $\mathbf{P}_u = (x_u, y_u, 1)^T$. According to the pinhole camera model, the transformation from the camera coordinate to the 2D undistorted image coordinate is expressed as

$$\rho\mathbf{P}_u = \mathbf{A}\mathbf{P}_c, \qquad (2)$$

where $\mathbf{A} = \begin{bmatrix} f_x & 0 & u_0 \\ 0 & f_y & v_0 \\ 0 & 0 & 1 \end{bmatrix}$ is the internal parameters matrix. f_x and f_y are the effective focal length of the camera in the x and y directions, (u_0, v_0) is the coordinate of the principal point in $o_{u1} - x_{u1}y_{u1}$, and ρ is a scale factor.

Real lenses do not satisfy the pinhole model and usually exhibit some degree of geometric distortion. Thus, considering the first two terms of the radial distortion for the camera

lens, we have the following equations for each point in each image:

$$x_u = x_d \left[1 + k_1 \left(x_d^2 + y_d^2 \right) + k_2 \left(x_d^2 + y_d^2 \right)^2 \right],$$
$$y_u = y_d \left[1 + k_1 \left(x_d^2 + y_d^2 \right) + k_2 \left(x_d^2 + y_d^2 \right)^2 \right], \tag{3}$$

where $\mathbf{P}_d = (x_d, y_d, 1)^T$ is the distortion image coordinates of p.

In camera 1 coordinate system, the space equation of light plane π_1^l is described by

$$ax_c + by_c + cz_c + d = 0. \tag{4}$$

The measurement coordinate system $o_m - x_m y_m z_m$ is established at the position of the world coordinate system where the first image is captured during the scanning process. It should be noted that the measurement coordinate system is fixed and does not move with the translation of the sensors. Since the sensors are moved linearly, the transformation relationship between the measurement coordinate system $o_m - x_m y_m z_m$ and the world coordinate system $o_w - x_w y_w z_w$ is only translation. Assume that the coordinate of point P in $o_m - x_m y_m z_m$ is $\mathbf{P}_m = (x_m, y_m, z_m)^T$, and then the translation can be described by

$$\mathbf{P}_m = \mathbf{P}_w + d\mathbf{V}, \tag{5}$$

where $\mathbf{V}$ is a 3×1 unit translation vector representing the scanning direction in the world coordinate system, and d is the translation distance read from the grating ruler (starting at 0).

Equations (1)–(5) are the complete measurement model of the system. In sensor 1, the 3D measurement coordinates $(x_m, y_m, z_m)^T$ of an illuminated point on the light stripe formed by light plane π_1^l can be derived from the corresponding 2D image coordinate. The process is as follows.

(1) Get the image coordinates $(x_d, y_d)^T$ of the center position of the light stripe corresponding to the light plane π_1^l by image processing.

(2) Calculate the nondistortion image coordinate $(x_u, y_u)^T$ from (3) to correct the radial distortion of the camera lens.

(3) Combine (2) and (4) to get the 3D coordinates in camera frame $(x_c, y_c, z_c)^T$.

(4) Convert the camera coordinates to world coordinates $(x_w, y_w, z_w)^T$ according to (1).

(5) Transform the world coordinates $(x_w, y_w, z_w)^T$ to measurement coordinates $(x_m, y_m, z_m)^T$ by (5).

The 3D measurement coordinates of the illuminated points on the other light stripes can also be calculated by the same method.

4. Light Stripes Extraction and Arrangement

In the MSSS, the captured light stripes are usually not continuous, as shown in Figure 4(a), which is caused by the uneven surface and the irregular surface material. However, according to the measurement model, the 3D coordinates of the points on the light stripes can be correctly calculated as long as the points correspond to the light plane equation. Therefore, it is necessary to find the one-to-one correspondence relationship between the light stripes and the light. The best solution is to arrange the light stripes in an appropriate order. We divided the extraction and arrangement of light stripes into four steps.

Firstly, extract light stripe, which means locating the center of the light stripe. We adopt a method presented by Steger [20]. For each pixel, the second order Taylor polynomial is computed by convolving the image with the derivatives of a Gaussian smoothing kernel. Line points are required to have a vanishing gradient and high curvature in the direction perpendicular to the line. The resulting filter generates a single response for each line. The line position can be determined with subpixel accuracy and the algorithm scales to lines with arbitrary width. The extracted results of light stripes are shown in Figure 4(b).

Secondly, eliminate the disturbances. The disturbances come from two aspects: one is the small thorns at the ends of the light stripes; the other is the short segment that is obviously out of the area covered by light stripes. Those disturbances can be eliminated easily by setting a threshold for the length of the light stripes. The length is calculated as the sum of the Euclidian distances between the successive points on light stripe as follows:

$$L = \sum_{i=0}^{m-2} \left\| \mathbf{P}_{i+1} - \mathbf{P}_i \right\|_2, \tag{6}$$

where $\mathbf{P}_i = (x_i, y_i)^T$ is the image coordinate of the ith point, $\mathbf{P}_{i+1} = (x_{i+1}, y_{i+1})^T$ is the image coordinate of the $(i + 1)$-th point, and m is the total number of the points on the light stripe. Figure 4(c) shows the light stripes after disturbances elimination, in which the length threshold is 20, and we consider all of them are effective.

Thirdly, link the light stripes. The purpose of this step is to tie up the light stripes that belong to the same light plane and prepare for next arrangement. For any two light stripes in Figure 4(c), if the difference between the abscissas of endpoints is less than the preset threshold, the two light stripes can be linked. Figure 4(d) is the light linked stripes from Figure 4(c) and the preset threshold is 30. It should be noted that this step is just to tie up the light stripes that belong to the same light plane, instead of adding light points at the gaps.

Finally, arrange the linked light stripes. The arrangement principle is based on the distance between the straight line determined by the left edge of the image and the light stripes: the light stripe with shorter distance is more close to the left. The distance between a straight line and a light stripe is
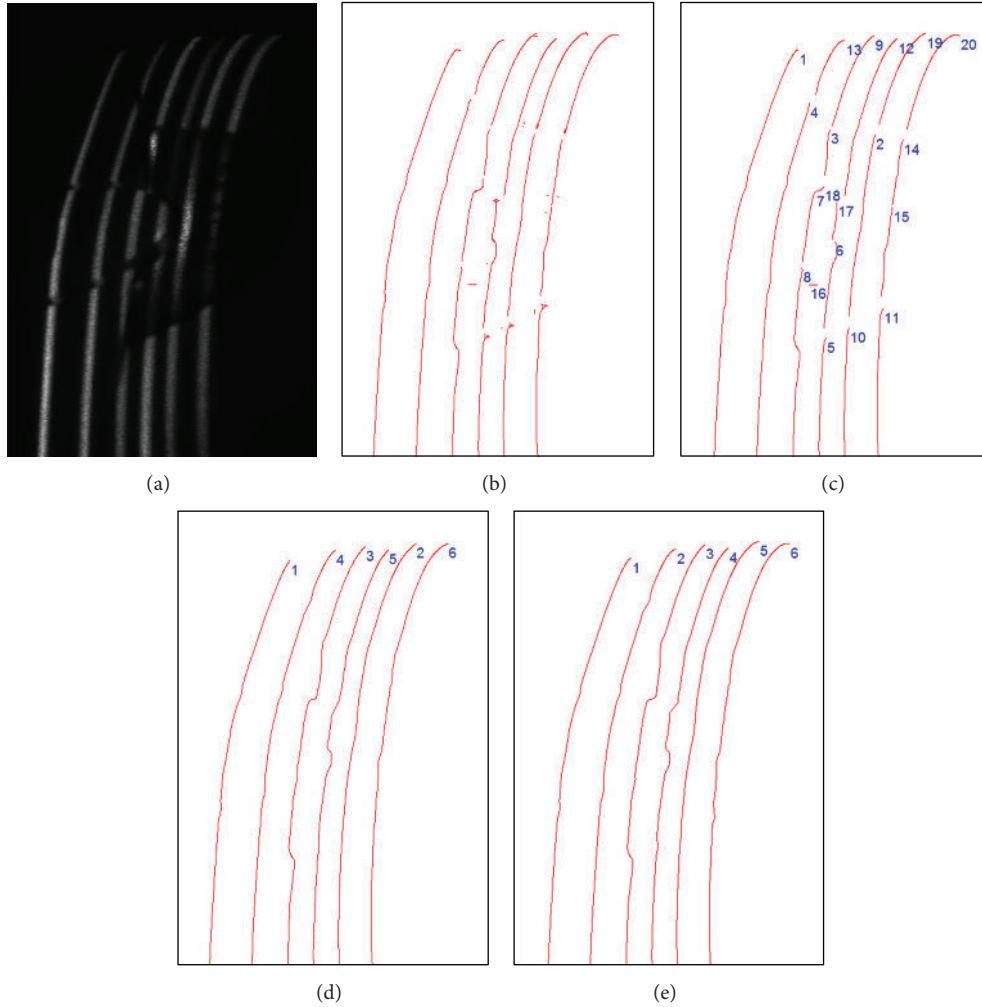
FIGURE 4: Light stripes extraction and arrangement. (a) Image with light stripes. (b) Extracted light stripes. (c) Light stripes after disturbances elimination. (d) Linked light stripes. (e) Light stripes arrangement.

defined as the minimum of distances from the points on the light stripe to the line:

$$d = \min_{1 \leq i \leq m} |ax_i + by_i + c|, \tag{7}$$

where $\mathbf{P}_i = (x_i, y_i)^T$ is the image coordinates of the ith point on the light stripe, m is the total number of points, $ax+by+c = 0$ is the equation of straight line on the image plane, and, here, the straight line is $x = 0$. The ordered light stripes are shown in Figure 4(e).

5. System Calibration

Calibration is the third major problem to be solved in MSSS. The parameters in the MSSS and their physical meanings are listed in Table 1 and all of them are determined by calibration.

5.1. Parameters of Camera and Light Plane Equations. The internal and external parameters of the two cameras can be calibrated by Zhang's method described in [21].

The calibration of light plane equation can be obtained by using a 2D planar target. Take sensor 1 as an example. The calibration model of line-structured-light sensor is shown in Figure 5. The world coordinate system $o_w - x_w y_w z_w$ is established as shown in Figure 5: $o_w - x_w y_w$ is the target plane and the z component is 0. Light stripe L, projected as l in the image plane, is the intersection of the structured-light plane π_1^l and the target plane.

Owing to the 2D projective transformation between the target plane and the image plane, the coordinates of the points on the image plane can be transformed from the coordinates of the points on the target plane through a 3×3 homography matrix:

$$s\mathbf{P}_u = \mathbf{H}\mathbf{P}'_w, \tag{8}$$

where $\mathbf{H}$ is the homography matrix; $\mathbf{P}_u = (x_u, y_u, 1)^T$ is the image coordinate of the feature points on the 2D target and $\mathbf{P}'_w = (x_w, y_w, 1)^T$ is the local 2D world coordinate of the corresponding points; s is a nonzero scale factor.

TABLE 1: System parameters.

Category	Parameters	Physical meaning	Remarks
Internal parameters	(f_x, f_y)	Focal length in the x and y directions	One each sensor
	(u_0, v_0)	Main point coordinates	One each sensor
	(k_1, k_2)	Radial distortion parameters	One each sensor
External parameters	$\mathbf{R}$	Rotation matrix	One each sensor
	$\mathbf{T}$	Translation vector	One each sensor
Light plane equation	(a, b, c, d)	Light plane equation coefficients	Three each sensor
Unit translation vector	$\mathbf{V}$	Scanning direction	Only sensor 1
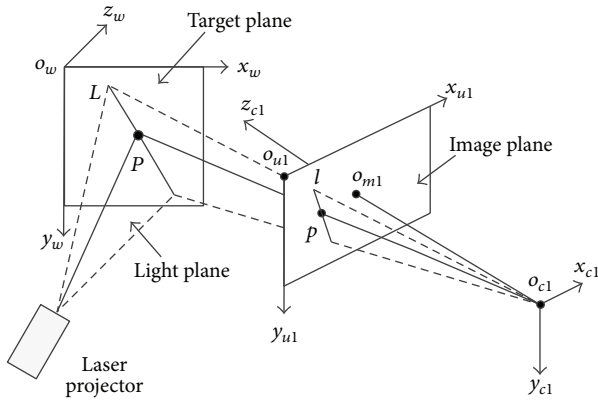
FIGURE 5: Calibration model of line structured-light sensor.

Matrix $\mathbf{H}$ has 8 degrees of freedom and it can be obtained with a scale factor from (8) requiring at least four non-collinear corresponding points. Since the matrix $\mathbf{H}$ obtained by the linear approach is susceptible to noise interference, we establish an objective function to optimize the matrix $\mathbf{H}$ in order to get an optimal solution. The objective function is the sum of the squares of the distance between two coordinates:

$$\sum_{i=1}^{m} \left\| \mathbf{P}_{ui} - \mathbf{F}\left(\mathbf{H}, \mathbf{P}'_{wi}\right) \right\|^2, \tag{9}$$

where $\mathbf{P}_{ui}$ is the image coordinate of the ith feature point on the planar target; $\mathbf{F}(\mathbf{H}, \mathbf{P}'_{wi})$ is the coordinate that $\mathbf{P}'_{wi}$ transformed to the image coordinate system through $\mathbf{H}$ matrix. $\mathbf{P}'_{wi}$ is the local 2D world coordinate of the ith feature point on the target, and m is the number of the feature points on the target. The nonlinear optimization problem is solved by Levenberg-Marquardt optimization algorithm, and initial value can be got from the linear solution.

Since matrix $\mathbf{H}$ is a nonsingular matrix, we can calculate the local 2D world coordinates of points on target plane from the corresponding image coordinate through the inverse matrix of $\mathbf{H}$:

$$\left(x_w, y_w, 1\right)^T = s\mathbf{H}^{-1}\left(x_u, y_u, 1\right)^T. \tag{10}$$

In summary, the camera coordinates of the points on the light stripe L can be obtained in the following three steps. Firstly, get the image coordinates of the feature points on the 2D planar target and calculate the homography matrix

$\mathbf{H}$ according to (8)-(9). Secondly, get the image coordinates $(u, v, 1)^T$ of the points in the light stripe l, and use (10) to calculate the local 2D world coordinate $(x_w, y_w, 1)^T$, whose corresponding 3D world coordinate is $\mathbf{P}_w = (x_w, y_w, 0)^T$. Finally, convert $(x_w, y_w, 0)^T$ to camera 1 coordinate system to get the camera coordinates of points on the light stripe L by (1).

After placing the planar target at several different positions, coordinates of a sufficiently large number of points in the camera coordinate system on the light plane π_1^l can be calculated using the above method, after which the space equation of light plane π_1^l can be fitted. Similarly, the space equations of the other light planes can also be obtained in the same way.

In practical, before calculating the space equation of light planes, the one-to-one corresponding relationship of the light planes and the straight light stripes in the images must be determined in advance. The simplest solution is to arrange the light stripes from left to right using the method described in Section 4.

5.2. Unit Translation Vector. As shown in Figure 6, the position of the world coordinate system is fixed while camera 1 is driven to move along the direction of the vector $\mathbf{V}$.

For a point F in the space, its world coordinates are denoted by $\mathbf{P}_w = (x_w, y_w, z_w)^T$ and its camera coordinates before and after translation are denoted by $\mathbf{P}'_c = (x'_c, y'_c, z'_c)^T$, $\mathbf{P}''_c = (x''_c, y''_c, z''_c)^T$. According to the rotation and translation relationship between world coordinate system and camera 1 coordinate system, we have

$$\mathbf{P}'_c = \mathbf{R}_1 \mathbf{P}_w + \mathbf{T}_1.$$
$$\mathbf{P}''_c = \mathbf{R}_2 \mathbf{P}_w + \mathbf{T}_2. \tag{11}$$

$\mathbf{R}_1$, $\mathbf{T}_1$ are the rotation matrix and translation vector between camera coordinate system and world coordinate system before translation, while $\mathbf{R}_2$, $\mathbf{T}_2$ are the rotation matrix and translation vector after translation. The translation vector $\mathbf{V}$ in camera 1 coordinate system is described by

$$\mathbf{V} = \mathbf{P}''_c - \mathbf{P}'_c = \left(\mathbf{R}_2 - \mathbf{R}_1\right)\mathbf{P}_w + \mathbf{T}_2 - \mathbf{T}_1. \tag{12}$$

To facilitate the calculation, the world coordinate system origin $\mathbf{P}_w = (0, 0, 0)^T$ is selected as the point F and then the translation vector in camera 1 coordinate system is

Table 2: Configuration information of MSSS.

Digital CCD camera					
Quantity	Interface	Resolution	Pixel size	Frame rate	Optic size
2	USB2.0	1280 (H) × 1024 (V)	5.2 (μm) × 5.2 (μm)	15 fps	1/1.8 inch
Lens					
Quantity	Focal length	Horizontal angle of view		Dimensions	
2	16 mm	22.72°		29.5 mm (D) × 32 mm (L)	
Laser projector					
Quantity	Size	Wavelength	Operating voltage	Output power	Fan angle
6	ϕ8 × 26 mm	650 nm	DC 5 V	2.5 mW	50°
Stepping motor					
Length	Rated current			Step angle	
51 mm	1 A			1.8°	
Stepping motor controller					
Input voltage		Output current		Support RS232	
24–48 VDC		0.1–5 A (peak)		RS232, CAN bus	
Grating ruler					
Operating voltage	Length	Resolution	Max speed	Interface	
5 V ± 5% DC	500 mm	5 μm	≥60 m/min	USB2.0	
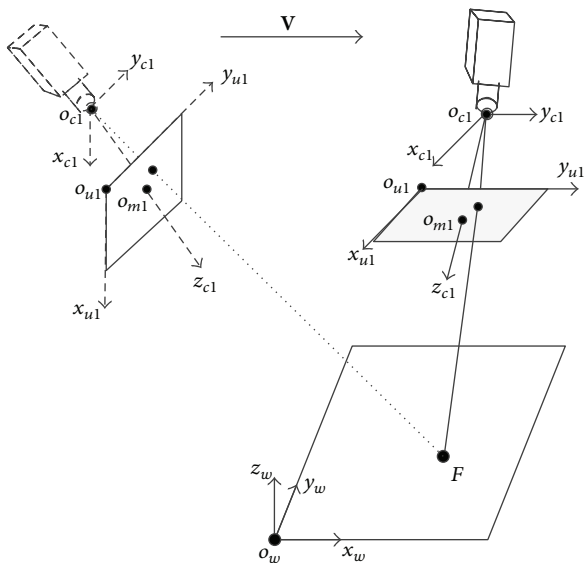
Figure 6: Mathematical model of the sensor translation.

Figure 7: The MSSS scanning measurement system. (1) Camera 1. (2) Camera 2. (3) Glass platform. (4) Linear motion stage. (5) Grating ruler. (6) Laser projectors of sensor 1. (7) Laser projectors of sensor 2. (8) Stepping motor.

transformed into $\mathbf{V} = \mathbf{T}_2 - \mathbf{T}_1$. After converting it to world coordinate system and vector unitization, the unit translation vector can be obtained.

Above describes the process of obtaining 3D coordinates in the world coordinate system for sensor 1. The process for sensor 2 is similar. Therefore, merging left and right scanners' 3D data is done by transforming them from camera 1 and camera 2 to the world coordinate system, respectively.

6. Experimental Results

6.1. System Calibration Setup. The MSSS is illustrated in Figure 7.

The configuration information of every part is listed in Table 2.

We designed a planar pattern with 10 × 11 circles for calibration, shown in Figure 8. The centers of the circles on the pattern are used as the calibration feature points. The diameter of the big circle is 15 mm and that of the small one is 9 mm. In the vertical direction, the distance between two adjacent centers is 15 mm, and the distance of two adjacent centers in the horizontal direction is 15 mm except that the fifth and the sixth column are 30 mm.

The system calibration process is as follows.

(1) Place the planar pattern randomly at 10 positions within the FOV of each camera and each camera
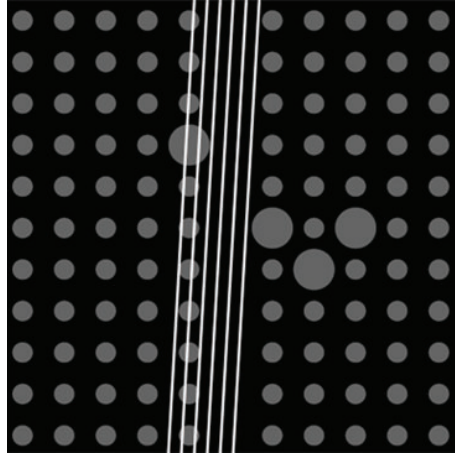
FIGURE 8: Target and the projected light stripes.
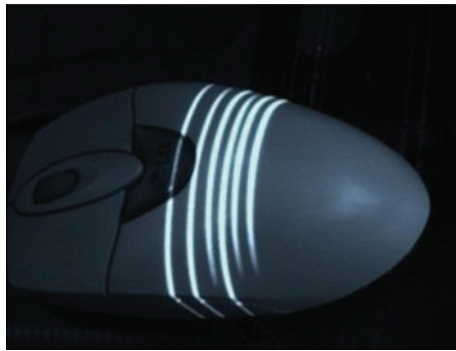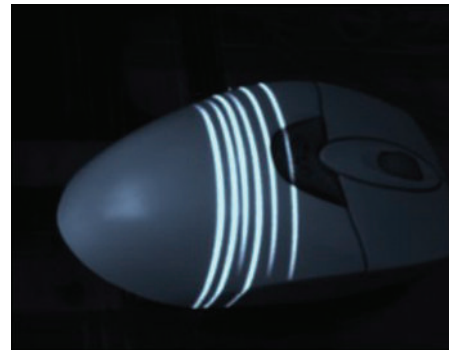
(a)   (b)
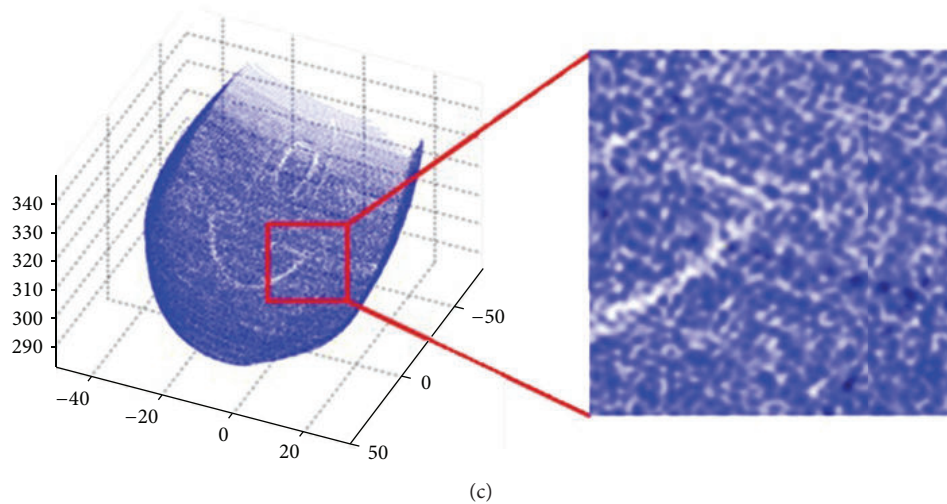
(c)

FIGURE 9: Measurement experiment of a mouse. (a) Light stripe image of the mouse captured by sensor 1. (b) Light stripe image of the mouse captured by sensor 2. (c) 3D reconstruction results of the mouse.

obtains an image at each position. Extract the image coordinates of the feature points on the pattern from the images. Then calibrate the internal parameters of the two cameras by Zhang's method.

(2) Place the planar pattern at the public area in the FOV of the two cameras and two cameras obtain

an image, respectively. Extract the image coordinates of the feature points on the pattern from the two images. Calibrate the camera external parameters by Zhang's method to obtain the rotation and translation relationship between the camera and the world coordinate systems.

(a)

(b)

(c)
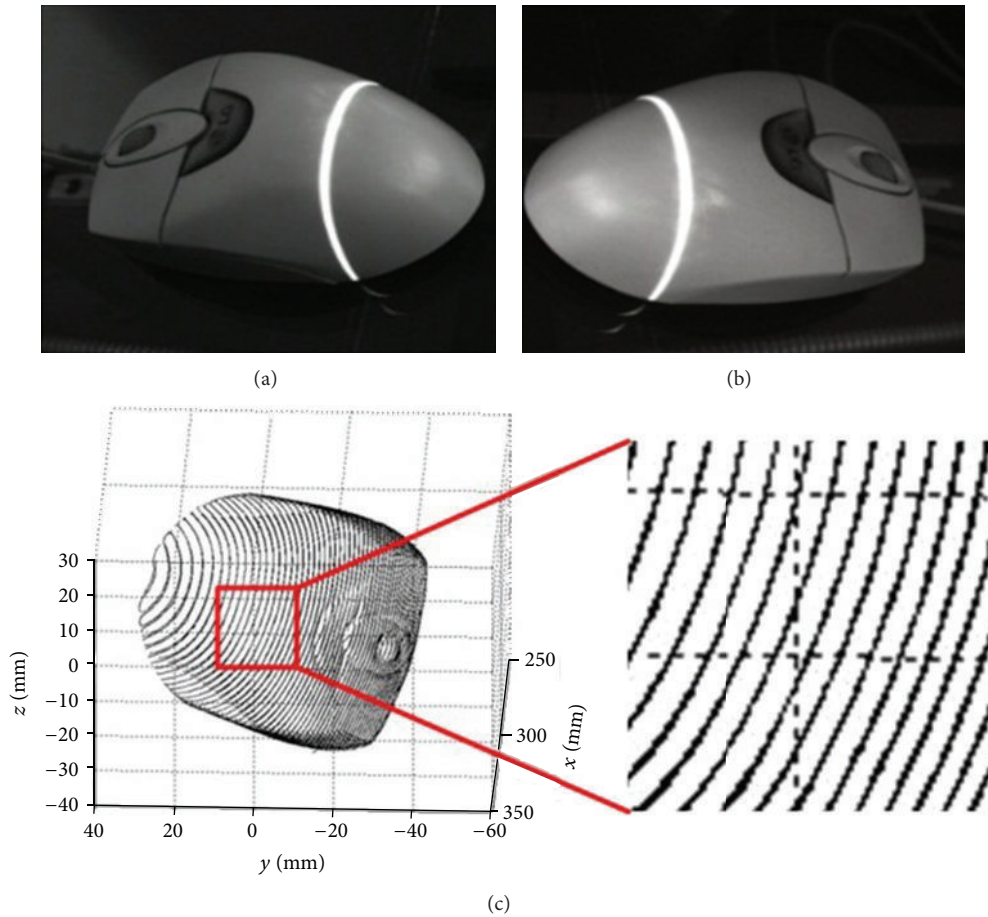
FIGURE 10: Comparison experiment using single scan line. (a) Single stripe image of the mouse captured by camera 1. (b) Single stripe image of the mouse captured by camera 2. (c) 3D reconstruction results of the mouse.

(3) Fix the pattern within the FOV of camera 1, start the stepping motor, and drive the sensors to move forward. Camera 1 captures an image before and after the movement, respectively. As the world coordinate system plane $o_w - x_w y_w$ coincides with the pattern plane, the location of the world coordinate system is fixed. Then calibrate the unit translation vector $\mathbf{V}$ using the two images as mentioned in Section 5.2.

(4) Open the line-structured-light projectors, and project the planar lights on the pattern. Randomly move the pattern to three positions within the FOV of the two cameras, and each camera captures an image for each position. Calculate the camera coordinates of the points on the light stripe on the pattern. Fit the six light plane equations of the two sensors in each camera coordinate system according to the method described in Section 5.1.

6.2. Experimental Results

6.2.1. Calibration Results. The calibration results of the MSSS are shown in Table 3.

6.2.2. Accuracy Evaluation Results. The line-structured-light sensor calibration accuracy is verified by comparing two values: one is the standard value, which is the camera coordinate of the intersection point of the ray $O_{c1} p$ and the target plane, as shown in the Figure 5, and the other is the measured value, which is the camera coordinate of the intersection point of $O_{c1} p$ and the light plane. Taking light plane π_1^l for example, two of the images used for structured-light calibration are chosen to evaluate the sensor calibration accuracy. We selected six points on the light stripe in each image and evaluated the sensor calibration accuracy. The calibration accuracy evaluation data is shown in Table 4, which shows that the RMS errors in x, y, and z directions are 0.004 mm, 0.008 mm, and 0.092 mm, respectively.

We placed the planar pattern at another random position, and calculate the errors of the light plane π_1^r of the calibrated system in the same way. Those data can serve as the evaluation for sensor measurement accuracy since they are not involved in calibration process. The RMS errors for the system measurement accuracy in each axis are RMSx = 0.006 mm, RMSy = 0.015 mm, and RMSz = 0.168 mm, as shown in Table 5.

TABLE 3: Calibration results of the MSSS scanning measurement system.

	Sensor 1	Sensor 2
(f_x, f_y)/pixels	(3129.509, 3128.652)	(3043.739, 3045.095)
(u_0, v_0)/pixels	(614.430, 536.804)	(632.633, 554.142)
(k_1, k_2)	(−0.1857, −0.0143)	(−0.1870, 0.1157)
Rotation matrix (**R**)	-9.375×10^{-1} 1.422×10^{-1} 3.177×10^{-1} -1.127×10^{-3} -9.139×10^{-1} 4.058×10^{-1} 3.481×10^{-1} 3.801×10^{-1} 8.569×10^{-1}	9.495×10^{-1} 1.373×10^{-1} -2.823×10^{-1} 3.787×10^{-3} 8.942×10^{-1} 4.476×10^{-1} 3.139×10^{-1} -4.260×10^{-1} 8.485×10^{-1}
Translation vector (**T**)	74.612 71.063 228.107	−92.646 −66.043 299.890
Light plane equation coefficients	$8.793 \times 10^{-3}, 1.444 \times 10^{-4}, -3.315 \times 10^{-3}, 1.000$ $9.456 \times 10^{-3}, 2.054 \times 10^{-4}, -3.504 \times 10^{-3}, 1.000$ $9.974 \times 10^{-3}, 1.280 \times 10^{-4}, -3.788 \times 10^{-3}, 1.000$	$-1.046 \times 10^{-2}, -2.670 \times 10^{-4}, -3.810 \times 10^{-3}, 1.000$ $-9.878 \times 10^{-3}, -2.885 \times 10^{-4}, -3.672 \times 10^{-3}, 1.000$ $-9.026 \times 10^{-3}, -2.965 \times 10^{-4}, -3.445 \times 10^{-3}, 1.000$
Translation union vector (**V**)	9.384×10^{-1} -5.897×10^{-3} -3.454×10^{-1}	

TABLE 4: Calibration accuracy evaluation data for π_1^l in sensor 1.

	Image coordinates	Intersection points of line and target plane			Intersection points of line and light plane			Errors of coordinates		
	(u, v)/pixels	x/mm	y/mm	z/mm	x/mm	y/mm	z/mm	Δx/mm	Δy/mm	Δz/mm
Position 1	(663.495, 20.000)	4.918	−51.840	312.263	4.920	−51.856	312.356	−0.002	0.016	−0.093
	(628.546, 216.800)	1.372	−31.127	303.753	1.372	−31.137	303.852	0.000	0.010	−0.099
	(593.597, 413.600)	−1.969	−11.649	295.753	−1.970	−11.653	295.837	0.001	0.003	−0.083
	(558.648, 610.400)	−5.138	6.780	288.186	−5.139	6.782	288.237	0.001	−0.001	−0.051
	(523.699, 807.200)	−8.160	24.324	280.985	−8.160	24.324	280.989	0.000	0.000	−0.004
	(488.750, 1004.000)	−11.059	41.118	274.094	−11.057	41.110	274.038	−0.002	0.008	0.056
Position 2	(583.124, 20.000)	−2.935	−48.434	291.751	−2.934	−48.422	291.678	−0.001	−0.012	0.074
	(546.201, 216.800)	−6.200	−29.084	283.792	−6.202	−29.091	283.855	0.001	0.007	−0.064
	(509.277, 413.600)	−9.289	−10.886	276.313	−9.294	−10.892	276.449	0.005	0.005	−0.136
	(472.353, 610.400)	−12.230	6.337	269.241	−12.237	6.340	269.395	0.007	−0.004	−0.154
	(435.429, 807.200)	−15.047	22.736	262.514	−15.054	22.746	262.639	0.007	−0.011	−0.124
	(398.506, 1004.000)	−17.761	38.439	256.079	−17.165	38.447	256.133	0.004	−0.008	−0.054
RMS errors (mm)								0.004	0.008	0.092

TABLE 5: Measurement accuracy evaluation data for π_1^r in sensor 2.

Image coordinates	Intersection points of line and target plane			Intersection points of line and light plane			Errors of coordinates		
(u, v)/pixels	x/mm	y/mm	z/mm	x/mm	y/mm	z/mm	Δx/mm	Δy/mm	Δz/mm
(449.701, 20.000)	−19.302	−56.272	319.259	−19.310	−56.297	319.400	0.008	0.024	−0.140
(475.684, 216.800)	−15.959	−34.264	308.722	−15.955	−34.256	308.647	−0.003	−0.008	0.075
(501.667, 413.600)	−12.870	−13.800	298.917	−12.862	−13.791	298.723	−0.008	−0.009	0.194
(527.650, 610.400)	−9.998	5.357	289.732	−9.990	5.352	289.501	−0.008	0.004	0.232
(553.633, 807.200)	−7.311	23.409	281.070	−7.306	23.393	280.870	−0.005	0.017	0.201
(579.616, 1004.000)	−4.782	40.528	272.851	−4.780	40.511	272.737	−0.002	0.017	0.113
RMS errors (mm)							0.006	0.015	0.168

6.3. Measurement Results. A mouse is scanned by the MSSS to demonstrate the applicability. Figures 9(a) and 9(b) show the captured mouse image pair with light stripes projected on. From Figures 9(a) and 9(b), we can see, with single sensor, that there is blind area, where 3D coordinates are unable to obtain. The whole mouse is covered when 2 sensors are adopted, complementing each other's blind area. Figure 9(c) shows the 3D scanning result of the mouse, in which the scanning speeding is 7 mm/s and the time consumption is 16 seconds. Compared to the existing single or double structured-light 3D surface measurement system, our MSSS greatly improved scanning efficiency and obtained richer

3D surface data at the same scanning speeding and time consumption. In order to compare with the single line scan method, we used only one laser generator in each sensor. Figures 10(a) and 10(b) show the single stripe image captured by cameras 1 and 2, respectively, and Figure 10(c) shows the 3D reconstruction results. Note that here we use the same scan speed and frame rate for both multiline and single-line experiments. Because, with the same scan speed and frame rate, multiline approach provides more features in one frame than that of single-line approach; therefore, it gains richer information of the target.

7. Conclusions

A novel approach is presented to capture the 3D surface based on multiline structured-light sensors. There are three superiorities for this method compared with the existing methods.

(1) The disadvantages of single structured-light 3D surface measurement system are overcome, such as limited measurement range, blind measurement area, and low scanning efficiency.

(2) The mathematical model of the MSSS is established without particular spatial relationship, making the system easy to implement.

(3) The system calibration is completed by a 2D planar pattern. It does not require complex calibration patterns or high-precision auxiliary equipment, which reduces the difficulty of the system calibration and ensures the measurement accuracy simultaneously.

In addition, note that the method proposed in this paper is not only applicable for the multi-line structured-light sensor with three light stripes, but also suitable for the sensor with more light stripes, which can further improve the scanning efficiency.

Conflict of Interests

The authors declare that there is no conflict of interests regarding the publication of this paper.

Acknowledgment

References

[1] G. Zhang, J. He, and X. Li, "3D vision inspection for internal surface based on circle structured light," *Sensors and Actuators A: Physical*, vol. 122, no. 1, pp. 68–75, 2005.

[2] C. Rocchini, P. Cignoni, C. Montani, P. Pingi, and R. Scopigno, "A low cost 3D scanner based on structured light," *Computer Graphics Forum*, vol. 20, no. 3, pp. C/299–C/308, 2001.

[3] P. Lavoie, D. Ionescu, and E. M. Petriu, "3-D object model recovery from 2-D images using structured light," *IEEE Transactions on Instrumentation and Measurement*, vol. 53, no. 2, pp. 437–443, 2004.

[4] W. Wei, C.-K. Sun, X.-D. Zhang, and S.-H. Ye, "Study on non-contact measurement method based on line-structured laser for vehicle wheel alignment parameters," *Journal of Optoelectronics Laser*, vol. 15, no. 12, pp. 1479–1482, 2004.

[5] C. Alippi, E. Casagrande, F. Scotti, and V. Piuri, "Composite real-time image processing for railways track profile measurement," *IEEE Transactions on Instrumentation and Measurement*, vol. 49, no. 3, pp. 559–564, 2000.

[6] H.-H. Loh and M.-S. Lu, "Printed circuit board inspection using image analysis," *IEEE Transactions on Industry Applications*, vol. 35, no. 2, pp. 426–432, 1999.

[7] K. Haug and G. Pritschow, "Robust laser-stripe sensor for automated weld-seam-tracking in the shipbuilding industry," in *Proceedings of the 24th Annual Conference of the IEEE Industrial Electronics Society (IECON '98)*, pp. 1236–1241, September 1998.

[8] J. Apolinar Muñoz Rodríguez, "On line self-calibration for mobile vision based on laser imaging and computer algorithms," *Optics and Lasers in Engineering*, vol. 49, no. 6, pp. 680–692, 2011.

[9] Y. Ju, T. Ju, J. Liu, and G. Liu, "Principle and system design of foot profile 3-D measuring device based on light-section method," *Journal of Transducer Technology*, vol. 21, pp. 18–21, 2002.

[10] A. Patiño and J. Meneses, "Optic system for the measurement of metrological parameters of the foot," in *5th Iberoamerican Meeting on Optics, and 8th Latin American Meeting on Optics, Lasers, and their Applications*, Proceedings of SPIE, pp. 84–90, October 2004.

[11] J. J. Koenderink and A. J. van Doorn, "Two-plus-one-dimensional differential geometry," *Pattern Recognition Letters*, vol. 15, no. 5, pp. 439–443, 1994.

[12] B. Andreas, "A common framework for the extraction of lines and edges," *International Archives of Photogrammetry and Remote Sensing*, vol. 31, pp. 88–93, 1996.

[13] L. Wang and T. Pavlidis, "Detection of curved and straight segments from gray scale topography," *CVGIP: Image Understanding*, vol. 58, no. 3, pp. 352–365, 1993.

[14] L. Wang and T. Pavlidis, "Direct gray-scale extraction of features for character recognition," *IEEE Transactions on Pattern Analysis and Machine Intelligence*, vol. 15, no. 10, pp. 1053–1066, 1993.

[15] R. Dewar, "Self-generated targets for spatial calibration of structured-light optical sectioning sensors with respect to all external coordinate system," in *Proceedings of the Robots and Vision Conference*, pp. 5–13, 1988.

[16] F. Duan, F. Liu, and S. Ye, "A new accurate method for the calibration of line structured-light sensor," *Chinese Journal of Scientific Instrument*, vol. 21, pp. 108–110, 2000.

[17] D. Q. Huynh, R. A. Owens, and P. E. Hartmann, "Calibrating a structured light stripe system: a novel approach," *International Journal of Computer Vision*, vol. 33, no. 1, pp. 73–86, 1999.

[18] C. Sun, Q. You, Y. Qiu, and S. Ye, "Online machine vision method for measuring the diameter and straightness of seamless steel pipes," *Optical Engineering*, vol. 40, no. 11, pp. 2565–2571, 2001.

[19] R. S. Lu and Y. F. Li, "A global calibration method for large-scale multi-sensor visual measurement systems," *Sensors and Actuators A: Physical*, vol. 116, no. 3, pp. 384–393, 2004.

[20] G. Steger, "An unbiased detector of curvilinear structures," *IEEE Transactions on Pattern Analysis and Machine Intelligence*, vol. 20, no. 2, pp. 113–125, 1998.

[21] Z. Zhang, "A flexible new technique for camera calibration," *IEEE Transactions on Pattern Analysis and Machine Intelligence*, vol. 22, no. 11, pp. 1330–1334, 2000.

Research Article

Profile Measurement Based on Focus Variation Method for Geometrical Defect Evaluation: A Case Study of Cold Forged Propeller Blade

A. B. Abdullah,[1] S. M. Sapuan,[2] and Z. Samad[1]

[1] *School of Mechanical Engineering, Universiti Sains Malaysia, Engineering Campus, 14300 Nibong Tebal, Penang, Malaysia*
[2] *Department of Mechanical and Manufacturing Engineering, Faculty of Engineering, Universiti Putra Malaysia,*
   43400 Serdang, Selangor, Malaysia

Correspondence should be addressed to A. B. Abdullah; mebaha@eng.usm.my

Geometrical defect is one of the main problems that will affect performance and perfect mating of produced parts. Coordinate measurement machine (CMM) is commonly used for the measurement, but the use of this machine is limited because of the small size and complexity of the component or features. This study aims to evaluate the defect that occurs on an AA6061 cold forging blade produced using cold forging process based on profile measurement technique. A systematic approach based on focus variation was proposed to evaluate two features, that is, roundness error and twist deviation. The profile was obtained with the use of InfiniteFocus Alicona 3D surface measurement system. Specific algorithms were developed for different cases as the evaluation of the features is discrete and the results were validated.

1. Introduction

Assembly accuracy depends on part quality, but defects damage part quality and its accuracy [1]. Accuracy is very crucial in manufacturing near-net or net-shape parts with complex profiles. The main goal of net-shape manufacturing is achieved when components are allowed for assembly without requirement of secondary processes such as machining [2]. Therefore, it is essential to detect and prevent the defect as early as possible during the production process. Cold forging, one of the net-shape manufacturing processes, is governed by many factors such as friction, part geometry, die shape, and temperature setting of the die and workpieces. Hence, the cold forging process has a high tendency to form defects. Arentoft and Wanheim [3] classified forging part defect into six: fold, shear defect, surface defect, form defect, crack, and structural defect. Causes of defects include die deflection, yielding or wear, and eccentricity or buckling due to flow imperfection. Kimura et al. [4] evaluated component assembly based on shape error. F. C. Lin and

S. Y. Lin [5] studied the folding defect during the cold extrusion of aluminum. The relationships between defect and geometrical shape were studied based on the radius ratio. A similar approach was employed to investigate the barreling formation during cylinder upsetting with hollow die [6]. Metal flow imperfection related defect has attracted the attention of many researchers. Chan et al. [7] proposed a dynamic change of tooling geometry to control the most common flow-induced defect such as folding. Other defects such as die filling and barrel formation during the lateral extrusion process have been discussed by Tahir [8]. Similarly, Liu et al. [9] studied the underfilling problem in the rotary rolling of a flange. On the other hand, Narayanasamy et al. [10] studied the reaction of various metals to barreling during the cold upsetting process. In his study, unlubricated truncated cone billets were used as a case study, and the relationship between the measured radius of curvature of the barrels and the stress ratio parameter was established. In addition, Baskaran and Narayanasamy [11] applied white grease as a lubricant to determine the dimensions such as
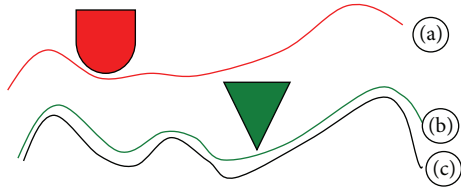
FIGURE 1: Comparison between (a) tactical and (b) optical surface measurement methods to (c) the measured surface [19].

FIGURE 2: The problem faced while using CMM: (a) small diameter and (b) inconsistent depth [19].

height, contact, and bulge diameter at different stress-ratio parameters. Yilmaz et al. [12] conducted an experimental investigation of conventional closed-die forging to study the effect of aspect ratios and indentation to the forging load and die filling. Lu and Zhang [13] found that forging defects are caused by improper die dimension. Their study was carried out, taking into consideration the temperature dependency of the thermal and mechanical properties of materials. Song and Im [14] studied the effect of process design parameters on the formation of underfilling and folding defect during closed-die forging of bevel gears. In another study, it was proposed that, by optimizing process sequence, surface defect can be solved [15]. On the other hand, Qamaz investigated the effect of shape complexity and dead metal zone on the quality of cold extruded part [16]. In addition, Sheu and Yu [17] introduced a new type of die design to solve the folding defect during the orbital forging process. The new design influenced the flow of the preform, resulting in lower tool stresses and preventing the folding problem. Sun et al. [18] studied the material flow behavior of magnesium alloy in the formation of hook, sidewall, and boss during the press forging of notebook cases. They introduced methods to prevent the material from flowing outwards, which causes the geometrical defect.

Noncontact methods such as vision system and image processing techniques are among the most recent approaches. They offer systems that are consistent, accurate, and highly repeatable [20]. The noncontact method produced better result as the probe size limit effective measurement compared to the lens used in the noncontact method, which is more focus as illustrated in Figure 1. In addition, the application of contact method such as CMM is also limited by the size and characteristics of the hole, as shown in Figure 2.

For circular features or component, defects such as out-of-roundness (outer or inner) may affect the quality and accuracy of assemblies [21] and fatigue life of the hole [22]. Roundness variations or out-of-roundness can be measured from the maximum inward deviations of the part's profile from the minimum inscribed circle. Roundness errors or out-of-roundness can be defined as the minimum radial separation of the bounding concentric circles, which contain an actual boundary of a measured section of manufactured workpiece [23]. Perfect roundness is the condition in which all surfaces of a circle are identical or equidistant from the center point or axis. Typically the evaluation process can be categorized into two stages, begin with data collection from the scanned image, and end with roundness measurement. There are two types of data collection methods, that is,
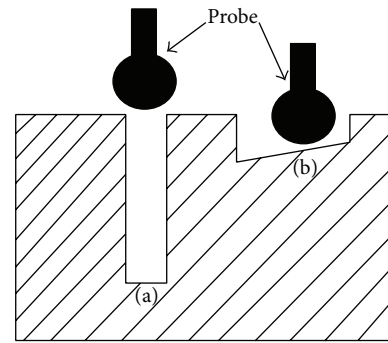
contact (tactical) and noncontact (optical). In most cases, a contact method such as coordinate measurement machine (CMM) is used in the data generation stage in the form of a Cartesian coordinate [24]. Once the coordinates are obtained, the parameters of the best-fitting geometrical features can be evaluated [23]. However, the system requires high-precision setup and is time consuming [25].

In evaluating roundness error, for example, researchers emphasize the development of fast and efficient algorithms or approaches. For example, in dealing with a large number of points gained from a profile, especially from CMM, Gadel-mawla [21] introduced a simple and efficient algorithm to evaluate the roundness error. The software is developed based on three criteria: maximum circumscribing circle, maximum inscribed circle, and least square circle. Li and Shi [23] used curvature techniques to evaluate roundness error. In their study, the computational geometrical concept of convex hulls is exploited to reduce computations. Other techniques include employing computational geometry, such as the application of Voronoi diagram [26, 27] and the introduction of outer and inner convex hulls to simplify evaluation [28]. Huang and Zheng [29] evaluated roundness based on area hunting. However, Wen et al. [30] proposed a method to unify all four models of roundness by employing genetic algorithm. Integration can be achieved through formulation of the objective function of the models, and then the initial populations are generated to solve this problem simultaneously. From the literature, no effort has been made to measure the roundness based on profile deviation gathered from optical method. In practice, various engineering components have been produced through forging or machining processes that involve roundness, such as cylinder bores and connecting rods. Measurements are typically performed to evaluate the roundness as a result of tool wear and chattering in machining of hole [31] and hole punching [32] after use for a period of time. Roundness has become one of the quality measures of parts [33]. Therefore, it needs to be evaluated rapidly and accurately.

The paper presents an introduction, and then the concept of surface measurement technique based on focus variation is explained. The problem statement is outlined, followed by the methodology of the study. The result is then discussed and a case study of cold forged propeller blade was performed to
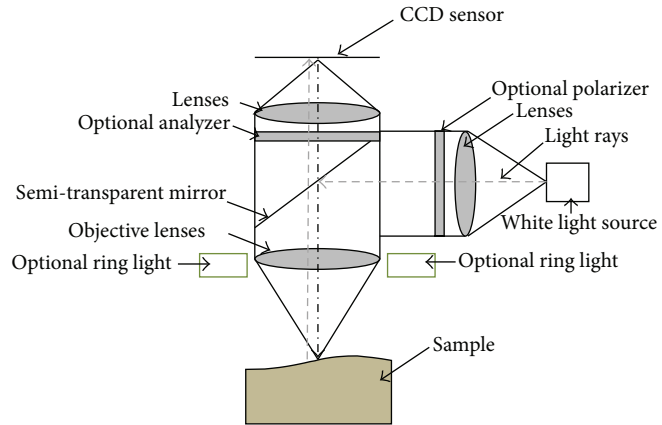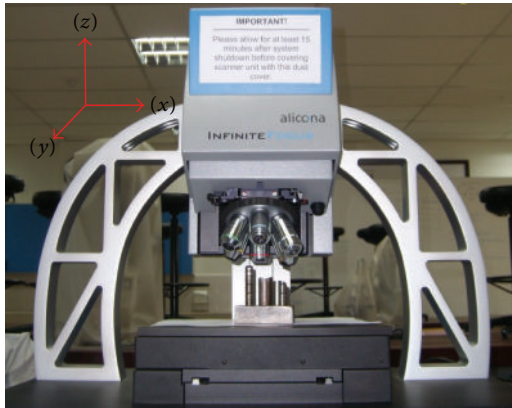
FIGURE 3: The coordinates system of the Alicona and mechanism of scanning.

clarify the developed technique. The paper ends with conclusions.

2. Focus Variation

Focus variation is a method that allows the measurement of a real surface topography with the use of optics with limited depths of field and vertical scanning [34]. In focus variation, the depth is determined through a search of the best focus position of an optical element pointing to a sample related to a certain distance from the depth value. The conduct of this procedure for many lateral positions results in the construction of a depth map. The diagrams of the Alicona system and the mechanism of focus variation are shown in Figure 3. The process begins as the white light from the light-emitting diode source is transmitted through a transparent mirror and the objective lenses to the sample. Because of variations in the topography and reflectivity of the sample, light is reflected in different directions. The reflected light is partly collected by the objective and projected through a semitransparent mirror and the tube lens to the charge-coupled device sensors. To measure the focus, the standard deviation of the grey values of a small local region can be calculated using this equation [35]:

$$F_z(x, y) = \text{FM}\left(\text{reg}_w\left(I_z, x, y\right)\right). \tag{1}$$

The amount of focus, F_z, is a function of a focus measure, FM to the region operator $\text{reg}_w(I_z, x, y)$, which extracts information from I_z at the lateral position (x, y) over a certain rectangular region of $w \times w$ pixels. The content of the I_z at height z is used an input. In order to make sure that the captured images are correct, the operator needs to make sure correct positioning and coordinate system, which will be further discussed in Section 4. Furthermore, for each measurement results, both measurement value and the measurement uncertainty will be provided. This can increase quality and validity of the measurement value.

3. Case Study

A propeller blade has a complex shape and typically comprises four parts, namely, the suction face, pressure face, leading edge, and trailing edge. In addition, there are other features that need to be added to the blade for assembly purposes [36], that is the pin head. In autonomous underwater vehicle assembly [36], which consists of the blade and hubs, the blade needs to be sandwiched between the rear and front hubs, as shown in Figure 4. The head has direct contact to the hub, so the quality of the hole is crucial to ensure perfect mating between the two parts. In contrast, the accuracy of the pin head is not critical as the shape will deform according to the cavity, as shown in Figure 5. Therefore, the roundness of the pin head is assumed to be perfect. The main problem is the hole produced on the front hub involved in the assembly. The size of the hole is considerably small and has inconsistent depth. Therefore, the use of CMM is quite limited, and setting up the machine is time consuming. In addition, the complex profile of the blade causes difficulties in the fixturing and in determining the reference points or surfaces.

The formation of twist bending is one of the primary sheet-forming processes currently employed by major automotive industries. However, the process results in a severe springback problem, which affects the accuracy of the finished part. Although springback is considered a manufacturing error, its proper assessment and precise control have been a rather challenging task [37]. This is because springback will affect the twist angle of the blade, which directly is related to the performance of the propeller [38]. A number of studies have already been conducted on the springback problem, but none have focused on the twist springback that involves thickness changes or thinning. From mechanics point of view, the twist springback results from torsional moments in the cross section of the workpiece. The torsional displacement develops from the unbalanced elastic deformation and residual stresses acting in part to create a torsional moment, which tends to rotate one end of the part relative to another. The torsional moment can originate from the in-plane residual stresses in the flange, in the sidewall, or both [39]. In the production of a propeller blade, bending
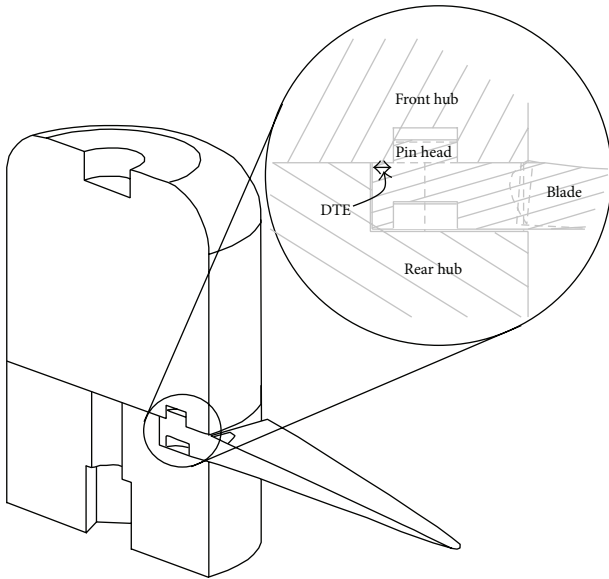
Figure 4: Final assembly of the AUV propeller.
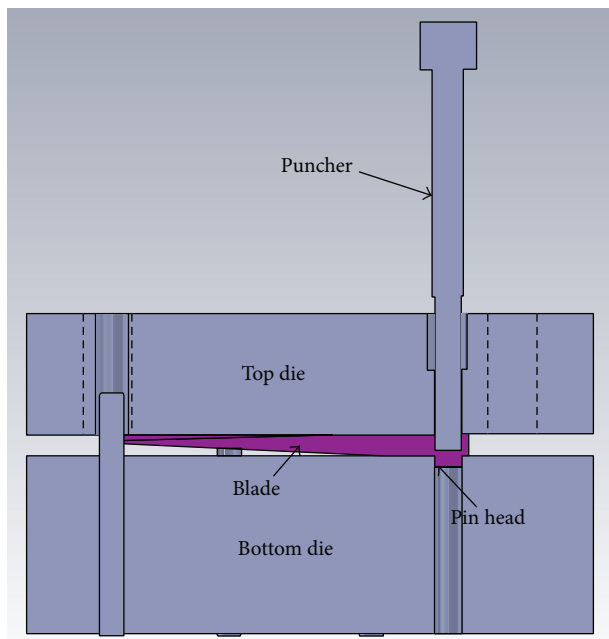
Figure 5: The embossing tooling of the blade.

Figure 6: The definition of the twist angle and chord length.
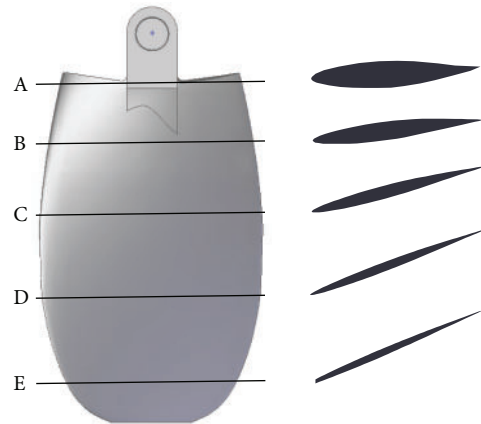
Figure 7: Five sections of the blade.

twist forming is commonly used to produce the twisted shape of the blade.

The springback is measured based on twist angle deviation and can be defined as $\beta_b - \beta_d$, where β_b is the twist angle of the blade and β_d is the twist angle measured on the punch. The twist angle β is defined in terms of the chord line with respect to the horizontal line, and blade twist angle defines the pitch settings at each position along the blade according to local flow conditions [40], as demonstrated in Figure 6. The chord length can be defined as the distance between the trailing edge and the point on the leading edge. Given that the twist angle varies along the blade, therefore for 2D

investigation, the blade is cut into few sections, as shown in Figure 7. Makem et al. [41] defined the similar phenomenon as twist deviation. Figure 6 shows the coordinate system of the blade and to ensure correct measurement, both blade and measurement equipment coordinate system must be the same.

4. Methodology

The methodology can be described into two stages. In the first stage, the scanning and mapping procedures of the profile are same. In the second stage, due to discrete features, specific algorithm was developed. The first stage begins with the construction of profile from scanned 3D surface. For scanning, the studied parts will be placed on the table, and lens with 2.5x magnification (vertical resolution of 2300 nm). Note that the magnification level will affect the quality of the scanned part and the time required for scanning. For this case, lens with 2.5x magnification is enough as recommended in the manual. The part is placed onto the motorized stage and for the blade, which is not flat, plasticine was used to avoid unnecessary movement during scanning. One of the advantages of Alicona system is a technology, namely, Smart-Flash Technology, which will ensure quality and reliability of the captured image at minimal part setting up. The resulted profiles can be converted into z-x coordinates, which then plot in Excel sheet.

4.1. Roundness Error. The raw data of the hole profile obtained from the scanning is in 3D. For roundness error measurement, which involved four stages as illustrated in Figure 6, the data then need to convert into 2D. Begin with

(a)

(b)

(c)

(d)
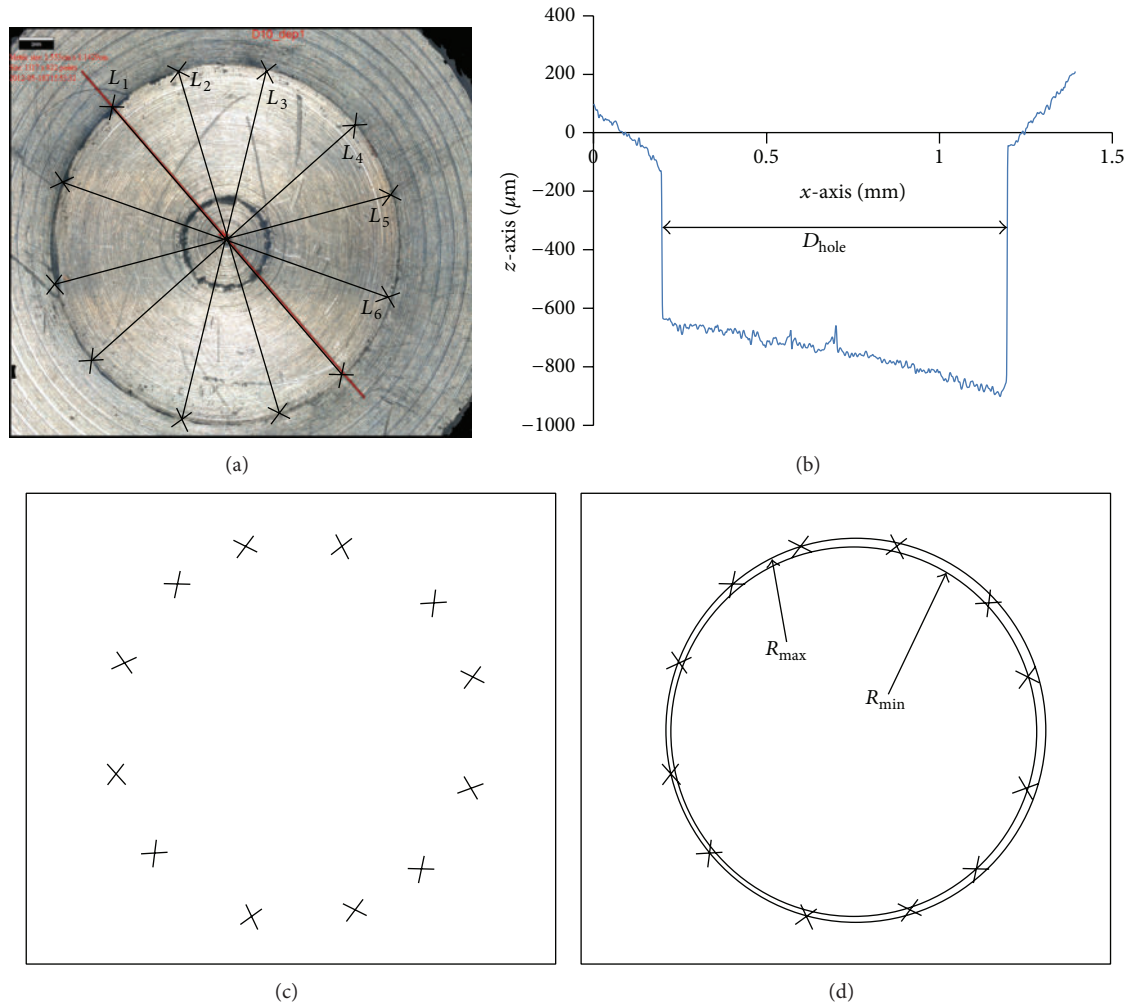
FIGURE 8: The steps in determining roundness error.

the construction of at least three straight lines ($n_{line} \geq 3$) that intersect at the center of the hole (Figure 8(a)). Intersection point at the center is assumed to be the center of the hole. Note that, for reference, the length of the lines must not exceed the nominal diameter of the hole, which has been determined from the mapped profile as shown in Figure 8(b). In addition, based on that reference, point at edge of each line will be determined named point cloud. Then, point cloud will be determined at the intersection between the constructed line and hole radius after the lines were deleted as illustrated in Figure 8(c). Using the MZC rules, the maximum and minimum radius as well as roundness error can be determined as shown in Figure 8(d). A simple programme has been developed using Matlab to automate this task, begins with the construction of the lines until determination of the center and radius of the hole. The nominal diameter of the hole is 1.0 ± 0.1 mm. The flowchart of the approach can be summarized in Figure 9.

Since the holes are made through embossing process, the problem or situation where the axial axis of the hole deviates from the scanning direction is slightly less, but the main problem that usually occurs is nonflat surface due to part tilting during forming process.

4.2. Twist Springback Measurement. The process begins with the filtering stage, where all undesired data or noises are deleted. In this case, noises depict the defective data that resulted from unexpected measurement error. The twist angle deviation is determined by comparing between two profiles which is in contact during forming process, that is, the die profile (profile *d*) which represents the targeted profile and the blade profile (profile *b*) which represents the manufactured profile. But the resulted profiles are at different direction curvature: one of the constructed profiles is in concave while another is in convex shape. Therefore, an algorithm is required to translate one of the profiles, which can be systematically compared. In this paper, the double-mirroring technique is proposed. The mirroring is performed on each point that comprises the profile. The steps of the mirroring algorithm are given below. The algorithm begins with determination of the midpoint (m_x, m_y) of the
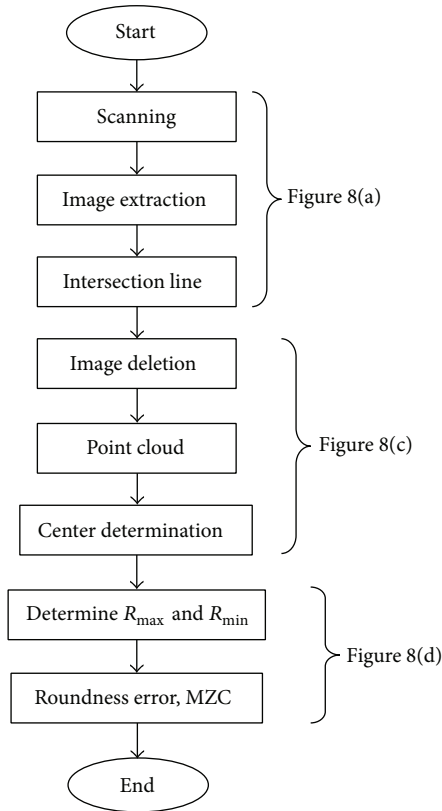
FIGURE 9: Flowchart for the roundness error determination.
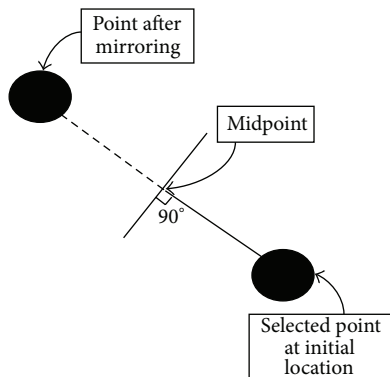
FIGURE 10: Example of the mirroring technique for one of the points.

profile, which is half of the chord length. Next, the selected point in vector unit will be computed. After mirroring from the midpoint, new translated point will be defined (x_2, y_2). The proposed algorithm named as double mirroring as the mirroring steps is repeated twice in order to complete the task. Figure 10 demonstrates the steps as follows:

(i) determination of the midpoint

(m_x, m_y) = half of the chord length;

(ii) computation of the vector of point

$d_x, d_y = (x_1 - m_x, y_1 - m_y)$;
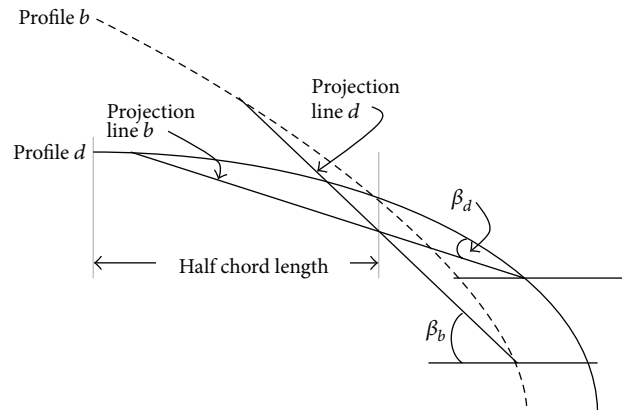
FIGURE 11: The twist angle deviation measurement.

(iii) applying first mirroring, 180 degrees from the midpoint

$d_{x1} = -d_y$ and $d_{y1} = d_x$;

(iv) determination of new points

$x_2 = m_x + d_{x1}$ and $y_2 = m_y + d_{y1}$;

(v) repetition of the same steps for all points.

After the completion of the mirroring process, the deviation can be measured. In this approach, the intersection of both profiles is equal to half of a chord length, that is, the midpoint which is assumed to be fixed for this case. A straight projection line can then be drawn between two points defined on both profiles, projection line b for the blade and projection line d for the die as shown in Figure 11. The starting and end points of the line must be at the same distance from the midpoint. The angle of both profiles can then be determined. This approach has been modified from the technique initiated by Makem et al., [41]. Notably, both projection lines must be intersected at the same intersection location and initial profiles. Finally both twist angles, twist angle for the blade, β_b, and twist angle for the die, β_d, can be defined before the twist springback can be determined.

5. Results and Discussion

In this study, two parameters, namely, the punch diameter and the depth of the embossing, were studied, and their effect on the quality of the hole was evaluated. Figures 12(a) to 12(c) present the measured roundness errors of the hole on the obtained profile at different diameters. For validation, measurement using Mitutoyo roundtest machine was performed, and the results agreed with those obtained with the presented method. Specimens with a diameter of 10 mm cannot be measured because of hole instability. From the experiment, the maximum roundness error is 13 μm. The results indicate that although the amount of error is different, both measurement techniques depict a similar pattern. The line without a marker is the profile measured with Alicona and the line with a marker is the profile measured with the roundtest machine.

(a)

(b)

(c)
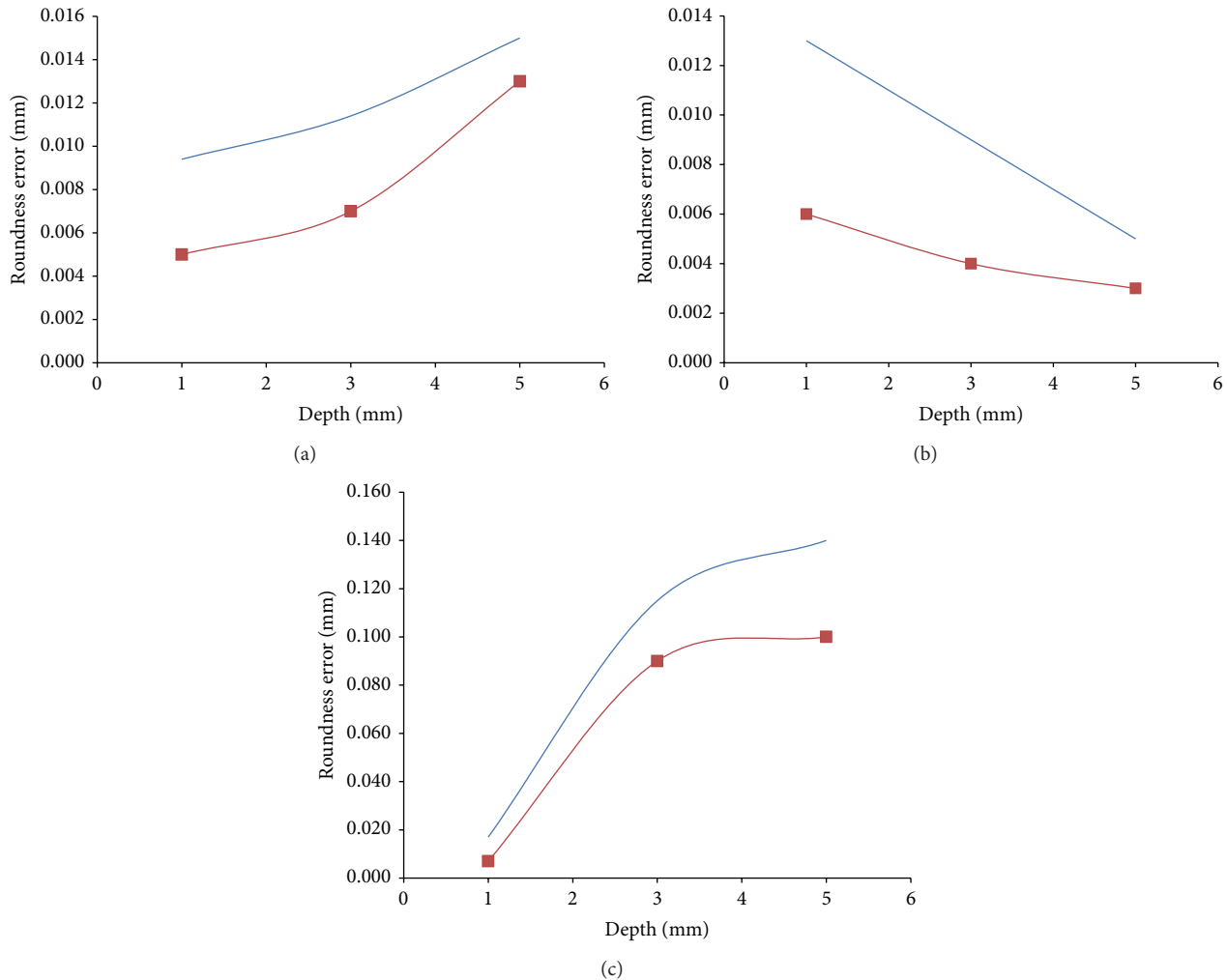
FIGURE 12: Roundness error pattern at different hole diameters (a) 3 mm, (b) 5 mm, and (c) 10 mm.

In this study, the profile of the punch is considered to be the targeted profile, whereas the profile of the blade is taken as the manufactured profile. To ensure better visualization, white acrylic spray was applied to the surface of the die and the punch. For benchmarking, the twist angle of the blade from the theoretical and nominal models was mapped, as shown in Figure 9, and a very good agreement was obtained.

Figure 13(a) shows the profile constructed by using the profile of the blade section obtained from Alicona after the filtering and cleaning processes. Figure 13(b) illustrates the profile obtained after the mirroring technique was applied. The measured twist springback is summarized in Table 1. The twist angle was measured based on the edge of the profile by referring to the chord length of each section.

Based on the result obtained from the measurement, the effect of the deformation ratio is considered to be significant, as depicted in Figure 11. As the deformation ratio increases, the springback also increases, especially at a deformation ratio of 3. However, beyond this deformation ratio, the increments gradually decline because twisting goes beyond the plastic region of the section.

TABLE 1: Twist springback measured.

Section	Deformation ratio	β_b (degree)	β_d (degree)	Springback (%)
A	1.990	47.54	48.80	2.58
B	2.802	49.27	51.76	4.81
C	2.969	52.67	58.90	10.58
D	3.219	56.20	65.48	14.17
E	5.704	56.50	67.35	16.11

6. Conclusion

This study aimed to evaluate the quality of a cold embossed hole. The evaluation is based on profile deviation gathered from 3D surface measurement. Overall, the produced hole is within acceptable limits. The quantified error agrees with the experimental value. The study also aimed to present a case study of the roundness error of the hole produced by cold embossing process of the pin head. The hole is embossed

(a)

(b)
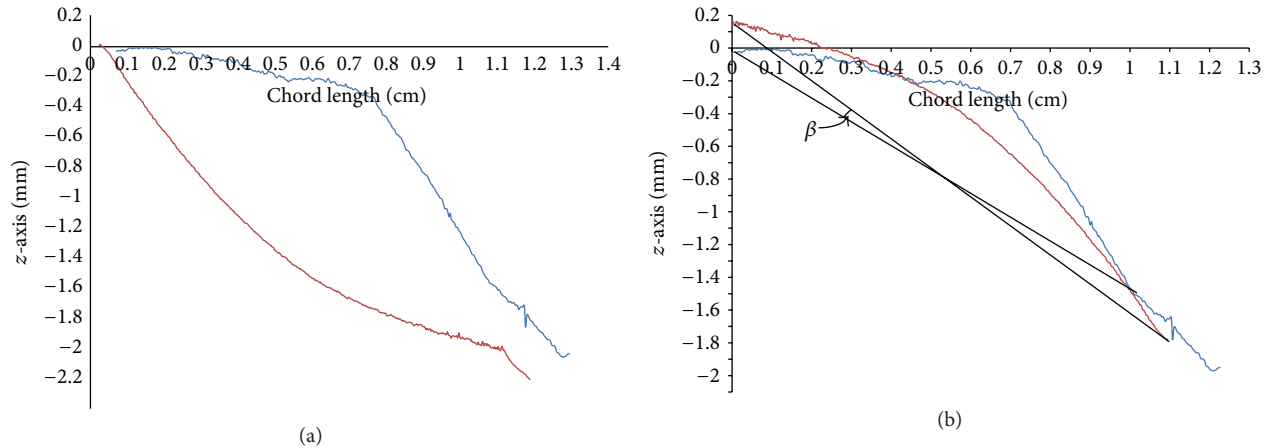
FIGURE 13: The resulted profiles of the blade and punch (a) before and (b) after applying the algorithm.

to produce a hole that is designed to ensure proper mating between the blade and the propeller's body. The results show that the roundness of the hole is within the control limit. The measurements were based on the difference between the profile obtained from the Alicona system, and CMM was used to validate the result. The error was measured based on a selected section of the propeller blade, which was assumed to represent the overall profile of the blade. The primary contributions of this paper found that optical images can provide a clear profile of the blade, which can be used to evaluate the geometrical defect of complex shape parts.

Comparisons were made between the resulted profiles and the established methods. For the case of roundness, comparison was made with the measurement of roundness error using Mitutoyo roundtest machine and the result depicted a deviation of less 5%, whereas in the case of twist springback measurement, a coordinate measurement machine (CMM) was utilized and the deviation is less than 10%.

Conflict of Interests

The authors declare that there is no conflict of interests regarding the publication of this paper.

Acknowledgment

References

[1] F. Vollertsen, "Accuracy in process chains using hydroforming," *Journal of Materials Processing Technology*, vol. 103, no. 3, pp. 424–433, 2000.

[2] J. Kopač and M. Soković, "Dimensional accuracy and cost optimisation in the finish machining of cold formed parts," *Journal of Materials Processing Technology*, vol. 92-93, pp. 335–343, 1999.

[3] M. Arentoft and T. Wanheim, "The basis for a design support system to prevent defects in forging," *Journal of Materials Processing Technology*, vol. 69, no. 1–3, pp. 227–232, 1997.

[4] F. Kimura, H. Suzuki, and K. Takahashi, "Product design evaluation based on effect of shape errors for part assembly," *CIRP Annals*, vol. 41, no. 1, pp. 193–196, 1992.

[5] F. C. Lin and S. Y. Lin, "Radius ratio estimation and fold situation prediction of the deformation profile in forging-extrusion process," *Computers & Structures*, vol. 80, no. 24, pp. 1817–1826, 2002.

[6] F. C. Lin and S. Y. Lin, "Prediction of fold defect in barreling formations of cylinder upsetting," *Finite Elements in Analysis and Design*, vol. 39, no. 4, pp. 325–341, 2003.

[7] W. L. Chan, M. W. Fu, J. Lu, and L. C. Chan, "Simulation-enabled study of folding defect formation and avoidance in axisymmetrical flanged components," *Journal of Materials Processing Technology*, vol. 209, no. 11, pp. 5077–5086, 2009.

[8] A. Tahir, "A study of barreling profile and effect of aspect ratio on material flow in lateral extrusion of gear-like forms," *Indian Journal of Engineering and Materials Sciences*, vol. 14, no. 3, pp. 184–192, 2007.

[9] G. Liu, L. B. Zhang, X. L. Hu et al., "Applications of numerical simulation to the analysis of bulk-forming processes—case studies," *Journal of Materials Processing Technology*, vol. 150, no. 1-2, pp. 56–61, 2004.

[10] R. Narayanasamy, A. S. A. Thaheer, and K. Baskaran, "Comparison of barreling in unlubricated truncated cone billets during cold upset forging of various metals," *Indian Journal of Engineering and Materials Sciences*, vol. 13, no. 3, pp. 202–208, 2006.

[11] K. Baskaran and R. Narayanasamy, "Effect of various stress ratio parameters on cold upset forging of irregular shaped billets using white grease as lubricant," *Indian Journal of Engineering and Materials Sciences*, vol. 13, no. 4, pp. 281–292, 2006.

[12] C. Yilmaz, A. M. Tahir, and A. H. Erol, "An investigation on forging loads and metal flow in conventional closed-die forging of preforms obtained by open-die indentation," *Indian Journal of Engineering and Materials Sciences*, vol. 11, no. 6, pp. 487–492, 2004.

[13] C. Lu and L.-W. Zhang, "Numerical simulation on forging process of TC4 alloy mounting parts," *Transactions of Nonferrous Metals Society of China*, vol. 16, no. 6, pp. 1386–1390, 2006.

[14] J.-H. Song and Y.-T. Im, "Process design for closed-die forging of bevel gear by finite element analyses," *Journal of Materials Processing Technology*, vol. 192-193, pp. 1–7, 2007.

[15] M. M. Mohammadi and M. H. Sadeghi, "Numerical and experimental investigation of forging process of a CV joint outer race," *International Journal of Research and Review in Applied Science*, vol. 2, no. 1, pp. 1–8, 2010.

[16] S. Z. Qamar, "Shape complexity, metal flow, and dead metal zone in cold extrusion," *Materials and Manufacturing Processes*, vol. 25, no. 12, pp. 1454–1461, 2010.

[17] J. J. Sheu and C. H. Yu, "The die failure prediction and prevention of the orbital forging process," *Journal of Materials Processing Technology*, vol. 201, no. 1–3, pp. 9–13, 2008.

[18] C. Sun, S.-H. Zhang, W.-D. Tang, and Z.-T. Wang, "Press forging of magnesium-alloy notebook case with complex geometry," *Materials and Manufacturing Processes*, vol. 25, no. 7, pp. 534–538, 2010.

[19] Alicona Infinitefocus IFM Manual, IFM 2.1.3, 2008.

[20] M.-C. Chen, "Roundness measurements for discontinuous perimeters via machine visions," *Computers in Industry*, vol. 47, no. 2, pp. 185–197, 2002.

[21] E. S. Gadelmawla, "Simple and efficient algorithms for roundness evaluation from the coordinate measurement data," *Measurement*, vol. 43, no. 2, pp. 223–235, 2010.

[22] J. Liu, X. J. Shao, Y. J. Liu, Y. S. Liu, and Z. F. Yue, "The effect of holes quality on fatigue life of open hole," *Materials Science and Engineering A*, vol. 467, no. 1-2, pp. 8–14, 2007.

[23] X. Li and Z. Shi, "The relationship between the minimum zone circle and the maximum inscribed circle and the minimum circumscribed circle," *Precision Engineering*, vol. 33, no. 3, pp. 284–290, 2009.

[24] G. L. Samuel and M. S. Shunmugam, "Evaluation of circularity from coordinate and form data using computational geometric techniques," *Precision Engineering*, vol. 24, no. 3, pp. 251–263, 2000.

[25] T.-H. Sun, "Applying particle swarm optimization algorithm to roundness measurement," *Expert Systems with Applications*, vol. 36, no. 2, pp. 3428–3438, 2009.

[26] U. Roy and X. Zhang, "Development and application of Voronoi diagrams in the assessment of roundness error in an industrial environment," *Computers & Industrial Engineering*, vol. 26, no. 1, pp. 11–26, 1994.

[27] K. Kim, S. Lee, and H.-B. Jung, "Assessing roundness errors using discrete Voronoi diagrams," *International Journal of Advanced Manufacturing Technology*, vol. 16, no. 8, pp. 559–563, 2000.

[28] X. Li and Z. Shi, "Development and application of convex hull in the assessment of roundness error," *International Journal of Machine Tools and Manufacture*, vol. 48, no. 1, pp. 135–139, 2008.

[29] F. Huang and Y. Zheng, "A method for roundness error evaluation based on area hunting," *Acta Metrologica Sinica*, vol. 29, no. 2, pp. 117–119, 2008.

[30] X. Wen, Q. Xia, and Y. Zhao, "An effective genetic algorithm for circularity error unified evaluation," *International Journal of Machine Tools and Manufacture*, vol. 46, no. 14, pp. 1770–1777, 2006.

[31] G.-B. Jeong, D. H. Kim, and D. Y. Jang, "Real time monitoring and diagnosis system development in turning through measuring a roundness error based on three-point method," *International Journal of Machine Tools and Manufacture*, vol. 45, no. 12-13, pp. 1494–1503, 2005.

[32] S. Y. Luo, "Effect of the geometry and the surface treatment of punching tools on the tool life and wear conditions in the piercing of thick steel plate," *Journal of Materials Processing Technology*, vol. 88, no. 1–3, pp. 122–133, 1999.

[33] Q. H. Kong and C. S. Liu, *Limit Conjunction and Measuring Technology*, Tongji University Press, Shanghai, China, 2002.

[34] R. Danzl, F. Helmli, and S. Scherer, "Focus variation—a robust technology for high resolution optical 3D surface metrology," *Journal of Mechanical Engineering*, vol. 57, no. 3, pp. 245–256, 2011.

[35] F. Helmli, "Focus variation instruments," in *Optical Measurement of Surface Topography*, R. Leach, Ed., pp. 131–166, Springer, Berlin, Germany, 2011.

[36] A. B. Abdullah, S. M. Sapuan, Z. Samad, H. M. T. Khaleed, and N. A. Aziz, "Numerical investigation of geometrical defect in cold forging of an AUV blade pin head," *Journal of Manufacturing Processes*, vol. 15, no. 1, pp. 141–150, 2013.

[37] A. B. Abdullah, S. M. Sapuan, Z. Samad, and N. A. Aziz, "A comprehensive review of experimental approaches used in the measurement of springback," *Advances in Natural and Applied Sciences*, vol. 6, no. 2, pp. 195–205, 2012.

[38] G. Q. Zhang, S. C. M. Yu, A. Chien, and Y. Xu, "Unsteady aerodynamic investigation of the propeller-wing interaction for a rocket launched unmanned air vehicle," *Advances in Mechanical Engineering*, vol. 2013, Article ID 735168, 12 pages, 2013.

[39] A. B. Abdullah, S. M. Sapuan, Z. Samad, H. M. T. Khaleed, and N. A. Aziz, "Geometrical error analysis of cold forged AUV propeller blade using optical measurement method," *Advanced Materials Research*, vol. 383–390, pp. 7117–7121, 2012.

[40] S. M. Habali and I. A. Saleh, "Local design, testing and manufacturing of small mixed airfoil wind turbine blades of glass fiber reinforced plastics—part I: design of the blade and root," *Energy Conversion and Management*, vol. 41, no. 3, pp. 249–280, 2000.

[41] J. Makem, H. Ou, C. G. Armstrong, A. Rennie, and S. Nikov, "A virtual inspection technique for assessing the dimensional accuracy of forged compressor blades using FE modeling and CMM inspection," *International Journal of Material Forming*, vol. 1, no. 1, pp. 375–378, 2008.

Research Article
Variable-Weighted Grayscale Centroiding and Accuracy Evaluating

Mingli Dong,[1] Liang Xu,[1] Jun Wang,[1] Peng Sun,[1,2] and Lianqing Zhu[1]

[1] *Beijing Key Laboratory of Opto-Electronic Measurement Technology, Beijing Information Science and Technology University, Beijing 100192, China*
[2] *Institute of Information Photonics and Optical Communications, Beijing University of Posts and Telecommunications, Beijing 100876, China*

Correspondence should be addressed to Mingli Dong; dongml@sina.com

Grayscale-weighted centroiding weights the pixel intensity to estimate the center of a circular image region such as a photogrammetric target or a star image. This is easy to realize with good robustness; however, locating accuracy varies with weight. There is no conclusion as to the relationship between weight and centroiding accuracy. To find this relationship and thus acquire the highest achievable accuracy of centroiding, one must first derive the general model of centroiding as follows. (1) Set weighting as a function that includes the grayscale intensity of each pixel and two undetermined parameters α and β. The centers were calculated from the new weights. (2) Design an accuracy evaluation method for centroiding based on a virtual straight-line target to obtain the accuracy of centroiding with various parameters. With these parameter values and accuracy records, the accuracy-parameter curve can be fitted. In the end, simulations and experiments are conducted to prove the accuracy improvement of this variable-weighted grayscale centroiding compared with traditional centroiding. The experimental result shows that the parameter α contributes significantly to accuracy improvement. When $\alpha = 1.5$, locating accuracy is 1/170 pixels. Compared to centroiding and squared centroiding, the new locating method has a 14.3% and 10.6% accuracy improvement indicating that it improves locating accuracy effectively.

1. Introduction

Large-scale photogrammetry is mainly applied to precise locating and measuring in automobile, aircraft, shipbuilding, and other large-scale industrial manufacturing and assembling; surface measurements of satellite antennas and radio telescopes; and deformation measurements in load tests of large parts [1, 2]. Unlike small-scale measurement [3], large-scale photogrammetry is always used to measure large objects; it requires extremely favorable relative precision to ensure high accuracy. As the source data of photogrammetric metrology, the accuracy of photogrammetry is greatly affected by the determination of the target image coordinates. Target image locating accuracy is affected by environmental conditions, target characteristics, imaging system performance, and the locating algorithm, where environmental conditions can be optimized according to specific

requirements. Since Brown applied retro-reflective target (RRT) to photogrammetry, target image quality has been greatly improved. It is easy to obtain a quasibinary image. Currently the limitation of locating accuracy is mainly caused by imaging system performance and the locating algorithm.

Digital imaging systems have great advantages over film imaging systems, and they are gradually replacing film imaging systems. A digital imaging system performance index includes the lens modulation transfer function, the resolution of the charge-coupled device (CCD, there are also other imaging sensors, for example, CMOS, but CCDs are most commonly used in digital close-range photogrammetry) resolution, the photoelectric conversion efficiency, and electrostatic noise. Nowadays, CCD resolution is the major factor that limits locating accuracy. Limited by the manufacturing process, digital cameras have resolutions of several megapixels when it was newly applied to photogrammetry,

(a) Microglass beads on RRT surface

(b) Light path in a microglass bead
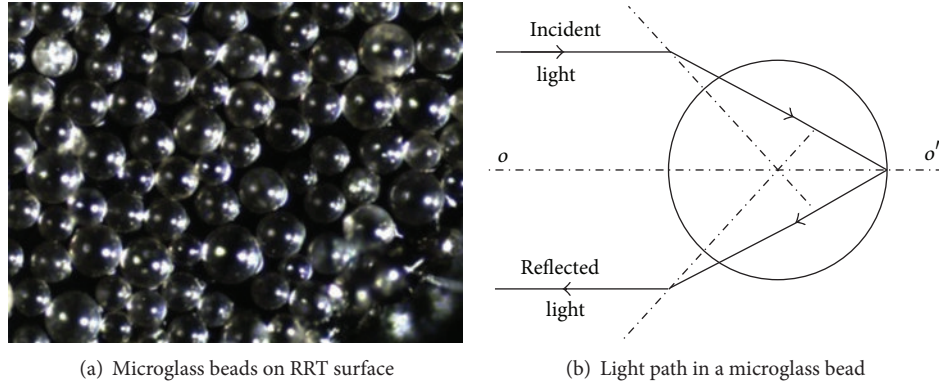
FIGURE 1: RRT structure and light path.

and it was only half size of the 135 film. Until now, the size of the CCD in most advanced digital camera backs on the market is generally about 50 mm × 40 mm. The resolution varies from 50 to 80 megapixels, while the film camera CRC-1 which was designed by Brown in 1984 has a film format of 230 mm × 230 mm with an equivalent pixel size of 3.1 μm × 2.5 μm [4]. That means that film has an equivalent resolution of 6 giga pixels, which is far higher than CCD cameras. This results in the fact that the highest accuracy the large field digital photogrammetry products can reach is about 1/200,000, which is lower than the film photogrammetry systems designed 20 years ago [5, 6]. Therefore, researchers turn to subpixel locating technology.

The proposed target image locating method can be divided into three main categories. The first is model fitting based on intensity distribution, such as Gaussian surface fitting. This method requires an intensity distribution model; however, it is difficult to model a facula precisely especially for large RRT, that may transfer or enlarge the error. The second is shape fitting based on target appearance, such as ellipse fitting. This method relies on the edge locating accuracy. It is more difficult to locate an edge precisely than the whole target image since there is less information. Moreover, the affine transformation distinguishes between the two centers in the image plane and the object space [7]. The third is weighted centroiding based on gray intensity weighting. This method calculates the whole target image and estimates its center as the gray intensity center. It has good robustness to noise, and the computing is simple. Locating accuracy differs as weights change with the form of a nonlinear function.

The two existing examples are centroiding and squared centroiding. Studies indicate that squared centroiding has superior accuracy [8]. But there is no evidence that squared grayscale weight has optimal accuracy for weighted centroid locating. This paper derives a general model of centroiding. The weight is set as a function of pixel grayscale intensity of two undetermined parameters α and β, and then an analysis is conducted to prove that there is a set of α and β providing the highest accuracy location for grayscale-weighted centroiding. Then an accuracy evaluating method is designed to obtain accurate centroiding with various

parameter values. With these parameter values and accuracy records, the accuracy-parameter curve can be fitted. Meanwhile the optimal values for α and β are obtained.

2. Variable-Weighted Grayscale Centroiding

2.1. Retro-Reflective Target (RRT). As already mentioned, applying RRT to photogrammetry has vastly contributed to the development of photogrammetry. RRT materials can be classified as glass beads or microprisms according to their basic structure. Considering the production process, costs, and reflection symmetry properties, the glass bead RRT is used most commonly. Glass bead is the basic reflective element (Figure 1(a)). The glass beads are deposited onto a reflective layer. The incident light is refracted through the glass beads, focused onto reflecting layer behind the glass beads, and then returned to the incident side through reflection and refraction (Figure 1(b)) [9]. To make sure that the whole reflecting surface of RRT is uniform, the size of glass beads must be small enough, typically 10–30 μm. To achieve good retro-reflective performance, the refractive index of the glass beads is generally between 1.9 and 2.2.

Due to the retro-reflectivity of RRT, the reflected light intensity in the light source direction is up to hundreds of even thousands of times that of a diffuse target [10]. Thus, it is easy to obtain a quasibinary image with a separated target image and background. This helps in target recognition and extraction as well as in high-precision locating (Figure 2).

RRT's quasibinary image feature is effective for noise suppression, and, because the entire region of the target image is calculated, random noise plays a tiny role in grayscale-weighted centroiding.

2.2. Variable Grayscale-Weighted Centroiding. Grayscale-weighted locating methods typically include the following three specific methods: grayscale centroiding, grayscale centroiding with threshold, and squared grayscale-weighted centroiding.
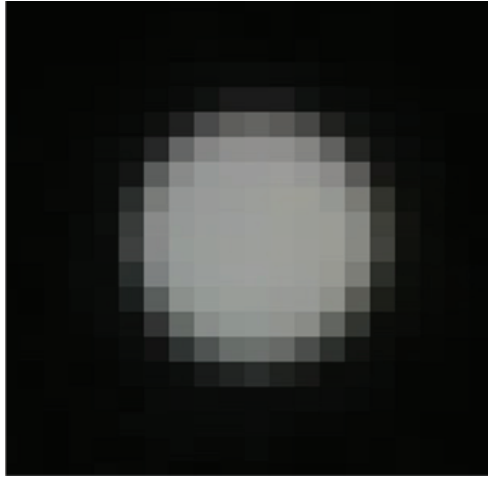
(a) Target image facula
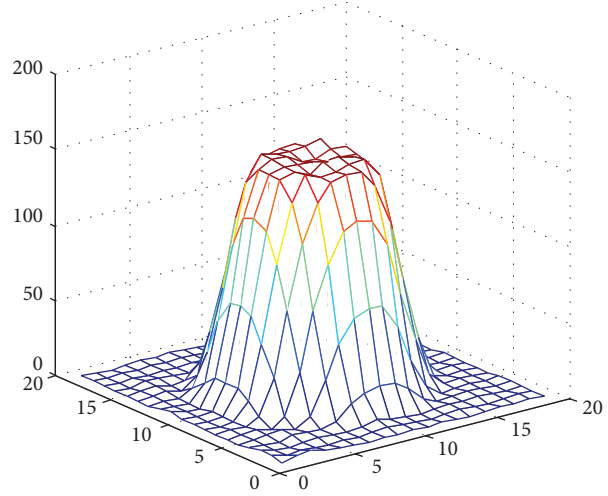
(b) Grayscale intensity distribution

FIGURE 2: Image of an RRT.

Grayscale centroiding is given by

$$x_0 = \frac{\sum_{i=h_1}^{h_2} \sum_{j=w_1}^{w_2} x_i f\left(x_i, y_j\right)}{\sum_{i=h_1}^{h_2} \sum_{j=w_1}^{w_2} f\left(x_i, y_j\right)},$$

$$y_0 = \frac{\sum_{i=h_1}^{h_2} \sum_{j=w_1}^{w_2} y_i f\left(x_i, y_j\right)}{\sum_{i=h_1}^{h_2} \sum_{j=w_1}^{w_2} f\left(x_i, y_j\right)}, \tag{1}$$

where $f(x_i, y_i)$ is the grayscale intensity at coordinate (x_i, y_i), $x_i \in [w_1, w_2]$, $y_j \in [h_1, h_2]$, and (x_0, y_0) is the calculated centroid.

Grayscale centroiding with threshold is given by

$$x_0 = \frac{\sum_{i=h_1}^{h_2} \sum_{j=w_1}^{w_2} x_i \left[f\left(x_i, y_j\right) - \text{th}\right]}{\sum_{i=h_1}^{h_2} \sum_{j=w_1}^{w_2} \left[f\left(x_i, y_j\right) - \text{th}\right]},$$

$$y_0 = \frac{\sum_{i=h_1}^{h_2} \sum_{j=w_1}^{w_2} y_i \left[f\left(x_i, y_j\right) - \text{th}\right]}{\sum_{i=h_1}^{h_2} \sum_{j=w_1}^{w_2} \left[f\left(x_i, y_j\right) - \text{th}\right]}. \tag{2}$$

Compared with grayscale centroid, this equation subtracts a constant th from the grayscale intensity. The value of th should be set to eliminate noise based on its expected value [8], particularly when the expected value is high.

Squared grayscale-weighted centroiding is as follows:

$$x_0 = \frac{\sum_{i=h_1}^{h_2} \sum_{j=w_1}^{w_2} x_i f\left(x_i, y_j\right)^2}{\sum_{i=h_1}^{h_2} \sum_{j=w_1}^{w_2} f\left(x_i, y_j\right)^2},$$

$$y_0 = \frac{\sum_{i=h_1}^{h_2} \sum_{j=w_1}^{w_2} y_i f\left(x_i, y_j\right)^2}{\sum_{i=h_1}^{h_2} \sum_{j=w_1}^{w_2} f\left(x_i, y_j\right)^2}. \tag{3}$$

This method weights the coordinate as a squared gray value, thereby changing the signal-to-noise ratio (SNR). Many studies have shown that this improves locating accuracy.

Based on the induction of the above grayscale centroid-locating algorithms, the general algorithm is derived. Let coordinate (x_i, y_i) be weighted by $[f(x_i, y_i) - \beta]^{\alpha}$; then

$$x_0 = \frac{\sum_{i=h_1}^{h_2} \sum_{j=w_1}^{w_2} x_i \left[f\left(x_i, y_j\right) - \beta\right]^{\alpha}}{\sum_{i=h_1}^{h_2} \sum_{j=w_1}^{w_2} \left[f\left(x_i, y_j\right) - \beta\right]^{\alpha}},$$

$$y_0 = \frac{\sum_{i=h_1}^{h_2} \sum_{j=w_1}^{w_2} y_i \left[f\left(x_i, y_j\right) - \beta\right]^{\alpha}}{\sum_{i=h_1}^{h_2} \sum_{j=w_1}^{w_2} \left[f\left(x_i, y_j\right) - \beta\right]^{\alpha}}, \tag{4}$$

where β is grayscale offset, α is the weighted index, and these two parameters are as yet undetermined. Studies have shown that the optimal β value should be set to the expectation value of the background noise to get the best locating accuracy [8, 11–13]. There is no conclusion as to α yet. The following section focuses on analyzing the existence of an optimal value for α.

For convenience, consider a one-dimensional model which is a particular case of (4). Assume that an ideal signal $s(x)$ is a rectangular window function as follows:

$$s(x) = \begin{cases} C, & x \in [a, b], \\ 0, & \text{else.} \end{cases} \tag{5}$$

Due to the low-pass characteristic of the lens, the signal that reaches the photosensitive surface of the CCD is

$$g(x) = s(x) * h(x), \tag{6}$$

where $h(x)$ is the unit impulse response of lens system. It has a Gaussian-shaped low-pass property in the frequency domain.

Since most CCD imaging noises (shot noise, dark current noise, reset noise, etc.) are all white noise [14, 15], the global noise can be taken as bandwidth-limited white noise whose power spectrum is N_c within the bandwidth. It is represented by $n(x)$, where $n(x) \sim N(0, N_c)$. The signal $g(x)$ combined

with global noise $n(x)$ can then be sampled and quantized by the CCD to the grayscale value $f(x_i)$ of each pixel as follows:

$$f(x_i) = \text{quant}\left[g(x_i) + n(x_i)\right], \tag{7}$$

where $g(x_i)$ and $n(x_i)$ are, respectively, the signal and noise at coordinate x_i, and quant represents the quantization process

$$x_0 = \frac{\sum_{i=h_1}^{h_2} x_i \{\text{quant}\left[g(x_i) + n(x_i)\right] - \beta\}^\alpha}{\sum_{i=h_1}^{h_2} \{\text{quant}\left[g(x_i) + n(x_i)\right] - \beta\}^\alpha}. \tag{8}$$

As seen from (8), the SNR changes along with the α and β values. The SNR has a maximum value, and the x_0 coordinate obtains its highest accuracy when the SNR reaches its maximum. This condition is also suitable for the two-dimensional case. As the SNR is the ratio of $g(x_i)$ to $n(x_i)$ which could not be measured accurately, it is unavailable to calculate the optimal values of α and β. In the present paper, these optimal values are obtained via experiment and supplemented by simulation results. The method of setting the undetermined parameters in the centroiding model and determining the parameter values by experiment is called variable-weighted grayscale centroiding.

3. Image Facula Locating Accuracy

To determine the optimal values of α and β and improve locating accuracy, a locating accuracy evaluating method is designed.

3.1. Accuracy Evaluating Method Based on Virtual Straight Line Target. Locating error cannot be measured directly because the true coordinates of the target image center are not available. Therefore it is generally given by a mathematical model or simulation, which may deviate greatly from the real situation. This paper applies an experimental method to measure the location error, thereby evaluating the accuracy of variable-weighted grayscale centroiding.

According to the pin-hole imaging theory, the projection of a straight line is a straight line. By moving a target point along a straight line in the object space, one can build a virtual straight-line target. Theoretically, during this moving process, all the corresponding target image coordinates should be on a straight line in the image plane [16, 17]. Noise and locating algorithm errors lead to deviations from this line (Figure 3). The deviations of all acquired coordinate residuals indicate the locating accuracy.

Lens distortion can also change the straightness, and the distortion value is currently not fully accurate; the virtual straight line target has deviations, vibration reduces straightness, and S-curve error may lead to deviations. All these error sources are analyzed in the present paper. Methods for eliminating or compensating for errors are found to ensure precise results. The accuracy evaluating principles and error eliminating methods are described as follows.

--- Target object coordinates
-·-· Theoretical target image coordinates
········ Measured target image coordinates
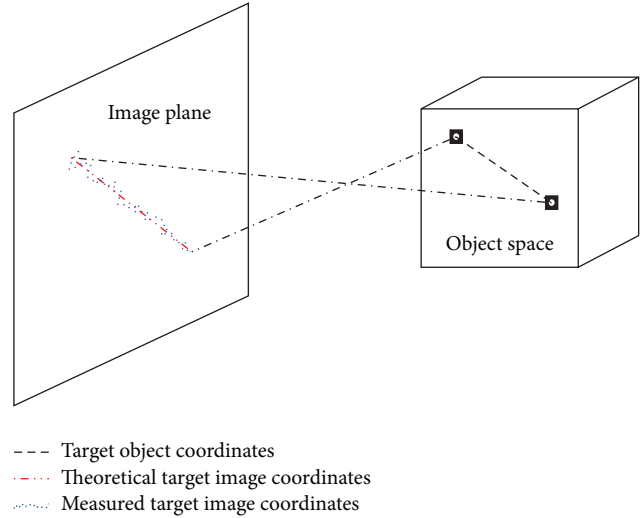
FIGURE 3: Target image coordinates.

Linearly fit the coordinates as shown in Figure 3, and calculate the standard deviation of the measurement. The fitted line is assumed to have the form $y = kx + b$. Let

$$S = \sum_{i=1}^{n} d_i^2 = \sum_{i=1}^{n} \left(\frac{|kx_i - y_i + b|}{\sqrt{k^2 + 1^2}}\right)^2, \tag{9}$$

where d_i represents the residual, and S is the quadratic sum of residuals. When

$$\frac{\partial S}{\partial k} = 0,$$
$$\frac{\partial S}{\partial b} = 0, \tag{10}$$

the minimum value of S is obtained. If the line is parallel to the x axis, it could be simply expressed as $y = b$. Thus $d_i = y_i - b$, and (9) is simplified to

$$S = \sum_{i=1}^{n} (y_i - b)^2. \tag{11}$$

The standard deviation of measurement can be obtained by

$$\sigma_m = \sqrt{\frac{S}{n-1}}. \tag{12}$$

3.2. Elimination and Compensation of Error

(1) Distortion. Due to distortion during imaging, a straight line in object space could appear as a curve in the image plane through projection. There are various distortion models [18–21]. Here a widely used distortion model with 10 parameters is considered [22]. The distortion can be expressed as

$$\Delta x = -x_0 - \frac{x'}{c}\Delta c + x'r^2 K_1 + x'r^4 K_2 + x'r^6 K_3$$
$$+ P_1\left(2x'^2 + r^2\right) + 2P_2 x'y' + b_1 x' + b_2 y',$$

$$\Delta y = -y_0 - \frac{y'}{c}\Delta c + y'r^2 K_1 + y'r^4 K_2$$
$$+ y'r^6 K_3 + 2P_1 x'y' + P_2\left(2y'^2 + r^2\right),$$

(13)

where (x_0, y_0) is the principle point, c represents the principle distance, $x' = x - x_0$, $y' = y - y_0$, and $r = \sqrt{x'^2 + y'^2}$.

According to the experimental data, when the target image location shift is small enough, the magnitude of the change in the distortion is far smaller than the target locating accuracy. Hence, the influence of distortion has no impact on the comparison of centroid locations. This objective can be achieved through manipulation of the experiment conditions. In this paper, the total shift of target image is about 6 pixels, and the straightness caused by distortion is 1.6×10^{-5} pixels.

(2) Vibration. Vibration occurs during the image capturing process. Vibration causes shifts in the camera station, thereby shifting the target image locations. Control points were used in order to eliminate the influence of vibration in the experiment. By fixing the control points and target point to the same stable precise platform, the control points do not move. The displacement of a target point is the relative displacement between the target point and the control points. The distribution of target point and control points is as shown in Figure 4.

Vibrations lead to shifts of control points. The shifts are on the subpixel level as observed in experiments, which is far less than the camera principle distance. For this reason, the shifts for each point in the whole image plane are equal. Compensation for all target points at time i can be obtained by subtracting the control point coordinates at time 0 (x'_0, y'_0) from those at time i (x'_i, y'_i).

Consider

$$\left(\delta x'_i, \delta y'_i\right) = \left(x'_i, y'_i\right) - \left(x'_0, y'_0\right).$$

(14)

The compensated moving target point coordinates are

$$\left(x_i, y_i\right) = \left(x_{ai}, y_{ai}\right) - \left(\delta x'_i, \delta y'_i\right),$$

(15)

where (x_{ai}, y_{ai}) represents the moving target image point coordinates at time i.

(3) Uncertainty of the Moving Device. Uncertainty of the moving axis in object space is transmitted to the final measurements. It might be necessary to consider this uncertainty if it exceeds a certain range. Assuming that the standard uncertainty in the location of the moving axis is u_c, and the standard uncertainty in the measurement of the target point coordinates is $u_m = \sigma_m$, where σ_m is acquired from (12), the standard uncertainty in the target locating method is u. The values of u_c and u are mutually independent, so

$$u = \sqrt{u_m^2 - u_c^2}.$$

(16)

(4) S-Curve Error of Centroiding. The CCD filling factor of the photosensitive material is less than 100%. This results in
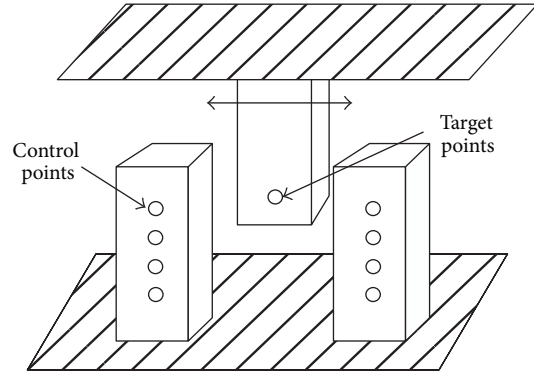
FIGURE 4: Vibration compensation.

an *S*-curve error when centroiding together with the discrete sampling and quantizing. This error fluctuates when the imaged facula is moving in one direction continuously. Thus, it is called the *S*-curve model [23]. In the experiment in the present study, the target image moves along the x direction of image plane, so this error in the y coordinate does not change, which means that the straightness of the line will not affected by this error. Usually this error can be compensated when centroiding [7, 22].

4. Simulation and Experiment

4.1. Simulation. A simulation was conducted according to the accuracy evaluating method described above. First, pictures of target image were generated. The grayscale level of the inner pixels of target image was set to 200 (of 256 levels) and that of the edge pixels in the target image was set by interpolation according to the illuminated area ratio. The image was smoothed with a Gaussian low-pass filtering function. An appropriate Gaussian noise based on the actual imaging results was then added. Several simulations were conducted to observe the results. The simulated target image was moved in the positive x direction in steps of 0.03 pixels for 200 steps. A target image was generated at each step in a different picture. The target image was then located using different parameters of centroiding. The accuracy of location was acquired from each set of parameter values. Finally, the parameter-accuracy curve and optimal parameter values were obtained. The simulation results are shown in Figure 5 and Table 1.

In Figure 5, n is the standard deviation of the noise added in simulation, and μ is the mean. The unit is one increment of grayscale intensity. As can be seen in Figure 5(a), for any case of $n = 1$ to 5 (based on experience, the actual noise of the imaging process will not ordinarily exceed this range), there is a minimum locating error which is close to $\alpha = 1.5$. Figure 5(b) shows that the accuracy *versus* β curve has a minimum value as well for each noise level. Some of the data are shown in Table 1.

As seen in Table 1, α contributes much more to accuracy improvement than β. When $\alpha = 1.5$, it resulted in 30% and 10% accuracy improvement compared to centroiding and

(a) Error (σ) versus parameter (α) and noise (n)

(b) Error (σ) versus parameter (β)
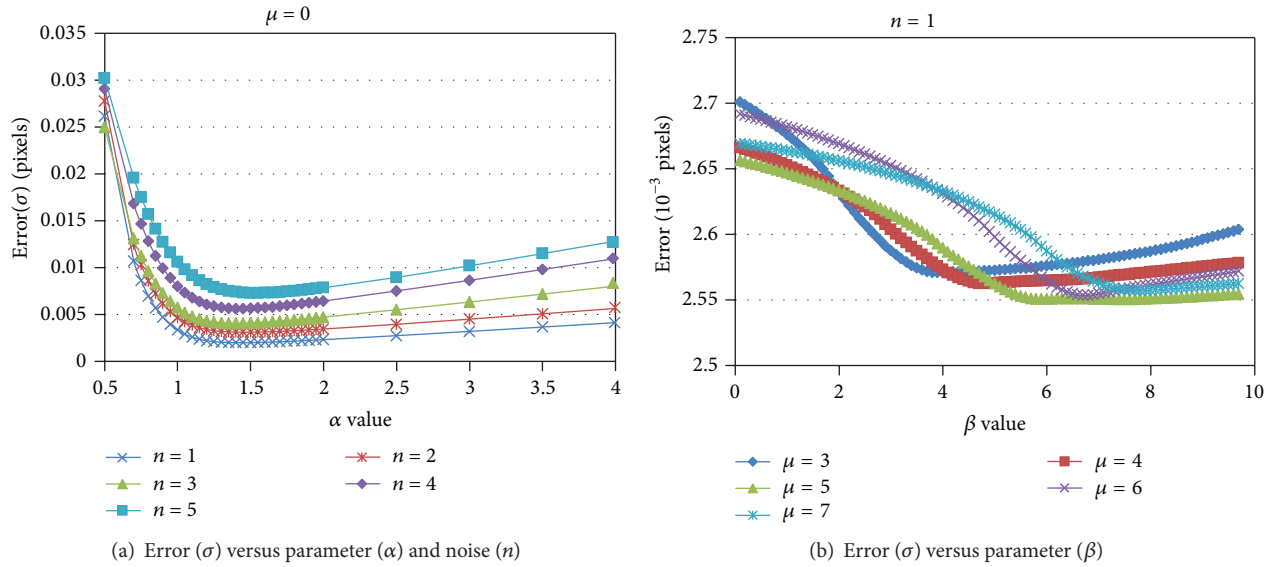
FIGURE 5: Simulated error *versus* parameters α and β.

TABLE 1: Simulated error versus parameters α and β.

	Error (σ)/pixels versus α				
α	$i = 0, n = 1$	$i = 0, n = 2$	$i = 0, n = 3$	$i = 0, n = 4$	i= 0, $n = 5$
0.50	0.026175	0.027798	0.024995	0.029100	0.030233
0.75	0.008611	0.010296	0.011212	0.014658	0.017515
1.00	0.003323	0.004663	0.005724	0.007995	0.010601
1.25	0.002090	0.003264	0.004182	0.005854	0.007892
1.50	0.001984	0.003098	0.004087	0.005625	0.007280
1.75	0.002114	0.003227	0.004354	0.005952	0.007437
2.00	0.002302	0.003438	0.004710	0.006429	0.007855
2.50	0.002730	0.003943	0.005496	0.007505	0.008952
3.00	0.003183	0.004492	0.006322	0.008639	0.010188
3.50	0.003648	0.005060	0.007167	0.009794	0.011489
4.00	0.004121	0.005638	0.008022	0.010960	0.012828
	Error (σ)/10^{-3} pixels versus β				
β	$i = 3, n = 1$	$i = 4, n = 1$	$i = 5, n = 1$	$i = 6, n = 1$	$i = 7, n = 1$
0.1	2.70087	2.66602	2.65650	2.69154	2.66910
1	2.67619	2.65256	2.64703	2.68204	2.66381
2	2.63253	2.63328	2.63369	2.66894	2.65605
3	2.58769	2.60380	2.61620	2.65242	2.64591
4	2.57097	2.57316	2.58985	2.63095	2.63275
5	2.57264	2.56286	2.56254	2.59796	2.61522
6	2.57598	2.56466	2.55091	2.56451	2.58725
7	2.58076	2.56713	2.55092	2.55493	2.56290
8	2.58713	2.57118	2.55111	2.56179	2.55759
9	2.59605	2.57529	2.55309	2.56783	2.56049
10	2.60361	2.57813	2.55453	2.57192	2.56250

squared centroiding, respectively. Additionally, β contributed about 4% to the accuracy for each noise value μ. The best β value is slightly larger than the expected value of noise. That is because the noise does not have an effect if it is negative in background pixels.

4.2. *Experiment.* A Nikon D2Xs camera, whose interior parameters have been calibrated, was used in the experiment. The pixel size of the camera was $6\,\mu$m $\times$ $6\,\mu$m, and the resolution was 4288×2848 pixels. A Hexagon Mistral 775 coordinate measuring machine (CMM) was used for
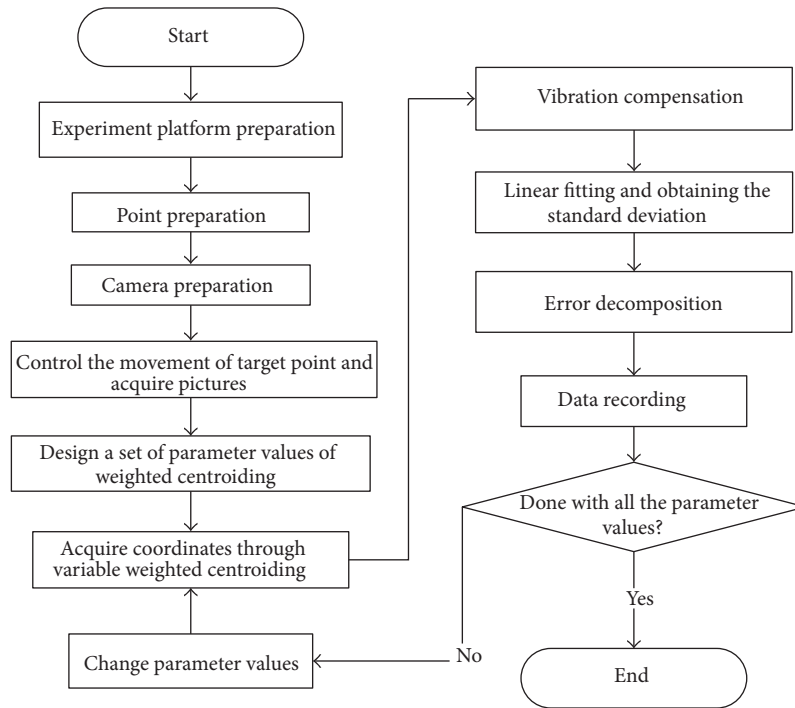
FIGURE 6: Flow diagram of the experiment.
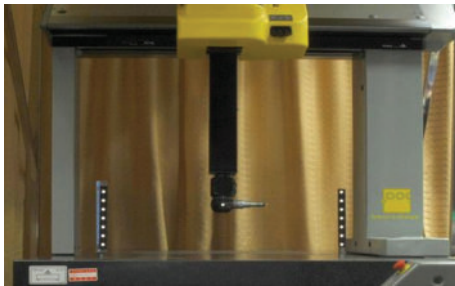
FIGURE 7: Experimental platform and RRT distribution.

high-precision movement of the target point. Accuracy of movement depends on the grating scale accuracy, which was $0.1\,\mu$m. Retro-reflective target points were used for imaging. The diameter of the targets was 6 mm. The target image facula diameter was about 10 pixels. The experiment was implemented under favorable environmental conditions.

A flow diagram of the experiment is shown in **Figure 6**.

Figure 7 shows the experimental scenario. The target in the middle is the measuring target point. There is a column of vibration compensation control points fixed on the CMM platform on both sides of the target. To facilitate comparison, all points are located in a plane, the optical axis of the camera is perpendicular to this plane, and the initial position of the target image center is imaged near the principle point. The camera is fixed on an optical table and set for automatic image capture. The target object moves 200 steps in steps of 30 μm in the positive x direction, and 201 pictures are taken as one

group of data. For reliable results, 10 groups of data were collected at different times.

The target image is located with variable grayscale-weighted centroiding for all 10 groups of data. The first group of data is taken as an example to analyze the influence of lens distortion. The point moves from (2160.4423, 1248.7070) to (2166.4188, 1248.7090) in the image plane. The shift in the y direction is 0.002 pixels. Equation (13) and the camera parameters are used to calculate the distortion. A distortion value sequence $\{(\Delta x_0, \Delta y_0), (\Delta x_1, \Delta y_1), \ldots, (\Delta x_i, \Delta y_i), (\Delta x_{200}, \Delta y_{200})\}$ which has a straightness of about 1.6×10^{-5} pixels and a standard deviation about 4×10^{-6} pixels is obtained. This distortion is small enough to be ignored. Equations (14) and (15) and the control points coordinates are used to compensate for vibration errors. Since the target image moves in the x direction, the S-curve error in y direction does not change; therefore, this error causes no deviation. The standard deviation (σ_m) of the residuals is obtained by linear fitting the coordinate sequence of each group of data. For the seeking of optimal values of α and β, there must be a α-σ_m curve and a β-σ_m curve for each picture group. Equation (16) is used to decompose the influence of target object locating uncertainty. Finally, the accuracy of the target image locating, the parameter-accuracy curve, and the optimal parameter value are obtained. The average of the experiment results is shown in **Figure 8** and **Table 2**. Selected data are listed in **Table 2**.

According to the experimental data, there are minimum errors in both the α-σ_m and β-σ_m curves. The minimum locating error is close to the position of $\alpha = 1.5$, which is

TABLE 2: Measured error versus parameters α and β.

	Error (σ) versus α				Error (σ) versus β		
α	Error (σ)	α	Error (σ)	β	Error (σ)	β	Error (σ)
0.50	0.019177	2.00	0.006589	0	0.005853	6	0.005872
0.75	0.010303	2.50	0.007486	1	0.005847	7	0.005886
1.00	0.006875	3.00	0.008423	2	0.005845	8	0.005901
1.25	0.005913	3.50	0.009372	3	0.005847	9	0.005918
1.50	0.005894	4.00	0.010321	4	0.005852	10	0.005936
1.75	0.006189	4.50	0.011267	5	0.005861	11	0.005953
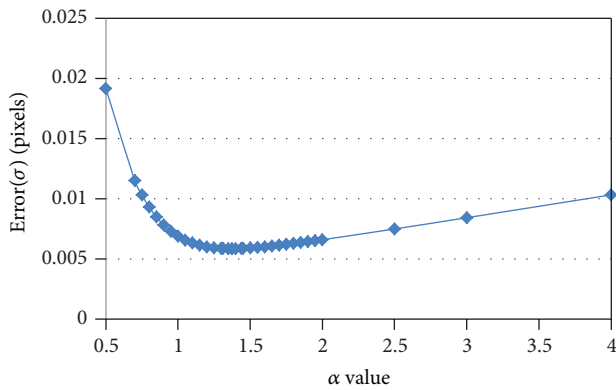
(a) Error (σ) *versus* parameter (α)
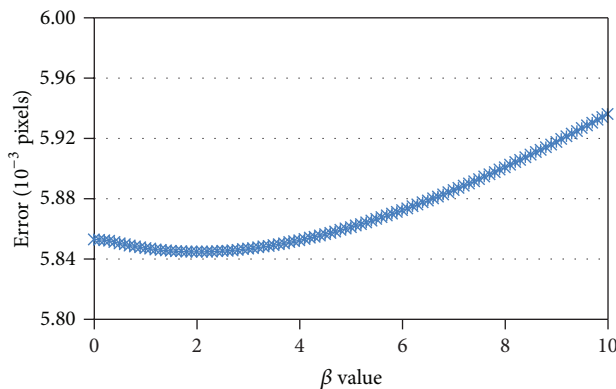
(b) Error (σ) *versus* parameter (β)

FIGURE 8: Measured error *versus* parameters α and β.

● Target image
⇨ Moving direction

FIGURE 9: Target location and moving direction.

(a) Optimal α value *versus* target location

(b) Optimal β value *versus* target location

FIGURE 10: Optimal α and β values *versus* target location.

the same as in the simulation result. When α is 1.5, the locating error σ is 1/170 pixels, and β has little effect on accuracy.

An additional experiment was conducted to determine the relationship between optimal α or β values and the target image location. Figure 9 shows how 8 groups of data were acquired with different target locations and moving directions. The results are shown in Figure 10. The data show that the optimal α value is always between 1.25 and 1.75 with an average of 1.505. This α value results in accuracy improvements of 18.4% and 10.2% compared with the centroid and squared centroid methods, respectively. The optimal β value is between 0 and 6. Still, β contributes little to accuracy improvement.

5. Conclusion

This paper derives a general algorithm for grayscale-weighted centroiding method. The general algorithm sets weight as a function of grayscale intensity and two undetermined parameters α and β where α is the weighted index, and β is

the grayscale shift. This paper analyzed and demonstrated the existence of minimum error in the domain of variability of α and β, and then designed an accuracy evaluating method to obtain the accuracy of a centroid with specific α and β values. Finally the accuracy-α and accuracy-β curves can be obtained by discrete sampling of α and β values as well as the optimal centroiding location. Simulations and experiments were conducted to confirm the accuracy improvement of this method. Results show that the optimal value of α improves locating accuracy more effectively than β. When $\alpha = 1.5$, both simulation and experimental results exhibit an improvement of accuracy by 10% compared to squared centroiding, while β contributes about 1% to accuracy improvement. Locating accuracy shows a distinct improvement overall. This means that more accurate target location coordinates can be provided to 3D reconstruction and bundle adjustment. It paves the way to improve accuracy of photogrammetry.

Acknowledgments
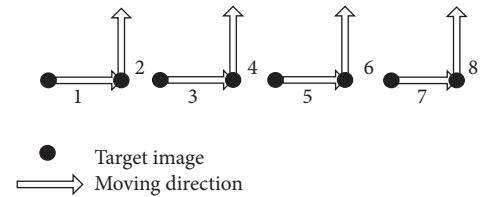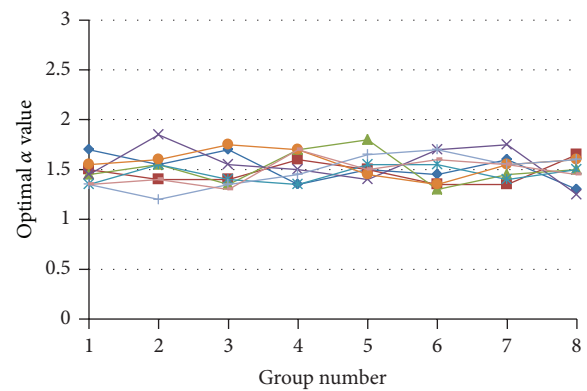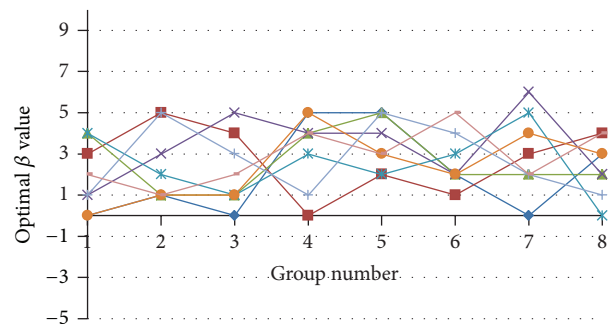
References

[1] T. Luhmann, "3D imaging: how to achieve highest accuracy," in *Videometrics, Range Imaging, and Applications XI*, vol. 8085 of *Proceedings of SPIE*, pp. 1–11, 2011, 808502.

[2] T. Luhmann, "Close range photogrammetry for industrial applications," *ISPRS Journal of Photogrammetry and Remote Sensing*, vol. 65, no. 6, pp. 558–569, 2010.

[3] L. Q. Zhu, Y. H. Wang, N. Xu et al., "Real-time monitoring of phase maps of digital shearography," *Optical Engineering*, vol. 52, no. 10, p. 101902, 2013.

[4] J. G. Fryer and D. C. Brown, "Lens distortion for close-range photogrammetry," *Photogrammetric Engineering and Remote Sensing*, vol. 52, no. 1, pp. 51–58, 1986.

[5] K. Edmundson and L. Baker, "Photogrammetric measurement of the Arecibo primary reflector surface," in *Proceedings of the 17th Annual Coordinate Measurement Systems Committee Conference*, pp. 13–17, Albuquerque, New Mexico, August 2001.

[6] C. S. Fraser, "Photogrammetric measurement to one part in a million," *Photogrammetric Engineering and Remote Sensing*, vol. 58, no. 3, pp. 305–310, 1992.

[7] G. Zhang and Z. Wei, "A position-distortion model of ellipse centre for perspective projection," *Measurement Science and Technology*, vol. 14, no. 8, pp. 1420–1426, 2003.

[8] M. R. Shortis, T. A. Clarke, and T. Short, "A comparison of some techniques for the subpixel location of discrete target images," *Videometrics*, vol. 3, pp. 239–250, 1994.

[9] G. Burgess, M. R. Shortis, and P. Scott, "Photographic assessment of retroreflective film properties," *ISPRS Journal of Photogrammetry and Remote Sensing*, vol. 66, no. 5, pp. 743–750, 2011.

[10] Q. Q. Feng, *Research and Practice of Digital Industrial Photogrammetry*, PLA Information Engineering University, Zhengzhou, China, 2010.

[11] Y. L. Yuan, Y. Zheng, and D. Lan, "High accuracy centroid algorithm of star points," *Journal of Geomatics Science and Technology*, vol. 29, no. 2, pp. 122–126, 2012.

[12] E. Mitishita, A. Habib, J. Centeno, A. Machado, J. Lay, and C. Wong, "Photogrammetric and lidar data integration using the centroid of a rectangular roof as a control point," *The Photogrammetric Record*, vol. 23, no. 121, pp. 19–35, 2008.

[13] R. Z. Lin, X. Y. Yang, and J. Zhou, "Study on the center extraction precision of image photographed by CCD for large scale inspection," *Transducer and Microsystem Technologies*, vol. 29, no. 12, pp. 51–53, 2010.

[14] J. R. Janesick, T. Elliott, S. Collins, M. M. Blouke, and J. Freeman, "Scientific charge-coupled devices," *Optical Engineering*, vol. 26, no. 8, p. 268692, 1987.

[15] M. X. Lu, *Investigation of Noise Generated by Imaging Devices in CCD Type*, Nanjing University of Science and Technology, Nanjing, China, 2009.

[16] D. Cosandier and M. A. Chapman, "High-precision target location for industrial metrology," vol. 1820, pp. 111–122, Proceedings of SPIE, 1993.

[17] Y.-J. Chen, Y. Feng, L.-A. Wei, H. Zhao, and Z.-W. Zhu, "Experiment research on subpixel location error of the facula centroid," *Opto-Electronic Engineering*, vol. 37, no. 2, pp. 80–84, 2010.

[18] H. Ziemann and S. F. El-Hakim, "On the definition of lens distortion reference data with odd- power polynomials," *Canadian Surveyor*, vol. 37, no. 3, pp. 135–143, 1983.

[19] D. C. Brown, "Close- range camera calibration," *Photogramm Eng*, vol. 37, no. 8, pp. 855–866, 1971.

[20] J. Wang, F. Shi, J. Zhang, and Y. Liu, "A new calibration model of camera lens distortion," *Pattern Recognition*, vol. 41, no. 2, pp. 607–615, 2008.

[21] J. Heikkila and O. Silven, "A four-step camera calibration procedure with implicit image correction," in *Proceedings of the IEEE Computer Society Conference on Computer Vision and Pattern Recognition*, pp. 1106–1112, June 1997.

[22] C. S. Fraser, "Digital camera self-calibration," *ISPRS Journal of Photogrammetry and Remote Sensing*, vol. 52, no. 4, pp. 149–159, 1997.

[23] X. G. Wei, J. Xu, and G. J. Zhang, "S-curve error compensation of centroiding location for star sensors," *Optics and Precision Engineering*, vol. 21, no. 4, pp. 849–857, 2013.

Research Article

Error Correction for Laser Tracking System Using Dynamic Weighting Model

W. L. Liu,[1] Zhankui Wang,[2] Shibo Wang,[1] and Xiaoyang Li[1]

[1] *School of Mechanical and Electrical Engineering, China University of Mining and Technology, Xuzhou 221116, China*
[2] *Henan Institute of Science and Technology, Xinxiang, Henan 453003, China*

Correspondence should be addressed to W. L. Liu; liuwanli218@126.com

Laser tracking system (LTS) has been widely used in energy industries to meet increasingly high accuracy requirements. However, its measuring accuracy is highly affected by the dynamic uncertainty errors of LTS, and also the current range and angle measurements of LTS are mainly weighted statically, obtaining the dynamic weighting model which is essential for LTS to improve the measuring accuracy. In this paper, a dynamic weighting model that describes not only the dynamic uncertainty but also the geometric variations of LTS is developed, which can be adjusted to the weighting factors of dynamic parameters according to the range observations relative to the angle observations. Intensive experimental studies are conducted to check validity of the theoretical results. The results show that the measuring accuracy of LTS has been increased 2 times after using this technique for correction.

1. Introduction

Conventional coordinate measuring machines (CMMs), as one of the powerful measuring instruments, have been widely used for dimensional and geometrical inspection in manufacturing industry for the past few decades. However, conventional CMMs are not appropriate when measuring large components (typical size from 5 m to 100 m). In addition, in some cases, it is not possible or necessary to bring the parts onto the CMMs. Therefore, mobile large scale metrological instruments are being used to meet these requirements. Among a broad range of large scale measuring systems, such as optical scanner, laser radar, indoor GPS, and digital photogrammetry, laser tracking system (LTS) has become the backbone for accurate dimensional measurement in many industrial and scientific fields due to its high accuracy, large measuring range, high sampling rate, and automatic target tracking. It has been widely used in manufacturing measurement for dimension inspection, robot calibration, machine alignment, surface contour mapping, and reverse engineering [1–7].

The LTS is an integrated measuring system with optical, mechanical, and electronic components. The errors from these components, together with the environmental and operational factors, determine the measurement uncertainty of the LTS. This paper classifies uncertainty sources in LTS measurement into two categories, namely, static or quasistatic uncertainty sources and dynamic uncertainty sources. In order to improve the LTS measuring accuracy and reduce the uncertainty sources, Umetsu et al. [8] proposed a novel method for error analysis and self-calibration of laser tracking mirror mechanism in LTS and developed a kinematics model of geometric variations for LTS. Liu and Wang [9–11] have described the misalignments for the laser tracker design that uses a gimbaled mirror for beam steering. The 15 parameters of their model are broadly categorized as offsets, tilt deviations, and angle encoder parameters. Manojlović and Lin [12, 13] derived formulae to correct the observed sensor readings for the influence of these error parameters and describe experimental setups that can be deployed to measure the error parameters of laser tracker. Muralikrishnan et al. modeled a laser tracker in which the laser beam source is inside the rotating head—this design does not require use of a gimbaled mirror. Bai and Wang [14] develop the dynamic model of the tracking gimbals of LTS using the Lagrange-Euler equations.
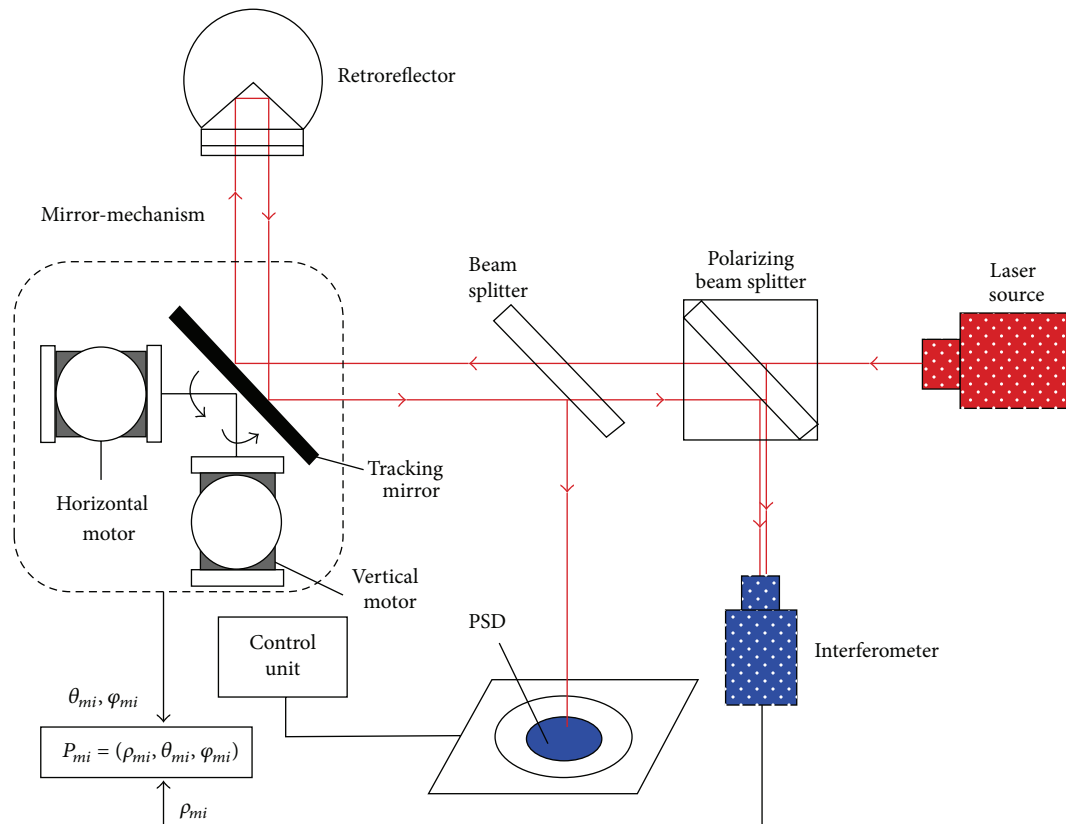
FIGURE 1: Working principle of LTS.

However, all the above researches are mainly focusing on static or quasi-static uncertainty models of LTS; the dynamic uncertainty sources are also highly affected by the LTS measuring accuracy, obtaining the dynamic weighting model which is essential for LTS to improve the measuring accuracy. Therefore, this paper developed a dynamic weighting model of LTS, which can be adjusted to the weighting factors of dynamic parameters according to the range observations relative to the angle observations. A virtual and real measured integration method is presented to correct LTS measurements with dynamic weighting model. The technique can be used to perform error correction for LTS and also to determine all parameters of the dynamic weighting model.

2. Working Principle of LTS

The LTS measuring principle is based on a spherical coordinate system; it can be regarded as a portable frameless coordinate measuring machine. The LTS includes a tracking mirror mechanism, a motor control unit, a laser interferometer, a retroreflector, and a position detector; the working principle of LTS is shown in Figure 1.

Firstly, the laser source emits a measuring laser beam, when the measuring laser beam passes through the beam splitter. Secondly, a portion of measuring laser beam is directed to the retroreflector by a 2-axis tracking mirror mechanism. Another portion of the return beam is directed

by a beam splitter onto a 2-dimensional position sensitive detector (PSD) that senses lateral motion of the target reflector. An interferometer measures the target retroreflector linear displacement. 2-axis high-resolution angle encoders provide the horizontal and vertical angles (θ, φ) of a spherical coordinate system. Finally, the displacement interferometer provides the radial coordinate ρ of the target center. The resultant error signal is used by motor control unit under a certain control algorithm to drive the tracking mirror mechanism so that the displacement measuring beam remains centered on the target as it moves through the space. When the initial optical path between the center of the mirror and the home position is calibrated, the spherical coordinate, $P_{mi} = (\rho_{mi}, \theta_{mi}, \varphi_{mi})$, of the reflector can be obtained in real time from the interferometer and encoder readings.

When LTS is used for high accuracy measurement, its measuring accuracy is highly affected by the dynamic uncertainty errors, obtaining the dynamic weighting model of LTS which is essential prior to using it for metrology.

3. Dynamic Weighting Model

3.1. The Ideal Model of LTS. In this model, it is assumed that the two gimbal axes are intersecting and perpendicular to each other and there is no mirror center offset.

As shown in Figure 2, $\{x, y, z\}$ is the world coordinate system of LTS. In order to model LTS, the three coordinate
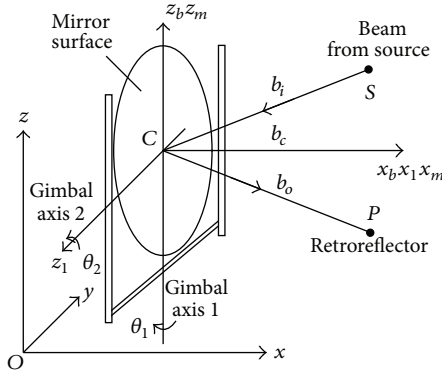
Figure 2: Ideal model of LTS.

Figure 3: Mirror center offset model of LTS.

systems are established as follows. They are the base coordinate system of the gimbal $\{x_b, y_b, z_b\}$, the first link frame $\{x_1, y_1, z_1\}$ and the mirror frame $\{x_m, y_m, z_m\}$. The origins of three frames are placed at the mirror center C. z_b is the rotation axis of the first joint, z_1 is the rotation axis of the second joint, and x_m is normal to the mirror surface. When the gimbal is at its home position ($\theta_1 = \theta_2 = 0$), the x-axes of the first two frames are coincident with the mirror surface normal; b_i represents the direction of the laser beam hitting on the mirror surface, b_c represents the direction of the mirror surface normal, and b_o represents the direction of the laser beam reflected from the mirror surface.

Coordinate system $\{x_b, y_b, z_b\}$ can be brought to coordinate system $\{x_m, y_m, z_m\}$ by the following sequence of 4×4 homogeneous transformations:

$$^{b}T_m = \mathrm{rot}\,(z, \theta_1)\,\mathrm{rot}\,(x, -90°)\,\mathrm{rot}\,(z, \theta_2)\,\mathrm{rot}\,(x, 90°). \quad (1)$$

Thus the mirror surface normal $b_c = (b_{cx}, b_{cy}, b_{cz})^T$ represented in $\{x_b, y_b, z_b\}$ is obtained from the three elements of the third column of $^{b}T_m$ by

$$b_{cx} = \cos\theta_1 \cos\theta_2,$$
$$b_{cy} = \sin\theta_1 \cos\theta_2, \quad (2)$$
$$b_{cz} = \sin\theta_2.$$

The direction of the incident beam is fixed, but that of the reflected beam varies with the position of the retroreflector. If the directions of the incident beam and the surface normal of the mirror are known, the direction of the reflected beam can be got by using the following formula:

$$b_o = -B\,(b_c)\,b_i, \quad (3)$$

where $B(b_c) = \begin{pmatrix} 2b_{cx}^2-1 & 2b_{cx}b_{cy} & 2b_{cx}b_{cz} \\ 2b_{cx}b_{cy} & 2b_{cy}^2-1 & 2b_{cy}b_{cz} \\ 2b_{cx}b_{cz} & 2b_{cy}b_{cz} & 2b_{cz}^2-1 \end{pmatrix}$ is the familiar of the mirror image reflection matrix [15].

Let R be a reference target point at which $\theta_1 = \theta_2 = 0$. If the distance between the mirror center and the retroreflector is known, the location r_P of the retroreflector at any point P can be computed by the following formula:

$$r_P = lb_o = (l_m + l_r)\,b_o = (l_m + l_r)\,B\,(b_c)\,b_i, \quad (4)$$

where l is the distance from the point at which the incident beam hits the mirror surface (point C in this ideal case) to the target location, l_m is the relative distance measured by the laser interferometer, and l_r is the distance from the reference point to point C.

To compute the target location r_P, the parameters l_r and b_i need to be obtained by calibration. l_m, θ_1, and θ_2 are provided by distance and angular measurements of the laser tracker, and b_c is computed by (2) using the measured θ_1 and θ_2.

3.2. Mirror Center Offset Model. Section 3.1 has described an ideal model, in assumption, without mirror center offset and gimbal axis misalignment. This model can be extended to include nonzero mirror center offset under assumption of perpendicularly intersecting mirror gimbal axis. c_r and c represent intersecting points between laser beam and mirror surface; c_m is the rotational point of mirror.

Figure 3 illustrates the LTS with mirror center offset; b_{or} and b_{cr} are the mirror surface normal and the direction of the reflected beam, respectively, when the retroreflector is at r_r. Similarly b_o and b_c are the vectors when the retroreflector is at r_P and b_i represents the direction of the laser beam hitting on the mirror surface.

Based on the 3D geometry of the system, the retroreflector coordinates can be computed by the following formula:

$$r_P = R_r\,{}^{m}c_r - (l_m + l_r - l_s)\,B\,(b_c)\,b_i + l_s b_i, \quad (5)$$

where $l_s = -b_c \cdot (R\,{}^{m}c_r)/b_c \cdot b_i$, R_r is the rotation submatrix of T_m (refer to (2)), when $\theta_1 = \theta_2 = 0$. Consider $^{m}c_r = (c_x, c_y, 0)^T$; c_x and c_y are the two parameters describing the mirror center offset. The rest of variables are the same as those in the last section.

3.3. Combined Mirror Center Offset and Gimbal Axis Misalignments Model. Calibration considerations of LTS must be taken into account during the modeling process of the gimbal-mirror mechanism. Compared with the model presented in the previous section, the new model should include both mirror center offset and gimbal axis misalignment. It is a complete and minimal model because it satisfies the

FIGURE 4: Mirror center offset and gimbal axis misalignment model.

two basic requirements. Firstly, there should be a sufficient number of kinematic parameters to completely describe the geometry and motion of the actual gimbal mechanism. Secondly, there should be no redundant parameters in the parameter identification process.

As shown in Figure 4, O_b, O_1, and O_m denote the origins of the three coordinate systems $\{x_b, y_b, z_b\}$, $\{x_1, y_1, z_1\}$, and $\{x_m, y_m, z_m\}$, respectively. When the LTS is at its home position, x_b and x_1 are along the common normal directions of z_b and z_1. If z_b and z_1 intersect, x_b and x_1 are assigned perpendicular to both z_b and z_1. Let O_b and O_1 are the intersection points of the common normal of axes z_b and z_1 with x_b and x_1, respectively. Thus an angular parameter α_1 and a translation a_1 are used to model the misalignment of the gimbal axes. Therefore, $\mathrm{rot}(x, \alpha_1)$ will align $\{x_b, y_b, z_b\}$ with $\{x_1, y_1, z_1\}$, and $\mathrm{tran}(a_1, 0, 0)$ will bring the resultant frame to be coincident with $\{x_1, y_1, z_1\}$. x_m is parallel to the direction of the mirror surface normal and passes through O_1. O_m is the intersection point of x_m with the mirror surface. z_m may lie arbitrarily on the mirror surface. Two angular parameters θ_2 and α_2 as well as one translation parameter e_2 are thus sufficient to model the case, in which the second rotation axis does not lie on the mirror surface. In other words, $\mathrm{rot}(z, \theta_2 + \Delta\theta_2)\, \mathrm{rot}(x, \alpha_2)$ will align $\{x_1, y_1, z_1\}$ with $\{x_m, y_m, z_m\}$, and $\mathrm{tran}(0, 0, e_2)$ will bring the result frame to be coincident with $\{x_m, y_m, z_m\}$.

In summary, the transformation matrix $^{b}T_m$ relating the coordinate system $\{x_m, y_m, z_m\}$ to $\{x_b, y_b, z_b\}$ is

$$
\begin{aligned}
^{b}T_m = {} & \mathrm{rot}\,(z, \theta_1)\, \mathrm{rot}\,(x, \alpha_1)\, \mathrm{tran}\,(a_1, 0, 0) \\
& \times \mathrm{rot}\,(z, \theta_2)\, \mathrm{rot}\,(x, \alpha_2)\, \mathrm{tran}\,(0, 0, e_2),
\end{aligned}
\tag{6}
$$

nominally $\alpha_1 = -90°$, $\alpha_2 = 90°$, and $e_2 = 0$.

The target coordinates can be computed through the following formula:

$$
r_P = R_r\,^{m}c_r + t_r - (l_m + l_r - l_s)\, B(b_c)\, b_i + l_s b_i, \tag{7}
$$

where $l_s = -b_c \cdot (R\,^{m}c_r)/b_c \cdot b_i$.

3.4. Dynamic Weighting Model with Mirror Center Offset and Gimbal Axis Misalignments. It is difficult to predict how a

given set of dynamic uncertainty sources will affect the range and angle measurements of LTS, and there is good reason to believe that the effect on range measurements will be different to that on the angle measurements. Therefore, it is necessary to obtain the dynamic weighting model with mirror center offset and gimbal axis misalignments of LTS for metrology.

Section 3.3 has described the target coordinates $r_P = [\rho, \theta, \varphi]^T$; it is assumed that the true measured ranges and azimuth and elevation angles ρ^*, θ^*, and φ^* arise through a sampling model of the form

$$
\begin{aligned}
\rho^* &= \rho\,(x, S) + \varepsilon_\rho, \\
\theta^* &= \theta\,(x, S) + \varepsilon_\theta, \\
\varphi^* &= \varphi\,(x, S) + \varepsilon_\varphi,
\end{aligned}
\tag{8}
$$

where x and S are fixed but to the target locations and static or quasi-static uncertainty parameters, respectively, and $\varepsilon_\rho, \varepsilon_\theta$ and ε_φ are samples from a dynamic uncertainty distribution with expectation zero and standard deviations $\sigma_\rho, \sigma_\theta$ and σ_φ, respectively. We assume that these standard deviations reflect an uncertainty component that is independent of the distance to the target. The quantities ρ^*, θ^*, and φ^* are what the model predicts the LTS measurements should be. For a given target x, we assume that

$$
\sigma_\rho^2 = \sigma_{\rho,S}^2 + \sigma_{\rho,D}^2 \left\| \varepsilon_\rho \right\|^2, \tag{9}
$$

where $\sigma_{\rho,S}$, $\sigma_{\rho,D}$ are the static and dynamic standard deviations of ρ^*.

The uncertainty associated with the displacement measurement, potentially, has a component dependent on the dynamic uncertainty from the LTS to the target. The dynamic uncertainty dependence could arise from the retroreflector moving velocity or acceleration, or random fluctuations in the refractive index, or random effects associated with the laser frequency, for example. The dynamical characterization is used to weight the displacement measurements with $\omega_\rho = 1/\sigma_\rho$. In practice, the observed ρ^* can be used as an estimate of $\|\varepsilon_\rho\|$ so that

$$
\omega_\rho = \frac{1}{\sqrt{\sigma_{\rho,S}^2 + \sigma_{\rho,D}^2 \left\| \varepsilon_\rho \right\|^2}}. \tag{10}
$$

For azimuth angle observations, the statistical characterization has the form of equation (8); the ε_θ is a realization of a random variable with expectation zero and variance σ_θ^2. We assume that, for each measurement, σ_θ depends on two parameters $\sigma_{\theta,S}$ and $\sigma_{\theta,D}$, with

$$
\sigma_\theta^2 = \frac{1}{\left\| \varepsilon_\rho \right\|^2 \cos^2\theta} \left(\sigma_{\theta,D}^2 + \frac{\sigma_{\theta,S}^2}{\left\| \varepsilon_\theta \right\|^2} \right). \tag{11}
$$

The term $\sigma_{\theta,D}$ accounts for random effects associated with the target that will have a larger impact on the angle measurements for targets closer to the station. The dependence of the variance parameter σ_θ^2 on the azimuth angle θ models the

fact that as the targets move away from the equatorial plane, the azimuth angle is less well defined. This leads to assigning weights according to

$$\omega_\theta = \frac{1}{\sigma_\theta} = \frac{\|\varepsilon_\theta\| \|\varepsilon_\rho\| \cos\theta}{\sqrt{\sigma_{\theta,S}^2 + \sigma_{\theta,D}^2 \|\varepsilon_\theta\|^2}}. \tag{12}$$

Similarly, for elevation angle measurements, the weights characterization has the following:

$$\omega_\varphi = \frac{\|\varepsilon_\varphi\| \|\varepsilon_\rho\| \sin\varphi}{\sqrt{\sigma_{\varphi,S}^2 + \sigma_{\varphi,D}^2 \|\varepsilon_\varphi\|^2}}. \tag{13}$$

According to (7), (8), (10), (12), and (13), the dynamic weighting model with mirror center offset and gimbal axis misalignments of LTS can be calculated as

$$r_P^* = r_P + J_i \begin{pmatrix} \omega_\rho & & \\ & \omega_\theta & \\ & & \omega_\varphi \end{pmatrix} J_i^T. \tag{14}$$

The Jacobian matrix J_i can be solved by

$$
\begin{aligned}
J_i &= \begin{pmatrix} \dfrac{\partial x}{\partial \rho} & \dfrac{\partial x}{\partial \theta} & \dfrac{\partial x}{\partial \varphi} \\ \dfrac{\partial y}{\partial \rho} & \dfrac{\partial y}{\partial \theta} & \dfrac{\partial y}{\partial \varphi} \\ \dfrac{\partial z}{\partial \rho} & \dfrac{\partial z}{\partial \theta} & \dfrac{\partial z}{\partial \varphi} \end{pmatrix} \\
&= \begin{pmatrix} \cos\theta_i \sin\varphi_i & -\rho_i \sin\theta_i \sin\varphi_i & \rho_i \cos\theta_i \cos\varphi_i \\ \sin\theta_i \sin\varphi_i & \rho_i \cos\theta_i \sin\varphi_i & \rho_i \sin\theta_i \cos\varphi_i \\ \cos\varphi_i & 0 & -\rho_i \sin\varphi_i \end{pmatrix}.
\end{aligned}
\tag{15}
$$

4. Experiments

The objective is to test the feasibility of the proposed method for the purpose of LTS error correction. The r_P and r_P^* were given in the above section. About a hundred 3D target points were randomly generated in a $1.5 \times 1.5 \times 1.5\,\text{m}^3$ work volume which were assumed to be "trackable" by the LTS system. In order to demonstrate the effectiveness of our proposed technique, we used it to perform a dynamical uncertainty correction of a commercial LTS (FARO SI) shown in Figure 5. The retroreflector is mounted on the z-axis of a CMM. The CMM that rides the retroreflector moves in space to simulate the dynamic constraint of LTS. Based on the nominal values provided by the high-accuracy CMM, the LTS tracks the retroreflector and measures the coordinates of the retroreflector in real time.

In the experiments, 100 points are measured with the dynamic constraint. Figure 6 shows the measuring results using our proposed technique. The horizontal axis represents the number of measurements and the vertical axis denotes the measuring error relevant to the standard value provided by CMM. The black line is the results, in which LTS has not been calibrated by the proposed technique. At the same time, the
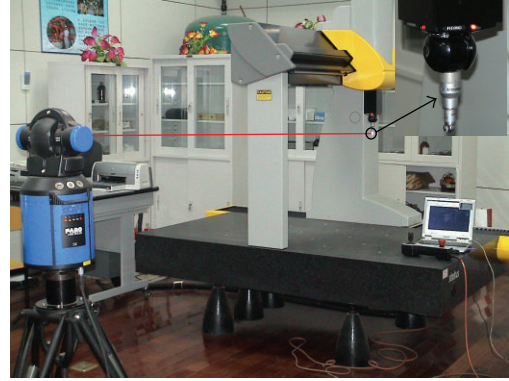

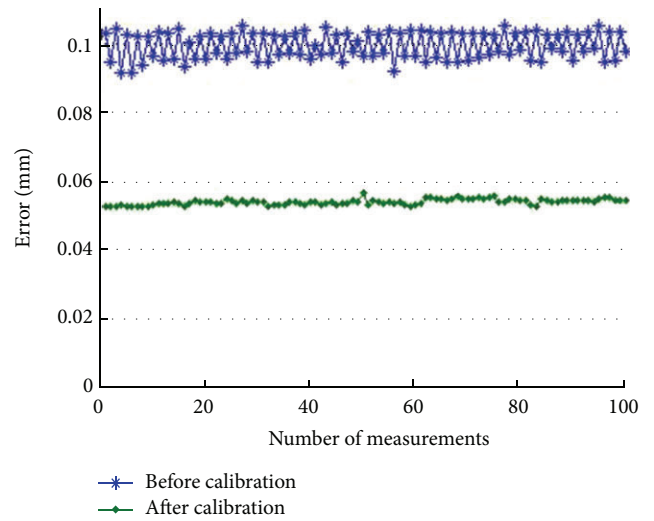Figure 5: Experiment layouts.

Figure 6: Measuring results using dynamic weighting model.

dash line denotes the results, in which LTS has been calibrated using the proposed technique. After being corrected using dynamic weighting model, the mean measuring error of the LTS has been decreased from 99.57 μm to 53.89 μm.

5. Conclusion

The dynamic weighting model that describes not only the dynamic uncertainty but also the geometric variations of LTS is developed, which can be adjusted to the weighting factors of dynamic parameters according to the range observations relative to the angle observations. The experimental results have demonstrated that, using this technique to correct the LTS measuring errors, the maximum value of LTS measurements has been decreased from 99.57 μm to 53.89 μm.

Acknowledgments

References

[1] F. Zhang and X. Qu, "Fusion estimation of point sets from multiple stations of spherical coordinate instruments utilizing uncertainty estimation based on Monte Carlo," *Measurement Science Review*, vol. 12, no. 2, pp. 40–45, 2012.

[2] B. Hughes, A. Forbes, A. Lewis, W. Sun, D. Veal, and K. Nasr, "Laser tracker error determination using a network measurement," *Measurement Science and Technology*, vol. 22, no. 4, Article ID 045103, 2011.

[3] B. Muralikrishnan, C. Blackburn, D. Sawyer, S. Phillips, and R. Bridges, "Measuring scale errors in a laser tracker's horizontal angle encoder through simple length measurement and two-face system tests," *Journal of Research of the National Institute of Standards and Technology*, vol. 115, no. 5, pp. 291–301, 2010.

[4] G. N. Peggs, P. G. Maropoulos, E. B. Hughes et al., "Recent developments in large-scale dimensional metrology," *Proceedings of the Institution of Mechanical Engineers B*, vol. 223, no. 6, pp. 571–595, 2009.

[5] B. Muralikrishnan, D. Sawyer, C. Blackburn, S. Phillips, B. Borchardt, and W. T. Estler, "ASME B89.4.19 performance evaluation tests and geometric misalignments in laser trackers," *Journal of Research of the National Institute of Standards and Technology*, vol. 114, no. 1, pp. 21–35, 2009.

[6] W. Liu and Z. Wang, "Coordinate uncertainty analyses of coupled multiple measurement systems," *Measurement Science and Technology*, vol. 21, no. 6, Article ID 065103, 2010.

[7] A. Salmanpour and N. S. Mohammad, "Random uncertainty propagation in estimates of sphere parameters from coordinate measurements," *International Journal of Machine Tools and Manufacture*, vol. 80, no. 12, pp. 548–551, 2011.

[8] K. Umetsu, R. Furutnani, S. Osawa, T. Takatsuji, and T. Kurosawa, "Geometric calibration of a coordinate measuring machine using a laser tracking system," *Measurement Science and Technology*, vol. 16, no. 12, pp. 2466–2472, 2005.

[9] W.-L. Liu and Z.-K. Wang, "A novel method for error verification of a handy laser scanner," *Measurement Science and Technology*, vol. 21, no. 2, Article ID 025303, 2010.

[10] Z. Wang, L. Mastrogiacomo, F. Franceschini, and P. Maropoulos, "Experimental comparison of dynamic tracking performance of iGPS and laser tracker," *International Journal of Advanced Manufacturing Technology*, vol. 56, no. 1–4, pp. 205–213, 2011.

[11] W. Liu, X. Qu, and J. Ouyang, "Modeling and simulation of laser tracking systems," *Kybernetes*, vol. 41, no. 9, pp. 1192–1199, 2012.

[12] L. M. Manojlović and Ž. P. Barbarić, "Optimization of optical receiver parameters for pulsed laser-tracking systems," *IEEE Transactions on Instrumentation and Measurement*, vol. 58, no. 3, pp. 681–690, 2009.

[13] P. D. Lin and C.-H. Lu, "Modeling and sensitivity analysis of laser tracking systems by skew-ray tracing method," *Journal of Manufacturing Science and Engineering, Transactions of the ASME*, vol. 127, no. 3, pp. 654–662, 2005.

[14] Y. Bai and D. Wang, "Dynamic modelling of the laser tracking gimbal used in a laser tracking system," *International Journal of Modelling, Identification and Control*, vol. 12, no. 3, pp. 149–159, 2011.

[15] D. Kopon, *The optical design of a visible adaptive optics system for the Magellan Telescope [Ph.D. thesis]*, The University of Arizona, Tucson, Ariz, USA, 2012.

Research Article

A Novel Solution for Camera Occlusion in Stereo Vision Technique

Junyi Lin,[1] Kaiyong Jiang,[1] and Ming Chang[2]

[1] *Key Laboratory of Digital Computer Vision, Huaqiao University, Xiamen, Fujian 361021, China*
[2] *Department of Mechanical Engineering, Chung Yuan Christian University, Chung Li 32023, Taiwan*

Correspondence should be addressed to Kaiyong Jiang; jiangky@hqu.edu.cn and Ming Chang; ming@cycu.edu.tw

Stereo version is a well-known technique for obtaining depth and surface information of objects from images captured by two cameras. In general, this technique is limited by camera occlusion inherent to grooved or steep profiles in 3D shape measurements. To alleviate this problem, a traditional dual-camera system accompanied with a projector based on the stereo vision principle is presented. The projector was considered as a virtual camera. Three sets of stereo vision systems were then obtained with each of the two cameras at the same global coordinates for 3D topography measurements. The data acquisition system constructed with the two real cameras was first calibrated. Then the two-camera-projector system can be calibrated based on the data obtained from the common measurement area of the three systems. Experiments were implemented to evaluate the accuracy of the merging profile integrated from the three sets of stereo vision systems. Experimental results show that the problem of camera occlusion encountered in the original dual-camera system was effectively resolved and a 0.05% error for the height measurement of a ladder-shaped specimen with camera occlusions was obtained in a measurement range of 640 mm × 480 mm.

1. Introduction

Accurate measurement of the 3D shape of objects is a rapidly expanding field, with applications in object recognition, inspection, design, and manufacturing [1]. Among the existing 3D shape measurement techniques, structured light [2] and stereo vision [3] are two of the most commonly used methods due to their advantages such as fast measurement, good accuracy, and noncontact nature. In both techniques, the most pressing concern that limits the measurable range is the camera occlusion introduced by the steep surface or shadow of the specimen. A solution to this problem combined a dual-camera system with structured illumination [4, 5]. This approach utilized two cameras to acquire images independently, so that the measured profile of one view can be extended by combining the measured range of the two cameras and removing the occlusion. However, since the two measured profiles were not based on the same coordinate system, the data integration process for the two different imaging systems is complicated and time consuming.

In this study, a novel stereo vision system consisting of two cameras and a digital projector is presented. The structure is similar to the dual-camera structured light system but the measurement principle is different. In general, through comparison of information about a scene from two vantage points in a stereo version system, 3D information can be extracted by examination of the relative positions of objects in the two panels. Here the use of the light projector has two main functions. First is to reduce the difficulty of the correspondence points searching in stereo matching for the original dual-camera. The second is to model the projector as a virtual camera [6], thereby creating three stereo pairs for each two cameras in the system. The calibration approach proposed by Zhang [7] was adopted for the data acquisition of the stereo vision of the dual camera, and then the calibration of the camera-projector systems can be carried out with the data from the projector itself and the two real cameras based on the stereo vision principle.

After calibration, the 3D data registration can then be executed to transform the 3D data obtained from the three
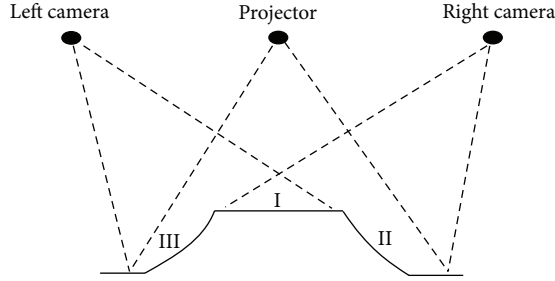
FIGURE 1: Schematic of the dual-camera accompanied with a projector system.

FIGURE 2: Optical geometry of a traditional stereo vision system.

sets of stereo vision systems into a single global coordinate system. Various registration approaches have been proposed, including the iterative closest point algorithm [8], the photogrammetric technique [9], and an additional scanner in the overlapping measurement positions [10, 11]. However, the 3D data merging on existing methods is mostly accomplished through a complicated postprocessing procedure. The 3D data is first calculated and aligned before an overlap region is identified [12, 13]. By using certain algorithms, redundant and overlapping data are then removed and thus multiple sets of data can be integrated into a single group. Therefore a reliable, rapid, and generic 3D registration is still a difficult and open problem. In this investigation, since the three systems were already unified to the same global coordinate, the three corresponding pairs of 3D profiles were automatically well aligned. In addition, an absolute phase-assisted method was proposed for the data merging. The overlapping area of the three sets of stereo vision systems can be clearly identified via the phase-based stereo matching technique and the redundant data can be removed automatically. This simplifies the reconstruction of the 3D information from the three sets of measured data. Experimental results show that the profile in the camera occlusion region of the original dual-camera system was effectively reconstructed in the final integrated surface profile.

2. Measurement Principle and System Calibration

The schematic of the proposed topography measurement system consists of two cameras and a projector as shown in Figure 1. The left camera acquires images of regions I and III, the right camera acquires images of regions I and II, and the projector covers the entire surface of the specimen. As shown, only the 3D shape of region I can be completely resolved with traditional dual-camera stereo vision system. Important surface features on regions II and III are concealed from view due to camera occlusion. However, if the projector is treated as a third camera, then all three regions can be measured. For this reason, the mechanism of using the projector as a virtual camera was developed and this was achieved by a simple calibration process.

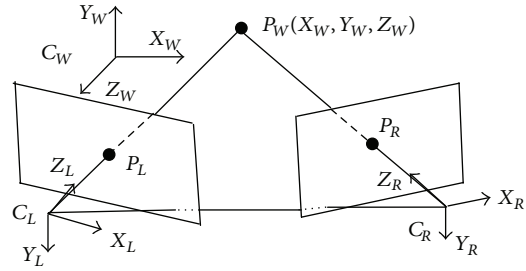*2.1. Calibration of the Dual-Camera System.* Figure 2 is the schematic of a traditional stereo vision approach, where

C_W denotes the three-dimensional world coordinate system, C_L and C_R are, respectively, the left and right camera coordinate systems, and $P_W(X_W, Y_W, Z_W)$ is the three-dimensional world coordinate for an arbitrary point P in space. The relationships between the world coordinate P_W and its corresponding image coordinates P_L and P_R in the left and right cameras are, respectively,

$$P_L = \lambda A_L \left[R_L, t_L \right] P_W, \tag{1}$$

$$P_R = \lambda A_R \left[R_R, t_R \right] P_W, \tag{2}$$

where λ is a scale factor, A_L and A_R are, respectively, the intrinsic parameters of the left and right cameras which depend on the position and focal length of the two cameras, R_L and t_L are, respectively, the rotation and translation matrices between the left camera coordinate system C_L and the three-dimensional world coordinate system C_W, and R_R and t_R are, respectively, the rotation and translation relationships between C_R and C_W.

Stereo calibration of the dual-camera is the most important process in this system. The calibration result directly influences the measurement accuracy. Numerous calibration methods have been developed which can be divided into two main categories: direct linear transformation method [14] and nonlinear transformation method [15, 16]. In this work, the template calibration method based on a planar checkerboard proposed by Zhang [7] was adopted to obtain the intrinsic parameters (A_L, A_R) and extrinsic parameters (R_L, t_L, R_R, t_R) of the stereo vision system. The main advantage of Zhang's approach is that it can obtain the camera parameters by only using few images from few different view angles of the planar template. This method also benefits from high accuracy, fast speed, and robustness.

Once the camera parameters of the dual-camera system are determined, for an arbitrary point P, the relationships between its world coordinate P_W and the left camera image coordinate $P_L(X_L, Y_L)$ and right camera image coordinate $P_R(X_R, Y_R)$ can be described as

$$P_L = R_L P_W + t_L, \tag{3}$$

$$P_R = R_R P_W + t_R. \tag{4}$$

Conversely, the relation between P_L and P_R is

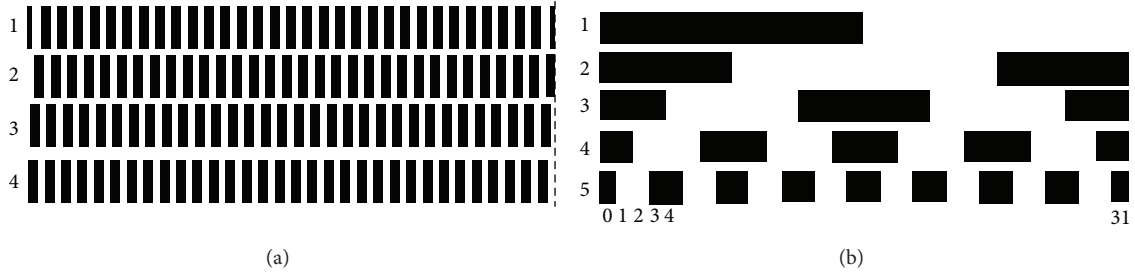$$P_L = R_L R_R^{-1} P_R + t_L - R_R^{-1} t_R = R_{LR} P_R + t_{LR}, \tag{5}$$

FIGURE 3: (a) Four phase-shifting grating images and (b) the Gray coded images.

where $R_{LR} = R_L R_R^{-1}$ and $t_{LR} = t_L - R_R^{-1} t_R$. This means that the position relations between two cameras can be described by a rotation matrix and a translation matrix.

2.2. Calibration of the Projector. Based on the virtual camera idea, a calibration process was implemented to determine the relationship between the world coordinate and the image coordinate of the projector. Similar to the calibration of the dual-camera, a checkerboard pattern was generated with the projector and projected onto the surface of a white flat screen. All the cross-corners of the checkerboard were extracted as sampling points. The world coordinates P_W of these sampling points can be determined with the calibrated dual-camera system based on the stereo vision principle. The relationship between the world coordinate P_W and the related image coordinate P_p in the projector can be seen as

$$P_P = \lambda A_P [R_P, t_P] P_W, \tag{6}$$

where λ is a scale factor and A_p is the projector intrinsic parameter matrix. R_p and t_p, are, respectively, the rotation and translation matrices between the world coordinate system of the checkerboard and the projector coordinate system. These variables also represent the projector extrinsic parameter matrices. Since the pixel positions P_p of these cross-corners in the projector are known and the related P_W can be found with the dual-camera system, these projector parameter matrices can be easily determined. In addition, similar to (5), the relationship between the left camera image coordinate $P_L(X_L, Y_L)$ and the projector image coordinate $P_P(X_P, Y_p)$ can be described as

$$P_L = R_L R_P^{-1} P_P + t_L - R_P^{-1} t_P = R_{LP} P_P + t_{LP}, \tag{7}$$

where R_{LP} and t_{LP} are the rotation and translation matrices for the transformation from the projector coordinate to the left camera coordinate, respectively.

3. Three-Dimensional Data Registration and Data Merging

Once the system calibration is completed, the topography measurement of 3D objects can be carried out with the three sets of stereo vision systems. In order to reduce the difficulty in corresponding points matching, an encoded structured light technology is adopted. Similar to the traditional structured light technique, a grating with sinusoidal stripe is projected onto the surface of the specimen by the projector. The deformed grating image is captured by the dual-camera system. The determination of the absolute phase value for each pixel of the cameras is important for the subsequent task in data registration and data merging. This study uses the digital phase-shifting technology to realize the phase distribution of the fringe pattern on the object surface. As shown in Figure 3(a), four sets of gratings with a continuous phase shift amounting to 90° were projected and deformed grating images are captured by the two cameras separately. The phase distribution of the 3D surface profile for each camera can be obtained as

$$\varphi(x, y) = \tan^{-1} \left[\frac{I_4(x, y) - I_2(x, y)}{I_1(x, y) - I_3(x, y)} \right], \tag{8}$$

where $\varphi(x, y)$ is the phase at an arbitrary point (x, y) and $I_1(x, y) \sim I_4(x, y)$ represent the four captured image intensities during the phase shift. From (8), the phase is wrapped between the range $[-\pi, +\pi]$. Due to its periodic characteristic, this wrapped phase cannot be directly used for the phase-based stereo matching as it might lead to phase ambiguity. In this study, an unwrapping method combined with the Gray code and digital phase-shifting technology was adopted to acquire the absolute phase value. By assigning the Gray code value of the pattern equal to the fringe order of the grating image, then the Gray code value difference for one period separation of the phase map is 1. Figure 3(b) shows the successive five Gray coded images, where the black region is marked 0 and the bright part is marked 1. The use of five Gray code images can divide the entire field of view (FOV) into 2^5 regions, each with a unique code value from 0 to 31, such that the Gray code value for each pixel can be obtained. Furthermore, setting the first region to have a Gray code value of zero, and so on, the absolute phase value after unwrapping can be seen as

$$\phi(x, y) = G(x, y) \times 2\pi + \varphi(x, y), \tag{9}$$

where $\varphi(x, y)$ is the initial phase value at each pixel (x, y), $G(x, y)$ is the Gray value of the pixel, and $\phi(x, y)$ represents the absolute phase value of the pixel.

The absolute phase value of the grating image linearly increases after unwrapping. Based on the comparison of phase value, the stereo matching can be approximately carried out with an accuracy of pixel resolution. Owing

to the different viewing angles of the two cameras and possibly surface profile modulation of the object, it is almost impossible to get equal fringe periods from the two images. Therefore, it is in general also very difficult to find pixels that have equal phase value. In this study, the absolute phase value is used as the stereo matching element. Since the absolute phase distribution is linearly increasing, the subpixel stereo matching point with equal absolute phase value can be found through a simple linear interpolation. Let pixels (x_L, y) and (x_R, y) be the corresponding matching points in pixel resolution, and the related absolute phase values are $\phi_L(x_L, y)$ and $\phi_R(x_R, y)$, respectively. Assuming that the phase value $\phi_L(x_L, y)$ is between $\phi_R(x_R, y)$ and the neighboring pixel $\phi_R(x_R + 1, y)$, then the corresponding point $(x_R + \delta, y)$ in the right camera image with subpixel resolution for the pixel (x_L, y) in the left image can be found, where δ is the subpixel value and can be obtained as

$$
\begin{aligned}
\delta &= \frac{\phi_L(x_L, y) - \phi_R(x_R, y)}{\phi_R(x_R + 1, y) - \phi_R(x_R, y)}, \\
&\phi_R(x_R + 1, y) \neq \phi_R(x_R, y), \\
\delta &= 1, \quad \phi_R(x_R + 1, y) = \phi_R(x_R, y).
\end{aligned}
\tag{10}
$$

Accordingly, enough dense disparity can be constructed with the linear interpolation process from the left image to obtain the subpixel stereo matching pairs.

In this system, aside from the images captured with the dual camera, the projected pattern generated in the projector can be considered as the image captured by the projector. As such, three sets of stereo vision systems are constructed and three independent profiles with dense sampling points were obtained using the calculated absolute phase distribution. Since the correspondence between each two cameras was found from the absolute phase value, three sets of measured data can be obtained in a single measurement. However, since the data were independently acquired by three different stereo vision systems, unifying the three measurement data into a common global coordinate system is necessary. Here, the 3D coordinate system of the left camera was chosen as the global coordinate system; it is also the original measurement coordinate system of the dual-camera infrastructure. Consistency of the coordinates can be accomplished easily through coordinate transformation as shown in (5) and (7).

As mentioned, the registration of the measured data can be completed with the obtained absolute phase distribution and a coordinate transformation process. The merging of the three sets of data can be automatically performed. The data measured by the original dual-camera stereo vision system was selected as the base data, wherein common overlapping area among the three systems can be marked off distinctly. Based on the marked region, the full-field profile data of the specimen can be automatically provided by supplementing the measured data from the other two camera-projector systems. Therefore, the original features hidden by camera occlusion region in the dual-camera system can be observed from the matching result.

FIGURE 4: Picture of the 3D surface profile measurement system.

4. Experiments

The 3D shape measurement system features two black-and-white CCD cameras and a digital light processing projector, as shown in Figure 4. The pixel resolution of the projector is 1024×768. The two CCD cameras have identical pixels of 1280×960. The focal length of the camera is 12 mm and the distance between the two cameras is 446 mm. The object is placed at a distance of about 1200 mm away from the cameras. Accordingly, the FOV for the measurement system is 640 mm × 480 mm.

Prior to measurements, the stereo calibration of the dual-camera system was first carried out with a black-and-white checkerboard with grids of 25×24. The checkerboard contains $24 \times 23 = 552$ cross-corner points as shown in Figure 5. The nominated grid size of the checkerboard is 15 mm × 15 mm with a machining precision of 0.0025 mm; therefore, the theoretical size of the imaging range covered by the grid points is 345 mm × 330 mm. During calibration, the checkerboard was placed at ten different positions in front of the cameras and the feature points on the board at these positions were separately captured by the two cameras. To get clear image position of the corner points, the checkerboard pattern was set up to occupy 70% to 90% of each image frame. Based on the measured data of these correspondent pairs, the intrinsic parameters of the two cameras from the ten measurements were

$$
\begin{aligned}
A_L &= \begin{bmatrix} 2120.791314 & 0 & 511.537238 \\ 0 & 2121.299506 & 383.707038 \\ 0 & 0 & 1 \end{bmatrix}, \\
A_R &= \begin{bmatrix} 2072.217325 & 0 & 510.133842 \\ 0 & 2071.877486 & 394.094748 \\ 0 & 0 & 1 \end{bmatrix}.
\end{aligned}
\tag{11}
$$

The extrinsic parameters R_L, t_L, R_R, and t_R were changed with the positions of the checkerboard. However, the position parameters R_{LR} and t_{LR} between the two cameras can be determined from the ten sets of data as

$$
R_{LR} = \begin{bmatrix} 0.854518 & 0.000384 & 0.519420 \\ -0.0103202 & 0.999814 & 0.0162384 \\ -0.519318 & -0.019237 & 0.854365 \end{bmatrix},
\tag{12}
$$

$$
t_{LR} = \begin{bmatrix} -636.617273 & 8.574418 & 195.781735 \end{bmatrix}^T.
$$

For evaluation of the measurement accuracy of the calibrated dual-camera system, the checkerboard was placed

Table 1: The measured heights of the seven sampling points of the central block.

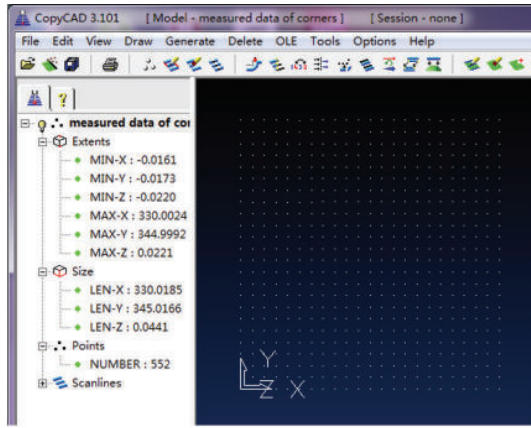| Sampling points	1	2	3	4	5	6	7
Measured height (mm)	100.010	100.008	100.002	99.997	99.989	99.987	99.984
Error (mm)	0.010	0.008	0.002	−0.003	−0.011	−0.013	−0.016

Figure 5: Check of the measurement accuracy of the calibrated dual-camera system.
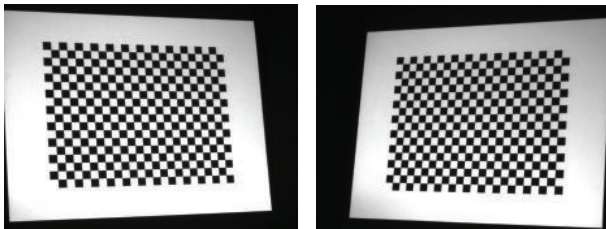

Figure 6: A projected checkerboard pattern captured by two cameras.

at a specific position and the corner coordinates of the checkerboard were determined with the above calibrated parameters. As shown in Figure 5, the measured size of the checkerboard is 345.0185 mm × 330.0166 mm. Compared to the actual size of the board, a lateral error below 0.02 mm was achieved in both X and Y directions. In addition, the resulting error in Z direction was ±0.022 mm. This indicates that a measurement error of roughly 20 μm could be expected with the calibrated dual-camera system.

Calibration of the camera-projector system was implemented by projecting a computer generated checkerboard pattern onto a white flat screen. As shown in Figure 6, the projected checkerboard has a total grid number of 24 × 18 with each grid sized at 30 × 30 pixels. The screen was moved progressively to seven different positions within the measurable range of the dual-camera system. The pictures of the projected pattern at these positions were successively captured with the two calibrated cameras. Again, the picture size of each projected checkerboard was restricted to 70% to 90% of the image size. The 3D space coordinates of these checkerboard corners were extracted through the process of

image rectification and stereo matching of the dual-camera system. Based on the 3D coordinates of these feature points in all positions and the known 2D coordinates in the projector and CCDs, the intrinsic parameters of the projector were obtained as

$$A_P = \begin{bmatrix} 2272.247446 & 0 & 389.140593 \\ 0 & 2268.515857 & 772.802800 \\ 0 & 0 & 1 \end{bmatrix}. \quad (13)$$

In addition, the calibrated transformation parameters between the left camera coordinate and the projector coordinate were, respectively,

$$R_{LP} = \begin{bmatrix} 0.954250 & 0.001407 & 0.299006 \\ 0.045013 & 0.987917 & -0.148304 \\ -0.295601 & 0.154979 & 0.942657 \end{bmatrix}, \quad (14)$$

$$t_{LP} = \begin{bmatrix} -307.760307 & -4.830472 & 46.019436 \end{bmatrix}^T.$$

Similarly, the transformation parameters between the right camera coordinate and the projector coordinate were

$$R_{PR} = \begin{bmatrix} 0.970919 & -0.036625 & 0.236591 \\ -0.004209 & 0.985465 & 0.169829 \\ -0.239372 & -0.165886 & 0.956652 \end{bmatrix}, \quad (15)$$

$$t_{PR} = \begin{bmatrix} -347.081662 & 4.643320 & 8.736196 \end{bmatrix}^T.$$

The performance of the proposed virtual camera approach of the calibrated stereo vision system was evaluated on two 3D objects, a ladder-shaped surface object, and a plaster statue. As shown in Figure 7(a), the first object to be profiled was a ladder-shaped surface constructed by combining three gauge blocks with heights of 60 mm, 100 mm, and 50 mm. A sinusoidal fringe was projected onto the surface of the block group and Figures 7(b) and 7(c) are, respectively, the images grabbed with the left and right cameras. As shown, both images emerge where one of the side blocks was hidden from the camera by the shadow of the central block. This clearly shows that only the central block can be measured with the original dual-camera system. Based on the calibrated parameters, the measurement result of the central block is shown in Figure 7(d). Seven points on the top surface as shown in Figure 7(e) were selected to evaluate the height measurement accuracy. The results are shown in Table 1 with a measurement accuracy within 0.016 mm. Measurements were repeated ten times and a repeatability of 0.005 mm was achieved. Figure 7(f) is the final full-field topography of the gauge block group after integration of the measured profiles from each of the three stereo vision systems. As discussed, all of the three profiles were unified to a single global coordinate. The overlapping
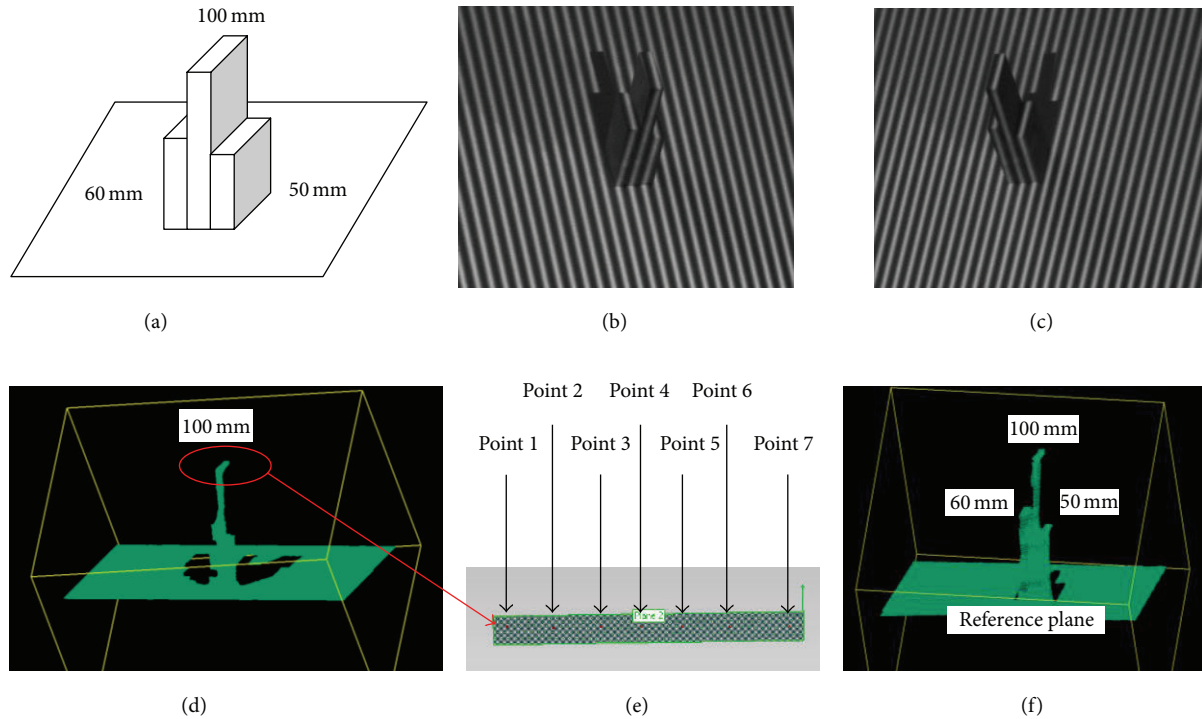
(a)

(b)

(c)

(d)

(e)

(f)

Figure 7: (a) Schematic diagram of the ladder-shaped specimen. (b) The projected grating image captured by the left camera. (c) The projected grating image captured by the right camera. (d) The measurement result of the central block based on the two-camera system. (e) Seven sampling points on the top surface of the central block. (f) Full-field topography of the ladder-shaped specimen.

Table 2: The measured heights of the seven sampling points of the left block.

Sampling points	1	2	3	4	5	6	7
Measured height (mm)	60.017	60.019	60.005	59.993	59.988	59.981	59.978
Error (mm)	0.017	0.019	0.005	0.007	−0.012	−0.019	−0.022

Table 3: The measured heights of the seven sampling points of the right block.

Sampling points	1	2	3	4	5	6	7
Measured height (mm)	50.020	50.023	50.013	50.001	49.995	49.983	49.975
Error (mm)	0.020	0.023	0.013	0.001	−0.005	−0.017	−0.025

area can be identified via the phase-based stereo matching and the redundant data can be removed automatically. Similarly, seven separate points on the top surfaces of the left and right gauges were selected as sampling points. The measured heights of the left and right blocks are, respectively, shown in Tables 2 and 3, where the maximum measurement error of the step height was roughly 0.05% of the height.

The second object to be profiled was a plaster statue with an approximate size of 500 mm × 300 mm. A sinusoidal grating was projected onto the surface of the statue. Figures 8(a) and 8(b) show the images captured by the left and right cameras, respectively. As shown, camera occlusion occurs on both sides of the nose and borders of the statue. Figure 8(c) shows the measured result of the dual-camera system, where the information at the border region of both sides was obviously lost. Figure 8(d) shows the final full-field topography of the statue integrated from the three measured

profiles of the three stereo vision systems. The merging result evidently shows that the blank area has been filled and the proposed method can alleviate camera occlusion significantly. Since the statue has a very complex free-form surface, the measurement accuracy is not discussed here.

For the above two experiments, the 3D stereo matching is required for the structured light binocular stereo vision system. In this study the adoption of phase-based stereo matching can automatically identify the overlapping area of the measurement data from different systems and achieve the automatic matching of 3D data. This avoids the search process for the overlapping area as in the traditional method and reduces the difficulty in data integration. Therefore, the computation time for the 3D profile measurement is much reduced. In addition, accurate extraction of the absolute phase determines the accuracy of the stereo matching and also directly affects the accuracy of the measurement.
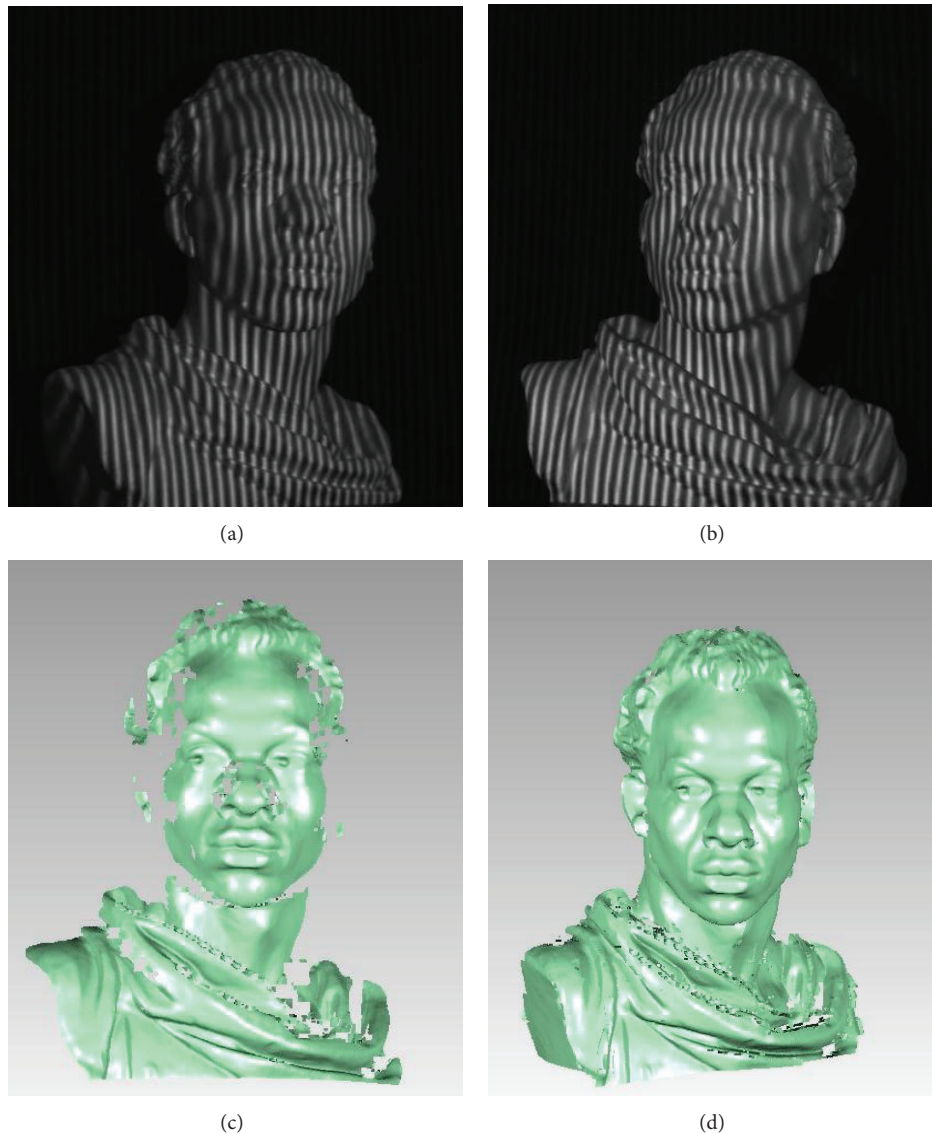
FIGURE 8: (a) The projected grating image of the left camera for a statue. (b) The projected grating image of the right camera. (c) The measured profile of the dual-camera system. (d) The data merging result based on the three stereo vision systems.

Experimental results show that an accuracy of tens of microns was obtained. This shows that the adoption of the interpolation technique can accurately determine the positions of corresponding stereo pairs, thus ensuring the measurement accuracy.

5. Conclusions

A novel 3D profile automated reconstruction technique for objects with complex free-form surface or step surface is presented. The system consists of two cameras and a projector. The measurement approach is based on the idea that the projector can be considered as a virtual camera; therefore, three stereo vision systems can be constructed to alleviate the problem of camera occlusion effectively. In addition, a 3D data merging method based on the absolute phase value and a unified coordinate system for the three sets of measured data is proposed; therefore, the three sets of 3D profiles can be well aligned and the redundant data can be removed automatically. This avoids the complicated and time-consuming process of data integration in the traditional dual-camera structured light system. Experimental results show that the measurement error below 0.03 millimeters could be expected in the camera occlusion region for a measurement range of 640 mm × 480 mm.

Acknowledgments

References

[1] J. Salvi, S. Fernandez, T. Pribanic, and X. Llado, "A state of the art in structured light patterns for surface profilometry," *Pattern Recognition*, vol. 43, no. 8, pp. 2666–2680, 2010.

[2] S. S. Gorthi and P. Rastogi, "Fringe projection techniques: whither we are?" *Optics and Lasers in Engineering*, vol. 48, no. 2, pp. 133–140, 2010.

[3] S. Zhang, "Recent progresses on real-time 3D shape measurement using digital fringe projection techniques," *Optics and Lasers in Engineering*, vol. 48, no. 2, pp. 149–158, 2010.

[4] S. Zhang and S.-T. Yau, "Three-dimensional shape measurement using a structured light system with dual cameras," *Optical Engineering*, vol. 47, no. 1, Article ID 013604, 2008.

[5] G.-H. Liu, X.-Y. Liu, and Q.-Y. Feng, "3D shape measurement of objects with high dynamic range of surface reflectivity," *Applied Optics*, vol. 50, no. 23, pp. 4557–4565, 2011.

[6] H. Anwar, I. Din, and K. Park, "Projector calibration for 3D scanning using virtual target images," *International Journal of Precision Engineering and Manufacturing*, vol. 13, no. 1, pp. 125–131, 2012.

[7] Z. Zhang, "A flexible new technique for camera calibration," *IEEE Transactions on Pattern Analysis and Machine Intelligence*, vol. 22, no. 11, pp. 1330–1334, 2000.

[8] P. J. Besl and N. D. McKay, "A method for registration of 3-D shapes," *IEEE Transactions on Pattern Analysis and Machine Intelligence*, vol. 14, no. 2, pp. 239–256, 1992.

[9] H. A. Beyer, V. Uffenkamp, and G. vanderVlugt, "Quality control in industry with digital photogrammetry," in *Optical 3DMeasurement Techniques III*, pp. 29–38, Wichmann, Heidelberg, Germany, 1995.

[10] J. H. Sun, G. j. Zhang, Z. Z. Wei, and F. Q. Zhou, "Large 3D free surface measurement using a mobile coded light-based stereo vision system," *Sensors and Actuators A*, vol. 132, no. 2, pp. 460–471, 2006.

[11] S. Barone, A. Paoli, and A. Viviano Razionale, "Shape measurement by a multi-view methodology based on the remote tracking of a 3D optical scanner," *Optics and Lasers in Engineering*, vol. 50, no. 3, pp. 380–390, 2012.

[12] Q. Hu, K. Harding, D. Hamilton, and J. Flint, "Multiple views merging from different cameras in fringe-projection based phase-shifting method," in *Two- and Three-Dimensional Methods for Inspection and Metrology V*, vol. 6762 of *Proceedings of SPIE*, September 2007.

[13] Y. C. Lin, M. Tong, M. J. Shi et al., "K-means optimization clustering algorithm based on particle swarm optimization and multiclass merging," *Advances in Intelligent and Soft Computing*, vol. 168, pp. 569–578, 2012.

[14] Y. I. Abdel-Aziz and H. M. Karara, "Direct linear transformation from comparator coordinates into object-space coordinates in close-range photogrammetry," in *Proceedings of the Symposium on Close-Range Photogrammetry*, pp. 1–18, American Society of Photogrammetry, Falls Church, Va, USA, 1971.

[15] R. Y. Tsai, "An efficient and accurate camera calibration technique for 3D machine vision," in *IEEE Computer Society Conference on Computer Vision and Pattern Recognition*, pp. 364–374, Miami Beach, Fla, USA, 1986.

[16] Q.-T. Luong and O. D. Faugeras, "Self-calibration of a moving camera from point correspondences and fundamental matrices," *International Journal of Computer Vision*, vol. 22, no. 3, pp. 261–289, 1997.

Research Article

High-Resolution Laser Scanning for Three-Dimensional Inspection of Drilling Tools

Roberto Marani, Massimiliano Nitti, Grazia Cicirelli, Tiziana D'Orazio, and Ettore Stella

Institute of Intelligent Systems for Automation (ISSIA-CNR), Via Amendola 122/DO, 70126 Bari, Italy

Correspondence should be addressed to Roberto Marani; marani@ba.issia.cnr.it

A high-resolution vision system for the inspection of drilling tools is presented. A triangulation-based laser scanner is used to extract a three-dimensional model of the target aimed to the fast detection and characterization of surface defects. The use of two orthogonal calibrated handlings allows the achievement of precisions of the order of few microns in the whole testing volume and the prevention of self-occlusions induced on the undercut surfaces of the tool. Point cloud registration is also derived analytically to increase to strength of the measurement scheme, whereas proper filters are used to delete samples whose quality is below a reference threshold. Experimental tests are performed on calibrated spheres and different-sized tools, proving the capability of the presented setup to entirely reconstruct complex targets with maximum absolute errors between the estimated distances and the corresponding nominal values below 12 μm.

1. Introduction

In the last few decades, starting from the early 1950's, the coordinate measurement machines (CMMs) have gained increasing importance in quality control in manufacturing industries up to play a key role in the inspection of complex assemblies in many mechanical fields, such as aeronautics and automotive.

Conventional CMMs can be represented as made of three simple blocks: a handling system for three-dimensional (3D) motion, a touching probe, and a data collector. Although many techniques aimed to reduce measurement uncertainty had been proposed [1–3], touching probes are implicitly sources of limitations in their applications. For instance, these systems can be unsuitable for delicate objects that could be damaged by an improper pressure or can lead to ambiguous measurements when the probe itself is deflected by the target.

For these reasons, contactless optical probes have been developed in order to get reliable measurements when the drawbacks of contact systems limit their effective applicability [4, 5]. Among them, those based on laser triangulation are very promising since they are not invasive and provide high precisions and fast measurements, whereas the low optical crosstalk and the high contrast gained by the use of

laser sources allow the suppression of the noise level [6–11]. Additionally, the high accuracy attainable exploiting laser scanning systems have opened the way for many new applications in different fields beyond mechanics, such as reverse engineering [12, 13], plastic surgery [14, 15], environmental reconstruction [16], and cultural heritage [17, 18]. Typical pros and cons of 3D optical sensors in relationship with the application fields have been clearly presented and discussed in [19].

The design of a laser triangulation scanner presents many challenges mainly ascribable to the accurate calibration of the whole system, the extraction of laser spots displayed on the camera plane, the presence of second-order reflections superposed on the actual meaningful signal, and the speckle noise sources [20, 21]. Many works have been done by researchers in order to achieve error compensation [22, 23] and the deep understanding of how the choice of the setup parameters can alter the results of the measurements [24]. Moreover, the inspection of complex surfaces can lead to self-occlusions when the field of view of the optical probe is cloaked by more external regions of the object under investigation. The first idea to solve this problem regards the use of path-planning techniques [25–27]. This issue is intended to find the best path, in terms of subsequent viewpoints for each laser
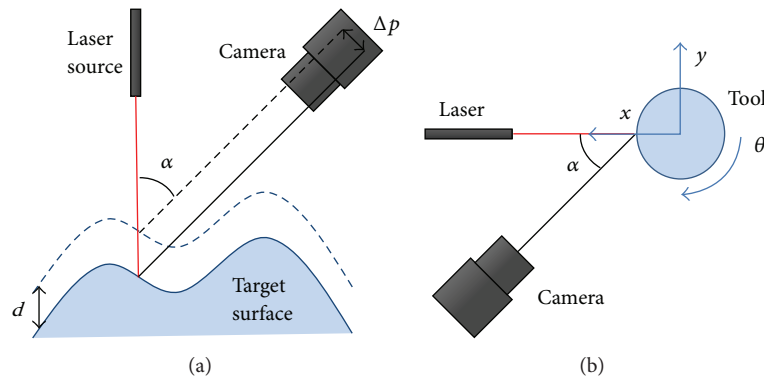
FIGURE 1: Sketches for the description of the principles of laser triangulation: (a) normal translation of a target surface and (b) simplified view of the presented system highlighting the adopted reference of coordinates.

scanning, that allows the complete coverage of the testing target, meeting some quality criteria on the reconstructed point cloud. This means that when the CAD model of the object is given, critical points are determined and a scanning path is then generated by checking the superimposed criteria. On the contrary, when CAD models of the target are not available, predictive blocks are integrated in the control system to define the following motion trajectories of the optical probe.

All the presented techniques have an important drawback that resides in the time required to perform a single acquisition, due to the need of preprocessing data to control the quality of results. In this paper, a high-resolution triangulation-based laser scanner is presented for the 3D reconstruction of complex objects. The field of application of the proposed system regards the entire characterization of drilling tools, whose geometry makes challenging their analysis. In particular, the presence of sharp edges, undercut surfaces, and fast repetitions of concave and convex regions induces occlusions together with the reduction of the quality of the measurement. As a consequence, these aspects have to be compensated through the use of suitable techniques. First, a procedure able to solve occlusion problems by handling the optical probe is presented together with the development of a robust analytical method for the exact data registration. Then, a filtering technique for image processing is defined to reduce the negative effects due to light scattering and second-order reflections. A calibration procedure is finally derived for the setting-up of a measurement prototype. The validation of the system is obtained through the analysis of a calibration sphere, with results in good agreement with the expected ones (absolute error in radius computation of few microns). Further experiments prove the capability of the prototype to investigate the shape of different-sized tools with the aim of looking for surface defects.

This paper is organized as follows: in Section 2, the analytical framework is introduced for the analysis of simple nonoccluded targets and then extended to more complex cases with undercut regions; the prototype description and the implemented image processing are reported in Section 3, whereas the calibration pipeline and the setup validation

are highlighted in Section 4; Section 5 shows experimental results of measurements on macro- and microtools, while final conclusions and remarks are in Section 6.

2. Analytical Framework

As shown in the previous section, the problem of laser triangulation had been widely discussed by researchers and its solution had been used in many industrial applications. In the following subsections, the acquisition strategy will be described under two different conditions. In the first case, the tool does not present self-occlusions due to undercut surfaces. Then, this condition is removed giving rise to an exhaustive analytical formulation of the problem. Further analyses are provided in order to define a strategy able to prevent the resolution decreasing due to the finite depth-of-field (DOF) of the elements of the setup.

2.1. Simple Case without Self-Occlusions. In two dimensions, the problem of laser triangulation can be addressed as shown in Figure 1(a). A laser beam impinging on a target surface is revealed on the sensor plane of a camera. The set is made by the laser source and the camera constitutes the optical probe of the system.

As known, a rigid translation d of the surface along the direction parallel to the optical axis of the laser is translated in a shift Δp of the reveled laser spot on the camera plane. For convenience, we assume that the camera is oriented in order that the pixel displacement is displayed vertically; that is, Δp is a difference of row coordinates in the camera plane. This relationship between d and Δp can be easily expressed by the following:

$$d = k \frac{\Delta p}{\sin \alpha}, \tag{1}$$

where α is the triangulation angle in Figure 1(a), whereas k is a term which reports the camera coordinates in the metric reference system. This term is implicitly related to the camera lenses and to the physical dimensions of the pixels of the camera. Since traditional lenses induce optical distortions, k nonlinearly depends on the position of the revealed spot

within the camera plane. In order to avoid the nonlinear behavior of the term k, a telecentric lens can be adopted, thus giving

$$k = \frac{s_p}{M}, \tag{2}$$

with s_p being as the size of the camera pixel and M as the magnification of the telecentric lens. It is important to remark that the constant term $s_p/(M \sin \alpha)$ represents the conversion factor from the vertical pixel coordinate on the camera plane to the metric one along the direction of d.

All the considerations reported before are valid for a single dot impinging the target surface, accordingly to the two-dimensional definition of the problem. This framework can be exported in 3D by considering an extended laser line. In this case, the laser line can be treated as an array of laser spots, whose horizontal positions give information about the displacement d in the third direction. Analytically, the third component can be easily translated in metric coordinates by multiplying the column coordinate of the corresponding pixel by the term k in (2).

Since this work is devoted to the efficient reconstruction of drilling tools, the actual setup can be drawn as in Figure 1(b) where a top view of the system is returned. In this case, the scanning of the tool is obtained by rotating the target around its drill axis, sampling the θ-axis with N_A points between 0 and 2π. Each frame captured by the camera reports the laser line distorted by the tool surface for a particular discrete angle θ_i, $i = 1, \ldots, N_A$. This means that the term d in (1) has to be further transformed in order to get the actual coordinates of the corresponding point.

Under the hypothesis of infinite DOF of both laser and camera, and supposing that the field-of-view (FOV) of the camera is able to cover the whole volume of the tool, the generic ith laser line, acquired when $\theta = \theta_i$, spans horizontally the camera plane (see Figure 2), whose dimension is equal to $N_C \times N_R$ pixels. Line peaks can be detected at coordinates $(I_j^{(i)}, J_j^{(i)})$, where $j = 1, \ldots, N_C$, which correspond the 3D real coordinates $(X_j^{(i)}, Y_j^{(i)}, Z_j^{(i)})$ expressed as follows:

$$X_j^{(i)} = \frac{s_p}{M \sin \alpha} \left(J_0 - J_j^{(i)}\right) \cos \theta_i,$$

$$Y_j^{(i)} = \frac{s_p}{M \sin \alpha} \left(J_0 - J_j^{(i)}\right) \sin \theta_i, \tag{3}$$

$$Z_j^{(i)} = -\frac{s_p}{M} I_j^{(i)}.$$

It is worth noting that the pixel increment has to be related to a reference axis. All pixel measurements are computed as the gap between the actual row position of the line peak and the drill axis reported on the camera plane. Its location is independent of θ and always equal to J_0 for each column of the plane, since the drill axis is aligned to the z-axis, orthogonal to the xy-plane. Moreover, the sign of $Z_j^{(i)}$ is added in order to get a consistent reference system, as the one reported in Figure 1(b).
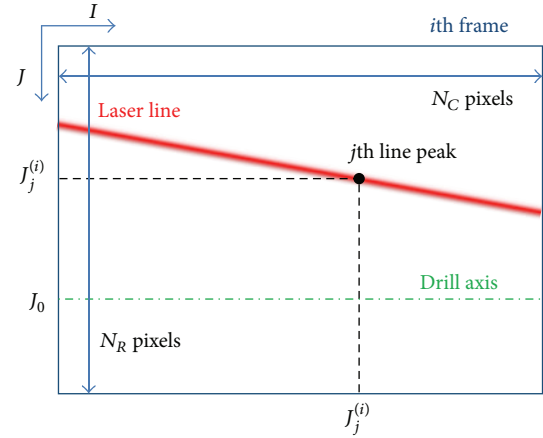

FIGURE 2: Schematic representation of the laser line reported on the camera plane.

Once the real coordinates of each detected point are determined, measurement resolutions can be derived. For convenience, these terms can be expressed in cylindrical coordinates (r, θ, z):

$$dr = \frac{s_p}{M \sin \alpha},$$

$$d\theta = \theta_{i+1} - \theta_i, \tag{4}$$

$$dz = \frac{s_p}{M}.$$

All resolution terms related to distance measurements are directly influenced by s_p and M, whose ratios have to be as small as possible, within the limits imposed by the camera fabrication technologies. Quantitatively, this ratio sets dz equal to 2.2 μm. At the same time, the triangulation angle α participates in the expression of the resolution terms dr, in the sense that its sine function has to be kept as high as possible to get lower values of dr. This means that the closer to $\pi/2$ this angle is, the better radial resolution is reached. However, this condition is not realistic since high values of α induce occlusions while scanning the tool surface. A good balance can be struck by considering α close to $\pi/4$, which leads to dr equal to about 3.1 μm. Finally, the angular resolution $d\theta$ directly depends on the angular aperture between two successive frames acquired by the camera, that is, on the value assumed by N_A. Under the assumption that the rate of change of the angular displacement can be arbitrarily adjusted, this term is only limited by the initial specification regarding the time required for the entire reading of the tool, in relationship to the camera frame rate. The experimental settings adopted in this paper bring to an angular resolution of 0.7° at a camera frame rate of 25 fps.

2.2. Complex Case with Self-Occlusions. The visual inspection of drilling tools is challenging because of the presence of undercut regions that induce self-occlusions of several articulated surfaces. In many cases, the reconstruction of these surfaces is mandatory for the complete quality control of
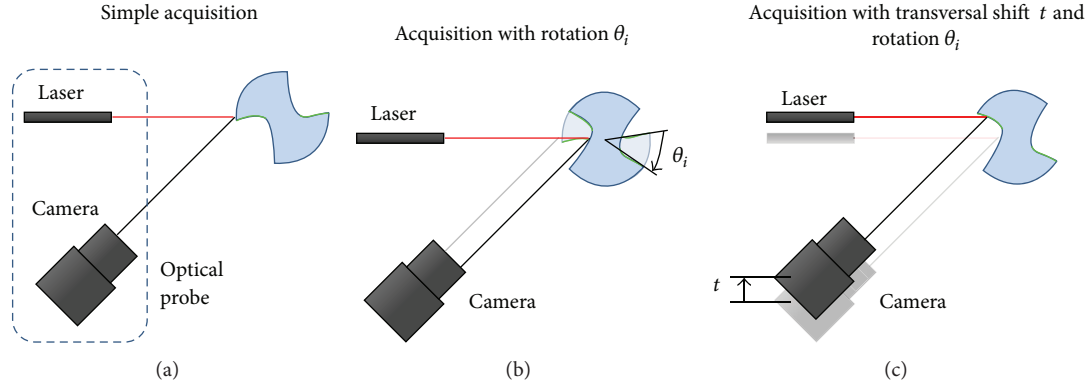
FIGURE 3: Acquisition schemes for the reconstruction of the whole surface of a complex tool. (a) Simple acquisition with $\theta_i = 0$; (b) first scanning round with increasing θ_i for the evaluation of nonoccluded surfaces (blue edges); and (c) second scanning round with superimposed transversal shift t for the achievement of occluded surfaces (green edges).
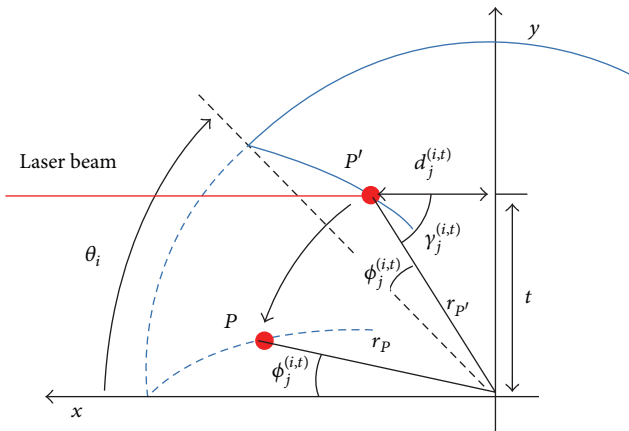

FIGURE 4: Schematic view of a tool section (blue contours) for the analytical registration of occluded points acquired by imposing a transversal shift t of the optical probe. World coordinates (x, y) are used in this context.

the tool. The problem of self-occlusions is shown in Figure 3, where undercut regions of the tool are reported in green.

By the analysis of Figures 3(a) and 3(b), it is clear that the single rotation of the tool around its axis is not able to reconstruct the surfaces of those undercut regions that are never reached by the laser line. This problem can be overcome by means of a transversal shift t of the optical probe. By this way, the laser line strikes the occluded surfaces at different rotation angles, whose value depends on the depth itself of the target surfaces. Moreover, the computed depth is also scaled by a factor still depending on the introduced shift t. Consequently, the process of point cloud registration is not merely subjected to a rotation of samples but is more complex and has to be computed analytically, knowing the term t.

With reference to Figure 4, where the two-dimensional problem is illustrated, the registration process aims to find the coordinates of the actual point P, corresponding to the point P', illuminated under the conditions of a transversal shift t. Triangulation rules permit the definition of the distance $d_j^{(i,t)}$

from y-axis, starting from the knowledge of the jth pixel coordinates $(I_j^{(i,t)}, J_j^{(i,t)})$ of the detected laser line:

$$d_j^{(i,t)} = \frac{s_p}{M \sin \alpha} \left(J_0 - J_j^{(i,t)} \right). \tag{5}$$

The angle $\gamma_j^{(i,t)}$ is easily derived as

$$\gamma_j^{(i,t)} = \tan^{-1} \left(\frac{t}{d_j^{(i,t)}} \right). \tag{6}$$

Consequently, the radial component $r_{P'}$ of the point P' can be written as

$$r_{P'} = r_P = \frac{d_j^{(i,t)}}{\cos \left(\gamma_j^{(i,t)} \right)}. \tag{7}$$

Once the radial component of the point P is identified, the actual coordinates of P can be obtained as the projection of r_P on the x- and y-axis, mediated by the angle $\phi_j^{(i,t)}$. In a more explicit way, the final 3D coordinates of the registered point P are

$$X_j^{(i,t)} = \frac{d_j^{(i,t)}}{\cos \left(\gamma_j^{(i,t)} \right)} \cos \left(\theta_i - \gamma_j^{(i,t)} \right),$$

$$Y_j^{(i,t)} = \frac{d_j^{(i,t)}}{\cos \left(\gamma_j^{(i,t)} \right)} \sin \left(\theta_i - \gamma_j^{(i,t)} \right), \tag{8}$$

$$Z_j^{(i,t)} = -\frac{s_p}{M} I_j^{(i,t)}.$$

Finally, it is easy to verify that the formulations in (8) converge to those in (3) when the transversal shift vanishes.

It is worth noting that the choice of the term t is directly related to the shape and the size of the tool under analysis. In principles, only two values of t, roughly t_0 equal to 0 and t_1 smaller than the tool radius, are enough to overcome self-occlusions. Nevertheless, if surface holes still affect the resulting point cloud, more observations of the object have to be performed at intermediate values of t in the range $[t_0, t_1]$.
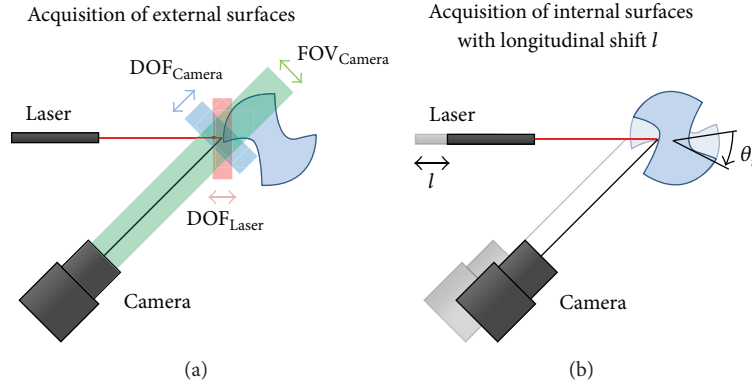
FIGURE 5: Strategy for the preservation of the system resolution: (a) acquisition of external surfaces and (b) inspection of internal surfaces subsequent to the longitudinal shift l of the optical probe.

2.3. Systems with Finite DOF. The formulations in (8) have been obtained under the fundamental hypothesis of infinite DOF of the element of the optical probe, both laser and camera, and considering a camera FOV able to cover the whole testing volume. In a more realistic scenario, these aspects are no longer valid. By looking at Figure 5(a), it is evident how laser and camera DOFs, together with the Camera FOV, shrink the volume in which nominal resolutions are those in (4). This has effects on the downsizing of the exploitable area of the camera plane where the target is correctly focused. In fact, the decrease of the allowed depth, where (8) can be correctly estimated, leads to a consistent reduction of the region-of-interest (ROI) along the J-direction of the camera plane.

Preventing the measurement resolution from getting worse is mandatory in high-definition systems. This aim can be reached by adding a new degree of freedom to the optical probe, that is, a longitudinal shift l in the x-direction, which enables the acquisition of those internal surfaces that, otherwise, would not be captured. Each round of the tool at a particular l value defines an isodepth observation. All frames in a single round are thus labeled by the specific longitudinal shift l that is then used to reconstruct the coordinates of the reconstructed points. The expression of $d_j^{(i,t)}$ in (5) can be now rewritten as

$$d_j^{(i,t,l)} = \frac{s_p}{M \sin \alpha} \left(J_0 - J_j^{(i,t,l)} \right) + (l - l_0), \qquad (9)$$

where l_0 represents the longitudinal shift needed to include the drill axis in the downsized ROI of the camera. The importance of this term will be further discussed in the Section 4 where the description of the calibration phase will be introduced.

The value of the parameter l has to be returned by an encoder able to transduce numerically the entity of the motion. These values are thus biased by an internal offset induced by the system of reference of the mechanical controller. Anyway, all values of l undergo the same offset that is then implicitly compensated by the term l_0.

TABLE 1: Technical data of the Lasiris TMFL laser.

Parameter name	Parameter value
Depth of field	200 μm
Working distance	55 mm
Line width	9 μm
Line length	10 mm
Laser wavelength	660 nm
Output diode power	100 mW

3. System Prototype

Once the analytical formulations have been derived, the next step in the system design is the appropriate choice of the optical components. The next subsections will be devoted to the description of the prototype, together with a brief introduction on the steps followed for the image processing.

3.1. Experimental Setup. As underlined in the previous section, the optical probe is made of two main elements: the laser source and the optical receiver (camera and telecentric lens).

The properties of the laser source are the basis of the whole resolution of the proposed system, since, as expressed in (4), the capability of the algorithm of image processing to distinguish between two adjacent peak positions comes in succession to the quality of the laser line itself. In particular, the small thickness of the laser line over its entire length is a fundamental requirement to attain high resolutions. This goal can be achieved by means of a telecentric laser which produces a uniform lengthwise and Gaussian widthwise beam. Such specifications are guaranteed by a Lasiris TMFL-55 laser emitter, whose generated line thickness is equal to 9 μm ($1/e^2$ estimation) at its working distance. The main features of this device are reported in Table 1 [28].

The system resolution is also affected by the physical properties of the set made by the camera and the telecentric lens, which determines the ratio s_p/M in (4). This ratio has to be set as low as possible in order to get the best conditions for the measurement resolution. Moreover, its value influences the sampling of the laser line that should

TABLE 2: Technical data of telecentric lens Lensation TC5M-10-110i.

Parameter name	Parameter value
Magnification	1X
Aperture (F)	6.5
Working distance	110 mm
Depth of field	260 μm

TABLE 3: Technical data of the UI-3480CP-M uEye camera.

Parameter name	Parameter value
Interface	USB 3
Lens mount	C-Mount
Sensor technology	CMOS (Aptina)
Resolution ($h \times v$)	2560×1920
Sensor size	$1/2''$
Max. fps in free running mode	15 fps
Pixel size	2.20 μm
Optical size	5.632×4.224 mm

lie widthwise over more than three pixels in order to enable efficient peak extraction strategies. The optical receiver is made of an IDS-uEye camera (Model USB-3-UI-3480CP-M) assisted by the telecentric lens Lensation TC5M-10-110i. The principal features of the lens and the camera are reported in Tables 2 and 3, respectively [30, 31].

The proposed choice has results in a ratio s_p/M equal to 2.2 μm. This value has to be further multiplied by the sine of the triangulation angle α in order to get the conversion factor from pixel shifts to metric displacements. Since typical values of α are close to $\pi/4$, the conversion term is approximately equal to 3 μm. This means that any laser line detected on the camera plane can be sampled in at least three pixels, as required.

Finally, it is important to observe that the laser source shows the minimum DOF of the elements of the optical probe (200 μm). As already discussed in Section 2.3, this value draws a line at the effective ROI within the camera plane, whose height has to be consequently reduced to approximately 70 pixels.

A picture of the prototype is highlighted in Figure 6, where the presence of micrometric slits which are only exploited during the calibration phase for the proper alignment of the optical components is evident.

3.2. Image Processing. As shown previously, resolution can be further improved via image processing aimed to the detection of laser peaks with subpixel precisions. Starting from a single frame acquired by the camera, the laser line is scanned along the columns. Then, a couple of vectors including the row positions and the corresponding intensities of the illuminated pixels is extracted for each column containing the line. These two vectors are inputs for the detector, whose task is

the estimation of the exact row position of the maximum laser intensity.

Many algorithms have been developed to determine the exact position of the laser peaks. Among these, the Gaussian approximation, linear interpolation, Blais and Rioux detectors, and parabolic estimators can be identified, just to mention a few [32].

Exploiting the knowledge of the physical shape of the emitted laser line, the implemented algorithm names the peak position as the expected value of the Gaussian distribution that fits the laser profile in the least squares sense. This method gives back an implicit quality index, that is, the standard deviation σ of the reconstructed Gaussian distributions. A simple threshold on this value is able to delete those peak estimations whose associate widths are higher than the expected ones (the threshold value σ_{th}), close to the nominal laser linewidth. Therefore, ambiguous estimations are removed preventing the increase of the measurement uncertainty. Henceforth, the mean value σ_{av} assumed by the standard deviations of the fitting Gaussian distributions will be used to express the quality of the reconstructed points.

Moreover, another threshold scheme can be used for the deletion of noise sources due to the presence of second-order reflections of light. Since noise signals have presumably lower light intensities, the peak extraction is enabled only when at least one pixel of the input vector has intensity higher than the threshold I_{th}. Therefore, columns that do not meet this specification are removed from the analysis, thus reducing also the computation time required for the image processing. This term has to be set properly depending on the emitted optical power. Experiments have proven that fixing I_{th} equal to a fraction of about 10–15% of the maximum laser intensity detected by the camera is enough to achieve the correct suppression of second-order reflections.

Further explication of how these terms affect results will be provided in the next paragraphs.

4. Preliminary Analysis

The preliminary phase of calibration of the setup is of primary importance for preventing systematic errors in the evaluation of relative distances among surfaces. In the following subsections, the calibration pipeline will be summarized together with the analysis of preliminary results of measurements carried out on a known target.

4.1. Calibration Pipeline. As can be seen in Figure 6, all optical components lie on positioning stages which introduce controlled translational shifts able to move separately the elements of the optical probe along the directions of the x-axis and y-axis. At the same time, two goniometers allow the rotations of both laser and camera around axes parallel to the corresponding optical directions.

The initial calibration phase can be listed as follows. Before starting, it is mandatory to notice that the calibration is run by placing a perfectly cylindrical tool with smooth surfaces in the mechanical spindle. Here, the radius of the tool is named r_c.

(1) Rotation stage of the tool

(2) Telecentric laser source (Lasiris TMFL-55)

(3) Telecentric lens (Lensation TC5M-10-110i)

(4) USB 3.0 Camera (uEye UI-3480CP-M)

(5) Translational positioning stage

(6) Goniometer for precise angular adjustment
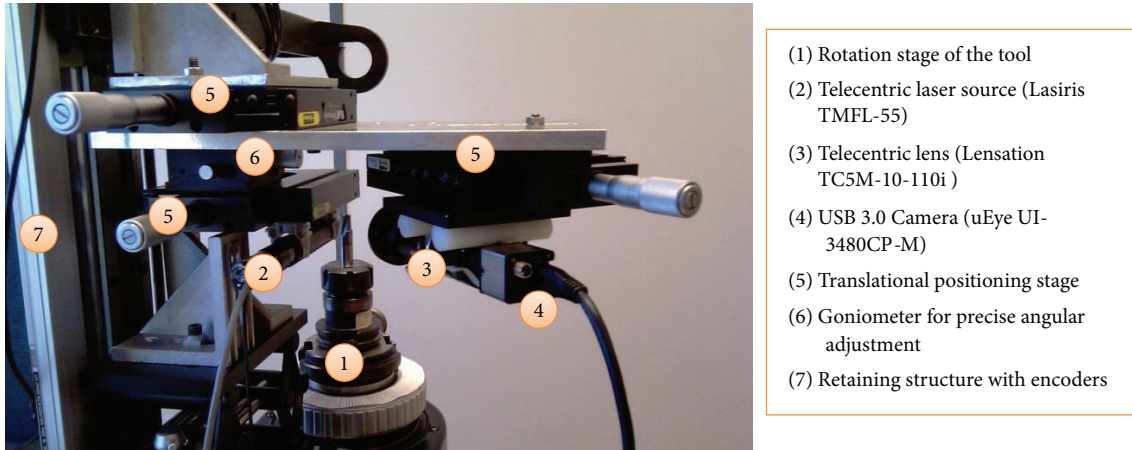
(7) Retaining structure with encoders

FIGURE 6: Picture of the prototype of the proposed setup. Micrometric slits are only used for the calibration phase of the acquisition process. All handlings, both translational and rotational, are numerically managed via an external controller. Legends describe corresponding setup components.

4.1.1. Positioning of Laser and Camera. The first step consists in checking the camera orientation. In this case, the laser is kept off and the camera is adjusted in order to focus on the cylindrical tool. The exposure time is then set high enough to get the tool smooth edge. The camera is thus oriented till the tool edge is perfectly aligned with the I-axis in Figure 2.

Then, the laser is fed with a suitable injection current and thus generates a line which impinges on the tool surface in the camera FOV. Hence, the laser source can be oriented till the produced line is perfectly aligned parallel to the I-axis of the camera plane.

Once both laser and camera are perfectly oriented, it is necessary to align the laser line on the drill axis. The laser source is shifted along the y-axis till the revealed line on the camera plane reaches the highest position along the J-axis. This position corresponds to the maximum distance from the drill axis; that is, the tool radius overlaps the x-axis.

Finally, laser and camera can be focused on the volume. This condition is found simultaneously by looking at the width of the detected laser line. The focus is reached when the laser linewidth reaches its minimum. Moreover, the focus coordinate along the J-axis of the camera plane determines the exact position of the ROI within the camera plane.

4.1.2. Choice of the Injection Current of the Laser. Scattering, specular reflections, and second-order reflections can worsen the measurement by increasing the width of the detected beam, although the laser line is correctly focused on the target surface. These aspects can limit the resolution of the system increasing the term *dr* over its nominal expected value.

Two different ways can be found to overcome this problem. The former is the fine-tuning of the feeding current of the laser in order to reduce its output power, thus finding the best condition against light scattering from the tool surface at the expense of the signal-to-noise ratio. The latter envisages modulation schemes of the laser amplitude. In this case, the camera has to be synchronized to the laser modulating signal in order to grab the line when the laser is switching off. For

the sake of simplicity, the proposed setup exploits the first technique to preclude the deterioration of the line quality.

At this step, the cylindrical smooth tool is changed by a complex one, whose surface is made of rough edges. Its volume is coarsely scanned by the optical probe with different injection currents till the best balancing between the laser linewidth and the signal-to-noise ratio is reached.

4.1.3. Estimation of the Triangulation Angle. The correct estimation of the triangulation angle α is fundamental in the correct reconstruction of 3D points, since it affects the in-plane components $X_j^{(i,t,l)}$ and $Y_j^{(i,t,l)}$, coming out form the peak coordinate $J_j^{(i,t,l)}$.

This value can be obtained exploiting an inverse fit on the parameters in (1) and (2). In this case, the optical probe approaches and leaves the target surface of known quantities returned by the mechanical encoder. When the detected line falls in the camera ROI, the mean position of the extracted peaks along the J-axis can be recorded. The collection of data is used to solve an overdetermined system of linear equations as a function of α in the least squares sense. Figure 7 shows an example of data fitting where red dots are related to the experimental measurements, whereas the blue line is derived by the solution of the calibration problem.

4.1.4. Identification of the Position of the Drill Axis. As shown in the analytical formulation of the problem, each range measurement has to be referred to the drill axis, which is also the origin of the x-axis and y-axis. This contribution is carried by the terms l_0 and J_0 in (9). Explicitly, the aim of this preliminary phase is the determination of the value assumed by $((s_p/(M\sin\alpha))J_0 - l_0)$, exploiting the simple technique reported in Figure 8.

With reference to Figure 8(a), as a first step, the optical probe is dragged playing on the x-handling to inspect the surface of the cylindrical tool. As a consequence, the laser
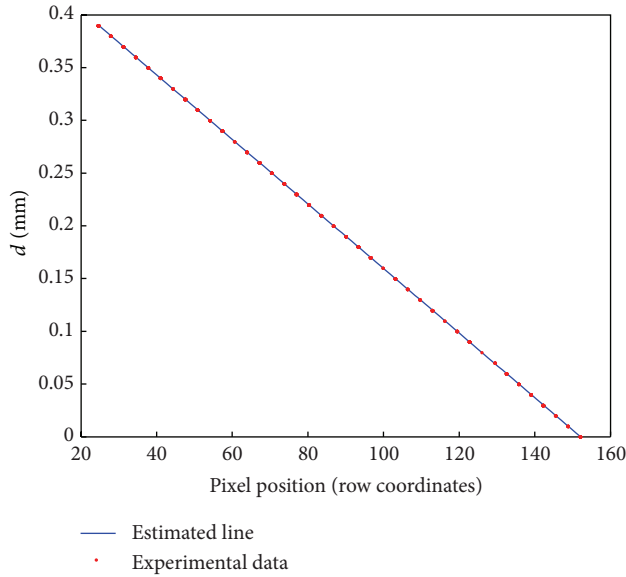
FIGURE 7: Results for the evaluation of the triangulation angle α. Experimental data (red dots) are obtained by moving the optical probe away from the target and recording the row coordinates of the detected laser lines. The blue line is the result of the curve fitting on the experimental data (depending on α).

line lies horizontally in the middle of the ROI, here 200-pixel-height, while the mechanical encoder returns an absolute position E_x. The optical probe is then moved away from the surface as far as the line reaches the edge of the ROI (Figure 8(b)). Under this condition, the value E_{x0} returned by the encoder is the actual distance of the ending depth boundary of the testing volume from the reference surface of the tool. Consequently, the exact position of the drill axis referred to the encoder system of coordinates can be derived by adding the known radius r_c of the cylindrical tool. This means that the objective term in (9) can be substituted by the sum $(E_{x0} + r_c)$, thus obtaining the following final formulation:

$$d_j^{(i,t,l)} = \frac{s_p}{M \sin \alpha} \left(h_{\text{ROI}} - J_j^{(i,t,l)} \right) + (E_{x0} + r_c) - l, \qquad (10)$$

where l is now directly the shift value returned by the encoder, whereas h_{ROI} is the height of the ROI in the camera plane. It is important to underline that the condition presented in Figure 8(b) has effects on the term J_0 in (9), now equal to h_{ROI}, as the laser line lies on the bottom of the camera ROI. Moreover, since the x-axis has origin in the center of the tool and comes out from it, in opposition to the handling system of reference, the term $(l - l_0)$ has to change in sign in (9), thus converging to the formulation in (10).

4.2. Setup Validation. Before going through the analysis of experimental results, the calibrated system has to be validated with the inspection of a known target. In this case, a standard ceramic probe sphere with diameter equal to 18 mm is used. The robustness of this experimental validation is further guaranteed by the proper location of the calibration sphere. In particular, the alignment of the center of the sphere along

the rotation axis is mediated by a high-precision mechanical comparator with results in a maximum positioning error of 2μm. The results of laser scanning are reported in Figure 9 where the initial point cloud and the corresponding reconstructed surfaces are shown. Both results are related to the analysis of 6 mm height section of the sphere, which corresponds to the maximum FOV reachable along the z-direction performing a single scanning of the sphere.

The estimated radius of the ceramic sphere is equal to 8.994 mm and thus is in good agreement with its nominal value (9 mm). The radial coordinates of all points have been further collected in order to derive the ~99% confidence interval of the measurement, which results equal to 49.8 μm. Unfortunately, this result is deeply affected by the constitutive medium of the target, which induces high light diffusion on the sphere surface with a consequent broadening of the detected laser line. Moreover, this second-order effects cannot be overcome applying the techniques described previously. For instance, it is not possible to decrease arbitrarily the injection current of the laser, since the noise level due to light scattering made by ceramic becomes ever more comparable to the signal component. Furthermore, even a soft threshold based on the selection of those Gaussian distributions having proper standard deviations causes the deletion of the majority of samples. As a consequence, even conservative filter parameters lead to the presence of the small holes in the reconstructed surface in Figure 9(b). Once again, it must be emphasized that this negative aspect is only ascribable to ceramic and will not concern the actual measurements that will be run on metallic tools.

5. Experimental Results

The next subsections report the results of experimental measurements run on two different drilling tools in order to show the capability of the setup to probe challenging surfaces. In the following lines, testing objects will be labeled as macro- or microtools depending on whether the size of their diameters is comparable with the DOF of the laser.

5.1. Macrotool Inspection. The first example of inspection of a drilling tool regards the analysis of a thread mill. This tool has many features that make its inspection challenging, such as the presence of sharp edges responsible for high light scattering. Moreover, internal faces are mostly occluded by the cutting lips which make the use of the transversal handling for their reconstruction necessary. Finally, as seen previously, also longitudinal shifts are required for the complete scanning of the tool since its diameter is much larger than the laser DOF (the diameter of the testing tool is equal to 12 mm).

At this preliminary stage, the only tip of the thread mill will be investigated. This means that the size of the inspection volume in the z-direction will be equal to about 5.6 mm that is equal to the optical size of the chip of the camera. This value can be easily derived by looking at (8), where the maximum value of $Z_j^{(i,t,l)}$ can be obtained as the product of the number of pixels in the I-direction of the camera plane by the pixel size s_p. It is important to notice that this value does not limit
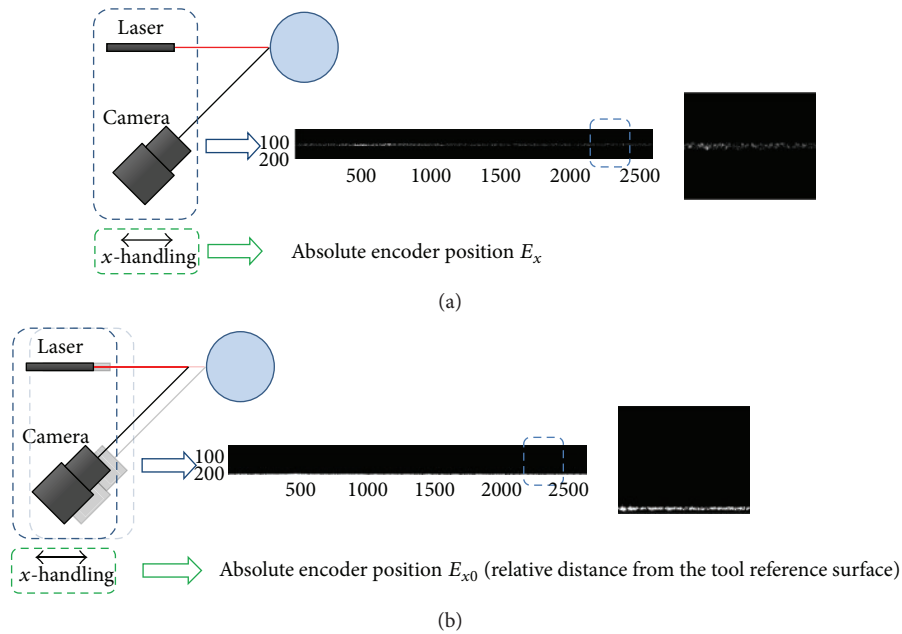
FIGURE 8: Scheme for the detection of the rotation axis of the tool. (a) Generic acquisition at the absolute encoder position E_x; (b) tuned acquisition run moving away the optical probe until the laser line lies on the boundary of the ROI on the camera plane (absolute encoder position E_{x0}). Windows show the snapshots of the ROI within the camera and the corresponding magnified views.

FIGURE 9: (a) Point cloud (79669 points) and (b) surface reconstruction (156135 elementary triangles) of the ceramic calibration sphere.

the effective inspection of tools to this restricted region, since the application of another encoded handling able to carry the probe to different vertical positions would allow the extension of the testing volume beyond this physical limit.

The first step regards the evaluation of the calibration pipeline described previously, which has results in a triangulation angle α of 36.62°. On the other hand, the identification of the position of the drill axis in the absolute system of reference defined by the x-encoder has been carried out exploiting the shank region of the testing tool itself. Consequently, the term $(E_{x0} + r_c)$ has been found equal to 6.138 mm.

Once the calibration of the system is accomplished, the peak extraction parameters for image processing have to be selected in order to guarantee the limitation of measurement uncertainty. Figure 10 reports an example of the detected laser line on the camera plane and the corresponding peaks extracted under different threshold conditions on either the pixel intensity (I_{th}) or the estimated Gaussian width (σ_{th}).

With reference to Figures 10(c) and 10(d), the effect of the threshold mediated by the term σ_{th} which controls the thickness of reconstructed Gaussian profile derived by the detected laser line is evident. When σ_{th} is set to 1 m (Figure 10(c)), and thus much higher than the expected line thickness, the threshold control and, therefore, the quality term σ_{av} are more than two times higher than the ones obtained when the filter is enabled (Figure 10(d)). This indicates that the results of the image processing are more reliable against light diffusion at the expense of the number of points extracted, which is reduced from 802 to 444 samples in this particular case.

At the same time the comparison of Figures 10(b) and 10(d) demonstrates that the intensity threshold expressed by the term I_{th} has great influence on the effectiveness of the measurements. In particular, isolated spots due to second-order reflections and to the camera noise are entirely passed through the peak extractor. Here, the Gaussian threshold is not able to filter these points since the associated Gaussian profiles have small standard deviations below the threshold.
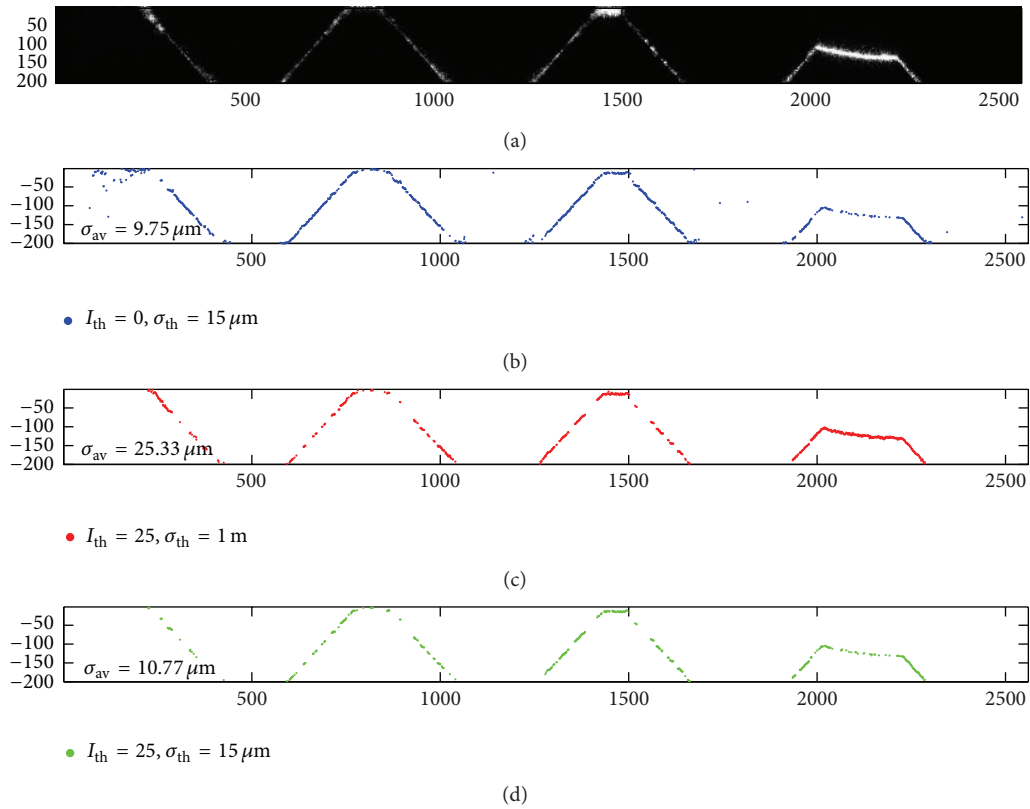
FIGURE 10: Laser line impinging on a thread mill (a) and corresponding points detected through the presented algorithm based on the Gaussian fit with: (b) $I_{th} = 0$ and $\sigma_{th} = 15 \, \mu m$, (c) $I_{th} = 25$ and $\sigma_{th} = 1 \, m$, and (d) $I_{th} = 25$ and $\sigma_{th} = 15 \, \mu m$.
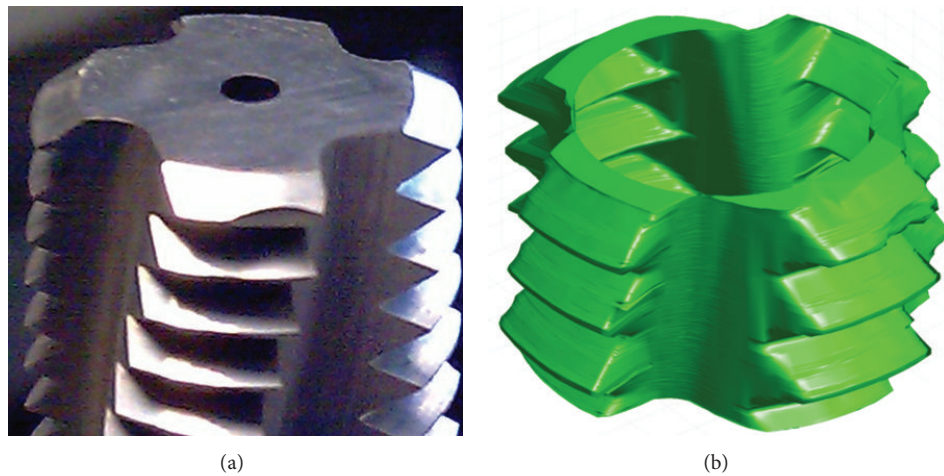

FIGURE 11: (a) Picture of the analyzed thread mill and (b) corresponding surface reconstruction.

As a consequence the measurement is completely invalidated by the presence of such samples, although quality terms σ_{av} are totally comparable. On the contrary, outliers are completely filtered out when the threshold is turned on, thus preserving the validity of the reconstruction.

Figure 11 shows a picture and the corresponding reconstructed surfaces of the thread mill under investigation.

The analysis of Figure 11 proves the capability of the prototype to completely inspect the thread mill exploiting the two encoded handlings along the in-plane directions. Both external and internal surfaces are reconstructed by properly shifting the optical probe in a range of 2 mm along the y-axis (transversal handling) and of about 2.5 mm along the x-axis (longitudinal shift).
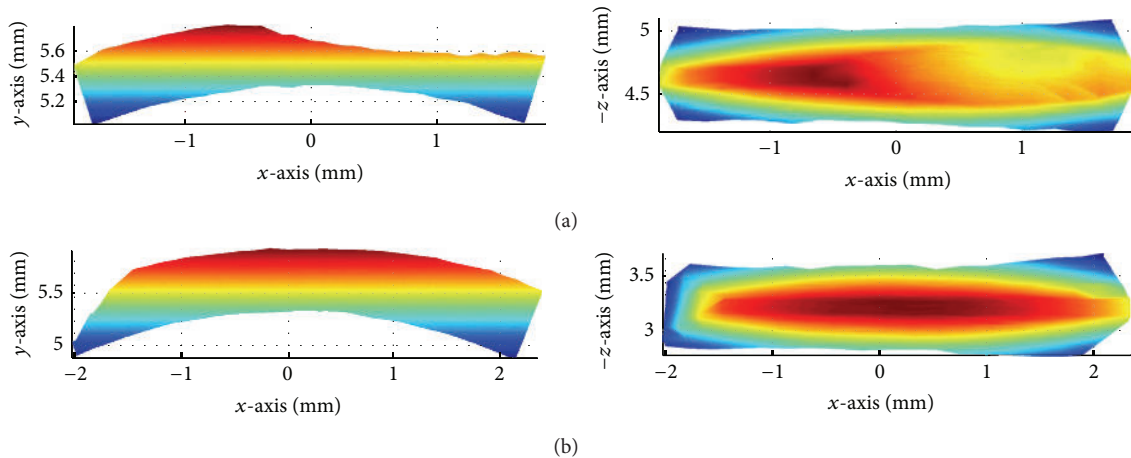
FIGURE 12: Top (left) and side (right) views of the defective (a) and defectless (b) cutting lips of the thread mill shown in Figure 11.
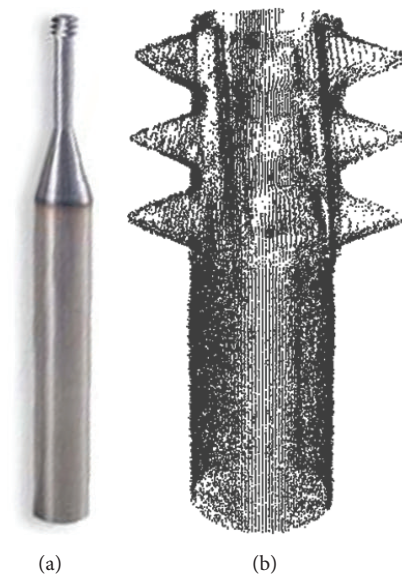

(a)   (b)

FIGURE 13: (a) Picture of a miniature solid carbide thread mill Vargus Vardex MilliPro and (b) corresponding reconstructed point cloud (59526 samples).

The presented tool is characterized by a surface defect on a cutting edge. Figure 12 highlights this region in comparison to a defectless one, in order to demonstrate how 3D reconstruction allows the deep insight of tools aimed to find the presence of defects together with their characterization.

5.2. Microtool Inspection. As seen in the previous sections, the physical properties of the laser line detected on the camera plane have consequences on the resolution of the measurements, following (4). Since this value has been demonstrated to be close to few microns, also microtool with small diameters, comparable to the laser DOF, can be tested. In this case, measurements are performed on a solid carbide thread mill by Vargus Vardex MilliPro, whose technical data are available in [29].

In this case, the calibration parameters, that is, the triangulation angle and the relative position of the drill axis, have been kept equal to those of the previous experiment. On the contrary, the small dimensions of the testing tool make the entire scanning of the whole tip in a single isodepth round, namely, without using the longitudinal handling to reach internal surfaces possible. On the other hand, the use of the transversal handling is still mandatory to avoid the presence of self-induced occlusions. In this case, the optical probe is handled in a range of $500\,\mu$m along the y-direction. The extracted point cloud is reported in Figure 13 together with a picture of the tool under investigation.

The main difference with regards to the macrotool inspection concerns the choice of the parameters for the image processing. The small radius of curvature of this class of tools reduces the quality of the detected laser line which
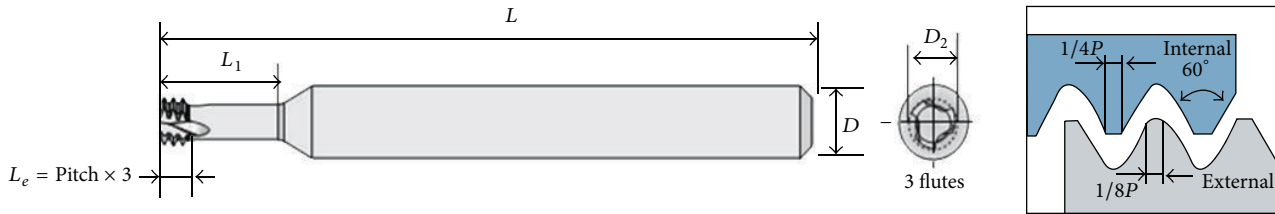
FIGURE 14: Geometric scheme of the Vargus Vardex Millipro tool [29].

TABLE 4: Comparison of results out of the analysis of the Vargus Vardex MilliPro tool. Nominal values are taken from [29].

Parameter name	Nominal value	Estimated value
Pitch P	450 μm	438 μm
D_2	1.651 mm	1.646 mm
Internal angle	60°	54.88°

increases in its width. Moreover, the fast repetition of concave and convex regions induces the presence of many secondary reflections displayed on the camera plane. As a consequence, the need of more preserving filter parameters, or, in other words, of higher values of I_{th} opposed to lower values of σ_{th} is implicit. Quantitatively, I_{th} and σ_{th} have been set equal to 40 and 12 μm, respectively, with results in a quality term σ_{av} being close to 7.1 μm, anyway lower than the one obtained in the case of the inspection of the macro-tool.

A comparison between estimated measurements on the extracted point cloud and their nominal counterparts has been reported in Table 4. Parameters are the ones highlighted in Figure 14.

The presented results are in good agreement with the nominal values with maximum absolute errors that are lower than 12 μm in computing distances and close to 5° when the measurement refers to angle evaluations.

6. Conclusions

In this paper, an experimental setup for high-resolution 3D reconstruction of drilling tools has been presented and tested. Well-known laser triangulation principles have been exploited in cooperation with an innovative acquisition procedure based on the application of a transversal handling of the system. In this way, occlusion problems due to the presence of undercut surfaces, which practically affect the great majority of ordinary tools, have been efficiently overcome. A second longitudinal handling of the optical probe, made of the laser source and the camera-lens set, has been added in order to prevent the decrease of the measurement resolution when illuminated surfaces are out of the minimum DOF of the system elements. As a consequence, numerical registrations of samples acquired in different rounds, which suffers from unavoidable computational errors, are no longer needed, therefore ensuring high accuracy in the whole measurement volume. Finally, the processing scheme ends with the application of filter techniques able to delete those samples that are not conform to initial quality specifications.

The setup has been validated through the analysis of a calibration sphere with an absolute error in the radius estimation of 6 μm. Two further experiments have been performed, thus demonstrating the capability of the presented system in reconstructing both macro- and microtools without occlusions, allowing the fast detection of surface defects with absolute errors of few microns.

References

[1] G. Zhang, R. Veale, T. Charlton, B. Borchardt, and R. Hocken, "Error compensation of coordinate measuring machines," *CIRP Annals*, vol. 34, no. 1, pp. 445–448, 1985.

[2] M. A. Donmez, D. S. Blomquist, R. J. Hocken, C. R. Liu, and M. M. Barash, "A general methodology for machine tool accuracy enhancement by error compensation," *Precision Engineering*, vol. 8, no. 4, pp. 187–196, 1986.

[3] J. W. M. C. Teeuwsen, J. A. Soons, P. H. J. Schellekens, and A. C. H. van der Wolf, "A general method for error description of CMMs using polynomial fitting Procedures," *CIRP Annals*, vol. 38, no. 1, pp. 505–510, 1989.

[4] W. L. Cheng and C. H. Menq, "Integrated laser/CMM system for the dimensional inspection of objects made of soft material," *The International Journal of Advanced Manufacturing Technology*, vol. 10, no. 1, pp. 36–45, 1995.

[5] H. Schwenke, F. Wäldele, C. Weiskirch, and H. Kunzmann, "Opto-tactile sensor for 2D and 3D measurement of small structures on coordinate measuring machines," *CIRP Annals*, vol. 50, no. 1, pp. 361–364, 2001.

[6] D. Lopez-Escogido and A. De Luca, "2-D high precision laser for detecting small defects in PCBs," in *Proceedings of the 9th International Conference on Electrical Engineering, Computing Science and Automatic Control (CCE '12)*, pp. 1–6, Mexico City, Mexico, September 2012.

[7] X. Ke and Y. Chaolin, "On-line defect detection algorithms for surface inspection of hot rolled strips," in *Proceedings of the International Conference on Mechanic Automation and Control*

Engineering (MACE '10), pp. 2350–2353, Wuhan, China, June 2010.

[8] Z. Qun, H. Wenbo, J. Chenghao, J. Yutong, and Y. Jinhua, "Studies on portable 3D laser scanner for surface flaws," in *Proceedings of the 2nd International Conference on Instrumentation & Measurement, Computer, Communication and Control (IMCCC '12)*, pp. 1297–1299, Harbin, China, December 2012.

[9] L. Zhang, M. Zhao, Y. Zou, and S. Gao, "A new surface inspection method of TWBS based on active laser-triangulation," in *Proceedings of the 7th World Congress on Intelligent Control and Automation (WCICA '08)*, pp. 1174–1179, Chongqing, China, June 2008.

[10] A. Zhou, J. Guo, and W. Shao, "Automated detection of surface defects on sphere parts using laser and CDD measurements," in *Proceedings of the 37th Annual Conference of the IEEE Industrial Electronics Society (IECON '11)*, pp. 2666–2671, Melbourne, Australia, November 2011.

[11] J. Kowal and A. Sioma, "Surface defects detection using a 3D vision system," in *Proceedings of the 13th International Carpathian Control Conference (ICCC '12)*, pp. 382–387, High Tatras, Poland, 2012.

[12] M. J. Milroy, D. J. Weir, C. Bradley, and G. W. Vickers, "Reverse engineering employing a 3D laser scanner: a case study," *The International Journal of Advanced Manufacturing Technology*, vol. 12, no. 2, pp. 111–121, 1996.

[13] S. Son, H. Park, and K. H. Lee, "Automated laser scanning system for reverse engineering and inspection," *International Journal of Machine Tools and Manufacture*, vol. 42, no. 8, pp. 889–897, 2002.

[14] S. C. Aung, R. C. K. Ngim, and S. T. Lee, "Evaluation of the laser scanner as a surface measuring tool and its accuracy compared with direct facial anthropometric measurements," *British Journal of Plastic Surgery*, vol. 48, no. 8, pp. 551–558, 1995.

[15] C. H. Kau, S. Richmond, A. I. Zhurov et al., "Reliability of measuring facial morphology with a 3-dimensional laser scanning system," *American Journal of Orthodontics and Dentofacial Orthopedics*, vol. 128, no. 4, pp. 424–430, 2005.

[16] F. Marino, P. De Ruvo, G. De Ruvo, M. Nitti, and E. Stella, "HiPER 3-D: an omnidirectional sensor for high precision environmental 3-D reconstruction," *IEEE Transactions on Industrial Electronics*, vol. 59, no. 1, pp. 579–591, 2012.

[17] M. Levoy, S. Rusinkiewicz, M. Ginzton et al., "The digital michelangelo project: 3D scanning of large statues," in *Proceedings of the 27th Annual Conference on Computer Graphics and Interactive Techniques (SIGGRAPH '00)*, pp. 131–144, ACM, July 2000.

[18] M. Kampel and R. Sablatnig, "Rule based system for archaeological pottery classification," *Pattern Recognition Letters*, vol. 28, no. 6, pp. 740–747, 2007.

[19] G. Sansoni, M. Trebeschi, and F. Docchio, "State-of-the-art and applications of 3D imaging sensors in industry, cultural heritage, medicine, and criminal investigation," *Sensors*, vol. 9, no. 1, pp. 568–601, 2009.

[20] H. Y. Feng, Y. Liu, and F. Xi, "Analysis of digitizing errors of a laser scanning system," *Precision Engineering*, vol. 25, no. 3, pp. 185–191, 2001.

[21] X. Sun, P. L. Rosin, R. R. Martin, and F. C. Langbein, "Noise analysis and synthesis for 3D laser depth scanners," *Graphical Models*, vol. 71, no. 2, pp. 34–48, 2009.

[22] F. Xi, Y. Liu, and H. Y. Feng, "Error compensation for three-dimensional line laser scanning data," *The International Journal of Advanced Manufacturing Technology*, vol. 18, no. 3, pp. 211–216, 2001.

[23] A. Isheil, J. P. Gonnet, D. Joannic, and J. F. Fontaine, "Systematic error correction of a 3D laser scanning measurement device," *Optics and Lasers in Engineering*, vol. 49, no. 1, pp. 16–24, 2011.

[24] N. Van Gestel, S. Cuypers, P. Bleys, and J. P. Kruth, "A performance evaluation test for laser line scanners on CMMs," *Optics and Lasers in Engineering*, vol. 47, no. 3-4, pp. 336–342, 2009.

[25] F. Xi and C. Shu, "CAD-based path planning for 3-D line laser scanning," *Computer-Aided Design*, vol. 31, no. 7, pp. 473–479, 1999.

[26] M. Mahmud, D. Joannic, M. Roy, A. Isheil, and J. F. Fontaine, "3D part inspection path planning of a laser scanner with control on the uncertainty," *Computer-Aided Design*, vol. 43, no. 4, pp. 345–355, 2011.

[27] H. Zhao, J. P. Kruth, N. Van Gestel, B. Boeckmans, and P. Bleys, "Automated dimensional inspection planning using the combination of laser scanner and tactile probe," *Measurement*, vol. 45, no. 5, pp. 1057–1066, 2012.

[28] http://www.coherent.com/downloads/TMFL_DS_0410.pdf.

[29] http://www.vargus.com/download/files/MilliPro-inch_1004.pdf.

[30] http://www.lensation.de/downloads/LS_CAT_2013.pdf.

[31] http://en.ids-imaging.com/IDS/spec_pdf.php?sku=AB00043.

[32] D. K. Naidu and R. B. Fisher, "A comparative analysis of algorithms for determining the peak position of a stripe to sub-pixel accuracy," in *Proceedings of the British Machine Vision Association Conference (BMVC '91)*, pp. 217–225, Springer, London, UK, 1991.

Research Article

Pipe Defect Detection and Reconstruction Based on 3D Points Acquired by the Circular Structured Light Vision

Wang Ying, Jin Cuiyun, and Zhang Yanhui

College of Information Science & Technology, Beijing University of Chemical Technology, Beijing 100029, China

Correspondence should be addressed to Wang Ying; wangying@mail.buct.edu.cn

The inspection of pipe inside is very important so as to ensure the safety of pipe transmission. The pipe defect detection method based on inside 3D points acquired by circle structured light vision system was discussed in this paper. Based on the characteristics of 3D points inside a pipe acquired by circle structured light, a method by which pipe inner surface convex defect and pit defect were identified by the normal vector angle between adjacent points change on the same circle was proposed. A distance constraint between each pair of corresponding adjacent two points was proposed in order to recognize holes in the pipe inside. Based on Delaunay triangulation principle, the triangulation method for pipe inner surface circle structured light vision 3D points with hole and without hole was discussed and 3D reconstruction of the pipe was then realized. On the VC++ 6.0 software platform, pipe inner surface defect simulation data, hole simulation data and real 3D data were used to test the correctness of pipe defect identification method.

1. Introduction

Pipe transmission is the most important mode for transmitting liquids and gases. Many aging pipes are suffering from corrosion caused by high causticity of the liquid or gas transmitted. Therefore the inspection of pipe inside is very important to ensure the safety of pipe transmission and avoid leakage.

The traditional pipe inspection technology includes ultrasonic technology [1] and magnetic flux leakage (MFL) technology [2], which make it necessary that the pipe be scanned along the concerned area because only a limited area of the pipe is measured each time by these methods and the detection efficiency of these techniques is very low. Video technology is used to inspect the pipe inside since quantity information can be obtained by cameras and information is visualized [3]. The video inspection system consists of a high-resolution video camera and a lighting system, with the camera connected via a multicore cable to a remote computer and the pipe corrosion status can be determined by acquired images. Duran et al. [4] tried to inspect the defect of the pipe inside with a laser-based transducer. But the accuracy was low and the method could not exactly

determine the pipe corrosive rate so the service period could not be estimated precisely. Machine vision technology is used to measure the 3D shape of the object and the accurate space dimension of the piece. It is expected that the pipe inside defect can be spotted by machine vision system accurately so that the pipe corrosive rate can be determined by the result of 3D measurement. And the pipe service period can be thus estimated accurately.

The visualization of the pipe inside defect can be conveniently utilized to determine the pipe corrosive status. So the reconstruction of the pipe inside and identification of the defect based on the 3D points are very important. The problem of surface reconstruction based on scattered points has been studied extensively and many surface reconstruction algorithms have been proposed [5, 6]. These algorithms can be generally classified into three types: computational geometry, algebraic and implicit methods. Computational geometry methods use mechanisms such as Delaunay triangulation and region growing. Algebraic methods reconstruct a surface by fitting a smooth function to the set of input points. Such methods cannot be used to reconstruct complex geometry or surfaces with boundaries. The most popular approach to surface reconstruction is based on the use of implicit

functions [7, 8]. But implicit function methods also cannot be used to directly reconstruct surfaces with boundaries. When the surface contains boundaries, all methods mentioned above tend to produce incorrect results.

The main defects in the pipe inside are protrude, depression, or holes eroded by the medium transmitted in the pipe. The accurate position and the boundary must be detected before reconstruction. So a new triangulate method built upon the regular 3D points is proposed and the problem of boundary detection is solved.

The rest of the paper is organized as follows: Section 2 describes the principle of the circle structured light vision system and discusses the defect detection methods of pipe inside; Section 3 provides a detailed description of the method of 3D reconstruction; the results of defect detection and reconstruction based on real and simulative 3D dataset are given in Section 4; the conclusion is summarized in Section 5.

2. Defect Detection Method Based on 3D Points Acquired by Circle Structured Light Vision

2.1. Principles of Circle Structured Light Vision System. It is feasible to obtain the 3D points by the structured light vision technology. Since the section of the pipe inside is usually circle, the circle structured light is used to inspect the pipe inside. The circle structured light vision system for pipe inside detection consists of the CCD camera A, the laser B, and the pipe inspected, which is shown in Figure 1. The light emitting from the laser B is modulated into the conic surface light by the cylindrical grating, and the conic surface light projecting onto the pipe inside intersects with the inner wall and forms a closed stripe. So it is obvious that a triangle is constituted by the CCD camera A, the laser B, and the arbitrary point C on the stripe, and the 3D information of the point C can be obtained by the optical triangle [9]. If there are protrusion and depression in the pipe inside, the shape of the stripe could be changed as shown in Figure 2, where the stripe is curved near to the circle center when the protrusion is detected in the inner side. The stripe is circular when no defect is detected in the pipe inside. The pipe can be moved along its axis within a fixed small interval and the 3D information of different sections along the axis can be obtained. The images of the stripe of the pipe inside gathered by the CCD camera are transmitted to the computer via the cable. So the 3D points on the same section of the axis obtained by the circle structured light vision form a circle, and all 3D points obtained by the circle structured light vision form different circles corresponding to different sections of the axis. The structured light vision measuring system for pipe inside is shown in Figure 3. The circle structured light emitting from the laser projected onto the pipe inner wall and formed a closed stripe, and this stripe was gathered by the CCD camera. The pipe was moved along its axis within a fixed small interval and the other stripe on the pipe inner wall at a different position was obtained and gathered. After the system was calibrated, the 3D information on different stripes
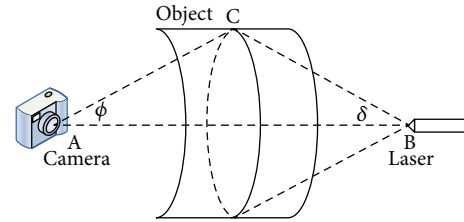

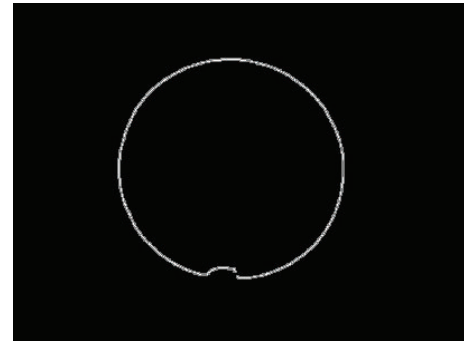FIGURE 1: The principle of circle structured light vision.

FIGURE 2: curved stripe of pipe inside with defection.

was obtained by the optical triangle. The pipe diameter size was measured due to the size of the laser and the CCD camera because the system should be put into the inside of the pipe.

2.2. The Detection Method of Protrusion and Depression Defects. Normally the 3D points of the pipe obtained by circle structured light vision system form many circles corresponding to different sections of the axis. When 3D points on the circle distribute equably, the tangent vector change of the neighbor points is continuous. This can be illustrated in Figure 4, where the points P_i, P_{i+1} are neighbor points on the same circle, their tangent vectors are t_i, t_{i+1}, respectively, and their corresponding normal vectors are n_i and n_{i+1}. The angle θ describes the normal vector change of the neighbor points, where θ equals the tangent vectors change of the points P_i, P_{i+1} because the tangent vectors are perpendicular to the normal vectors, respectively. It can be seen that the angle θ is very small when the pipe inside is smooth. But when there is a defect in the interior, the tangent vectors of the neighbor points change sharply at the start position of the defect, as shown in Figure 5, where P_i and P_{i+1}, P_j and P_{j+1} are the neighbor points on the same circle and points P_{i+1} and P_j are the start positions of the defection. The angle θ_i between the normal vectors of n_i and n_{i+1} and the angle θ_j between the normal vectors of n_j and n_{j+1} equal the angle of their tangent vectors, respectively. It can be seen that the tangent vectors of the neighbor points change sharply in the defect position, as the angle θ_i and the angle θ_j are larger than angle θ where no defection is detected. So it can be concluded that if the angle between the normal vectors of adjacent points is larger than the threshold θ_t, we can determine that the defect must exist in this area. Otherwise, no defection exists in the area.
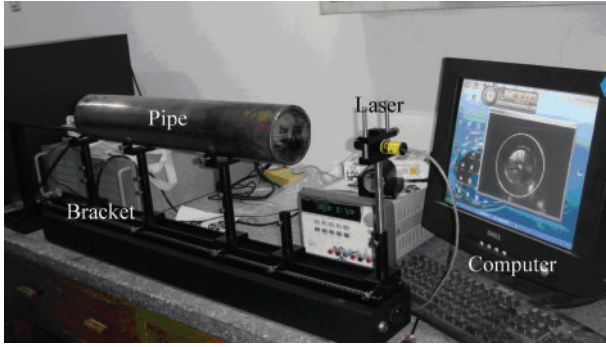
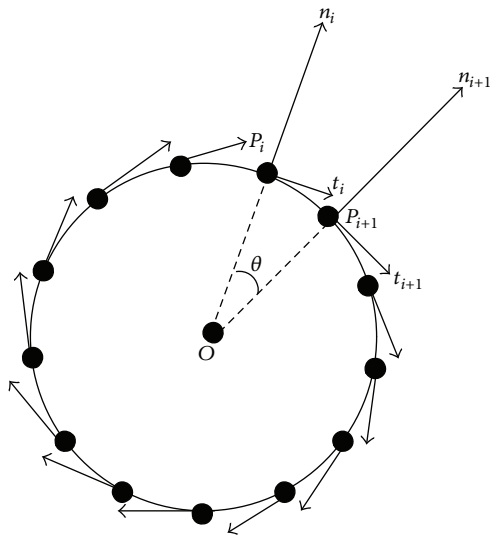FIGURE 3: Circular structured light inspection system.

FIGURE 5: The normal vector and tangent vector of points on a defective circumference.

FIGURE 4: The normal vector and tangent vector of points on a full circle.

between the point lying on the defect area and the center of the circle, and let r denote the inside radius of the pipe. The distance d can be calculated by formula (3), where the 3D coordinate of the defective point is $(x_{i+1}, y_{i+1}, z_{i+1})$ and that of the center of the circle is (x_0, y_0, z_0) as follows:

$$d = \sqrt{(x_{i+1} - x_0)^2 + (y_{i+1} - y_0)^2 + (z_{i+1} - z_0)^2}. \quad (3)$$

If $d - r > d_t$, where d_t is the threshold distance, then the pipe inner side has a protrusion. Otherwise, if $d - r < d_t$, the pipe inner side is cupped.

The point P_0 on the circle is not an isolated point because there are many points around the point P_0. Therefore, the normal vector of the point P_0 is related to the normal vector of the triangle plane including point P_0. Let us assume that there are m points near the point P_0 as shown in Figure 6, and these points can determine m different triangle planes together with the point P_0. The unit normal vector n_i of the triangle plane determined by P_0 and its neighbor point P_i and P_{i+1} can be calculated by the following formula:

$$n_i = \frac{(P_i - P_0) \times (P_{i+1} - P_0)}{\|(P_i - P_0) \times (P_{i+1} - P_0)\|}. \quad (4)$$

Accordingly the area S_i of the triangle plane can be calculated by

$$S_i = \frac{\|(P_i - P_0) \times (P_{i+1} - P_0)\|}{2}. \quad (5)$$

Then the normal vector n_0 of the center point P_0 can be calculated by formula (6) where the weight value of the normal vector of each triangular plane is the area of each plane:

$$n_0 = \frac{\sum_{i=1}^{m} s_i n_i}{\sum_{i=1}^{m} s_i}. \quad (6)$$

The threshold angle θ_t is determined by formula (1), where n is the number of the points on the same circle as follows:

$$\theta_t = \frac{360°}{n}. \quad (1)$$

In general, the angle between the normal vectors of the adjacent points on the same circle can be calculated by formula (2) based on the space geometry theory. $|n_i|$ and $|n_{i+1}|$ describe the modules of the normal vector n_i and n_{i+1}, respectively:

$$\theta = \arccos\left(\frac{n_i \cdot n_{i+1}}{|n_i| |n_{i+1}|}\right). \quad (2)$$

So the defection can be recognized by comparing the normal vector angle θ of the neighbor points at the start position of the defect to the threshold θ_t. If the angle θ is larger than θ_t, the defect must exist. Let d denote the distance
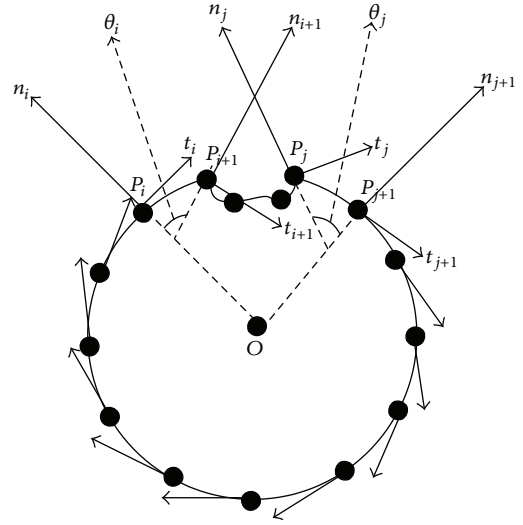
FIGURE 6: The vertex normal vector and triangle normal vector.

(a)   (b)

FIGURE 8: Retaining holes during triangulation.

FIGURE 7: Holes identification schematic of circle structured light.

The value d'_p is related to the point density of the circle. If the distance between the point P_i and the point next is denoted by d_i, the average distance d_{pj} of all neighbor points on the same circle can be calculated by formula (7), where n denotes the number of the points in the circle, and the average distance of all neighbor points in all circles can be calculated by formula (8), where N denotes the number of circles along the p axis, and k is the coefficient which equals 1 normally:

$$d_{pj} = \frac{\sum_{i=1}^{n} d_i}{n}, \tag{7}$$

$$d'_p = \frac{\sum_{j=1}^{N} d_{pj}}{N}, \quad d' = k \cdot d'_p. \tag{8}$$

3. The Three-Dimensional Reconstruction of the Pipe with a Hole

The aim of reconstruction is to restore the real shape of the object based on space points obtained by 3D measurement technology, which makes the object display visually. The triangulation of the space points is the key step of reconstruction on which the topology relationship of the neighbor points can be expressed by triangle meshes and the initial shape of the object can be restored precisely by these triangle meshes. The 3D points obtained by the circle structured light vision form different circles which distribute regularly, compared to the scattered points, and the triangulation of the regular points is simpler than that of the scattered points. So a new triangulation method based on the 3D points distributed on the different circles is proposed. This triangulation principle is explained in Figure 8, where L_1 and L_2 denote expanded lines of the neighbor circles, and $P_{11}, P_{12}, \ldots, P_{1m}$ and $P_{21}, P_{22}, \ldots, P_{2n}$ denote the points on the circles L_1 and L_2, respectively, in which m and n are the numbers of the points on the circle L_1 and L_2. The points P_{11} and P_{12} on the L_1 and the point P_{21} on the L_2 compose the triangle patch $S_1(P_{11}P_{12}P_{21})$. Symmetrically, the points P_{21} and P_{22} on the L_2 and the point P_{12} on the L_1

2.3. The Detection Method of Holes on the Pipe. A hole is one of the main defects caused by erosion after the pipe has worked for a long time. The characteristics of 3D points measured by structured light vision technology with a hole on the pipe are different from those measured when no hole exists. Generally the 3D points of the pipe inner side measured by the structured light vision technology form different circles corresponding to different sections of the axis. To explain characteristics of the distribution of 3D points, each circle is rolled out as a line, as shown in Figure 7, where $L_1 \sim L_9$ denote different pipe inner side circles measured by structured light vision system along the axis, respectively. When no hole exists, the distance between the neighbor points located on the same circle is short, while the distance between the neighbor points is long if there is a hole in this area. So the hole can be detected by comparing the distance between the neighbor points to the value d'_p. It can be seen that the distances of neighbor points on the circles L_3 to L_7 are denoted by B_1B_2, C_1C_2, D_1D_2, E_1E_2, F_1F_2, and all these distances are larger than d'_p. Thus, there must be a hole in this area. The distance of neighbor points on the circle L_1 and L_2 is shorter than d'_p, so there is no hole in this area.
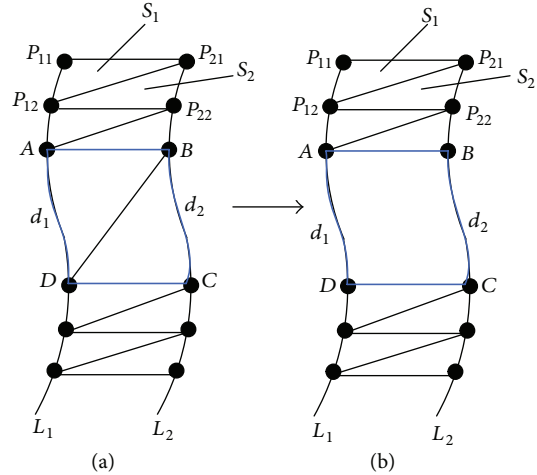
compose the triangle patch $S_2(P_{12}P_{21}P_{22})$. This process is repeated continuously until all points on the L_1 and L_2 are traversed. It can be seen that this triangulation method is simpler than the triangulation method of scattered points mentioned previously. It is noticed that when a hole exists, the triangulation should not be done on this area so as to restore the real status of the object.

If a hole exists, which is shown in Figure 8(a), the area ABCD is a hole triangulated into the triangles mesh ABD and DBC, according to the principle mentioned above. To reserve the real shape of the object, the triangulation must not be done on the hole. So the boundaries of the hole must be identified in advance. Overall, steps of the triangulation with a hole are described as follow.

(1) L_i denotes the expanded line of the space points circle, where subscript i denotes the circle serial number, and P_1, P_2, P_x denote the three vertices of the small triangle patch in which P_1 is the first point on the line L_i and P_2 is the first point on the line L_{i+1} next to the L_i.

(2) Calculate the distance d_1 between the point P_1 and the next point on the line L_i and the distance d_2 between the point P_2 and the next point on the line L_{i+1}. If all the distances d_1 and d_2 are smaller than the threshold value d'_p, then the triangulation is done (the detailed step was described in (3) and (4)). Otherwise the triangulation is not done. After that, the point next to P_1 is set to be P_1, the point next to P_2 is set to be P_2, and then the step mentioned above is repeated.

(3) The point next to the point P_1 on the line L_i is set to be P_x, and the points P_1, P_2, P_x form a triangle. After the triangulation is done, the point P_x is set to be point P_1.

(4) The point next to the point P_2 on the line L_{i+1} is set to be P_x, and then the new point P_1 on the line L_i, the new point P_x, and the point P_2 on the line L_{i+1} form a new triangle patch.

The steps (2), (3), and (4) are repeated until all points on the line L_i and line L_{i+1} are triangulated.

4. Results of the Defect Detection and Reconstruction

4.1. The Results of Defect Detection and Reconstruction with a Hole. The simulation was done to demonstrate the effectiveness of our approach. The work was fulfilled by VC++ software platform and OPGL tool package. Figure 9 shows the reconstruction stages with the hole defect on the pipe. The simulated pipe was composed by 15 circles and 1380 points on these 15 circles. The radius of the pipe was 5.0 centimeters, the average distance between the neighbor points on all the circles was 0.32 centimeters, and the d'_p was set to be 0.66 centimeters. It is obvious that the hole was identified by the approach explained in Section 2.2. Figure 9(a) shows the identified hole and Figure 9(b) is a local zoom-in out of the triangle mesh near the hole. It can be seen that the hole was
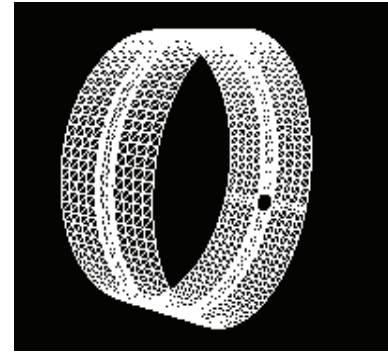
(a)
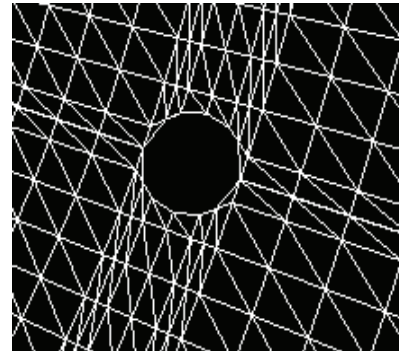
(b)

(c)

FIGURE 9: Three-dimensional reconstruction of circular hole on the pipe surface.

not triangulated and was reserved. Figure 8(c) is the result of reconstruction of the pipe in which illumination condition was considered.

Figure 10 shows the stages of reconstruction with an irregular hole on the pipe. The pipe is composed by 8 circles and 720 points on these 8 circles. The radius of the pipe was 5.0 centimeters, the average distance between the neighbor points on the all circles was 0.35 centimeters, and the d'_p was set to be 0.58 centimeters. Figure 10(a) shows the identified hole and Figure 10(b) is a local zoom-in out of the tri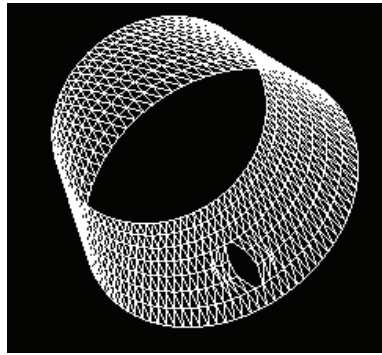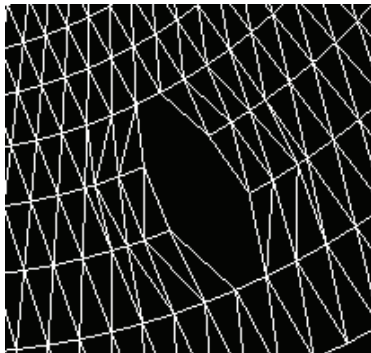angle mesh near the hole. It can be seen that the hole was not triangulated. Figure 10(c) is the result of reconstruction of the pipe in which illumination condition was considered. It can
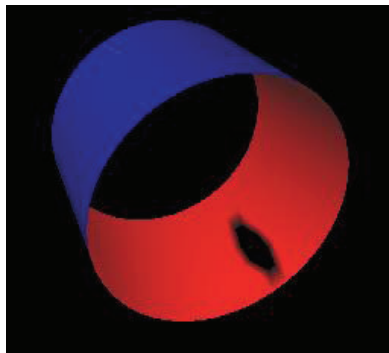
(a)

(b)

(c)

Figure 10: Three-dimensional reconstruction of irregular polygon hole on the pipe surface.

(a)

(b)

(c)

Figure 11: Three-dimensional reconstruction of protrude defection of the pipe inside.

be concluded that the hole detection method proposed in this paper is effective both for regular holes and irregular holes.

4.2. The Results of the Defect Detection and Reconstruction with a Protrusion. Both real and simulative data sets were used to demonstrate the effectiveness of our defection detection method. Figure 11 shows the stages of reconstruction with the protrude defection in the pipe inside. The pipe is composed by 14 circles and 952 points on these 14 circles. The radius of the pipe is 5.0 centimeters, the angle θ_t is set to 5.5°, and the distance d_t is set to 0.05 centimeters. Figure 11(a) is the space points of the pipe inside and Figure 11(b) is the triangulate mesh of the pipe, where the area marked with red color is the identified protrude defection. Figure 11(c) is

the result of reconstruction of the pipe with defect in which illumination condition was considered.

Figure 12 shows the stages of reconstruction of a real cupped defect in the pipe inside. The pipe is composed by 11 circles and 2123 points on the 11 circles obtained by the circle structured light vision. The radius of the pipe is 4.45 centimeters, the threshold value θ_t of the adjacent points is set to 2.0°, and the distance d_t is set to 0.25 centimeters. When the normal vector angle of the neighbor point is larger than 2.0° and the distance between the defect point and the center of the circle is smaller than 4.20 centimeters, the area which includes this point can be determined as a protrude defect. Figures 12(a) and 12(b) describe the space points and the

(a)

(b)

(c)

FIGURE 12: Three-dimensional reconstruction of cupped defection of the pipe inside.

result of triangulate mesh of the pipe, where the area marked with red color is the identified protrude defect. Figure 12(c) is the result of reconstruction of the pipe in which illumination condition was considered. It can be concluded that the defect detection method proposed in this paper is effective.
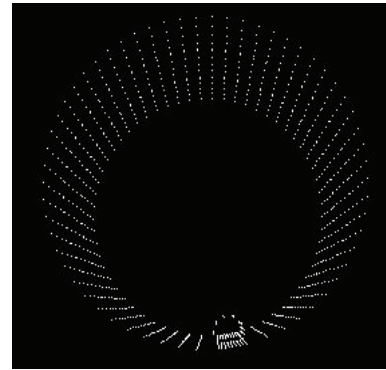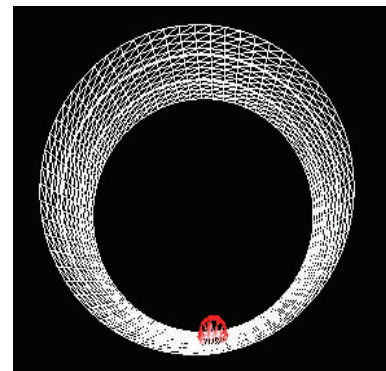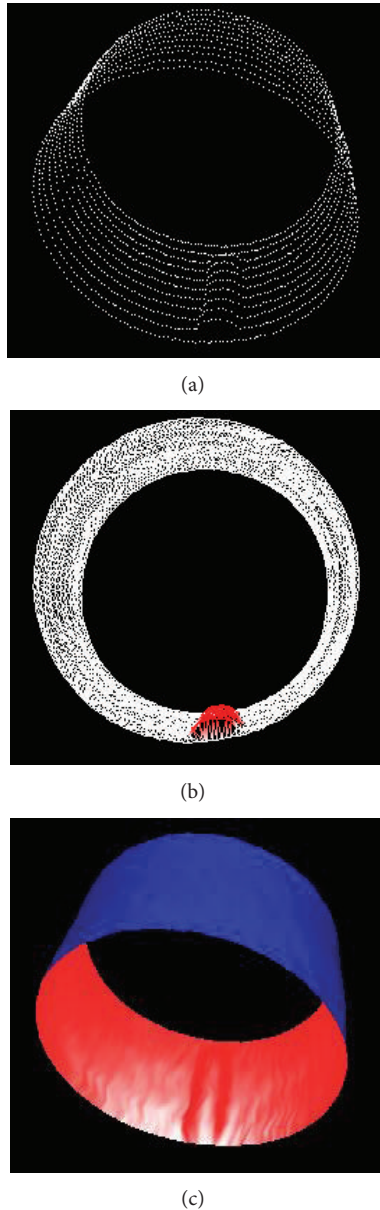
5. Conclusion

In this paper, the pipe defect detection methods based on space points for both the holes and inside concavoconvex were proposed. The holes in the pipe can be identified by comparing the distance of neighbor points to the threshold value which can be determined by density of the points. The defects of protrusion and being cupped are detected by

identifying where the normal vector angle of the neighbor point changes sharply. The new triangulation method based on the regular 3D points was proposed in this paper. The results showed that the reconstruction method for the regular points was simpler than that of the scattered points and the hole could be reserved. The defect detection and reconstruction result for the 3D points distributing regular is satisfied by the methods mentioned above, but the result for the 3D scattered points is not suitable for these methods. The defect detection and reconstruction methods were validated by a test built upon the VC++ and OPGL tool package.

Acknowledgment

References

[1] F. Gomez, K. Althoefer, and L. D. Seneviratne, "Modeling of ultrasound sensor for pipe inspection," in *Proceedings of the IEEE International Conference on Robotics and Automation*, pp. 2555–2560, September 2003.

[2] Y. Tang, M. C. Pan, F. L. Luo et al., "Detection of corrosion in pipeline using pulsed magnetic flux leakage testing," *Computer Measurement and Control*, vol. 18, no. 1, pp. 38–43, 2010.

[3] L. Song, X. Zhou, K. Xu, X. Qu, and S. Ye, "Three-dimensional defect detection based on single measurement image," *Acta Optica Sinica*, vol. 25, no. 9, pp. 1195–1200, 2005.

[4] O. Duran, K. Althoefer, and L. D. Seneviratne, "Automated pipe defect detection and categorization using caniera/laser-based profiler and artificial neural network," *IEEE Transactions on Automation Science and Engineering*, vol. 4, no. 1, pp. 118–126, 2007.

[5] S. Cunliang, *The Study of Triangulation About Space Scattered Points*, Nanjing University of Aeronautics and Astronautics, Nanjing, China, 2009.

[6] Z. Yang, Y.-H. Seo, and T.-W. Kim, "Adaptive triangular-mesh reconstruction by mean-curvature-based refinement from point clouds using a moving parabolic approximation," *CAD Computer Aided Design*, vol. 42, no. 1, pp. 2–17, 2010.

[7] J. Wang and M. M. Oliveira, "Filling holes on locally smooth surfaces reconstructed from point clouds," *Image and Vision Computing*, vol. 25, no. 1, pp. 103–113, 2007.

[8] A. Sharf, M. Alexa, and D. Cohen-Or, "Context-based surface completion," in *Proceedings of the ACM SIGGRAPH*, pp. 878–887, August 2004.

[9] R. Zhang, *Study of in-Pipe Surface Circle Structured Light Vision 3D Inspection Technology*, Beijing University of Chemical Technology, Beijing, China, 2012.

Research Article

Manifold Adaptive Kernel Semisupervised Discriminant Analysis for Gait Recognition

Ziqiang Wang, Xia Sun, Lijun Sun, and Yuchun Huang

School of Information Science and Engineering, Henan University of Technology, Zhengzhou 450001, China

Correspondence should be addressed to Ziqiang Wang; wzqagent@126.com

A manifold adaptive kernel semisupervised discriminant analysis algorithm for gait recognition is proposed in this paper. Motivated by the fact that the nonlinear structure captured by the data-independent kernels (such as Gaussian kernel, polynomial kernel, and Sigmoid kernel) may not be consistent with the discriminative information and the intrinsic manifold structure information of gait image, we construct two graph Laplacians by using the two nearest neighbor graphs (i.e., an intrinsic graph and a penalty graph) to model the discriminative manifold structure. We then incorporate these two graph Laplacians into the kernel deformation procedure, which leads to the discriminative manifold adaptive kernel space. Finally, the discrepancy-based semi-supervised discriminant analysis is performed in the manifold adaptive kernel space. Experimental results on the well-known USF HumanID gait database demonstrate the efficacy of our proposed algorithm.

1. Introduction

In the past two decades, gait recognition has become a hot research topic in pattern recognition and computer vision, owing to its wide applications in many areas such as information surveillance, identity authentication, and human-computer interface. While many algorithms have been proposed for gait recognition [1–5], the most successful and popular approaches to date are the average silhouettes-based methods with subspace learning. The common goal of theses approaches is to find a compact and representative low-dimensional feature subspace for gait representation, so that the intrinsic characteristics of the original gait image are well preserved. Representative algorithms include principal component analysis (PCA) [6], linear discriminant analysis (LDA) [6], locality preserving projection (LPP) [7], and marginal Fisher analysis (MFA) [8].

PCA aims to generate a set of orthonormal basis vectors where the samples have the minimum reconstruction error. Since PCA is an unsupervised method, it is optimal in terms of reconstruction, but not for discriminating one class from others. LDA is a supervised subspace learning approach which seeks the projection directions that maximize interclass scatter and at the same time minimize intraclass scatter. When the label information is available, LDA usually outperforms PCA for pattern classification tasks. However, LDA has a critical drawback: its available feature dimension is limited by the number of classes in the data. To overcome this problem, Tao et al. proposed the general averaged divergence analysis (GADA) [9] framework and the maximization of the geometric mean of all divergences (MGMD) [10] method, respectively. In addition, in order to efficiently and robustly estimate the low-rank and sparse structure of high-dimensional data, Zhou and Tao [11] developed "Go Decomposition" (GoDec) method and proved its asymptotic and convergence speed. While these algorithms have attained reasonable good performance in gait recognition, face recognition, and object classification, they are designed for discovering only the global Euclidean structure, whereas the local manifold structure is ignored.

Recently, various researches have shown that images possibly reside on a nonlinear submanifold [12–14]. Therefore, gait image representation is fundamentally related to

the manifold learning, which aims to derive a compact low-dimensional embedding that preserves local geometric properties of underlying high-dimensional data. The most representative manifold learning algorithm is locality preserving projection (LPP) [7], which aims to find the optimal linear approximation to eigenfunctions of the Laplace-Beltrami operator on the data manifold. Since LPP is originally unsupervised and does not take the class label information into account, it does not necessarily work well in supervised dimensionality reduction scenarios. By jointly considering the local manifold structure and the class label information, as well as characterizing the separability of different classes with the margin criterion, marginal Fisher analysis (MFA) [8] delivers reasonably good performance in many pattern classification applications. While the motivations of these methods are different, they can be interpreted into a general graph embedding framework (GEF) [8] or the patch alignment framework (PAF) [15]. In addition, the discriminative information preservation (DIP) [16] algorithm was also proposed by using PAF. Although the above vector-based dimensionality reduction algorithms have achieved great success in image analysis and computer vision, they seriously destroyed the intrinsic tensor structure of high-order data. To overcome this issue, Tao et al. [17, 18] generalized the vector-based learning to the tensor-based learning and proposed the supervised tensor learning (STL) framework. More recently, it has been shown that the slow feature analysis (SFA) [19] can extract useful motion patterns and improve the recognition performance.

In general, the supervised dimensionality reduction approaches are suitable for pattern classification tasks when there are sufficient labeled data available. Unfortunately, in many practical applications of pattern classification, one often faces a lack of sufficient labeled data, since the labeling process usually requires much human labor. Meanwhile, in many cases, large numbers of unlabeled data can be easier to obtain. To effectively utilize the labeled and unlabeled data simultaneously, semisupervised learning [20] was proposed and introduced into the dimensionality reduction process. The motivation behind semisupervised learning is to employ a large number of unlabeled data to help build more accurate models from the labeled data. In the last decades, many semisupervised learning methods have been proposed, such as transductive SVM (TSVM) [21], cotraining [22], and graph-based semisupervised learning algorithms [23]. In addition, motivated by the recent progress in Hessian eigenmaps, Tao et al. [24] introduced the Hessian regularization into SVM for semisupervised learning and mobile image annotation on the cloud. All these algorithms only considered the classification problem, either transductive or inductive. Semisupervised dimensionality reduction has been considered recently, the most representative algorithm is semisupervised discriminant analysis (SDA) [25], which aims to extract discriminative features and preserve geometrical information of both labeled and unlabeled data for dimensionality reduction. While SDA has achieved reasonably good performance in face image and image retrieval, there are still some problems that are still not properly addressed till now.

(1) The original SDA is still a linear technique in nature. It can only extract the linear features of input patterns, and it fails for nonlinear features. So SDA is inadequate to describe the complexity of real gait images because of viewpoints, surface, and carrying status variations.

(2) The original SDA suffers from the singular (small sample size) problem, which exists in high-dimensional pattern recognition tasks such as gait recognition, where the dimension of the samples is much larger than the number of available samples.

To address the above issues, we propose a novel manifold adaptive kernel semisupervised discriminant analysis (MAKSDA) algorithm for gait recognition in this paper. First, we reformulate the optimal objective function of SDA using the discrepancy criterion rather than the ratio criterion, so that the singular problem can be avoided. Second, the discrepancy-based SDA is extended to the nonlinear case through kernel trick [26]. Meanwhile, the discriminative manifold adaptive kernel function is proposed to enhance the learning capability of the MAKSDA. Finally, experimental results on gait recognition are presented to demonstrate the effectiveness of the proposed algorithm.

In summary, the contributions of this paper are as follows.

(1) We propose MAKSDA algorithm. MAKSDA integrates the discriminative information obtained from the labeled gait images and the manifold adaptive kernel function explored by the unlabeled gait images to form the low-dimensional feature space for gait recognition.

(2) In order to avoid the singular problem, we explore the discrepancy criterion rather than the ratio criterion in the kernel space.

(3) We have analyzed different parameter settings of MAKSDA algorithm, including the kernel function type, the nearest neighbor size in the intrinsic graph, and the nearest neighbor size in the penalty graph.

The remainder of this paper is organized as follows. Section 2 describes how to extract the Gabor-based gait representation. Section 3 briefly reviews SDA. In Section 4, we propose the MAKSDA algorithm for gait recognition. The experimental results are reported in Section 5. Finally, we provide the concluding remarks and suggestions for future work in Section 6.

2. Gabor Feature Representation of Gait Image

The effective representation of gait image is a key issue of gait recognition. In the following, we employ the averaged gait image as the appearance model [1, 2], since it can employ a compact representation to characterize the motion patterns of the human body. In addition, the Gabor wavelets [27], whose kernels are similar to the 2D receptive field profiles of the mammalian cortical simple cells, exhibit desirable characteristics of spatial locality and orientation selectivity. Therefore, it is reasonable to use Gabor functions to model

averaged gait images. Partialarly, the averaged gait image is first decomposed by using Gabor filters; we then combine the decomposed images to give a new Gabor feature representation, which has been demonstrated to be an effective feature for gait recognition.

The Gabor filters are the product of an elliptical Gaussian envelope and a complex plane wave, which can be defined as follows:

$$\psi_{\mu,\nu}(z) = \frac{\left\|k_{\mu,\nu}\right\|^2}{\sigma^2} \exp\left(-\frac{\left\|k_{\mu,\nu}\right\|^2 \|z\|^2}{\sigma^2}\right)$$
$$\times \left[\exp\left(ik_{\mu,\nu}z\right) - \exp\left(-\frac{\sigma^2}{2}\right)\right], \tag{1}$$

where μ and ν define the orientation and scale of Gabor filters, respectively, $z = (\mu,\nu)$, $\|\cdot\|$ denotes the norm operator, and the definition of wave vector $k_{\mu,\nu}$ is as follows:

$$k_{\mu,\nu} = k_\nu e^{i\phi_\mu}, \tag{2}$$

where $k_\nu = k_{\max}/f^\nu$ and $\phi_\mu = \pi\mu/8$. $k_{\max}$ represents the maximum frequency and its value is usually set as $\pi/2$. f denotes the spacing factor between kernels in the frequency domain and its value is usually set as $\sqrt{2}$.

The Gabor filters defined in (1) are all self-similar since they can be generated from one filter (the mother wavelet) by scaling and rotating via the wave vector $k_{\mu,\nu}$. The term $\exp(-\sigma^2/2)$ is subtracted in order to make the kernel DC-free. Thus, a band of Gabor filters is generated by a set of various scales and rotations.

In this paper, following the conventional settings, we use Gabor filters at five scales $\nu \in \{0, 1, 2, 3, 4\}$ and eight orientations $\mu \in \{0, 1, 2, 3, 4, 5, 6, 7\}$ with the parameter $\sigma = 2\pi$. Then, we have 40 Gabor kernel functions from five scales and eight orientations. Figures 1 and 2 show the real part of the Gabor filters used in this paper and their magnitude, respectively. As can be seen, the Gabor filters demonstrate desirable features of spatial localization, orientation selectivity, and frequency selectivity.

The Gabor feature representation of a gait image is obtained by convolving the Gabor filters with the averaged gait image. Let $\text{AT}(x, y)$ be the averaged gait image; the convolution of the gait image AT and Gabor filters $\psi_{\mu,\nu}(z)$ can be defined as follows:

$$O_{\mu,\nu}(z) = \text{AT}(x, y) * \psi_{\mu,\nu}(z), \tag{3}$$

where $z = (x, y)$, $*$ represents the convolution operator, and $O_{\mu,\nu}(z)$ is the convolution result corresponding to the Gabor filters $\psi_{\mu,\nu}(z)$. As a result, the set

$$S = \left\{O_{\mu,\nu}(z) : \mu \in \{0, 1, 2, 3, 4, 5, 6, 7\}, \nu \in \{0, 1, 2, 3, 4\}\right\} \tag{4}$$

forms the Gabor feature representation of the gait image $\text{AT}(z)$. As can be seen, for each averaged gait image, we can obtain 40 Gabor-filtered images after convolving

the averaged gait image with the Gabor filters. In addition, as suggested in [28, 29], in order to encompass different spatial frequencies (scales), spatial localities, and orientation selectivity, we concatenate all these representation results and derive the final Gabor feature vector. Before the concatenation, $O_{\mu,\nu}(z)$ is downsampled by a factor ρ to reduce the space dimension and normalize it to zero and unit variance. We then construct a vector out of the $O_{\mu,\nu}(z)$ by concatenating its rows (or columns). Now, let $O^\rho_{\mu,\nu}(z)$ represent the normalized vector constructed from $O_{\mu,\nu}(z)$; the final Gabor feature vector O^ρ can be defined as follows:

$$O^\rho = \left\{O^\rho_{\mu,\nu}(z) : \mu \in \{0, 1, 2, 3, 4, 5, 6, 7\}, \nu \in \{0, 1, 2, 3, 4\}\right\}. \tag{5}$$

Consequently, the vector O^ρ serves as the Gabor feature representation of the averaged gait image for gait recognition.

3. Brief Review of SDA

Given a set of l labeled samples $\{x_1, \ldots, x_l\}$, each of them has a class label $c_i \in \{1, \ldots, C\}$ and m unlabeled samples $\{x_{l+1}, \ldots, x_{l+m}\}$ with unknown class labels. Let $l + m = n$ and $x_i \in \mathbb{R}^D$; the optimal objective function of SDA is defined as follows:

$$U_{\text{opt}} = \max_U \frac{U^T S_b U}{U^T S_t U + \beta J(U)}, \tag{6}$$

where S_b and S_t denote the between-class scatter matrix and total scatter matrix, respectively. According to the graph perspective of LDA in [7, 8], S_b and S_t can be defined as follows:

$$S_b = XWX^T,$$
$$S_t = XX^T, \tag{7}$$

where $X = [x_1, \ldots, x_l]$ and the weight matrix W is defined as follows:

$$W_{ij} = \begin{cases} \dfrac{1}{|c_i|}, & c_i = c_j, \\ 0, & \text{otherwise}, \end{cases} \tag{8}$$

where $|c_i|$ denotes the total number of data samples belonging to the class label c_i.

In addition, the regularizer item $J(U)$ is used to model the manifold structure. By using locally invariant idea of manifold learning, $J(U)$ is defined as follows:

$$J(U) = \frac{1}{2}\sum_{i,j}\left(U^T x_i - U^T x_j\right)^2 W_{ij} = U^T XLX^T U, \tag{9}$$

where $L = D - S$ is the graph Laplacian, D is a diagonal matrix given by $D_{ii} = \sum_j S_{ij}$, and S denotes the following weight matrix:

$$S_{ij} = \begin{cases} 1, & \text{if } x_i \text{ is among the } k\text{-nearest neighbor of } x_j \\ & \text{or } x_j \text{ is among the } k\text{-nearest neighbors of } x_i, \\ 0, & \text{otherwise}. \end{cases} \tag{10}$$
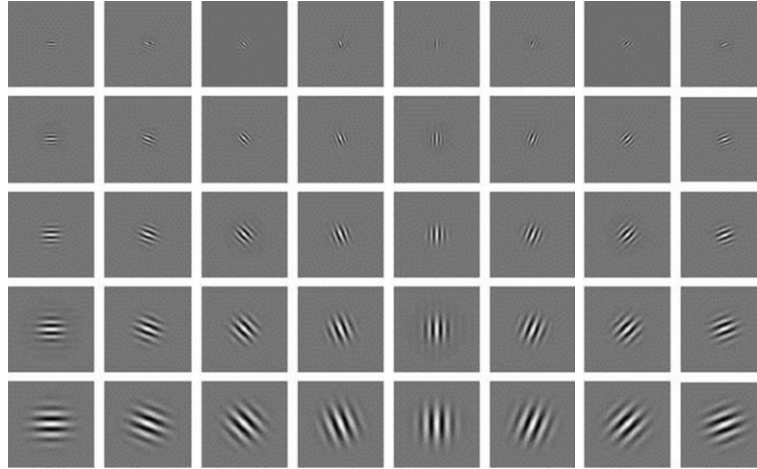
FIGURE 1: The real part of the Gabor filters at five scales and eight orientations.
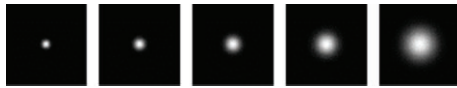

FIGURE 2: The magnitude of the Gabor filters at five scales and eight orientations.

By substituting (7) and (9) into (6), we have

$$U_{\text{opt}} = \arg\max_{U} \frac{U^T X W X^T U}{U^T X X^T U + \beta U^T X L X^T U}. \tag{11}$$

Then, the projection vector U is given by the maximum eigenvalue solution to the generalized eigenvalue problem:

$$X W X^T U = \lambda \left(X X^T + \beta X L X^T \right) U. \tag{12}$$

Although SDA has exploited both discriminant and geometrical information for dimensional reduction and achieved reasonably good performance in many fields, there are still some problems that are not properly addressed until now.

(1) SDA suffers from the singular problem in gait recognition, since the number of gait images is much smaller than the dimension of each gait image.

(2) SDA is a linear technique in nature, so it is inadequate to describe the complexity of real gait images. Although the nonlinear extension of SDA through kernel trick has been proposed in [25], it still has two shortcomings: (1) it suffers from the singular problem and (2) it adopts the data-independent kernels which may not be consistent with the intrinsic manifold structure revealed by labeled and unlabeled data samples.

To fully address the above issues, we propose a novel manifold adaptive kernel semisupervised discriminant analysis (MAKSDA) algorithm for gait recognition in the following section.

4. Manifold Adaptive Kernel SDA (MAKSDA) Algorithm

Although SDA can produce linear discriminating feature, the problem of numerical computation for gait recognition still exists; that is, the matrix $(X X^T + \beta X L X^T)$ in (12) may suffer from the singular problem. In this paper, the discrepancy criterion [30–32] is proposed as an alternative way to avoid the singular problems of SDA, since the ratio criterion can be well solved by the discrepancy criterion. Then, the discrepancy-based SDA can be defined as follows:

$$\begin{aligned}
Q(U) &= \arg\max_{U} \left(U^T S_b U - \left(U^T S_t U + \beta J(U) \right) \right) \\
&= \arg\max_{U} \left(U^T X W X^T U \right. \\
&\qquad \left. - \left(U^T X X^T U + \beta U^T X L X^T U \right) \right) \\
&= \arg\max_{U} \left(U^T \left(X W X^T - X X^T - \beta X L X^T \right) U \right).
\end{aligned} \tag{13}$$

Then, maximizing $Q(U)$ is equivalent to maximizing S_b and minimizing $(S_t + \beta J(U))$ simultaneously, which is consistent with the ratio criterion of the original SDA.

Since we can freely multiply U by some nonzero constant, we assume $\|U\| = 1$. Then, the maximization problem in (13) can be equivalently transformed into the following Lagrange function:

$$L(U, \lambda) = Q(U) - \lambda \left(\|U\| - 1 \right). \tag{14}$$

Let $\partial L(U, \lambda)/\partial U = 0$; we can obtain

$$\left(X W X^T - X X^T - \beta X L X^T \right) U = \lambda U. \tag{15}$$

Then, the SDA problem can be transformed into finding the leading eigenvectors of matrix $(X W X^T - X X^T - \beta X L X^T)$. Since no matrix inverse operation needs to be calculated, the discrepancy-based SDA successfully avoids the singular problem of the original SDA.

Let the column vectors $U_1, U_2, \ldots, U_d$ be the solution of (15) ordered in terms of their eigenvalues $\lambda_1, \lambda_2, \ldots, \lambda_d$. Thus, the SDA embedding is given by $y_i = U^T x_i$, where y_i denotes the lower-dimensional feature representation of x_i and $U = (U_1, U_2, \ldots, U_d)$ is the optimal projection matrix of SDA.

Although the above discrepancy-based SDA algorithm avoids the singular problem of the original SDA algorithm, it is still a linear algorithm. It may fail to discover the nonlinear geometry structure when gait images are highly nonlinear. Thus, in order to solve the nonlinear problem, the discrepancy-based SDA needs to be generalized to its nonlinear version via kernel trick. The main idea of kernel trick is to map the input data into a feature space with a nonlinear mapping function, where the inner products in the feature space can be easily computed through a kernel function without knowing the nonlinear mapping function explicitly. In the following, we discuss how to perform the discrepancy-based SDA in reproducing kernel hilbert Space (RKHS) and how to produce a manifold adaptive kernel function which is consistent with the intrinsic manifold structure, which gives rise to the manifold adaptive kernel SDA (MAKSDA).

To extend SDA to MAKSDA, let $\varphi : x \in \mathbb{R}^N \to \varphi(x) \in F$ be a nonlinear mapping function from the input space to a high-dimensional feature space F. The idea of MAKSDA is to perform the discrepancy-based SDA in the feature space F instead of the input space $\mathbb{R}^N$. For a proper chosen φ, an inner product $\langle, \rangle$ can be defined on F, which makes for a so-called RKHS. More specifically, $\langle \varphi(x), \varphi(y) \rangle = K(x, y)$ holds, where $K(\cdot, \cdot)$ is a positive semidefinite kernel function.

Let S_b^φ, S_t^φ, and $J^\varphi(U)$ denote the between-class scatter matrix, the total scatter matrix, and the regularizer item in the feature space, respectively. According to (7) and (9), we can obtain

$$S_b^\varphi = \varphi(X) W \varphi^T(X),$$

$$S_t^\varphi = \varphi(X) \varphi^T(X),$$

$$J^\varphi(U) = \frac{1}{2} \sum_{i,j} \left(U^T \varphi(x_i) - U^T \varphi(x_j) \right)^2 W_{ij} \quad (16)$$

$$= U^T \varphi(X) L \varphi^T(X) U,$$

where $\varphi(X) = [\varphi(x_1), \varphi(x_2), \ldots, \varphi(x_n)]$ and the definition of L is similar to the definition in Section 3.

Then, according to (13), the optimal objective function of MAKSDA in the feature space F can be defined as follows:

$$Q^\varphi(U) = \arg\max_U \left(U^T S_b^\varphi U - \left(U^T S_t^\varphi U + \beta J^\varphi(U) \right) \right)$$

$$= \arg\max_U \left(U^T \varphi(X) W \varphi^T(X) U \right.$$

$$- \left(U^T \varphi(X) \varphi^T(X) U \right.$$

$$\left. + \beta U^T \varphi(X) L \varphi^T(X) U \right) \right)$$

$$= \arg\max_U \left(U^T \left(\varphi(X) W \varphi^T(X) \right. \right.$$

$$- \varphi(X) \varphi^T(X)$$

$$\left. \left. - \beta \varphi(X) L \varphi^T(X) \right) U \right) \quad (17)$$

with the constraint

$$\|U\| = 1. \quad (18)$$

To solve the above optimal problem, we introduce the following Lagrangian multiplier method:

$$L^\varphi(U, \lambda) = Q^\varphi(U) - \lambda(\|U\| - 1) \quad (19)$$

with the multiplier λ.

Let $\partial L^\varphi(U, \lambda)/\partial U = 0$; we can obtain

$$\left(\varphi(X) W \varphi^T(X) - \varphi(X) \varphi^T(X) - \beta \varphi(X) L \varphi^T(X) \right) U = \lambda U. \quad (20)$$

Since any solution $U \in F$ must be the linear combinations of $\varphi(x_i)$, there exist coefficients α_i $(i = 1, 2, \ldots, n)$ such that

$$U = \sum_{i=1}^{n} \alpha_i \varphi(x_i) = \varphi(X) \alpha = \varphi \alpha, \quad (21)$$

where φ denotes the data matrix in F; that is, $\varphi = \varphi(X) = [\varphi(x_1), \varphi(x_2), \ldots, \varphi(x_n)]$, and $\alpha = [\alpha_1, \alpha_2, \ldots, \alpha_n]^T$.

Substituting (21) into (20) and following some algebraic transformation, we can obtain

$$\left(\varphi(X) W \varphi^T(X) - \varphi(X) \varphi^T(X) \right.$$

$$\left. - \beta \varphi(X) L \varphi^T(X) \right) \varphi(X) \alpha = \lambda \varphi(X) \alpha, \quad (22)$$

$$\left(\varphi^T(X) \varphi(X) W \varphi^T(X) \varphi(X) \right.$$

$$- \varphi^T(X) \varphi(X) \varphi^T(X) \varphi(X)$$

$$\left. - \beta \varphi^T(X) \varphi(X) L \varphi^T(X) \varphi(X) \right) \alpha$$

$$= \lambda \varphi^T(X) \varphi(X) \alpha, \quad (23)$$

$$(KWK - KK - \beta KLK) \alpha = \lambda K \alpha, \quad (24)$$

where K denotes the kernel matrix $K = \varphi^T(X) \varphi(X)$ and its element is $K_{ij} = K(x_i, x_j)$.

Thus, the MAKSDA problem can be transformed into finding the leading eigenvectors of $(KWK - KK - \beta KLK)$. Since no matrix inverse operation needs to be computed, MAKSDA successfully avoids the singular problem. Meanwhile, each eigenvector α gives a projective function U in the feature space. For a new testing data sample x, its low-dimensional embedding can be computed according to $\langle U, \varphi(x) \rangle = \alpha^T K(\cdot, x)$, where kernel matrix $K(\cdot, x) = [K(x_1, x), K(x_2, x), \ldots, K(x_n, x)]^T$.

From the above derivation procedure, we can observe that the kernel function K plays an important role in the MAKSDA algorithm. The traditional kernel-based methods commonly adopt data-independent kernels, such as Gaussian kernel, polynomial kernel, and Sigmoid kernel. However, the nonlinear structure captured by those data-independent kernels may not be consistent with the discriminative information and the intrinsic manifold structure [33]. To address this issue, in the following, we discuss how to design the discriminative manifold adaptive kernel function of MAKSDA, which fully takes account of the discriminative information and the intrinsic manifold structure, thus leading to much better performance.

Let V be a linear space with a positive semidefinite inner product(quadratic form) and let $E : H \rightarrow V$ be a bounded linear operator. In addition, we define $\widetilde{H}$ to be the space of function from H with the modified inner product:

$$\langle f, g \rangle_{\widetilde{H}} = \langle f, g \rangle_H + \langle Ef, Eg \rangle_V. \tag{25}$$

Sindhwani et al. have proved that $\widetilde{H}$ is still a RKHS [33].

Given the data examples $x_1, x_2, \ldots, x_n$, let $E : H \rightarrow \mathbb{R}^n$ be the evaluation map

$$E(f) = (f(x_1), \ldots, f(x_n)). \tag{26}$$

Denote $f = (f(x_1), \ldots, f(x_n)) \in V$ and $g = (g(x_1), \ldots, g(x_n)) \in V$; thus we can obtain

$$\begin{aligned} \langle Ef, Eg \rangle_V &= \langle f, g \rangle = f^T M g, \\ \|Ef\|_V^2 &= f^T M f, \end{aligned} \tag{27}$$

where M is a positive semidefinite matrix. Let K_x denote

$$K_x = (K(x_1, x), \ldots, K(x_n, x)). \tag{28}$$

Reference [33] has shown that the reproducing kernel $\widetilde{K}$ in $\widetilde{H}$ is

$$\widetilde{K}(x, z) = K(x, z) - K_x^T (I + MK)^{-1} M K_z, \tag{29}$$

where K denotes the kernel matrix in H and I is an identity matrix. The key issue now is the choice of M, so that the deformation of the kernel induced by the data-dependent norm is motivated with respect to the discriminative information and the intrinsic manifold structure of gait images.

In order to model the discriminative manifold structure, we construct two nearest neighbor graphs, that is, an intrinsic graph G_c and a penalty graph G_p. For each data sample x_i, the intrinsic graph G_c is constructed by finding its k_1 nearest neighbors from data samples that have the same class label with x_i, and putting an edge between x_i and its neighbors. The weight matrix W^c on the intrinsic graph G_c is defined as follows:

$$W_{ij}^c = \begin{cases} 1, & \text{if } x_i \in N_{k_1}(x_j) \text{ or } x_j \in N_{k_1}(x_i); \\ 0, & \text{otherwise,} \end{cases} \tag{30}$$

where $N_{k_1}(x_i)$ denotes the data sample set of the k_1 nearest neighbors of x_i that are in the same class.

Similarly, for each data sample x_i, the penalty graph G_p is constructed by finding its k_2 nearest neighbors from data samples that have class labels different from that of x_i and putting an edge between x_i and its neighbors from different classes. The weight matrix W^p on the penalty graph G_p is defined as follows:

$$W_{ij}^p = \begin{cases} 1, & \text{if } (x_i, x_j) \in P_{k_2}(c_i) \text{ or } (x_i, x_j) \in P_{k_2}(c_j); \\ 0, & \text{otherwise,} \end{cases} \tag{31}$$

where $P_{k_2}(c)$ denotes a set of data pairs that are the k_2 nearest pairs among the data pair set $\{(x_i, x_j) \mid c_i = c, c_j \neq c\}$.

To encode the discriminative information, we maximize margins between different classes. The between-class separability is modeled by the graph Laplacian defined on the penalty graph:

$$f^T L^p f = \frac{1}{2} \sum_{i,j} (f(x_i) - f(x_j))^2 W_{ij}^p, \tag{32}$$

where $L^p = D^p - W^p$ is the Laplacian matrix of the penalty graph and the ith element of the diagonal matrix D^p is $D_{ii}^p = \sum_j W_{ij}^p$.

To encode the intrinsic manifold structure, the graph Laplacian provides the following smoothness penalty on the intrinsic graph:

$$f^T L^c f = \frac{1}{2} \sum_{i,j} (f(x_i) - f(x_j))^2 W_{ij}^c, \tag{33}$$

where $L^c = D^c - W^c$ is the Laplacian matrix of the intrinsic graph G_c and the ith element of the diagonal matrix D^c is $D_{ii}^c = \sum_j W_{ij}^c$.

We minimize (33) to retain the intrinsic manifold structure information and maximize (32) to make the data samples in different classes separable. Thus, by combining discriminative information and the intrinsic manifold structure information together, we can set M in (29) as

$$M = \left((L^p)^{-1/2} \right)^T L^c (L^p)^{-1/2}. \tag{34}$$

Then, by substituting (34) into (29), we eventually get the following discriminative manifold adaptive kernel function:

$$\begin{aligned} \widetilde{K}(x, z) = &\, K(x, z) \\ &- K_x^T \left(I + \left((L^p)^{-1/2} \right)^T L^c (L^p)^{-1/2} K \right)^{-1} \\ &\times \left((L^p)^{-1/2} \right)^T L^c (L^p)^{-1/2} K_z. \end{aligned} \tag{35}$$

As can be seen, the main idea of constructing discriminative manifold adaptive kernel is to incorporate the discriminative information and the intrinsic manifold structure information into the kernel deformation procedure simultaneously. Thus, the resulting new kernel can take advantage of

information from labeled and unlabeled data. When an input initial kernel is deformed according to (35), the resulting manifold-adaptive kernel function may be able to achieve much better performance than the original input kernel function. In this paper, we simply use the Gaussian kernel as the input initial kernel.

In summary, by combining the above discussions, we can outline the proposed manifold-adaptive kernel SDA (MAKSDA) algorithm as follows.

(1) Calculate the initial kernel matrix K : $K_{ij} = K(x_i, x_j)$ in the original data space. Construct an intrinsic graph G_c with the weight matrix defined in (30) and calculate the graph Laplacian $L^c = D^c - W^c$. Construct a penalty graph G_p with the weight matrix defined in (31) and calculate the graph Laplacian $L^p = D^p - W^p$. Calculate M and the discriminative manifold-adaptive kernel function $\widetilde{K}$ in terms of (34) and (35), respectively.

(2) Replace K in (24) with $\widetilde{K}$ defined in (35) and obtain the following generalized eigenproblem:

$$\left(\widetilde{K}W\widetilde{K} - \widetilde{K}\widetilde{K} - \beta\widetilde{K}L\widetilde{K}\right)\alpha = \lambda\widetilde{K}\alpha. \qquad (36)$$

(3) Compute the eigenvectors and eigenvalues for the generalized eigenproblem (36). Let the column vector $\alpha = [\alpha_1, \alpha_2, \ldots, \alpha_d]$ be solutions of (36) ordered according to their eigenvalues $\lambda_1 > \lambda_2 > \cdots > \lambda_d$. Thus, the MAKSDA embedding can be computed as follows:

$$
\begin{aligned}
\langle U, \varphi(x) \rangle &= \sum_{i=1}^{n} \alpha_i \langle \varphi(x_i), \varphi(x) \rangle \\
&= \sum_{i=1}^{n} \alpha_i \widetilde{K}(x_i, x) \\
&= \alpha^T \widetilde{K}(\cdot, x),
\end{aligned}
\qquad (37)
$$

where the discriminative manifold adaptive kernel $\widetilde{K}(\cdot, x) = [\widetilde{K}(x_1, x), \widetilde{K}(x_2, x), \ldots, \widetilde{K}(x_n, x)]^T$.

Now, we obtain the low-dimensional representations of the original gait images with (37). In the reduced feature space, those images belonging to the same class are close to each other, while those images belonging to different classes are far apart. Thus, the traditional classifier algorithm can be applied to classify different gait images. In this paper, we apply the nearest neighbor classifier for its simplicity, and the Euclidean metric is used as the distance measure.

The time complexity analysis of MAKSDA is outlined as follows. Computing the input initial kernel matrix needs $O(n^2)$. Constructing the intrinsic graph and the penalty graph needs $O(k_1 n^2)$ and $O(k_2 n^2)$, respectively. Computing the discriminative manifold adaptive kernel matrix and the generalized eigenproblem needs $O(n^3)$. Projecting the original image into the lower-dimensional feature space needs $O(dn^2)$. Thus, the total computational complexity of MAKSDA is $O(n^3)$, which is the same as the traditional kernel SDA algorithm in the kernel space.

FIGURE 3: Some original binary images and the average silhouette images of two different peoples in the USF HumanID gait database.

5. Experimental Results

In this section, we report experimental results on the well-known USF HumanID gait database [1] to investigate the performance of our proposed MAKSDA algorithm for gait recognition.

The system performance is compared with the kernel PCA (KPCA) [34], kernel LDA (KLDA) [35], kernel LPP (KLPP) [36], kernel MFA (KMFA) [8], and kernel SDA (KSDA) [25], five of the most popular nonlinear methods in gait recognition. We adopt the commonly used Gaussian kernel as kernel function of these four algorithms. In the following experiments, the Gaussian kernel with parameters $\delta = 2^{(n-10)/2.5}\delta_0$, $n = 0, 1, \ldots, 20$ is used, where δ_0 is the standard deviation of the data set. We report the best result of each algorithm from among the 21 experiments. There are two important parameters in our proposed MAKSDA algorithm, that is, the number of nearest neighbor k_1 in the intrinsic graph and the number of nearest neighbor k_2 in the penalty graph. We empirically set them to 6 and 15, respectively. In the following section, we will discuss the effect on the recognition performance with different values of k_1 and k_2. In addition, since the original SDA algorithm is robust to the regularization parameter β, we simply set $\beta = 1$ in KSDA and MAKSDA for fair comparison.

We carried out all of our experiments upon the USF HumanID gait database, which consists of 1870 sequences from 122 subjects (people). As suggested in [1], the whole sequence is partitioned into several subsequences according to the gait period length N_{gait}, which is provided by Sarkar et al. [1]. Then, the binary images within one gait cycle are averaged to acquire several gray-level average silhouette images as follows:

$$\text{AT}_i = \frac{1}{N_{\text{gait}}} \sum_{k=(i-1)N_{\text{gait}}+1}^{k=iN_{\text{gait}}} T(k), \quad i = 1, \ldots, \left\lfloor \frac{F}{N_{\text{gait}}} \right\rfloor, \quad (38)$$

where $\{T(1), \ldots, T(F)\}$ represent the binary images for one sequence with F frames and $\lfloor F/N_{\text{gait}} \rfloor$ denotes the largest integer less than or equal to F/N_{gait}. Some original binary images and the average silhouettes of two different peoples are shown in Figure 3, where the first seven images and the last image in each row denote the binary silhouette images and the average silhouette image, respectively. As can be seen, different individuals have different average silhouette images.

In this paper, to perform gait recognition, the averaged gait image is decomposed by Gabor filters introduced in

Section 2. We combine the decomposed images to give a new Gabor feature representation defined in (5), which is suitable for gait recognition. Our use of the Gabor-based feature representation for the averaged gait-image-based recognition is based on the following considerations: (1) Gabor functions provide a favorable tradeoff between spatial resolution and frequency resolution, which can be implemented by controlling the scale and orientation parameters; (2) it is supposed that Gabor kernels are similar to the 2D-receptive field profiles of the mammalian cortical simple cells; and (3) Gabor-function-based representations have been successfully employed in many machine vision applications, such as face recognition, scene classification, and object recognition.

In short, the gait recognition algorithm has three steps. First, we calculate the Gabor feature representation of the averaged gait image. Then, the Gabor feature representations are projected into lower-dimensional feature space via our proposed MAKSDA algorithm. Finally, the nearest neighbor classifier is adopted to identify different gait images. As suggested in [1–3], the distance measure between the gallery sequence and the probe sequence adopts the following median operator, since it is more robust to noise than the traditional minimum operator. Consider

$$\text{Dist}\left(\text{LS}_P, \text{LS}_G\right) = \text{Median}_{i=1}^{N_p}\left(\text{Min}_{j=1}^{N_g}\|\text{LS}_P(i) - \text{LS}_G(j)\|^2\right), \tag{39}$$

where $\text{LS}_P(i)$, $i = 1,\ldots,N_p$, and $\text{LS}_G(j)$, $j = 1,\ldots,N_g$, are the lower-dimensional feature representations from one probe sequence and one gallery sequence, respectively. N_p and N_g denote the total number of average silhouette images in the probe sequence and one gallery sequence, respectively.

Three metrics (the Rank-1, Rank-5, and Average recognition accuracies) are used to measure the recognition performance. Rank-1 means that the correct subject is ranked as the top candidate, Rank-5 means that the correct subject is ranked among the top five candidates, and Average denotes the recognition accuracy among all the probe sets, that is, the ratio of correctly recognized persons to the total number of persons in all the probe sets. Tables 1 and 2 show the best results obtained by KPCA, KLDA, KLPP, KMFA, KSDA, and MAKSDA. From the experimental results, we can make the following observations.

(1) Our proposed MAKSDA algorithm consistently outperforms KPCA, KLDA, KLPP, KMFA, and KSDA algorithms, which implies that extracting the discriminative feature by using both labeled and unlabeled data and explicitly considering the discriminative manifold adaptive kernel function can achieve the best gait recognition performance.

(2) KPCA obtains the worst performance on the USF HumanID gait database even though it is a kernel-based method. The possible reason is that it is unsupervised and only adopts the data-independent kernel function, which are not necessarily useful for discriminating gait images with different persons.

(3) The average performances of KLDA and KLPP are almost similar. For some probe sets, KLPP outperforms KLDA, while KLDA is better than KLPP for other probe sets. This indicates that it is hard to evaluate whether manifold structure or the class label information is more important, which is consistent with existing studies [37, 38].

(4) KMFA is superior to KLDA and KLPP, which demonstrates that KMFA can effectively utilize local manifold structure as well as the class label information for gait recognition.

(5) The semisupervised kernel algorithms (i.e., KSDA and MAKSDA) consistently outperform the pure unsupervised kernel algorithms (i.e., KPCA and KLPP) and the pure supervised kernel algorithms (i.e., KLDA and KMFA). This observation demonstrates that the semisupervised learning can effectively utilize both labeled and unlabeled data to improve gait recognition performance.

(6) Although KSDA and MAKSDA are all the nonlinear extensions of SDA via kernel trick, MAKSDA performs better than SDA. The main reason could be attributed to the following fact. First, MAKSDA avoids the numerical computation problem without computing matrix inverse. Second, KSDA adopts the commonly used data-independent kernel functions; thus the nonlinear structure captured by these kernel functions may not be consistent with the intrinsic manifold structure of gait image. For MAKSDA, it adopts the discriminative manifold-adaptive kernel function; thus the nonlinear structure captured by these data-adaptive functions is consistent with the discriminative information revealed by labeled data as well as the intrinsic manifold structure information revealed by unlabeled data.

(7) MAKSDA obtains the best recognition performance on all the experiments, which implies that both discriminant and geometrical information contained in the kernel function are important for gait recognition.

We also conduct an in-depth investigation of the performance of Gabor-based feature with respect to different parameters, such as the number of scales and orientations of Gabor features. In this study, we adopt the default settings; that is, we have 40 Gabor kernel functions from five scales $\nu \in \{0, 1, 2, 3, 4\}$ and eight orientations $\mu \in \{0, 1, 2, 3, 4, 5, 6, 7\}$. By using MAKSDA algorithm, we test the performance of Gabor-based feature under different parameters, in which we still adopt the nearest neighbor classifier with the distance defined in (39) for fair comparison. The average Rank-1 and Rank-5 recognition accuracies of Gabor-based feature with different parameters are shown in Table 3. As can be seen, the recognition accuracies using the default parameter setting (i.e., five scales and eight orientations) are unanimously better than using other parameter settings, which is consistent with recent studies from several other research groups [13].

The construction of the kernel function is one of the key points in our proposed MAKSDA algorithm. Our proposed

TABLE 1: Performance comparison in terms of Rank-1 recognition accuracies (%).

Probe	A	B	C	D	E	F	G	H	I	J	K	L	Average
KPCA	85	87	73	25	28	16	18	58	62	52	7	9	43.3
KLDA	88	90	79	34	31	20	24	65	70	64	15	17	49.8
KLPP	89	91	78	36	34	19	22	66	73	61	14	19	50.2
KMFA	90	93	80	41	45	23	29	81	79	65	23	22	55.9
KSDA	92	96	84	43	47	26	31	82	83	67	24	24	58.3
MAKSDA	96	98	85	47	49	28	35	86	86	70	29	28	61.4

TABLE 2: Performance comparison in terms of Rank-5 recognition accuracies (%).

Probe	A	B	C	D	E	F	G	H	I	J	K	L	Average
KPCA	89	94	82	69	57	44	40	87	81	63	19	16	61.8
KLDA	94	96	90	71	62	47	45	91	83	82	21	18	66.7
KLPP	95	97	89	74	66	45	44	93	85	81	19	20	67.3
KMFA	96	97	92	75	70	51	53	94	89	82	32	33	72.0
KSDA	97	98	93	77	71	53	57	96	91	85	34	36	74.0
MAKSDA	99	99	95	83	79	56	61	98	97	87	35	38	77.3

TABLE 3: Average Rank-1 and Rank-5 recognition accuracies (%) under different Gabor parameters.

Parameter settings	Average Rank-1	Average Rank-5
Five scales and eight orientations	61.4	77.3
Five scales and four orientations	56.2	71.8
Three scales and eight orientations	57.8	73.4
Three scales and four orientations	56.5	71.9

TABLE 4: Average Rank-1 and Rank-5 recognition accuracies (%) under different kernel functions.

Kernel functions	Average Rank-1	Average Rank-5
Discriminative manifold adaptive kernel	61.4	77.3
Gaussian kernel	57.5	70.4
Polynomial kernel	55.3	68.7
Sigmoid kernel	55.8	68.6

MAKSDA algorithm adopts the discriminative manifold adaptive kernel function to capture the discriminative information and the intrinsic manifold structure information. Of course, we can also use other kinds of traditional kernel functions, such as Gaussian kernel, polynomial kernel, and Sigmoid kernel. To illustrate the superiority of our proposed discriminative manifold adaptive kernel function, we test the average Rank-1 and Rank-5 recognition accuracies under different kernel functions. The experimental results are shown in Table 4. As can be seen, our proposed discriminative manifold adaptive kernel function achieves the best performance, while the rest kernel functions have comparative performance. The superiority of discriminative manifold adaptive kernel is due to the fact that it is the data-dependent kernel, and the nonlinear structure captured by it may be consistent with the intrinsic manifold structure of gait image, which has been shown very useful for improving the learning performance by many previous studies. However, Gaussian kernel, polynomial kernel, and Sigmoid kernel are all data-independent common kernels, which might not be optimal in discriminating gait images with different semantics. This also demonstrates that simultaneously considering the local manifold structure and discriminative information is essential in designing kernel SDA algorithms for gait recognition.

In addition, our proposed MAKSDA algorithm has two essential parameters: the number of nearest neighbor k_1 in the intrinsic graph and the number of nearest neighbor k_2 in the penalty graph. We empirically set k_1 to 6 and k_2 to 15 in the previous experiments. In this section, we investigate the influence of different choices of k_1 and k_2. We vary k_1 while fixing k_2 and vary k_2 while fixing k_1. Figures 4 and 5 show the performance of MAKSDA as a function of the parameters k_1 and k_2, respectively. As can be seen, the performance of MAKSDA is very stable with respect to the two parameters. It achieves much better performance than other kernel algorithms when k_1 varies from 4 to 8 and k_2 varies from 10 to 20. Therefore, the selection of parameters is not a very crucial problem in our proposed MAKSDA algorithm.

6. Conclusions

We have introduced a novel manifold adaptive kernel semisupervised discriminant analysis (MAKSDA) algorithm for gait recognition. It can make use of both labeled and unlabeled gait image to learn a low-dimensional feature space for gait recognition. Unlike the traditional kernel-based SDA algorithm, MAKSDA not only avoids the singular problem by not computing the matrix inverse, but also can explore the data-dependent nonlinear structure of the gait image by using the discriminative manifold adaptive kernel function. Experimental results on the widely used gait database are presented to show the efficacy of the proposed approach.
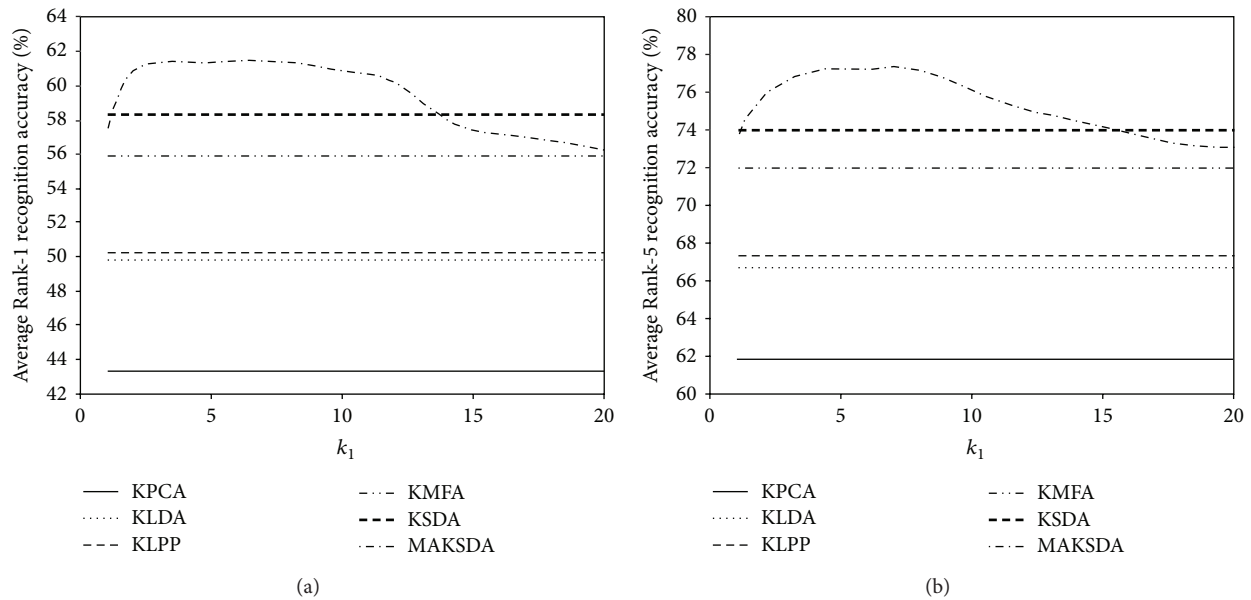
FIGURE 4: The performance of MAKSDA versus parameter k_1: (a) Average Rank-1 recognition accuracy versus k_1; (b) Average Rank-5 recognition accuracy versus k_1.
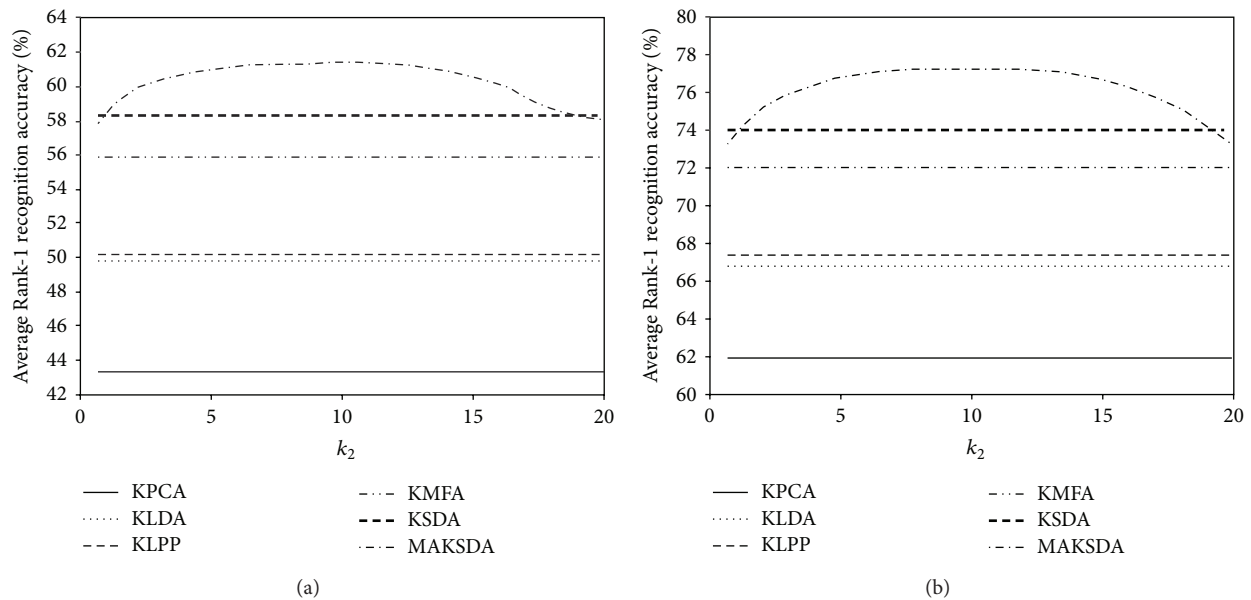

FIGURE 5: The performance of MAKSDA versus parameter k_2: (a) Average Rank-1 recognition accuracy versus k_2; (b) Average Rank-5 recognition accuracy versus k_2.

Conflict of Interests

The authors declare that there is no conflict of interests regarding the publication of this paper.

Acknowledgments

References

[1] S. Sarkar, P. J. Phillips, Z. Liu, I. R. Vega, P. Grother, and K. W. Bowyer, "The humanID gait challenge problem: data sets, performance, and analysis," *IEEE Transactions on Pattern Analysis and Machine Intelligence*, vol. 27, no. 2, pp. 162–177, 2005.

[2] J. Han and B. Bhanu, "Individual recognition using gait energy image," *IEEE Transactions on Pattern Analysis and Machine Intelligence*, vol. 28, no. 2, pp. 316–322, 2006.

[3] D. Tao, X. Li, X. Wu, and S. J. Maybank, "General tensor discriminant analysis and Gabor features for gait recognition," *IEEE Transactions on Pattern Analysis and Machine Intelligence*, vol. 29, no. 10, pp. 1700–1715, 2007.

[4] L. Wang, T. Tan, H. Ning, and W. Hu, "Silhouette analysis-based gait recognition for human identification," *IEEE Transactions on Pattern Analysis and Machine Intelligence*, vol. 25, no. 12, pp. 1505–1518, 2003.

[5] Z. Liu and S. Sarkar, "Improved gait recognition by gait dynamics normalization," *IEEE Transactions on Pattern Analysis and Machine Intelligence*, vol. 28, no. 6, pp. 863–876, 2006.

[6] R. O. Duda, P. E. Hart, and D. G. Stork, *Pattern Classification*, Wiley-Interscience, Hoboken, NJ, USA, 2nd edition, 2000.

[7] X. He, S. Yan, Y. Hu, P. Niyogi, and H.-J. Zhang, "Face recognition using Laplacianfaces," *IEEE Transactions on Pattern Analysis and Machine Intelligence*, vol. 27, no. 3, pp. 328–340, 2005.

[8] S. Yan, D. Xu, B. Zhang, H.-J. Zhang, Q. Yang, and S. Lin, "Graph embedding and extensions: a general framework for dimensionality reduction," *IEEE Transactions on Pattern Analysis and Machine Intelligence*, vol. 29, no. 1, pp. 40–51, 2007.

[9] D. Tao, X. Li, X. Wu, and S. J. Maybank, "General averaged divergence analysis," in *Proceedings of the 7th IEEE International Conference on Data Mining (ICDM '07)*, pp. 302–311, October 2007.

[10] D. Tao, X. Li, X. Wu, and S. J. Maybank, "Geometric mean for subspace selection," *IEEE Transactions on Pattern Analysis and Machine Intelligence*, vol. 31, no. 2, pp. 260–274, 2009.

[11] T. Zhou and D. Tao, "GoDec: randomized low-rank & sparse matrix decomposition in noisy case," in *Proceedings of the 28th International Conference on Machine Learning (ICML '11)*, pp. 33–40, usa, July 2011.

[12] D. Cai, X. He, J. Han, and H.-J. Zhang, "Orthogonal laplacianfaces for face recognition," *IEEE Transactions on Image Processing*, vol. 15, no. 11, pp. 3608–3614, 2006.

[13] D. Xu, Y. Huang, Z. Zeng, and X. Xu, "Human gait recognition using patch distribution feature and locality-constrained group sparse representation," *IEEE Transactions on Image Processing*, vol. 21, no. 1, pp. 316–326, 2012.

[14] X. Li, S. Lin, S. Yan, and D. Xu, "Discriminant locally linear embedding with high-order tensor data," *IEEE Transactions on Systems, Man, and Cybernetics B*, vol. 38, no. 2, pp. 342–352, 2008.

[15] T. Zhang, D. Tao, X. Li, and J. Yang, "Patch alignment for dimensionality reduction," *IEEE Transactions on Knowledge and Data Engineering*, vol. 21, no. 9, pp. 1299–1313, 2009.

[16] D. Tao and L. Jin, "Discriminative information preservation for face recognition," *Neurocomputing*, vol. 91, pp. 11–20, 2012.

[17] D. Tao, X. Li, W. Hu, S. Maybank, and X. Wu, "Supervised tensor learning," in *Proceedings of the 5th IEEE International Conference on Data Mining (ICDM '05)*, pp. 450–457, November 2005.

[18] D. Tao, X. Li, X. Wu, W. Hu, and S. J. Maybank, "Supervised tensor learning," *Knowledge and Information Systems*, vol. 13, no. 1, pp. 1–42, 2007.

[19] Z. Zhang and D. Tao, "Slow feature analysis for human action recognition," *IEEE Transactions on Pattern Analysis and Machine Intelligence*, vol. 34, no. 3, pp. 436–450, 2012.

[20] X. Zhu, "Semi-supervised learning literature survey," Tech. Rep. 1530, Computer Science Department, University of Wisconsin, Madison, Wis, USA, 2008.

[21] V. N. Vapnik, O. Chapelle, and J. Weston, "Transductive inference for estimating values of functions," in *Advances in Neural Information Processing*, pp. 421–427, 1999.

[22] A. Blum and T. Mitchell, "Combining labeled and unlabeled data with co-training," in *Proceedings of the 11th Annual Conference on Computational Learning Theory (COLT '98)*, pp. 92–100, July 1998.

[23] M. Belkin, P. Niyogi, and V. Sindhwani, "Manifold regularization: a geometric framework for learning from labeled and unlabeled examples," *Journal of Machine Learning Research*, vol. 7, pp. 2399–2434, 2006.

[24] D. Tao, L. Jin, W. Liu, and X. Li, "Hessian regularized support vector machines for mobile image annotation on the cloud," *IEEE Transactions on Multimedia*, vol. 15, no. 4, pp. 833–844, 2013.

[25] D. Cai, X. He, and J. Han, "Semi-supervised discriminant analysis," in *Proceedings of the 11th IEEE International Conference on Computer Vision (ICCV '07)*, pp. 1–7, Rio de Janeiro, Brazil, October 2007.

[26] V. N. Vapnik, *The Nature of Statistical Learning Theory*, Springer, New York, NY, USA, 1995.

[27] T. S. Lee, "Image representation using 2d gabor wavelets," *IEEE Transactions on Pattern Analysis and Machine Intelligence*, vol. 18, no. 10, pp. 959–971, 1996.

[28] C. Liu and H. Wechsler, "Gabor feature based classification using the enhanced Fisher linear discriminant model for face recognition," *IEEE Transactions on Image Processing*, vol. 11, no. 4, pp. 467–476, 2002.

[29] C. Liu, "Gabor-based kernel PCA with fractional power polynomial models for face recognition," *IEEE Transactions on Pattern Analysis and Machine Intelligence*, vol. 26, no. 5, pp. 572–581, 2004.

[30] H. Li, T. Jiang, and K. Zhang, "Efficient and robust feature extraction by maximum margin criterion," *IEEE Transactions on Neural Networks*, vol. 17, no. 1, pp. 157–165, 2006.

[31] T. Zhang, D. Tao, and J. Yang, "Discriminative locality alignment," in *Computer Vision—ECCV 2008*, vol. 5302 of *Lecture Notes in Computer Science*, pp. 725–738, 2008.

[32] W. Zhang, Z. Lin, and X. Tang, "Learning semi-Riemannian metrics for semisupervised feature extraction," *IEEE Transactions on Knowledge and Data Engineering*, vol. 23, no. 4, pp. 600–611, 2011.

[33] V. Sindhwani, P. Niyogi, and M. Belkin, "Beyond the point cloud: from transductive to semi-supervised learning," in *Proceedings of the 22nd International Conference on Machine Learning*, pp. 824–831, August 2005.

[34] B. Schölkopf, A. Smola, and K.-R. Müller, "Nonlinear component analysis as a kernel eigenvalue problem," *Neural Computation*, vol. 10, no. 5, pp. 1299–1319, 1998.

[35] G. Baudat and F. Anouar, "Generalized discriminant analysis using a kernel approach," *Neural Computation*, vol. 12, no. 10, pp. 2385–2404, 2000.

[36] X. He and P. Niyogi, "Locality preserving projections," in *Proceedings of the International Conference on Advances in Neural Information Processing Systems (NIPS '03)*, pp. 585–591, 2003.

[37] D. Xu, S. Yan, D. Tao, S. Lin, and H.-J. Zhang, "Marginal fisher analysis and its variants for human gait recognition and

content- based image retrieval," *IEEE Transactions on Image Processing*, vol. 16, no. 11, pp. 2811–2821, 2007.

[38] M. Sugiyama, "Dimensionality reduction of multimodal labeled data by local fisher discriminant analysis," *Journal of Machine Learning Research*, vol. 8, pp. 1027–1061, 2007.

Research Article

An Efficient and Accurate Method for Real-Time Processing of Light Stripe Images

Xu Chen, Guangjun Zhang, and Junhua Sun

Key Laboratory of Precision Opto-Mechatronics Technology, Ministry of Education, Beihang University, Beijing 100191, China

Correspondence should be addressed to Junhua Sun; sjh@buaa.edu.cn

This paper describes a direction-guided method for real-time processing of light stripe images in practical active vision applications. The presented approach consists of three main steps. Firstly, we select two thresholds to divide the image into three classes, that is, the foreground, the background, and the undecided area. Then, we locate a feature point of the light stripe in the image foreground and calculate the local line direction at that point. Finally, we detect succeeding points along that direction in the foreground and the undecided area and directly exclude pixels which are in the normal direction of the line. We use synthetic and real images to verify the accuracy and efficiency of the proposed method. The experimental results show that the proposed algorithm gains a 1-fold speedup compared to the prevalent method without any loss of accuracy.

1. Introduction

Due to the merit of the wide measurement range, noncontact capability, and high accuracy, active vision techniques have been widely used in fields of surface reconstruction, precision measurement, and industrial inspection [1, 2]. Nowadays, more and more vision systems for real-time measurement and inspection tasks have appeared [3]. Among the variety of active vision methods, line structured light vision technique is perhaps the most widespread. In this paper, we focus on the line structured light vision in real-time measurement applications.

Light stripe processing plays an important role in line structured light vision applications in the following aspects. Firstly, the processing method should ensure the integrality of light stripes which are modulated by the surface of the object and contain the desired information. Secondly, the line point detection accuracy directly influences the measurement accuracy. Finally, the speed of the stripe processing algorithm is crucial in real-time applications. A time-consuming method is apparently not eligible for those tasks despite its high accuracy and robustness.

To detect centric lines of curvilinear structures, there are many methods which can be roughly classified into two categories. The first approach detects line points by only taking the gray values of the image into consideration and uses some local criteria such as extrema or centroids of gray values in a subregion [4, 5]. This kind of method is inclined to be affected by noisy pixels and the detection accuracy is relatively low.

The second approach uses differential geometric properties to extract feature lines. These algorithms regard ridges and ravines in the image as the desired lines [6, 7]. Among those methods, the one proposed by Steger [8] is widely used in the community. Steger's method firstly extracts line points by locally approximating the image function by its second order Taylor polynomial and determines the direction of the line at the current point from the Hessian matrix of the Taylor polynomial. After individual line points have been detected, a point linking algorithm is applied to facilitate further process. The linking step is necessary since we often want to get some characteristics about the feature line such as its length. Steger's method has the advantages of high accuracy and nice robustness, whereas it also suffers from the drawback that the algorithm is computationally expensive, which is not sustainable in real-time applications.

Based on Steger's method, many revised algorithms aiming at processing light stripe images more efficiently have

(a) Wheel image with disturbing reflection lights

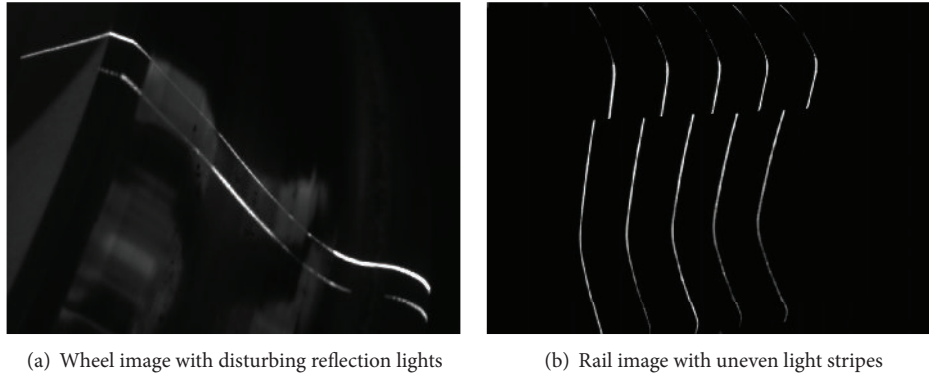(b) Rail image with uneven light stripes

FIGURE 1: Real light stripe images affected by serious reflection.

been proposed. Hu et al. [9] utilize the separability of the Gaussian smoothing kernels and implement a recursive version of the Gaussian derivatives to approximate the original ones.Besides, Zhou et al. [10] present a composite processing method to detect the subpixel centers of light stripes based on region of interest (ROI). The method combines image thresholding with image dilation to automatically segment the ROIs of light stripes and then detects feature points in limited area. These algorithms have greatly improved the original Steger method, but it is still important to develop more efficient ones for real-time vision applications.

In this paper, a direction-guided algorithm is given to accelerate the speed of line detection procedure. In the presented algorithm, the input light stripe image is firstly bilevel thresholded into image foreground, background, and the undecided area. Then, the first feature point of a new line in the light stripe is detected in the image foreground and the local line direction is calculated. Finally, succeeding line points are located in the foreground and undecided area along the direction and pixels which are in the normal direction of the line are excluded. Experiments on synthetic and real images have been conducted to verify the accuracy and efficiency of the proposed method and conclusions are drawn.

2. Bilevel Thresholding of the Light Stripe Image

Most existing light stripe image processing methods can be divided into two stages, that is, image thresholding and line detection. Those methods assume that gray values of light stripes are markedly greater than those of the image background, and the threshold can be easily selected using Otsu's method [11]. But the actual gray levels of light stripes may vary in a wide range and some stripe segments resemble the image background due to the serious reflection and large curvature of the object surface. In addition, some images may even be affected by serious disturbing lights which cannot be removed by optical filters. This circumstance occurs frequently when we try to recover profiles of some large scale metal parts whose surfaces are curving.

Figure 1 exemplifies the aforementioned situation. Figure 1(a) is an image captured from a real freight wheel,

and Figure 1(b) is an image captured from a real train rail. We can see that there exists large area of disturbing lights in Figure 1(a), and the upper segments of light stripes in Figure 1(b) are relatively weaker than the lower parts. Given these conditions, thresholding simply using Otsu's method may lead to the undesired results that some weak stripe segments are treated as the image background or the disturbing lights are seen as the foreground.

To deal with light stripe images including those affected by serious reflection, we choose the bilevel thresholding strategy. That is, pixels with gray values greater than the higher threshold are treated as the foreground and those with gray values smaller than the lower threshold are seen as the background. Pixels with gray values which are between the two thresholds are treated as the undecided area. In the succeeding operations, we search the beginning feature point of a new line in the foreground and detect the potential points in the foreground and the undecided area.

To determine the two thresholds, we combine the methods proposed by Otsu [11] and Rosin [12]. After calculating the image histogram, we can locate two gray values $T_{\min}$ and $T_{\max}$ which are corresponding to the highest peak and the last nonzero value of the histogram, respectively. Besides, gray levels T_{otsu} and T_{rosin} are selected using the methods proposed by Otsu and Rosin, respectively. We then determine the two thresholds T_l and T_h according to the following rules:

$$
\begin{aligned}
T_l &= \alpha T_{\min} + (1 - \alpha) \min \left\{ T_{\mathrm{rosin}}, T_{\mathrm{otsu}} \right\} \\
T_h &= \beta T_{\max} + (1 - \beta) \max \left\{ T_{\mathrm{rosin}}, T_{\mathrm{otsu}} \right\}, \\
&\quad \alpha \in [0, 1], \quad \beta \in [0, 1].
\end{aligned}
\tag{1}
$$

Actually, the parameters α and β are usually set as zeros for ordinary light stripe images. We only have to tune the two parameters when confronted with images which contain large area of disturbing reflection lights. Besides, we can utilize the entropy and the peak number of the histogram to decide whether the input image contains large area of disturbing reflection lights or not. Images with disturbing

lights often have larger entropies and more than two peaks in their histograms. The entropy calculation is given by

$$E = -\sum_{i=0}^{L} p_i \log p_i. \tag{2}$$

Here, p_i is the ith index of the normalized histogram $h(t)$ and L is the maximum gray value.

3. Determination of the First Feature Point of a New Line

After bilevel thresholding the image into three classes, we can detect the first feature point of a new line by examining each unprocessed pixel in the image foreground using Steger's method. In brief, if we denote the direction perpendicular to the line by $n(t)$, then the first directional derivative of the desired line point in the direction $n(t)$ should vanish and the second directional derivative should be of large absolute value.

To compute the direction of the line locally for the image point to be processed, the first and second order partial derivatives r_x, r_y, r_{xx}, r_{xy}, and r_{yy} of the image pixel $f(x, y)$ have to be estimated by convolving it and its neighborhood points with the discrete two-dimensional Gaussian partial derivative kernels as follows:

$$
\begin{aligned}
r(x, y) &= f(x, y) \otimes g(x, y), \\
r_x(x, y) &= f(x, y) \otimes g_x(x, y), \\
r_y(x, y) &= f(x, y) \otimes g_y(x, y), \\
r_{xx}(x, y) &= f(x, y) \otimes g_{xx}(x, y), \\
r_{xy}(x, y) &= f(x, y) \otimes g_{xy}(x, y), \\
r_{yy}(x, y) &= f(x, y) \otimes g_{yy}(x, y).
\end{aligned}
\tag{3}
$$

The Gaussian kernels are given by

$$
\begin{aligned}
g(x, y) &= \frac{1}{2\pi\sigma^2} \exp\left(-\frac{x^2 + y^2}{2\sigma^2}\right), \\
g_x(x, y) &= \frac{\partial g(x, y)}{\partial x} = -\frac{x}{2\pi\sigma^4} \exp\left(-\frac{x^2 + y^2}{2\sigma^2}\right), \\
g_y(x, y) &= \frac{\partial g(x, y)}{\partial y} = -\frac{y}{2\pi\sigma^4} \exp\left(-\frac{x^2 + y^2}{2\sigma^2}\right), \\
g_{xx}(x, y) &= \frac{\partial^2 g(x, y)}{\partial x^2} = \frac{x^2 - \sigma^2}{2\pi\sigma^6} \exp\left(-\frac{x^2 + y^2}{2\sigma^2}\right), \\
g_{xy}(x, y) &= \frac{\partial^2 g(x, y)}{\partial x \partial y} = \frac{xy}{2\pi\sigma^6} \exp\left(-\frac{x^2 + y^2}{2\sigma^2}\right), \\
g_{yy}(x, y) &= \frac{\partial^2 g(x, y)}{\partial y^2} = \frac{y^2 - \sigma^2}{2\pi\sigma^6} \exp\left(-\frac{x^2 + y^2}{2\sigma^2}\right).
\end{aligned}
\tag{4}
$$

According to Steger's conclusions, the parameter σ should satisfy the inequality

$$\sigma \geq \frac{w}{\sqrt{3}}. \tag{5}$$

The parameter w is defined as the half width of the light stripe in the image. Then the normal direction $n(t)$ can be determined by calculating the eigenvalues and eigenvectors of the Hessian matrix

$$H(x, y) = \begin{pmatrix} r_{xx} & r_{xy} \\ r_{xy} & r_{yy} \end{pmatrix}. \tag{6}$$

The eigenvector corresponding to the eigenvalue of maximum absolute value is used as the normal direction $n(t) = (n_x, n_y)$ with $\|(n_x, n_y)\|_2 = 1$.

After determining the local normal direction, the Taylor polynomial of the image function at the pixel (x_0, y_0) along the direction (n_x, n_y) can be approximated by

$$
\begin{aligned}
f&\left(x_0 + tn_x, y_0 + tn_y\right) \\
&= r(x_0, y_0) + tn_x r_x(x_0, y_0) + tn_y r_y(x_0, y_0) \\
&\quad + t^2 n_x n_y r_{xy}(x_0, y_0) + \frac{1}{2} t^2 n_x^2 r_{xx}(x_0, y_0) \\
&\quad + \frac{1}{2} t^2 n_y^2 r_{yy}(x_0, y_0).
\end{aligned}
\tag{7}
$$

Thus, by setting the derivative of the Taylor polynomial along t to zero, the subpixel point can be obtained:

$$(p_x, p_y) = (tn_x, tn_y), \tag{8}$$

where

$$t = -\frac{r_x n_x + r_y n_y}{r_{xx} n_x^2 + 2 r_{xy} n_x n_y + r_{yy} n_y^2}. \tag{9}$$

Finally, the point $(x_0 + p_x, y_0 + p_y)$ is declared a line point if $(p_x, p_y) \in [-0.5, 0.5] \times [-0.5, 0.5]$.

Using the aforesaid line point detection method, we can search the first feature point of a new line by examining every unprocessed pixel in the foreground. After detecting the first feature point, we can search succeeding line points and simultaneously exclude undesired pixels until no more line points exist in the current line. If there are no feature points left in the image foreground, the total processing procedure of the input light stripe image finishes.

4. Search of Potential Line Points and Exclusion of Undesired Pixels

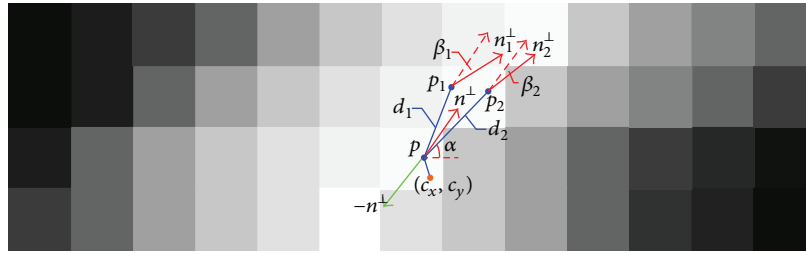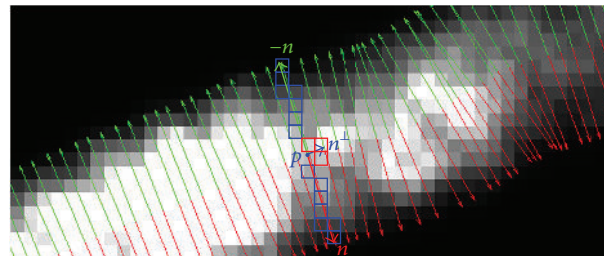Beyond the ROI-based techniques which exclude the operations on the image background, the proposed method utilizes

FIGURE 2: Search of potential line points.

☐ Potential line points
☐ Undesired pixels

FIGURE 3: Exclusion of undesired pixels.

a further fact that the center line is only a little portion of the light stripe to be extracted. Therefore, it is unnecessary to process those undesired pixels around the feature points which are in the normal direction of the line. As a result, once we detect one feature point in the line, we can directly extract and link the succeeding points along the local direction of the line and then exclude pixels in the normal direction. It is the exclusion of undesired pixels that makes the presented method intrinsically gain great speedup when compared with other methods. Herein, we divide the light stripe extraction into two main steps: one is the search of potential line points and the other is the exclusion of undesired pixels.

4.1. Search of Potential Line Points. Starting from the first line point (c_x, c_y), we can directly search the succeeding points along both line directions $n^\perp$ and $-n^\perp$. In fact, we only have to process three neighboring pixels according to the current orientation of the line. We still use the feature point detection method described in Section 3 to determine whether a potential pixel is a line point or not. If there are two or more points found, we choose the one which minimizes the summation of the distance between the respective subpixel locations and the angle difference of the two points. Once a new line point is found, we update the local line direction. If there is no point eligible, we finish the search along the current direction and turn to the other direction. We end the line point linking until the searching operations along both directions finish and start to find a new line.

Figure 2 exemplifies the aforementioned direction-guided line point searching step. As shown in the figure, the current orientation is assumed to be in the interval of $[\pi/8, 3\pi/8]$, and the points $(c_x + 1, c_y - 1)$ and $(c_x, c_y - 1)$ are both found to be line points except for $(c_x + 1, c_y)$. Then, the distances d_1, d_2 and the angle differences β_1, β_2 can be easily obtained. Suppose that $d_2 + \beta_2$ is smaller than $d_1 + \beta_1$; the point $(c_x + 1, c_y - 1)$ is then chosen as the new jumping-off point of the line, and the direction $n_2^\perp$ is regarded as the new orientation.

4.2. Exclusion of Undesired Pixels. Previous methods consider the light stripe extraction problem as two separated issues, that is, line point detection and feature point linking. Without exception, they first process all pixels in the region of interest, pick up the line points, and then link those points into lines. Actually, this kind of schemes often wastes calculations on pixels which are unnecessary to be processed, since it is only the central lines of light stripes that are the needed features in most cases.

To avoid the unwanted line point detection operations on the undesired pixels, the proposed algorithm fuses the point detection and linking steps and utilizes the normal directions of detected points to exclude the pixels which are perpendicular to the line. Figure 3 illustrates the way of determining the undesired pixels. As shown in the figure, the three pixels with the red frame are the potential line points. Meanwhile, the fourteen pixels with the blue frame in both normal directions
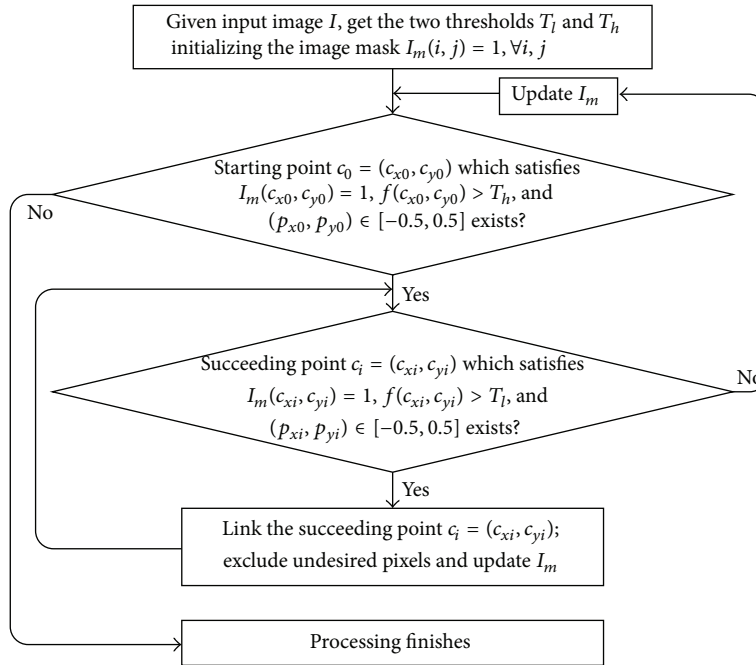
FIGURE 4: The flow chart of the proposed direction-guided approach.

n and $-n$ are treated as undesired pixels and should be omitted. It is evident that the undesired pixels occupy the great mass of the light stripe, and thus it is significant to exclude them for the purpose of the speedup.

4.3. The Entire Direction-Guided Algorithm. Figure 4 summarizes the entire approach based on the idea of direction guidance. Note that starting points of feature lines are detected in the image foreground and potential line points are searched in the image foreground and undecided area.

5. Results and Discussion

In order to demonstrate the accuracy and efficiency of the proposed method, experiments on synthetic and real images have been conducted, respectively.

5.1. Synthetic Image Data. To verify the accuracy of the line point detection, we manually generate an ideal image with one light stripe. The synthetic image shown in Figure 5(a) is 512×512, and the horizontal coordinate of the ideal center line of the light stripe is 256. After adding Gaussian white noise of 0 mean and σ standard deviation to the image, we use the presented method to detect line points and calculate the detection error e by

$$e = \sqrt{\frac{1}{N} \sum_{k=1}^{N} \|x_k - \widehat{x}_k\|^2}. \tag{10}$$

Here, x_k and $\widehat{x}_k$ are the ideal and detected position of the kth line point, respectively, and N is the number of detected line points. Figure 5(b) is an example of the degraded image affected by Gaussian noise with 0 mean and $\sigma = 0.4$. We vary the noise level from 0.05 to 0.4. For each noise level, we perform 100 independent trials, and the results shown are the average. As we can see from Figure 5(c), errors increase linearly with the noise level. For $\sigma = 0.4$ (which is larger than the normal noise in practical situation), the detection error is less than 0.35.

5.2. Real Image Data. Here, we provide four representative examples to demonstrate the efficiency of the proposed method. All of those images are 960×700. Figure 6(a) is an image captured from a running train wheel using an exposure time of 50 us. Figure 6(b) is an image of a flat metal part with cross light stripes. Besides, Figure 6(c) is an image of a steel pipe with three light stripes and the image with five light stripes shown in Figure 6(d) is captured from a rail in use.

Figure 7 displays the histograms of the example images and shows the positions of four important gray levels in green circles and two thresholds in red crosses. For all the test images, we directly use the gray level selected by Otsu's method as the higher threshold. As for the lower threshold, we tune the parameter α to be 0.75 for the wheel image affected by serious reflection lights and use the gray level selected by Rosin's method as the lower threshold for other images. Figure 8 exhibits the bilevel thresholding results of the four images. From the thresholding results of the wheel and rail images, we can see that image thresholding merely utilizing Otsu's method will mistake the weak segments of

(a) The ideal image

(b) Degraded image with $\sigma = 0.4$

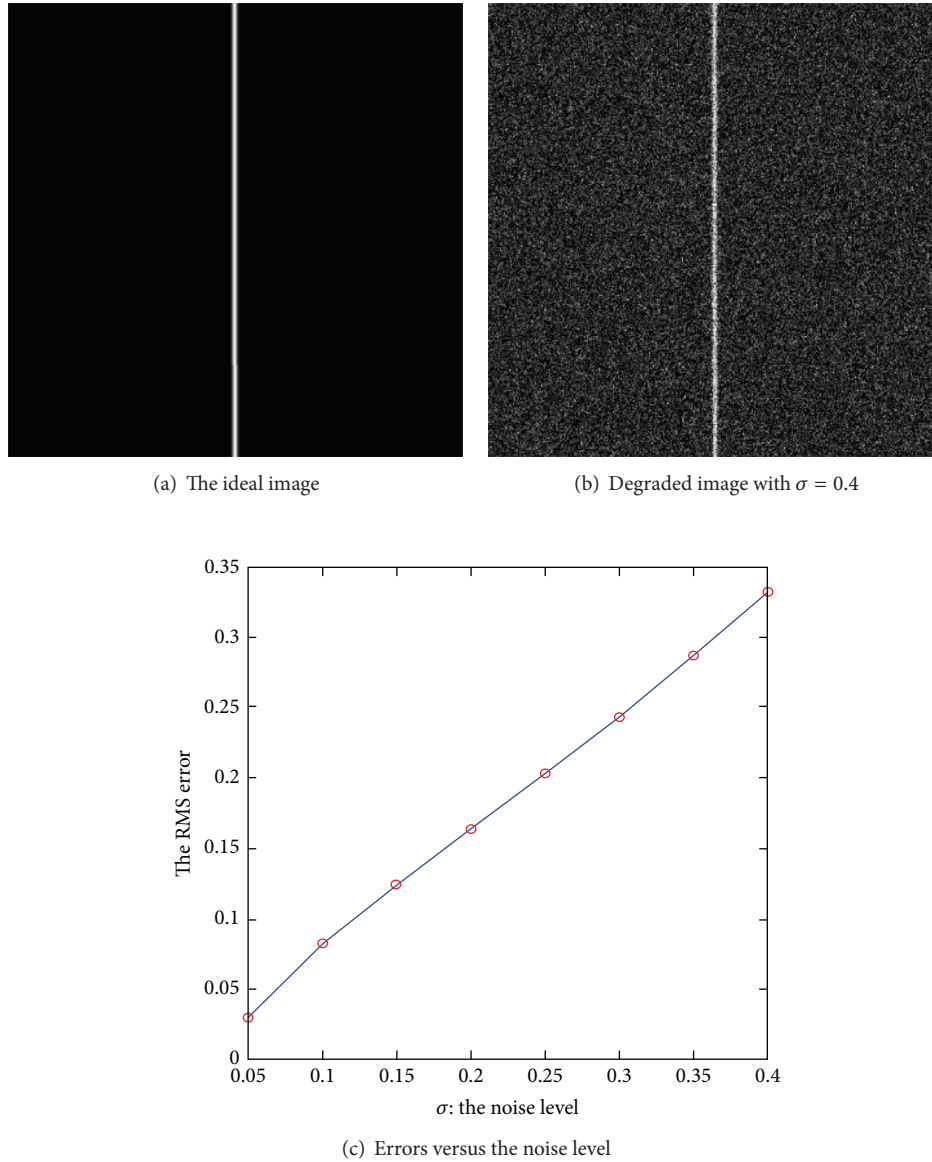(c) Errors versus the noise level

FIGURE 5: Accuracy verification experiment using a synthetic image.

light stripes for background just as expected. We can also observe that images are better segmented using bilevel thresholding especially for Figure 6(a). Figure 9 shows the line detection results. Although there may be several line points missing in the cross-sections of the light stripes due to the exclusion operations, the results are satisfying as a whole.

To demonstrate the gain in speed, we compared the presented algorithm with those proposed by Steger [8] and Zhou et al. [10]. The experiments were conducted on an Intel Core2 2.93 GHz machine running Windows 7 and the three algorithms were implemented under the Visual Studio 2012 environment. For every test image, experiments were repeated 100 times under the same conditions and a comparison of mean running time is shown in Table 1. From the table, we can see that the time consumed by the proposed method is less than

TABLE 1: Comparison of mean running time of different line detection methods (ms).

Images	Steger	Zhou	Proposed
Figure 6(a)	265	45	15
Figure 6(b)	254	39	18
Figure 6(c)	255	42	25
Figure 6(d)	256	41	22

half of the time consumed by Zhou's method and about tenth of the time consumed by Steger's method.

Furthermore, the excluded pixels of the test images during processing are shown in Figure 10 with black brush to illustrate the effect of the exclusion operations of undesired pixels and visually explain the speedup of the proposed
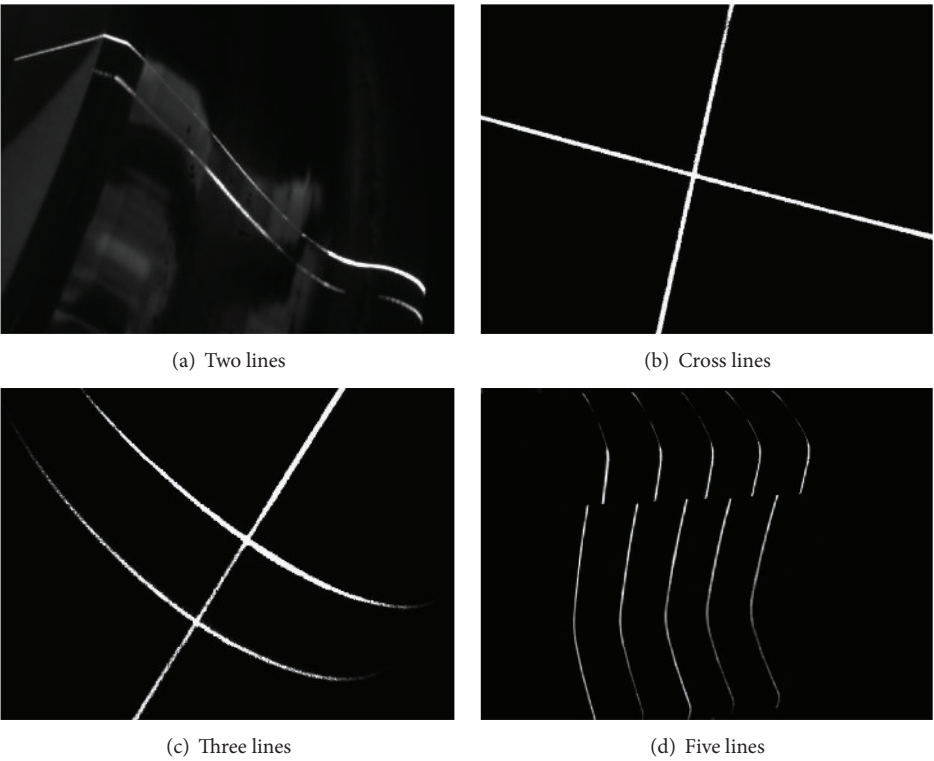
(a) Two lines

(b) Cross lines

(c) Three lines

(d) Five lines

FIGURE 6: Real example images to verify the efficiency.

(a)

(b)

(c)

(d)
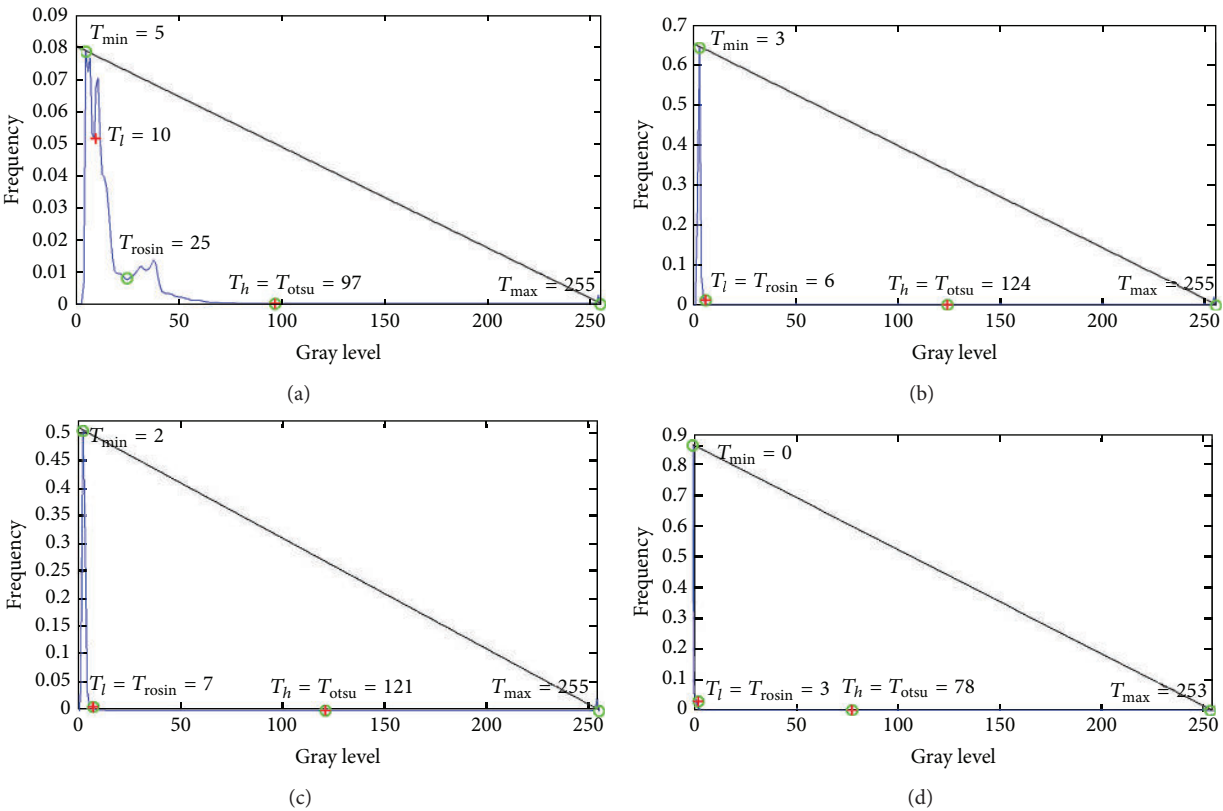
FIGURE 7: Selected thresholds for test images.

(a)

(b)

(c)

(d)

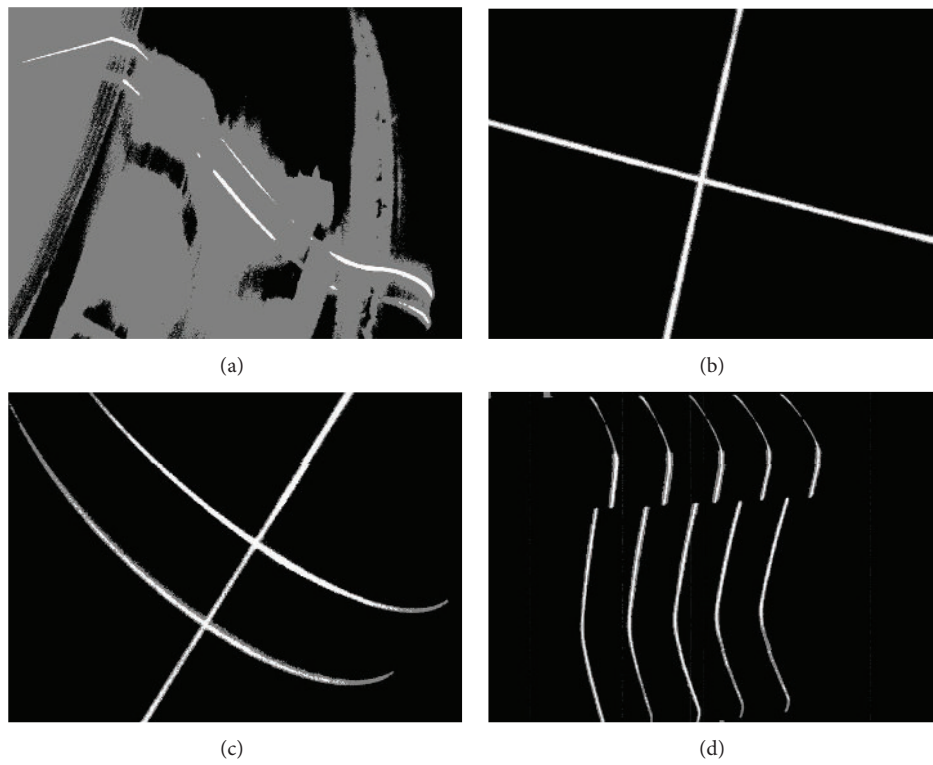FIGURE 8: Bilevel thresholding results of test images.

(a)

(b)

(c)

(d)
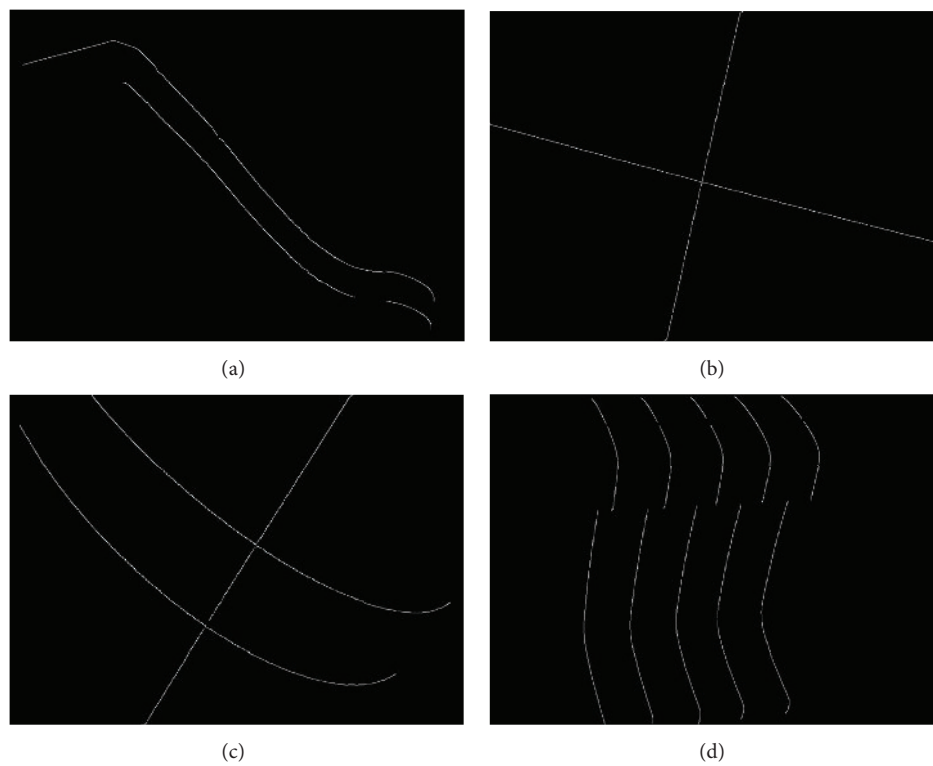
FIGURE 9: Line detection results of test images.

(a) Excluded pixels of Figure 6(a)

(b) Excluded pixels of Figure 6(b)

(c) Excluded pixels of Figure 6(c)

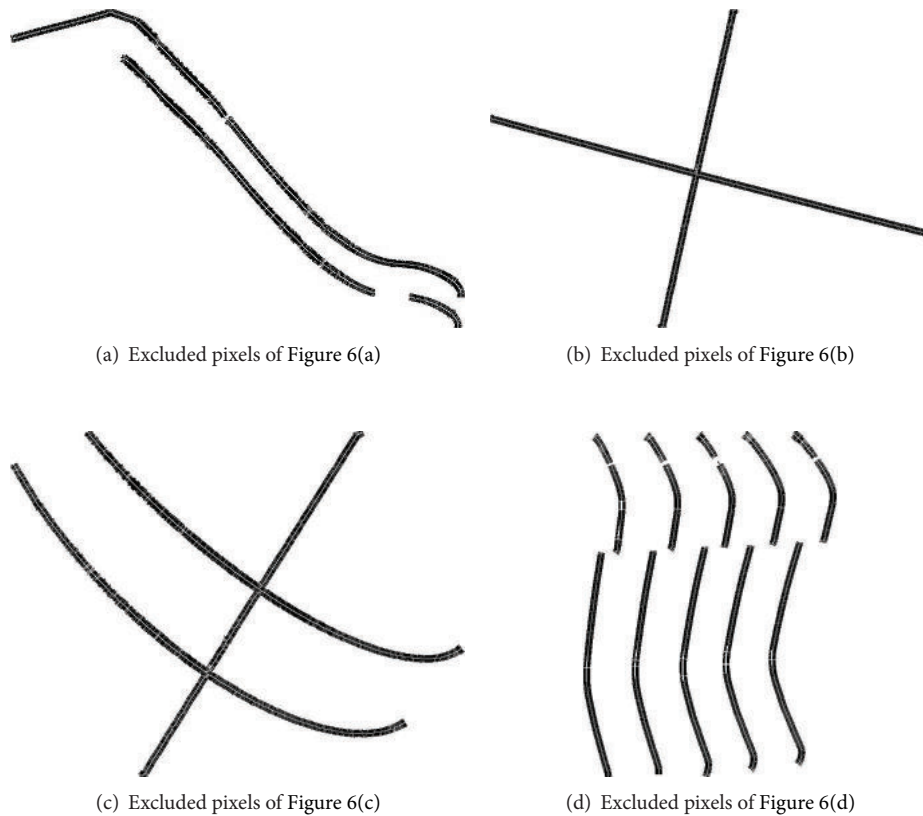(d) Excluded pixels of Figure 6(d)

FIGURE 10: Excluded pixels of the test images during processing.

algorithm. It is noticeable that most of the undesired pixels around the line points are excluded during the line detection process, and thus a lot of unnecessary calculations are eliminated in advance.

6. Conclusion

A direction-guided light stripe processing approach is presented. This method is characterized by its sound utilization of the local orientations of light stripes and has the following advantages. Firstly, the proposed method utilizes a bilevel thresholding method which not only ensures the integrality of uneven light stripes but also avoids blind calculations on undecided pixels. Secondly, the method retains the high accuracy of line point detection, since the point extraction algorithm is the same as the state-of-the-art one. Thirdly, the point detection and linking steps are combined tightly, and thus it is more flexible to do some specific operations such as selective processing without the need of extracting all the line points. Finally, the exclusion operations of undesired pixels successfully avoid a mass of unwanted calculations and bring a remarkable speedup. Although there may be several feature points missing when dealing with cross light stripes due to the exclusion operation, the data loss is extremely limited. As a whole, the proposed method may be more suitable to be applied in real-time structured light vision applications considering its high accuracy and great efficiency.

References

[1] P. Lavoie, D. Ionescu, and E. M. Petriu, "3-D object model recovery from 2-D images using structured light," *IEEE Transactions on Instrumentation and Measurement*, vol. 53, no. 2, pp. 437–443, 2004.

[2] Z. Liu, J. Sun, H. Wang, and G. Zhang, "Simple and fast rail wear measurement method based on structured light," *Optics and Lasers in Engineering*, vol. 49, no. 11, pp. 1343–1351, 2011.

[3] J. Xu, B. Gao, J. Han et al., "Realtime 3D profile measurement by using the composite pattern based on the binary stripe pattern," *Optics & Laser Technology*, vol. 44, no. 3, pp. 587–593, 2012.

[4] D. Geman and B. Jedynak, "An active testing model for tracking roads in satellite images," *IEEE Transactions on Pattern Analysis and Machine Intelligence*, vol. 18, no. 1, pp. 1–14, 1996.

[5] M. A. Fischler, "The perception of linear structure: a generic linker," in *Proceedings of the 23rd Image Understanding Workshop*, pp. 1565–1579, Morgan Kaufmann Publishers, Monterey, Calif, USA, 1994.

[6] D. Eberly, R. Gardner, B. Morse, S. Pizer, and C. Scharlach, "Ridges for image analysis," Tech. Rep. TR93-055, Department of Computer Science, University of North Carolina, Chapel Hill, NC, USA, 1993.

 [7] A. Busch, "A common framework for the extraction of lines and edges," *International Archives of the Photogrammetry and Remote Sensing*, vol. 31, part B3, pp. 88–93, 1996.

 [8] C. Steger, "An unbiased detector of curvilinear structures," *IEEE Transactions on Pattern Analysis and Machine Intelligence*, vol. 20, no. 2, pp. 113–125, 1998.

 [9] K. Hu, F. Zhou, and G. Zhang, "Fast extrication method for sub-pixel center of structured light stripe," *Chinese Journal of Scientific Instrument*, vol. 27, no. 10, pp. 1326–1329, 2006.

[10] F.-Q. Zhou, Q. Chen, and G.-J. Zhang, "Composite image processing for center extraction of structured light stripe," *Journal of Optoelectronics.Laser*, vol. 19, no. 11, pp. 1534–1537, 2008.

[11] N. Otsu, "A threshold selection method from gray-level histograms," *IEEE Transactions on Systems, Man, and Cybernetics*, vol. 9, no. 1, pp. 62–66, 1979.

[12] P. L. Rosin, "Unimodal thresholding," *Pattern Recognition*, vol. 34, no. 11, pp. 2083–2096, 2001.

Research Article

2-DOF Angle Measurement of Rocket Nozzle with Multivision

Yubo Guo,[1] Gang Chen,[2] Dong Ye,[2] Xiaoyu Yu,[2] and Feng Yuan[1]

[1] *Postdoctoral Research Station of Instrument Science and Technology Discipline, Harbin Institute of Technology,*
  P.O. Box 305, Harbin 150001, China
[2] *Department of Automatic Measurement & Control, Harbin Institute of Technology, P.O. Box 305, Harbin 150001, China*

Correspondence should be addressed to Dong Ye; yedong@hit.edu.cn

A real-time measurement method is presented for the 2-DOF swing angles of rocket nozzle by the use of multivision and rocket nozzle rotation axes. This method takes offline processing to measure the position of two nozzle rotation axes in image coordinate system by means of multi-vision and identify the rotation transformation relation between image coordinate system and fixed-nozzle coordinate system. During real-time measurement, the nozzle 2-DOF swing angles can be measured with transformation of marker coordinate from image coordinate system to fixed-nozzle coordinate system. This method can effectively resolve the problem of occlusion by markers in wide swing range of the nozzle. Experiments were conducted to validate its correctness and high measurement accuracy.

1. Introduction

To ensure the flight control, range, and impact point of rocket nozzle, it is important to measure the 2-DOF (Degree of Freedom) swing angles of the rocket engine nozzle [1, 2]. At present, the two angles are obtained with geometric transformation and conversion based on the angular displacement of motion servo control rod measured with rotary potentiometer during the cold and hot test run of the nozzle. It is an indirect measurement method and is much deviated from the actual nozzle motions [3]. Reference [4] proposes to measure the geometric parameters of the rocket engine with laser tracker. Laser tracker can achieve high measurement accuracy. However, it is difficult to make adjustment, and it is usually used for static measurement. Reference [5] measures the pitching angle and yawing angle with electronic theodolite for investigation on the swing angle calibration of rocket engine nozzle. With electronic theodolite, the measurement accuracy of the swing angles can be ensured, but the efficiency is low due to point-by-point measurement and cannot meet real-time measurement requirements. Reference [6] puts forward a multivision measurement for nozzle motion parameters. It uses high speed cameras to achieve proper real-time measurement. For measuring the nozzle motion

parameters, it adopts nozzle cone surface fitting method, which requires more markers and can only realize one-dimension swing angle measurement for the nozzle. What is more, the nozzle surface machining error and marker form error will certainly cause large measurement error.

Vision measurement shows broad application prospect in the field of measurement field [7–10] for its easy-to-move, noncontact, and real-time features. This paper presents a measurement method based on multivision and rocket nozzle rotation axes so as to improve the accuracy of vision-based measurement for rocket nozzle swing angles and to avoid occlusion problem during measurement.

2. Multivision Measurement Model of Nozzle Motion

The coordinate systems for the multivision measurement of rocket nozzle swing angles are shown in Figure 1, including image coordinate systems $o_1 x_1 y_1, \ldots, o_m x_m y_m$ (where m is the number of cameras), world coordinate system $o_w x_w y_w z_w$, fixed-nozzle coordinate system $o_{n0} x_{n0} y_{n0} z_{n0}$, and dynamic nozzle coordinate system $o_{nd} x_{nd} y_{nd} z_{nd}$.
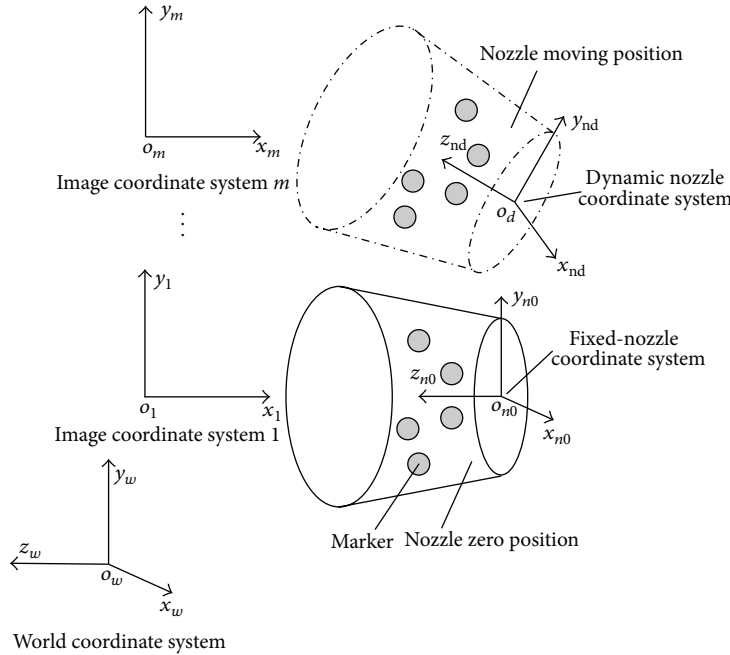
FIGURE 1: Coordinate systems.

In image coordinate system, the origin is at the intersection point of optical axis and image plane, the coordinate axes are parallel to the lines and rows, respectively, and the markers are imaged at the two cameras. The image coordinate of marker center can be obtained by image processing. The coordinate of marker centers in world coordinate system and in image coordinate system conforms to vision image relation. With camera calibration, the coordinate in world system can be obtained from the image coordinate. The fixed-nozzle coordinate system is defined as a fixed coordinate system with nozzle at zero position, and the nozzle motion consists of translation in three directions relative to origin (rotation center) o_{n0} and swing angles around axes x_{n0} and y_{n0}. The dynamic nozzle coordinate system $o_{nd}x_{nd}y_{nd}z_{nd}$ is fixed on the nozzle, and it coincides with $o_{n0}x_{n0}y_{n0}z_{n0}$ while the nozzle is at zero position. The swing angles of the nozzle can be determined by the use of the transformation relations between coordinate systems $o_{nd}x_{nd}y_{nd}z_{nd}$ and $o_{n0}x_{n0}y_{n0}z_{n0}$. The measurements of nozzle swing angles can be divided into two stages. The first stage is offline processing, including defining the transformation relation between fixed-nozzle coordinate system and world

coordinate system and obtaining the coordinate of marker center in fixed-nozzle coordinate system while, nozzle is at zero. The second stage is real-time measurement, consisting of the following steps: firstly, take 3 or more marker centers image coordinates and employ vision image relation to complete marker measurement in world coordinate system; secondly, transform the marker coordinate from world coordinate system to fixed-nozzle coordinate system; finally, calculate nozzle swing angles according to marker coordinate in fixed-nozzle coordinate systems and values at zero position. The multivision coordinate measurement model, fixed-nozzle coordinate system model, and swing angle measurement model are established as below.

2.1. Multivision Coordinate Measurement. Set the world coordinate of the center of marker $i(\leqslant n)$ at $(x_{w,i}, y_{w,i}, z_{w,i})$, and the corresponding image point on camera j $(\leqslant m)$ at $(x_{j,i}, y_{j,i})$; then, at the pinhole model, it gives

$$AP = E, \tag{1}$$

where,

$$P = \begin{bmatrix} x_{w,i} & y_{w,i} & z_{w,i} \end{bmatrix}^T, \tag{2}$$

$$E = \begin{bmatrix} f_1 t_{1,x} - t_{1,z} x_{1,i} & f_1 t_{1,y} - t_{1,z} y_{1,i} & \cdots & f_m t_{m,x} - t_{m,z} x_{m,i} & f_m t_{m,y} - t_{m,z} y_{m,i} \end{bmatrix}_{2m \times 1}^T,$$

$$A = \begin{bmatrix} r_{1,31} x_{1,i} - f_1 r_{1,11} & r_{1,32} x_{1,i} - f_1 r_{1,12} & r_{1,33} x_{1,i} - f_1 r_{1,13} \\ r_{1,31} y_{1,i} - f_1 r_{1,21} & r_{1,32} y_{1,i} - f_1 r_{1,22} & r_{1,33} y_{1,i} - f_1 r_{1,23} \\ \vdots & \vdots & \vdots \\ r_{m,31} x_{2,i} - f_m r_{m,11} & r_{m,32} x_{m,i} - f_m r_{m,12} & r_{m,33} x_{m,i} - f_m r_{m,13} \\ r_{m,31} y_{2,i} - f_m r_{m,21} & r_{m,32} y_{m,i} - f_m r_{m,22} & r_{m,33} y_{m,i} - f_m r_{m,23} \end{bmatrix}_{2m \times 3}. \tag{3}$$

The viable $f_1, f_m, r_{j,11}, \ldots, r_{j,33}, t_{j,x}, t_{j,y}, t_{j,z}$ is defined by camera calibration.

Apply the least square method to (1) to obtain the world coordinate of the center of marker i as follows:

$$P = \left(A^T A\right)^{-1} A^T E. \tag{4}$$

2.2. Fixed-Nozzle Coordinate System Model. Rocket nozzle can rotate by certain angle around axes x_{n0} and y_{n0}, respectively. Therefore, the position of these axes in the world coordinate system can be defined with multivision, and the fixed-nozzle coordinate model can be accordingly established as follow.

Given axis x_{n0} across point $Q(x_0, y_0, z_0)$, unit vector $\mathbf{e} = (e_x, e_y, e_z)$, the world coordinate of n markers on nozzle $P_1(x_1, y_1, z_1), P_2(x_2, y_2, z_2), \ldots, P_n(x_n, y_n, z_n)$, after rotating around axis x_{n0} by angle θ, the world coordinate is $P_1'(x_1', y_1', z_1'), P_2'(x_2', y_2', z_2'), P_n'(x_n', y_n', z_n')$. Then,

$$\begin{bmatrix} x_1' - x_1 & y_1' - y_1 & z_1' - z_1 \\ x_2' - x_2 & y_2' - y_2 & z_2' - z_2 \\ \vdots & \vdots & \vdots \\ y_n' - y_n & y_n' - y_n & z_n' - z_n \end{bmatrix} \begin{bmatrix} e_x \\ e_y \\ e_z \end{bmatrix} = s \begin{bmatrix} 1 \\ 1 \\ \vdots \\ 1 \end{bmatrix}, \tag{5}$$

where s is the nozzle displacement along the axis during rotation. Equation (5) is denoted as

$$H\mathbf{e}^T = sD. \tag{6}$$

According to [11], $\mathbf{e}$ and θ are calculated by

$$\mathbf{e}^T = \frac{1}{\left|(H^T H)^{-1} H^T D\right|}\left(H^T H\right)^{-1} H^T D, \tag{7}$$

$$\cos\theta = \frac{\overrightarrow{P_1 P_2} \times \mathbf{e}}{\left|\overrightarrow{P_1 P_2} \times \mathbf{e}\right|} \cdot \frac{\overrightarrow{P_1' P_2'} \times \mathbf{e}}{\left|\overrightarrow{P_1' P_2'} \times \mathbf{e}\right|},$$

$$\tag{8}$$

$$\mathbf{e}\sin\theta = \frac{\overrightarrow{P_1 P_2} \times \mathbf{e}}{\left|\overrightarrow{P_1 P_2} \times \mathbf{e}\right|} \times \frac{\overrightarrow{P_1' P_2'} \times \mathbf{e}}{\left|\overrightarrow{P_1' P_2'} \times \mathbf{e}\right|}.$$

Then, the least square solution of $\mathbf{Q}$ is

$$\mathbf{Q} = \left(B^T B\right)^{-1} B^T C. \tag{12}$$

Thus, we can obtain unit vector of axis x_{n0} and any point on the axis by (7) and (12). Define y_{n0} similarly. Then, define z_{n0} with right hand rules. The intersection point of axes x_{n0}, y_{n0}, and z_{n0} is the rotation center of the nozzle, and the three

Given a point $Q(x_0, y_0, z_0)$ on the axis, taking $z_0 = 0$, we can deduce that $Q(x_0, y_0, z_0)$, world coordinate of n markers before and after rotation, displacement s, rotation angle θ, and unit vector $\mathbf{e}$ satisfy the following relations:

$$BQ = C, \tag{9}$$

where B, Q, and C are expressed as

$$B = \begin{bmatrix} (1 - r_{11}(e, \theta)) & (0 - r_{12}(e, \theta)) \\ (0 - r_{21}(e, \theta)) & (1 - r_{22}(e, \theta)) \\ (0 - r_{31}(e, \theta)) & (0 - r_{32}(e, \theta)) \\ \vdots & \vdots \\ (1 - r_{11}(e, \theta)) & (0 - r_{12}(e, \theta)) \\ (0 - r_{21}(e, \theta)) & (1 - r_{22}(e, \theta)) \\ (0 - r_{31}(e, \theta)) & (0 - r_{32}(e, \theta)) \end{bmatrix},$$

$$Q = \begin{bmatrix} x_0 \\ y_0 \end{bmatrix}, \tag{10}$$

$$C = \begin{bmatrix} x_1' - se_x - x_1 r_{11}(e, \theta) - y_1 r_{12}(e, \theta) - z_1 r_{13}(e, \theta) \\ y_1' - se_y - x_1 r_{21}(e, \theta) - y_1 r_{22}(e, \theta) - z_1 r_{23}(e, \theta) \\ z_1' - se_z - x_1 r_{31}(e, \theta) - y_1 r_{32}(e, \theta) - z_1 r_{33}(e, \theta) \\ \vdots \\ x_n' - se_x - x_n r_{11}(e, \theta) - y_n r_{12}(e, \theta) - z_n r_{13}(e, \theta) \\ y_n' - se_y - x_n r_{21}(e, \theta) - y_n r_{22}(e, \theta) - z_n r_{23}(e, \theta) \\ z_n' - se_z - x_n r_{31}(e, \theta) - y_n r_{32}(e, \theta) - z_n r_{33}(e, \theta) \end{bmatrix},$$

where $r_{ij}(e, \theta)$ is the element of matrix $R(e, \theta)_{3 \times 3}$ and $R(e, \theta)_{3 \times 3}$ is expressed as

$$R(e, \theta)_{3\times 3} = \begin{bmatrix} e_x^2 (1 - \cos\theta) + \cos\theta & e_x e_y (1 - \cos\theta) - e_z \sin\theta & e_x e_z (1 - \cos\theta) + e_y \sin\theta \\ e_x e_y (1 - \cos\theta) + e_z \sin\theta & e_y^2 (1 - \cos\theta) + \cos\theta & e_y e_z (1 - \cos\theta) - e_x \sin\theta \\ e_x e_z (1 - \cos\theta) - e_y \sin\theta & e_y e_z (1 - \cos\theta) + e_x \sin\theta & e_z^2 (1 - \cos\theta) + \cos\theta \end{bmatrix}. \tag{11}$$

unit vectors are row vectors of rotation transformation matrix R of world coordinate system and fixed-nozzle coordinate system, while rotation center coordinate T is translation vector.

2.3. Swing Angle Measurement. Matrix R and vector T are used to denote the transformation relation between
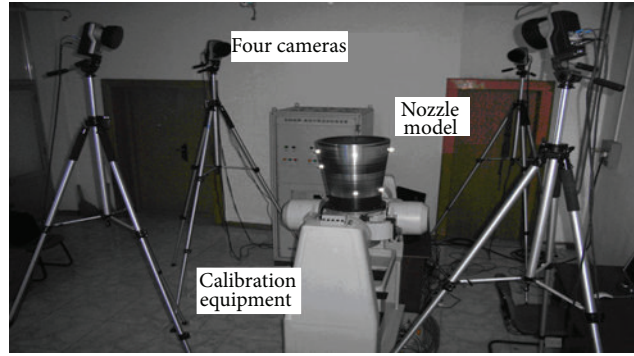
FIGURE 2: Multivision measurement system for swing angles of nozzle.
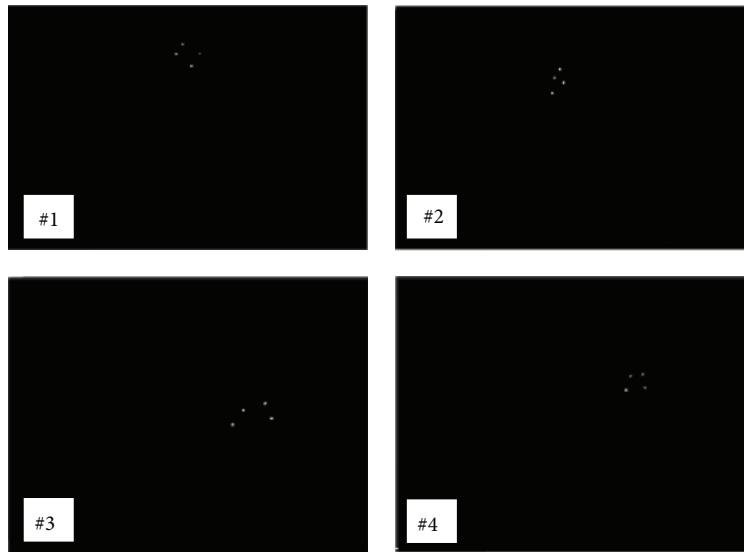

FIGURE 3: Marker images at a given time.

fixed coordinate system and world coordinate system. Suppose that the world coordinate of marker i is $P_{w0,i}(x_{w0,i}, y_{w0,i}, z_{w0,i})$ when the nozzle is at zero position, and $P_{wd,i}(x_{wd,i}, y_{wd,i}, z_{wd,i})$ when moving to a certain position. Then, the corresponding coordinates $P_{n0,i}(x_{n0,i}, y_{n0,i}, z_{n0,i})$ and $P_{nd,i}(x_{nd,i}, y_{nd,i}, z_{nd,i})$ in fixed-nozzle coordinate system, respectively, satisfy

$$
\begin{bmatrix} x_{n0,i} \\ y_{n0,i} \\ z_{n0,i} \end{bmatrix} = R \begin{bmatrix} x_{w0,i} \\ y_{w0,i} \\ z_{w0,i} \end{bmatrix} + T,
$$

$$
\begin{bmatrix} x_{nd,i} \\ y_{nd,i} \\ z_{nd,i} \end{bmatrix} = R \begin{bmatrix} x_{wd,i} \\ y_{wd,i} \\ z_{wd,i} \end{bmatrix} + T. \tag{13}
$$

The swing angles α_x and α_y of the nozzle around axes x_{n0} and y_{n0} satisfy

$$
\begin{bmatrix} x_{nd,i} \\ y_{nd,i} \\ z_{nd,i} \end{bmatrix} = \begin{bmatrix} \cos\alpha_y & \sin\alpha_y \sin\alpha_x & -\sin\alpha_y \cos\alpha_x \\ 0 & \cos\alpha_x & \sin\alpha_x \\ \sin\alpha_y & -\cos\alpha_y \sin\alpha_x & \cos\alpha_y \cos\alpha_x \end{bmatrix}
$$

$$
\times \begin{bmatrix} x_{n0,i} \\ y_{n0,i} \\ z_{n0,i} \end{bmatrix} + \begin{bmatrix} m_x \\ m_y \\ m_z \end{bmatrix}, \tag{14}
$$

where (m_x, m_y, m_z) is the translation in three directions of the rotation center.

Equation (14) is a nonlinear equation set for swing angle. When there are three or more markers and not all the markers are in the same line, the Gauss-Newton method can be used for iteration solution.

3. Experimental Results

Figure 2 shows the multivision measurement system for swing angles of the nozzle. Four high speed cameras with infrared emitter and infrared filter are used as a multivision angle measurement system. Nozzle swing angles are simulated with dual axes rotating calibration equipment. The calibration equipment has high motion accuracy and can be used as motion reference. Infrared reflecting markers are arranged on the surface of the calibration equipment.

Table 1: Contrast results of geometrical parameters.

Maximum measurement error (°)	Optical axis angle				
	30°	45°	60°	75°	90°
Baseline length (m)					
3	0.51	0.36	0.26	0.22	0.19
4	0.68	0.48	0.35	0.29	0.25

Table 2: Contrast results of different numbers of markers.

	Number of markers				
	4	5	6	7	8
Maximum measurement error (°)	0.51	0.36	0.26	0.22	0.19

Table 3: Swing angle measurement error (°).

$(\delta\alpha_x, \delta\alpha_y)$	Swing angle α_x				
	−20	−10	0	10	20
Swing angle α_y					
−20	(0.16, 0.11)	(0.14, 0.10)	(0.12, 0.08)	(0.13, 0.11)	(0.15, 0.13)
−10	(0.12, 0.10)	(0.11, 0.11)	(0.10, 0.09)	(0.11, 0.10)	(0.11, 0.12)
0	(0.05, 0.04)	(0.04, 0.06)	(0.03, 0.04)	(0.08, 0.07)	(0.06, 0.05)
10	(0.07, 0.08)	(0.05, 0.07)	(0.04, 0.06)	(0.05, 0.06)	(0.11, 0.12)
20	(0.09, 0.11)	(0.08, 0.09)	(0.07, 0.08)	(0.07, 0.11)	(0.18, 0.17)

The exposure and data acquisition of four cameras are the synchronous by synchronous control system, and the Ethernet is used to realize data transmission between the four cameras and the host computer.

Experiments are conducted by using ball markers with infrared reflecting surface. These markers will generate highlighted spots at image plane. The marker image can be separated from the background by grey scale threshold setting. During the movement of the nozzle by large angle, the markers may be sheltered. The markers will be considered effective only when their image can be identified by two or more cameras. Otherwise, they will not be involved in the measuring process. The method in this paper can achieve 2-DOF angle measurement when 3 or more effective markers are identified. Figure 3 shows the marker image identification results at a given time. And in this case, all the cameras numbers 1, 2, 3, and 4 can identify four markers.

3.1. Contrast Experiments for Geometrical Parameters of Cameras. The main parameters representing the geometrical configuration of cameras consist of camera focus, baseline length, and angle between optical axes of two cameras. Since the camera focus in the experiments is fixed as 24 mm, the effects of optical axis angle and baseline length are discussed as follows.

The cameras are arranged at circumference and in such a way that the baseline length and the optical axis angle of any adjacent cameras are the same (with optical axis oriented to the center of measurement field of view). Put 8 markers on the nozzle surface, let the nozzle make 2-DOF movement by ±20°, and take measurements at 1000 equally spaced positions. The maximum measurement errors are shown in Table 1.

The experiment results show that the system achieves the highest measurement accuracy at 90° optimal axis angle and 3 m baseline length.

3.2. Contrast Experiments for Different Numbers of Markers. Different marker numbers will affect the measurement accuracy. When the nozzle makes 2-DOF movement by ±20°, measurements are taken at 1000 equally-spaced positions with the cameras arranged at 90° optimal axis angle and 3 m baseline length. The maximum measurement errors are shown in Table 2.

Above, Table 2 shows that the system measurement accuracy can be improved by increasing the number of markers.

Rotate the calibration equipment in 2-DOF by angle within ±20° with 90° optical axis angle and 3 m baseline length in case of 8 markers, and take real-time measurements at several positions with the method stated in this paper. Table 3 lists the absolute value of measurement errors of rotation angle, in which $\delta\alpha_x$, $\delta\alpha_y$ denote the angle errors at given position in two directions, respectively. The Table shows that the maximum measurement error of swing angle is 0.18°. And the results confirm that this method can achieve high accuracy of 2-DOF angle measurement.

4. Conclusion

This paper presents a real-time measurement method for swing angles of the rocket nozzle by means of multivision and rocket nozzle rotation axes. The experimental results show that this method can achieve a measurement accuracy that

is better than 0.2° in ±20° angle range with 90° optical axis angle and 3 m baseline length in case of 8 markers. It is greatly significant for the actual measurement of swing angles of the rocket nozzle.

Acknowledgments

References

[1] I. V. Sorokin and A. V. Markov, "Utilization of space stations: 1971–2006," *Journal of Spacecraft and Rockets*, vol. 45, no. 3, pp. 600–607, 2008.

[2] B. Burchett and M. Costello, "Model predictive lateral pulse jet control of an atmospheric rocket," *Journal of Guidance, Control, and Dynamics*, vol. 25, no. 5, pp. 860–867, 2002.

[3] Z. Yongbin, "Discussion on control precision of single swing nozzle," *Modern Defence Technology*, vol. 35, no. 3, pp. 54–57, 2007.

[4] C. F. Zhang, W. Y. Tang, H. P. Li, J. Wang, and J. C. Chen, "Application of laser tracker to thrust line measurement of solid rocket motor," *Journal of Solid Rocket Technology*, vol. 30, no. 6, pp. 548–551, 2007.

[5] X. Ma and X. Liu, "Swing angle calibration method of SRM nozzle," *Journal of Astronautic Metrology and Measurement*, vol. 28, no. 5, pp. 38–42, 2008.

[6] L. F. Zhang, Y. B. Guo, G. Chen, D. Ye, and R. S. Che, "Estimation of nozzle axis and vector angle by infrared photoelectric measurement technology," *Journal of Harbin Institute of Technology*, vol. 42, no. 1, pp. 24–28, 2010.

[7] T. Pinto, C. Kohler, and A. Albertazzi, "Regular mesh measurement of large free form surfaces using stereo vision and fringe projection," *Optics and Lasers in Engineering*, vol. 50, no. 7, pp. 910–916, 2012.

[8] M. Ceccarelli, A. Speranza, D. Grimaldi, and F. Lamonaca, "Automatic detection and surface measurements of micronucleus by a computer vision approach," *IEEE Transactions on Instrumentation and Measurement*, vol. 59, no. 9, pp. 2383–2390, 2010.

[9] Y. Zhang, S. Wang, X. Zhang, F. Xie, and J. Wang, "Freight train gauge-exceeding detection based on three-dimensional stereo vision measurement," *Machine Vision and Applications*, vol. 24, no. 3, pp. 461–475, 2013.

[10] G. Chen, Y. Guo, H. Wang, D. Ye, and Y. Gu, "Stereo vision sensor calibration based on random spatial points given by CMM," *Optik*, vol. 123, no. 8, pp. 731–734, 2012.

[11] G. Yubo, Y. Dong, C. Gang, and Y. Feng, "Binocular vision-based measurement for motion parameters of rocket nozzle," *Applied Mechnics and Materials*, vol. 220–223, pp. 1056–1061, 2012.

Research Article
A New Method to Calibrate Robot Visual Measurement System

Yali Wang, Zhenzhong Wei, Mingwei Shao, and Guangjun Zhang

Key Laboratory of Precision Opto-Mechatronics Technology, Beihang University, Ministry of Education, Beijing 100191, China

Correspondence should be addressed to Yali Wang; wangyali_buaa@163.com

This paper presents a new method to calibrate the robot visual measurement system. In the paper, a laser tracker is used to calibrate the robot twist angles. Each axis of the robot is moved to many positions and the positions measured by the laser tracker fit a plane. The normal vectors of the planes are the directions of the Z axes. According to the definition of the robot kinematics model parameters, the errors of the twist angles can be calculated. The joint angles zero offsets are calibrated by the constraint that the rotation relationship between the world frame and the robot base frame is relatively constant. A planar target with several parallel lines is used to obtain the pose of the camera relative to the planar target by the lines in the target plane and the vanishing line of the plane. The quantum behaved particle swarm optimization (QPSO) algorithm is used to calculate the parameters. Experiments are performed and the results show that the accuracy of the robot visual measurement system is improved about 10 times after being calibrated.

1. Introduction

3D surface topography measurement and the aiming and positioning of the butt joint are key technology in large scale equipment manufacture and assemble process. With the developing of computer vision technology, visual measurement system as a kind of noncontact measurement method is used more and more widely. Besides noncontact, it has the advantages of high measuring precision and measuring speed. When the tested objects have fixed testing characteristics, or are mass produced, the framework structure is used. But, with the increase of the structure complexity and high machining precision requirement of mechanical parts, the demand to measuring is more and more strict. The framework structure cannot meet the measuring requirement. A flexible measurement system which can measure any part of the tested object is needed. Robot visual measurement system is a combination of robot and visual measurement system. Robot vision is seen to be the most important sensory ability for the robot [1]. Cameras fixed on the robot arm allow it not only to have the robot advantages of large flexible global motion but also to have the advantages of the visual measurement system.

Generally, industrial robots have high repeatability but low absolute accuracy, and the characteristic of the robot makes robot visual measurement systems cannot meet the requirement in some situations. Therefore, it is important to improve the absolute accuracy to enhance the measuring accuracy of robot visual measurement systems. Five error sources are known to lead to robot inaccuracy, such as errors in geometrical parameters, environment, measurement, calculation, and use. The geometrical parameter errors are the dominant error source which account for 90% of the errors [2]. So it is important to identify the geometrical parameter errors. There are a lot of researches about robot calibration [3–10], and most of them are based on the distance constraint. On this occasion, although the robot kinematical parameters are calibrated, the results are inaccurate without using the rotation constraint sufficiently. In the paper, the rotation constraint is introduced. The pose of the world frame relative to the camera frame can be obtained by a planar target with parallel lines using the features of the vanishing points and vanishing lines.

For the robot visual measurement system, it is important to know the relationship between the robot and the camera, which is called the hand-eye calibration. The hand-eye

calibration methods are mature [11–14], and most of them are solved by the equation $AX = XB$. The rotation is calculated first, and then the translations are attained. So, in the paper, the procedure of calculating the hand-eye relationship is not introduced.

For most conventional optimization methods, for example, least squared algorithm [15], which is based on quadratic error functions, the iterative initial values have a great contribution to the results. That means that the optimization results are not the global optimum while they are just the approximate extreme points in the solution space. Now that the traditional methods cannot deal with nonlinear systems effectively, some new methods drawn from the field of biology are proposed to be the alternation. Genetic algorithms (GA) [16–19], artificial neural networks [20–22], and particle swarm optimization algorithm [23, 24] are used to identify parameters to improve the robot accuracy. Hassan et al. [25] had proved that the particle swarm optimization algorithm had better optimization capability than other optimization algorithms. Though the PSO [26] algorithm can solve some problems efficiently, it has disadvantage that it does not guarantee the global optimum [27, 28]. To overcome the shortcoming, the QPSO algorithm is proposed [29]. In the paper, the QPSO algorithm is used to obtain the real joint angles zero offsets.

According to the D-H model, the rotation of the transformation from the robot end effector to the robot base frame is only related to the robot twist angles and joint angles. So the twist angles and the joint angles can be calibrated using the rotation constraint. The errors from twist angles and joint angles have more contributions to the robot accuracy than link lengths and link joint offsets. So the proposed method is a simple way to calibrate robot when the measuring requirement is not too strict.

This paper is organized as follows. The calibration principle will be presented in Section 2. Experiment results will be shown in Section 3, and the conclusion will be provided in Section 4.

2. Calibration Principle

As shown in Figure 1, there is a camera fixed on the robot end effector. The camera frame is denoted by F_c. The world frame is created on the left top corner of the planar target, which has black and white lines on it, and is denoted by F_w. The robot base frame F_r and the world frame F_w are relatively stationary. The camera is moved to different positions with the robot, and the transformations ${}^rT_c$ and ${}^cT_w$ are changed at the same time. But the product of the two matrices is constant, where ${}^cT_w$ is the transformation from the world frame F_w to the camera frame F_c and ${}^rT_c$ is the transformation from the camera frame F_c to the robot base frame F_r, which is the product of the transformations T_6 and T_h.

2.1. Calibration of Twist Angles. According to the definition of the kinematical parameters of D-H model, the twist angle describes the angle between two Z axes of the adjacent links. When the robot is given, the twist angles are determinate. So
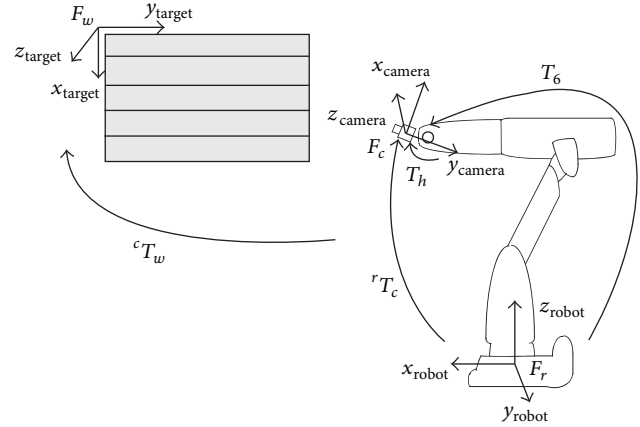

FIGURE 1: Robot visual measurement system calibration model.

the real Z axes should be determined first to calibrate the twist angles. A laser tracker is used to measure the real Z axes directions of the robot. The reflector is fixed on the robot end effector, and the first axis of the robot is moved in the joint angle range uniformly. The motion curve of the reflector is a spatial circular arc, and the normal vector of the arc plane is the direction of the robot first link Z axis.

Suppose that the positions of the reflector are (x_1^i, y_1^i, z_1^i), where i is the ith position when the first axis is moved. Then, the plane can be written as

$$a_1 x_1^i + b_1 y_1^i + c_1 z_1^i + d_1 = 0, \tag{1}$$

where $v_1 = (a_1, b_1, c_1)$ is the unit normal vector of the plane fitted by the positions (x_1^i, y_1^i, z_1^i). And it is also the direction of the first link Z axis.

The same operations are performed to the rest links, and the directions of the Z axes are obtained and denoted as $v_{\text{axis}} = (a_{\text{axis}}, b_{\text{axis}}, c_{\text{axis}})(\text{axis} = 2, 3, 4, 5, 6)$.

So the angle between the first and the second links can be obtained as

$$\alpha = \arccos(v_1 \cdot {*} v_2). \tag{2}$$

The sign can be determined by the definition of the twist angle. Therefore, the real twist angle can be written as

$$\alpha_1' = (\text{sign})\,\alpha. \tag{3}$$

The rest twist angles can be attained as (2) and (3), and the twist angles errors can be obtained as follows:

$$
\begin{aligned}
\Delta\alpha_1 &= \alpha_1' - \alpha_1, \\
\Delta\alpha_2 &= \alpha_2' - \alpha_2, \\
\Delta\alpha_3 &= \alpha_3' - \alpha_3, \\
\Delta\alpha_4 &= \alpha_4' - \alpha_4, \\
\Delta\alpha_5 &= \alpha_5' - \alpha_5, \\
\Delta\alpha_6 &= \alpha_6' - \alpha_6,
\end{aligned}
\tag{4}
$$

No.	Joint angle range $\theta/°$	Link joint offset d/mm	Link length a/mm	Link twist angle $\alpha/°$
1	−170~170	475	150	−90
2	−70~70	0	600	0
3	−65~70	0	120	90
4	−150~170	720	0	−90
5	−115~115	0	0	90
6	−300~300	85	0	0

where α_i', α_i, and $\Delta\alpha_i$ $(i = 1, 2, \ldots 6)$ are the true value, the ideal value, and the error of the twist angles.

But it is worth noting that there is a link gear between the link 2 and link 3. When the link 2 is moved, the link 3 is moved at the same time. But it is not the same for the reverse condition. So when the operation is performed to the link 2, the reflector should be fixed on the arm of the link 2, rather than on the robot end effector.

2.2. Calibration of Joint Angles. The resolution of the robot axes is about $0.01°$, so the errors from the recorders can be ignored. The joint angles errors mentioned there mean errors of the joint angle zero offsets.

The robot base frame F_r and the world frame F_w are relatively stationary. Therefore, there is a constant equation as

$$^{r}T_w = \,^{r}T_c * \,^{c}T_w = T_6 * T_h * \,^{c}T_w, \tag{5}$$

where the matrix T_h is the hand-eye relationship transformation, which has been obtained already. The matrices T_6 and $^{c}T_w$ are variable with the robot moving.

According to (5), we have

$$^{r}R_w = R_6 * R_h * \,^{c}R_w, \tag{6}$$

where $^{r}R_w$, R_6, R_h, and $^{c}R_w$, are the rotations of the transformations $^{r}T_w$, T_6, T_h, and $^{c}T_w$.

2.2.1. Solving R_6. The robot is a six-degree-of-freedom serial industrial robot. According to the D-H model, the pose and position of each link can be expressed as (7). The kinematical parameters are shown in Table 1. Consider

$$^{r}T_1 = \begin{bmatrix} c\theta_1 & -c\left(\alpha_1 - \dfrac{\pi}{2}\right)*s\theta_1 & s\left(\alpha_1 - \dfrac{\pi}{2}\right)*s\theta_1 & a_1*c\theta_1 \\ s\theta_1 & c\left(\alpha_1 - \dfrac{\pi}{2}\right)*c\theta_1 & -s\left(\alpha_1 - \dfrac{\pi}{2}\right)*c\theta_1 & a_1*s\theta_1 \\ 0 & s\left(\alpha_1 - \dfrac{\pi}{2}\right) & c\left(\alpha_1 - \dfrac{\pi}{2}\right) & d_1 \\ 0 & 0 & 0 & 0 \end{bmatrix},$$

$$^{1}T_2 = \begin{bmatrix} c\left(\theta_2 - \dfrac{\pi}{2}\right) & -c(\alpha_2)*s\left(\theta_2 - \dfrac{\pi}{2}\right) & s(\alpha_2)*s\left(\theta_2 - \dfrac{\pi}{2}\right) & a_2*c\left(\theta_2 - \dfrac{\pi}{2}\right) \\ s\left(\theta_2 - \dfrac{\pi}{2}\right) & c(\alpha_2)*c\left(\theta_2 - \dfrac{\pi}{2}\right) & -s(\alpha_2)*c\left(\theta_2 - \dfrac{\pi}{2}\right) & a_2*s\left(\theta_2 - \dfrac{\pi}{2}\right) \\ 0 & s(\alpha_2) & c(\alpha_2) & d_2 \\ 0 & 0 & 0 & 1 \end{bmatrix},$$

$$^{2}T_3 = \begin{bmatrix} c(\theta_3 - \theta_2) & -c\left(\alpha_3 - \dfrac{\pi}{2}\right)*s(\theta_3 - \theta_2) & s\left(\alpha_3 - \dfrac{\pi}{2}\right)*s(\theta_3 - \theta_2) & a_3*c(\theta_3 - \theta_2) \\ s(\theta_3 - \theta_2) & c\left(\alpha_3 - \dfrac{\pi}{2}\right)*c(\theta_3 - \theta_2) & -s\left(\alpha_3 - \dfrac{\pi}{2}\right)*c(\theta_3 - \theta_2) & a_3*s(\theta_3 - \theta_2) \\ 0 & s\left(\alpha_3 - \dfrac{\pi}{2}\right) & c\left(\alpha_3 - \dfrac{\pi}{2}\right) & d_3 \\ 0 & 0 & 0 & 1 \end{bmatrix},$$

$$^{3}T_4 = \begin{bmatrix} c\theta_4 & -c\left(\alpha_4 + \dfrac{\pi}{2}\right)*s\theta_4 & s\left(\alpha_4 + \dfrac{\pi}{2}\right)*s\theta_4 & a_4*c\theta_4 \\ s\theta_4 & c\left(\alpha_4 + \dfrac{\pi}{2}\right)*c\theta_4 & -s\left(\alpha_4 + \dfrac{\pi}{2}\right)*c\theta_4 & a_4*s\theta_4 \\ 0 & s\left(\alpha_4 + \dfrac{\pi}{2}\right) & c\left(\alpha_4 + \dfrac{\pi}{2}\right) & d_4 \\ 0 & 0 & 0 & 1 \end{bmatrix},$$

$$
^4T_5 = \begin{bmatrix} c\left(\theta_5 + \pi\right) & -c\left(\alpha_5 + \dfrac{\pi}{2}\right) * s\left(\theta_5 + \pi\right) & s\left(\alpha_5 + \dfrac{\pi}{2}\right) * s\left(\theta_5 + \pi\right) & a_5 * c\left(\theta_5 + \pi\right) \\[2mm] s\left(\theta_5 + \pi\right) & c\left(\alpha_5 + \dfrac{\pi}{2}\right) * c\left(\theta_5 + \pi\right) & -s\left(\alpha_5 + \dfrac{\pi}{2}\right) * c\left(\theta_5 + \pi\right) & a_5 * s\left(\theta_5 + \pi\right) \\[2mm] 0 & s\left(\alpha_5 + \dfrac{\pi}{2}\right) & c\left(\alpha_5 + \dfrac{\pi}{2}\right) & d_5 \\[2mm] 0 & 0 & 0 & 1 \end{bmatrix},
$$

$$
^5T_6 = \begin{bmatrix} c\theta_6 & -c\alpha_6 * s\theta_6 & s\alpha_6 * s\theta_6 & a_6 * c\theta_6 \\[1mm] s\theta_1 & c\alpha_6 * c\theta_6 & -s\alpha_6 * c\theta_6 & a_6 * s\theta_6 \\[1mm] 0 & s\alpha_6 & c\alpha_6 & d_6 \\[1mm] 0 & 0 & 0 & 1 \end{bmatrix},
$$

$$(7)$$

where $c\theta$ is the cosine value of the angle θ and $s\theta$ is the sine value of the angle θ.

The transformation from the robot end effector to the robot base frame can be written as

$$
T_6 = {}^rT_1 * {}^1T_2 * {}^2T_3 * {}^3T_4 * {}^4T_5 * {}^5T_6. \tag{8}
$$

From (7), we can see that R_6 is only determined by the twist angles α and the joint angles θ.

2.2.2. Solving ^cR_w. The camera is calibrated using the method proposed by Zhang [30].

If there are at least three coplanar equally spaced parallel lines on the scene plane, the ^cR_w can be computed according to the properties of the vanishing point and vanishing line [31].

There are a set of parallel lines on the planar target, and the lines are coplanar and equally spaced parallel. Three equally spaced lines on the scene plane are represented as

$$
\begin{aligned} a_1 x + b_1 y + c_1 &= 0, \\ a_2 x + b_2 y + c_2 &= 0, \\ a_3 x + b_3 y + c_3 &= 0. \end{aligned} \tag{9}
$$

The vanishing point of the three parallel lines is named as $v = (x_v, y_v, 1)^T$, which is the intersection point of the three parallel lines.

According to the equation

$$
v = Kd, \tag{10}
$$

the direction of the parallel lines measured in the camera frame can be expressed as

$$
d = \frac{K^{-1}v}{\left\lVert K^{-1}v \right\rVert}, \tag{11}
$$

where K are the internal calibration parameters of the camera.

The direction d is the Y axis of the world frame expressed in the camera frame.

The three equally spaced lines on the planar target can be represented as

$$
\begin{aligned} l_1 &= (a_1, b_1, c_1), \\ l_2 &= (a_2, b_2, c_2), \\ l_3 &= (a_3, b_3, c_3). \end{aligned} \tag{12}
$$

The solution for the vanishing line is,

$$
l = \left((l_1 \times l_3)^T (l_2 \times l_3)\right) l_2 + 2\left((l_1 \times l_2)^T (l_3 \times l_2)\right) l_3. \tag{13}
$$

According to the equation

$$
l = K^{-T}n, \tag{14}
$$

the orientation of the target plane can be represented in the camera frame as

$$
n = \frac{K^T l}{\left\lVert K^T l \right\rVert}. \tag{15}
$$

The direction n is the Z axis of the world frame expressed in the camera frame.

Then, the direction of X axis of the world frame expressed in the camera frame can be obtained as

$$
X = Y \times Z. \tag{16}
$$

Therefore, the transformation ^cR_w can be represented as

$$
^cR_w = \begin{bmatrix} X & Y & Z \end{bmatrix}. \tag{17}
$$

2.2.3. Quantum Behaved Particle Swarm Optimization. Particle swarm optimization (PSO) was first introduced by Kennedy and Eberhart. In the PSO algorithm, every swarm particle explores a possible solution. At first, the initial particles are generated in the searching space randomly. Then, the particles as their personal best positions are used to evaluate the fitness function determined by the optimization problem. And the best position of the whole flock is the global best solution. Then, the swarms adjust their own velocities and positions dynamically based on the personal best positions and global best positions as the following equations:

$$V_i(t+1) = \omega V_i(t) + c_1 r_1 \left(P_i(t) - X_i(t) \right)$$
$$+ c_2 r_2 \left(P_g(t) - X_i(t) \right), \tag{18}$$
$$X_i(t+1) = X_i(t) + V_i(t+1),$$

where c_1 and c_2 are the acceleration coefficients, ω is the inertia weight factor, r_1 and r_2 are random numbers in the range of $(0, 1)$, $X_i(t)$ is the ith particle, $P_i(t)$ is the personal best position of the ith particle, and $P_g(t)$ is the global best position of the entire population.

Every swarm continuously updates itself through the above mentioned best positions. In this way, the particles tend to reach better and better solutions in the searching space.

In the PSO algorithm, the particles will follow a particular course after several iterations. And then the particles will be trapped into local optima. So the global convergence cannot be guaranteed which has been proved by Bergh. To make sure that the particles escape from a local minimum, the QPSO algorithm is proposed. In the QPSO algorithm, the particle position is described not by the velocity but by the particle's appearing probability density function. There is no fixed orbit for the particles, and the particles constrained by δ potential trough can appear at any position in the feasible solution space with certain probability. So the QPSO can guarantee the global convergence and it has been proved by Sun.

The particle position updating equations are as follows:

$$C_j = (C_1, C_2, \ldots, C_D) = \frac{1}{M} \sum_{i=1}^{M} P_i$$
$$= \left(\frac{1}{M} \sum_{i=1}^{M} P_{i,1}, \frac{1}{M} \sum_{i=1}^{M} P_{i,2}, \ldots, \frac{1}{M} \sum_{i=1}^{M} P_{i,D} \right), \tag{19}$$
$$p_{i,j} = \phi \cdot P_{i,j} + (1 - \phi) \cdot G_{i,j},$$
$$x_{i,j} = p_{i,j} \pm \alpha \cdot \left| C_j - x_{i,j} \right| \cdot \ln \left[\frac{1}{u} \right],$$

where $\phi \sim U(0 \sim 1)$, $u \sim U(0 \sim 1)$, D is the dimension of the problem space, M is the population size, $x_i = (x_{i1}, x_{i2}, \ldots, x_{iD})$ are the particle current positions, $P_i = (P_{i,1}, P_{i,2}, \ldots, P_{iD})$ are the personal best positions, $G_i = (G_{i,1}, G_{i,2}, \ldots, G_{iD})$ are the global best positions, and α is the Contraction-Expansion coefficient which is the only parameter in the QPSO algorithm depicted as

$$\alpha = \frac{0.5 * (\text{MAXITER} - t)}{\text{MAXITER} + 0.5}, \tag{20}$$

where t is the current iterative number and the MAXITER is the maximum iterative number.

2.2.4. Objective Function. The zero offsets of joint angles need to be computed using the optimization algorithm.

Suppose the true joint angle values are expressed as

$$\theta_1' = \theta_1 + \Delta\theta_1,$$
$$\theta_2' = \theta_2 + \Delta\theta_2,$$
$$\theta_3' = \theta_3 + \Delta\theta_3,$$
$$\theta_4' = \theta_4 + \Delta\theta_4, \tag{21}$$
$$\theta_5' = \theta_5 + \Delta\theta_5,$$
$$\theta_6' = \theta_6 + \Delta\theta_6,$$

where θ_i', θ_i, and $\Delta\theta_i$ ($i = 1, 2, \ldots 6$) are the true value, the ideal value, and the error of joint angles zero offsets, respectively.

Equations (4) and (21) can be substituted to (7), and the true value R_6' can be obtained and then can be substituted to (6).

After the robot moved several positions, the objective function is obtained as

$$F(\Delta\theta_1, \Delta\theta_2, \ldots, \Delta\theta_6) = \sum_{i=1}^{n-1} \sum_{j=i}^{n} \sum_{k=1}^{9} \left\| {}^r R_w^i(k) - {}^r R_w^j(k) \right\|^2, \tag{22}$$

where n is the number of the positions and ${}^r R_w^i(k)$ is the kth element of the rotation matrix at the ith position.

3. Experimental Results

3.1. Experiment Setup. The robot visual measurement system is composed of an industrial robot and a visual measurement system. The visual measurement system consists of a binocular stereo vision system, laser generators, a computer, and the image process system. The robot is an industrial robot IRB1400 from ABB (a Swiss-Swedish conglomerate). The binocular stereo vision system consists of two industrial cameras AVT F504B, with 16 mm lens from Mage. The image resolution of the camera is $2452 * 2056$ pixels. The field of view is about $300 * 300$ mm^2, and the work distance is about 600 mm. The laser generators are HK130209307-10 from HUAKE. The laser beams produced by laser generators are projected on the tested surface and form light stripes on the surface. The contour of the light stripes is the contour of the test surface, which is simple for measuring.

The two cameras are calibrated using the Zhang [30] method, the left camera frame is the camera frame F_c, and the right camera is an auxiliary camera to measure. The planar gridding target is placed in the robot work space, and the cameras are moved with robot to capture the images of the planar target in different positions.

TABLE 2: The errors of the twist angles.

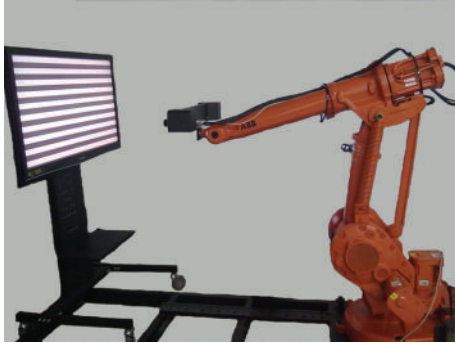|	$\Delta\alpha_1$	$\Delta\alpha_2$	$\Delta\alpha_3$	$\Delta\alpha_4$	$\Delta\alpha_5$	$\Delta\alpha_6$
Error/rad	0.00059930	−0.00009572	−0.00389624	0.00378916	0.01663513	0

FIGURE 2: The robot visual measurement system.

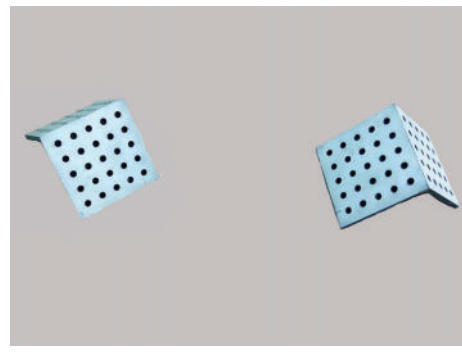FIGURE 4: The reflector on the axis 2.

FIGURE 3: Adapting part.

FIGURE 5: Verified experiment.

In the calibrating procedure, a laser tracker and a planar target will be used. The laser tracker is AT901-B from Leica, with the measuring resolution of 0.01 mm. There are parallel lines on the planar target, and the resolution is 5 μm.

The work space of the measuring system is about $1500 * 1500 * 1000 \, \text{mm}^3$. And the system is shown in Figure 2.

3.2. Calibration of Twist Angles. As shown in Figure 3, there is an adapting part fixed on the robot end effector, and the reflector of the laser tracker is fixed on the other end of the adapting part. Each single axis is moved in its joint angle range mentioned in Section 2.1, and 100 pause points are captured uniformly. It is worth noting that, when the axis 2 is moved, the reflector is fixed on the arm of axis 2, as shown in Figure 4. The pause points are measured by the laser tracker, and planes are fitted based on these points. The normal vectors of the planes are the directions of Z axes, and the twist angles are obtained. There are only five twist angles which can be obtained. The last frame is created on the robot end effector, and the sixth twist angle is zero which cannot be calibrated by the method we proposed. The calibration results of the twist angles are shown in Table 2.

3.3. Solving the Joint Angle Zero Offsets. The camera is moved with the robot to 100 different positions, and at least three parallel lines on the planar target are captured by the left camera. The images are saved and the corresponding joint angles are recorded at the same time. According to Section 2.2.1 and Section 2.2.2, R_6 and ^cR_w are computed.

According to the objective functions in Section 2.2.4, the errors of the joint angle zero offsets are computed using the QPSO algorithm.

The particle size is 60, the dimension is 6, the maximum iteration number is 20000, and the range of parameters are $(−1, 1)$. The errors of the joint angle zero offsets are shown in Table 3.

3.4. Verified Experiments. To verify the validity of the proposed method, a verified experiment system is set up. The round hole target is put in the robot work space, as shown in Figure 5.

The centers of the holes on the target are measured by the binocular stereo vision system. Then, they can be represented in the robot base frame, by the transformation matrices T_6 and T_h, where the matrix T_6 is obtained by the D-H model

TABLE 3: The errors of the joint angle zero offsets.

	$\Delta\theta_1$	$\Delta\theta_2$	$\Delta\theta_3$	$\Delta\theta_4$	$\Delta\theta_5$	$\Delta\theta_6$
Error/rad	0.00029334	−0.00018536	−0.00152726	0.00254384	−0.00709304	0.00004102

TABLE 4: Verified experiment results.

No.	Laser tracker/mm	Kinematics model/mm	Error/mm	Calibrated/mm	Error/mm
1	1407.3618	1412.3042	4.9424	1407.6420	0.2802
2	1452.8959	1454.6046	1.7087	1453.2856	0.3897
3	1063.4934	1061.4067	−2.0867	1063.2350	−0.2584
4	1456.6879	1456.8733	0.1854	1456.7918	0.1039
5	1316.1796	1314.8049	−1.3747	1315.7760	−0.4036
6	1048.7702	1042.8337	−5.9365	1048.3021	−0.4681
7	1139.2491	1135.6079	−3.6412	1139.0911	−0.1580
8	1273.4407	1268.1671	−5.2736	1273.0968	−0.3439
9	1478.7534	1474.3281	−4.4253	1478.2286	−0.5248
10	1482.4442	1478.8035	−3.6407	1481.8039	−0.6403
11	1078.8065	1077.6482	−1.1583	1078.5412	−0.2653
12	1485.2963	1478.9914	−6.3049	1484.7494	−0.5469
13	1478.5834	1484.2214	5.6380	1478.9045	0.3211
14	1242.6878	1248.9148	6.2270	1243.2032	0.5154
15	1400.1402	1400.0122	−0.1280	1399.8832	−0.2570
16	1070.9431	1070.7926	−0.1505	1070.8120	−0.1311
17	1210.8806	1208.6086	−2.2720	1210.6297	−0.2509
18	1457.8677	1463.4684	5.6007	1458.2994	0.4317
19	1396.1036	1394.2730	−1.8306	1395.7513	−0.3523
20	1479.7462	1474.3030	−5.4432	1478.9971	−0.7491
Mean/mm		0.9682		0.1654	
RMS/mm		4.0248		0.4046	

with the calibrated parameters α_i' and θ_i'. At the same time, they are measured using the laser tracker.

Five hole centers measured randomly in the left target and four in the right target have been recorded and the distances of any two hole centers are calculated. Compare the distances measured by the laser tracker and the robot visual measurement system; the results are shown in Table 4.

From Table 4, we can see that the measuring accuracy is improved after calibration.

4. Conclusion

This paper represents a two-step calibration method for the robot visual measurement system. Firstly, the twist angles are calibrated using a laser tracker. And then, according to the constraint that the world frame and the robot base frame are relatively constant, the joint angles zero offsets are calibrated. The rotation constraint is introduced and the accuracy is improved. The results show that the proposed calibration method in the paper can improve the measuring accuracy greatly. In the calibrating procedure, there are some key problems that need to be noted.

(1) To improve the accuracy, the pause points should be as much as possible when calibrating the twist angles.

(2) In the calibrating procedure, adjust the camera to make sure that the planar target is in the range of the camera depth of field.

(3) The scene plane should be as much lean as possible with the planar target to decrease the effect by the vanishing point position error when calibrating the rotation parameters.

(4) The robot should be moved to cover all the real measuring space to guarantee the measuring accuracy.

The calibration method proposed in the paper has broad applications including numerous other kinds of robot visual measurement systems. After calibration, there is no additional measuring equipment needed in the measuring procedure. The proposed method is simple and easy to perform. It can meet the large scale measurement requirement. But, if the measurement requirement is more restrict, the distance constraint should be used and the link length and link joint offsets should be calibrated. The effects about temperature and elasticity are not discussed either, and the studies on them should be done in the future.

References

[1] Y. Zhong, B. Qiao, and S. Li, *Robot Vision*, National Defense Industry Press, 1994.

[2] R. P. Judd and A. B. Knasinski, "Technique to calibrate industrial robots with experimental verification," *IEEE Transactions on Robotics and Automation*, vol. 6, no. 1, pp. 20–30, 1990.

[3] A. Y. Elatta, P. G. Li, L. Z. Fan et al., "An overview of robot calibration," *Information Technology Journal*, vol. 3, pp. 74–78, 2004.

[4] C. H. Wu, "The kinematic error model for the design of robot manipulators," in *Proceedings of the American Control Conference*, pp. 22–24, San Francisco, Calif, USA, June 1983.

[5] W. K. Veitschegger and C.-H. Wu, "Robot accuracy analysis based on kinematics," *IEEE Journal of Robotics and Automation*, vol. 2, no. 3, pp. 171–179, 1986.

[6] G. Gatti and G. Danieli, "A practical approach to compensate for geometric errors in measuring arms: application to a six-degree-of-freedom kinematic structure," *Measurement Science and Technology*, vol. 19, no. 1, Article ID 015107, 2008.

[7] G. Chen, Q. Jia, T. Li, and H. Sun, "Calibration method and experiments of robot kinematics parameters based on error model," *Robot*, vol. 34, no. 6, pp. 680–688, 2012.

[8] P. Wang, Q.-Z. Liao, Y.-F. Zhuang, and S.-M. Wei, "Simulation and experimentation for calibration of general 7R serial robots," *Robot*, vol. 28, no. 5, pp. 483–494, 2006.

[9] Y.-J. Ren, J.-G. Zhu, X.-Y. Yang, and S.-H. Ye, "Measurement robot calibration model and algorithm based on distance accuracy," *Acta Metrologica Sinica*, vol. 29, no. 3, pp. 198–202, 2008.

[10] D. Wu, A. Li, Z. Ma, Y. Wang, and X. Wu, "Novel approach to calibrate main body of a three-dimensional scanning robotic system," *Journal of Mechanical Engineering*, vol. 47, no. 17, pp. 9–14, 2011.

[11] Y. C. Shiu and S. Ahmad, "Calibration of wrist-mounted robotic sensors by solving homogeneous transform equations of the form AX = XB," *IEEE Transactions on Robotics and Automation*, vol. 5, no. 1, pp. 16–29, 1989.

[12] R. Y. Tsai and R. K. Lenz, "New technique for fully autonomous and efficient 3D robotics hand/eye calibration," *IEEE Transactions on Robotics and Automation*, vol. 5, no. 3, pp. 345–358, 1989.

[13] F. Dornaika and R. Horaud, "Simultaneous robot-world and hand-eye calibration," *IEEE Transactions on Robotics and Automation*, vol. 14, no. 4, pp. 617–622, 1998.

[14] G.-L. Yang, L.-F. Kong, and J. Wang, "A new calibration approach to hand-eye relation of manipulator," *Robot*, vol. 28, no. 4, pp. 400–405, 2006.

[15] A. Nubiola and I. A. Bonev, "Absolute calibration of an ABB IRB 1600 robot using a laser tracker," *Robotics and Computer Integrated Manufacturing*, vol. 29, pp. 236–245, 2013.

[16] J. K. Parker, A. R. Khoogar, and D. E. Goldberg, "Inverse kinematics of redundant robots using genetic algorithms," in *Proceedings of the IEEE International Conference on Robotics and Automation*, pp. 271–276, Scottsdale, Ariz, USA, May 1989.

[17] Y. Tang and Y. Xu, "Application of fuzzy Naive Bayes and a real-valued genetic algorithm in identification of fuzzy model," *Information Sciences*, vol. 169, no. 3-4, pp. 205–226, 2005.

[18] J. L. Chen and W. D. Chang, "A multi-crossover genetic algorithm for parameters estimation of a two-link robot," in *Systems Modeling and Simulation*, pp. 198–202, Springer, 2007.

[19] Y. Liu, B. Liang, W. Y. Qiang et al., "Improvement on robots positioning accuracy based on genetic algorithm," in *IMACS Multiconference on Computational Engineering in Systems Applications*, pp. 387–392, Beijing, China, October 2006.

[20] J. M. Lewis, X. L. Zhong, and H. Rea, "Neural network approach to the robot inverse calibration problem," in *Proceedings of the 2nd International Conference on Intelligent Systems Engineering*, pp. 342–347, September 1994.

[21] X. Zhong, J. M. Lewis, and F. L. N-Nagy, "Inverse robot calibration using artificial neural networks," *Engineering Applications of Artificial Intelligence*, vol. 9, no. 1, pp. 83–93, 1996.

[22] J. H. Jang, S. H. Kim, and Y. K. Kwak, "Calibration of geometric and non-geometric errors of an industrial robot," *Robotica*, vol. 19, no. 3, pp. 311–321, 2001.

[23] X. Q. Wang, H. D. Liu, Y. Shi, B. Liang, and Y.-C. Zhang, "Research on identification method of kinematics for space robot," *Procedia Engineering*, vol. 29, pp. 3381–3386, 2012.

[24] P. Asgharifard-Sharabiani, A. Hannaneh, and M. Nikkhah-Bahrami, "Calculation of helical gear's basic parameters using COP-data acquired by optical 3D digitizer," *Proceedings of the Institution of Mechanical Engineers, Part C: Journal of Mechanical Engineering Science*, vol. 225, no. 12, pp. 2953–2962, 2011.

[25] R. Hassan, B. Cohanim, O. De Weck, and G. Venter, "A comparison of particle swarm optimization and the genetic algorithm," in *Proceedings of the 46th AIAA/ASME/ASCE/AHS/ASC Structures, Structural Dynamics and Materials Conference*, pp. 1138–1150, April 2005.

[26] J. Kennedy and R. Eberhart, "Particle swarm optimization," in *Proceedings of the IEEE International Conference on Neural Networks*, pp. 1942–1948, Perth, Australia, December 1995.

[27] F. van den Bergh and A. P. Engelbrecht, "A new locally convergent particle swarm optimiser," in *Proceedings of the IEEE International Conference on Systems, Man and Cybernetics*, pp. 94–99, October 2002.

[28] F. V. Bergh, *An analysis of particle swarm optimizers [Ph.D. thesis]*, University of Pretoria, 2001.

[29] J. Sun, B. Feng, and W. Xu, "Particle swarm optimization with particles having quantum behavior," in *Proceedings of the Congress on Evolutionary Computation (CEC '04)*, pp. 325–331, June 2004.

[30] Z. Zhang, "A flexible new technique for camera calibration," *IEEE Transactions on Pattern Analysis and Machine Intelligence*, vol. 22, no. 11, pp. 1330–1334, 2000.

[31] R. Hartley and A. Zisserman, *Multiple View Geometry in Computer Vision*, Cambridge University Press, 2003.

Research Article

Multicamera Fusion-Based Leather Defects Marking System

Chao-Ching Ho,[1] Jheng-Ciao Li,[1] Tzu Hsin Kuo,[2] and Chun-Chi Peng[2]

[1] *Department of Mechanical Engineering, National Yunlin University of Science and Technology, 123 University Road, Section 3, Douliou, Yunlin 64002, Taiwan*
[2] *Mechanical and Systems Research Laboratories, Industrial Technology Research Institute, Hsinchu 31040, Taiwan*

Correspondence should be addressed to Chao-Ching Ho; hochao@yuntech.edu.tw

Real-time acquisition of ultra-high wide view video images is essential in leather defects marking systems because this enables either the leather manufacturing process or an inspector to identify leather defects. The major challenge in this work is blending and stitching the multiple camera views to form a single fusion image map. In the fusion video image, the viewer is quite sensitive to incorrect stitching and blending when the marking pen is passing through the border between views. Hence, a set of geometric and photometric corrections have to be applied to each camera view in addition to careful blending of the image borders. In this paper, we present a real-time image capturing system that uses four cameras at 30 fps and stitches their views together to create a panoramic video with a resolution of 1280×960 px. The real-time fusion video image can be observed on a large screen next to the leather defects marking system and no manual alignment is necessary, resulting in savings in both labor and time.

1. Introduction

The leather defects marking process utilizes the assessment of human experts in the classification of leather according to their surface quality. In modern times, the leather manufacturing process is digitized using an image processing system. Consequently, leather image analysis and surface defects detection require the establishment of a coordinate system in order to evaluate the location of defects. However, real natural leather is quite large, and so it is difficult to detect all of the defects that may exist on the leather surface using a single camera. A single camera typically provides only a limited field of view. The piece of leather could be as large as $2\,\mathrm{m} \times 3\,\mathrm{m}$, which means that the resolution of the leather image provided by a single camera is not very high. In recent years, great efforts have been made by researchers to automate the leather manufacturing process by applying machine vision.

Lerch and Chetverikov [1, 2] proposed a machine vision system for the analysis of hide images for a computer-aided layout design system used in the leather industry. Aranda Penaranda et al. [3] implemented an automatic artificial vision-based system for the inspection, distribution, and water-jet cutting of leather. Anand et al. [4] used a machine vision system as a front end to acquire the image of each irregular sheet and part and thereby solve the two-dimensional stock cutting problem in the leather and apparel industries. Paakkari et al. [5] employed machine vision to provide accurate real-time data on the outline and position of the preform utilized in the nesting process, leading to material and cost savings. Lanzetta and Tantussi [6] proposed a vision-based laboratory prototype for leather trimming to increase the automation level in the leather industry. Yeh and Perng [7] established a reference standard of defects for inspectors to classify leather. Krastev and Georgieva [8, 9] proposed using fuzzy neural networks to determine leather quality. However, in their proposal, exact features values determination is difficult to achieve and misclassification errors pose a problem. Governi et al. [10] designed and built a machine vision-based system for automatically dyeing free-form leather patch contours. He et al. [11] proposed to use wavelet transform and the energy of the wavelet coefficients distributed in different frequency channels for leather inspection.

The research cited above deals with many aspects of the leather manufacturing process associated with vision;

however, to the best of our knowledge, a multiple camera calibration method to increase the resolution of the system discussed above is not yet available. For large leather machines, multiple camera fusion is the solution for constructing high quality and high resolution image maps [12]. In addition to the development of an effective defect classification algorithm, the other main task tackled in our work is the development of a highly accurate multiple camera fusion system. Detection of accuracy is affected by distortion of camera lenses; further, high fusion quality must be assured in processing a number of leather patches with multiple cameras.

In this paper, to address these problems, we propose a multiple images fusion method that utilizes four cameras and homography matrices to calculate overlapping pixels and finally implement boundary resampling to blend the images. The rest of this paper is organized as follows. A camera calibration method capable of compensating for optical distortions caused by the camera lenses is presented in Section 2. Multiple camera fusion and the results obtained from evaluation of our proposed system are discussed in Section 3. Finally, we conclude this paper in Section 4.

2. Calibration of the Leather Defects Marking System

Our proposed leather defects marking system comprises the following main parts: a machine vision system consisting of the illumination devices and four acquisition cameras that facilitate the acquisition of images of any piece of leather placed on the working plane. The illumination devices are designed to highlight the differences between the leather and the supporting working plane. Image acquisition is conducted using four commercial cameras placed above the working plane at a distance of approximately 1200 mm. The size of the working plane is 2 m × 3 m; hence, the spatial resolution of the cameras is approximately 2 mm/px. Each of the cameras is connected to a graphic card, with resolution 640×480 px, in a personal computer (PC). The overall system is depicted in Figure 1. The leather is positioned on a bright white panel table to enhance the contrast with most leather types.

The system requires precalibration to compensate for lens distortions and camera misalignments. In our proposed leather defects marking system, the video signal-capturing process is conducted using four cameras with pixel resolution of 640×480. The captured synchronized video frames are transmitted via a grabber card to a PC, which functions as the image processor, and then buffered in the PC's system memory. The next step is to process them. However, camera calibration is a fundamental step that needs to be taken into consideration before any reliable image processing or even further defect marking can be performed. Camera calibration can be used to obtain the intrinsic parameters of the cameras. The intrinsic parameters, which are independent of a camera's position in the physical environment, describe the camera's focal length (f_x, f_y), principal point (C_x, C_y), and distortion coefficients. Distortion compensation is carried out by means
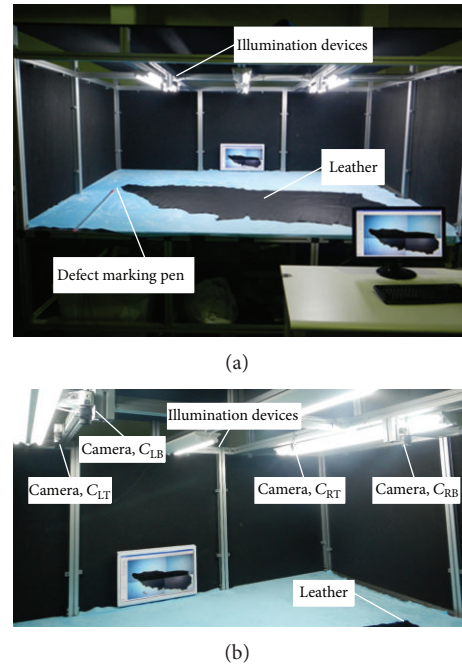

(a)

(b)

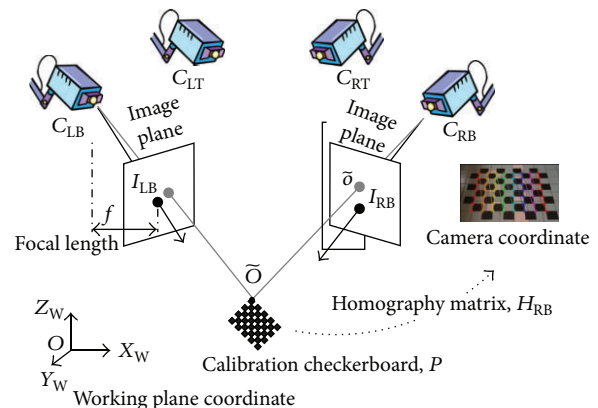FIGURE 1: The proposed leather defects marking system.

FIGURE 2: System calibration to recognize intrinsic parameters and homography matrices of cameras.

of a flat calibration pattern. The calibration methods used here also employ digital checkerboard-patterned images. The pattern is a checkerboard with 11×8 checkers and 100 mm edge length. A set of 10 images of the calibration pattern in different positions is acquired for each individual camera, as illustrated in Figure 2. To verify the calibration results, raw images from another checkerboard are captured for each camera. The raw images from each individual camera, that is, C_{LT} (positioned at top left), C_{RT} (positioned at top right), C_{LB} (positioned at bottom left), and C_{RB} (positioned at bottom right), are shown in Figure 3. The undistorted images for the individual cameras, obtained following distortion compensation, are shown in Figure 4.

Large pieces of leather are partially captured by the four separate cameras; the image of each leather object can then
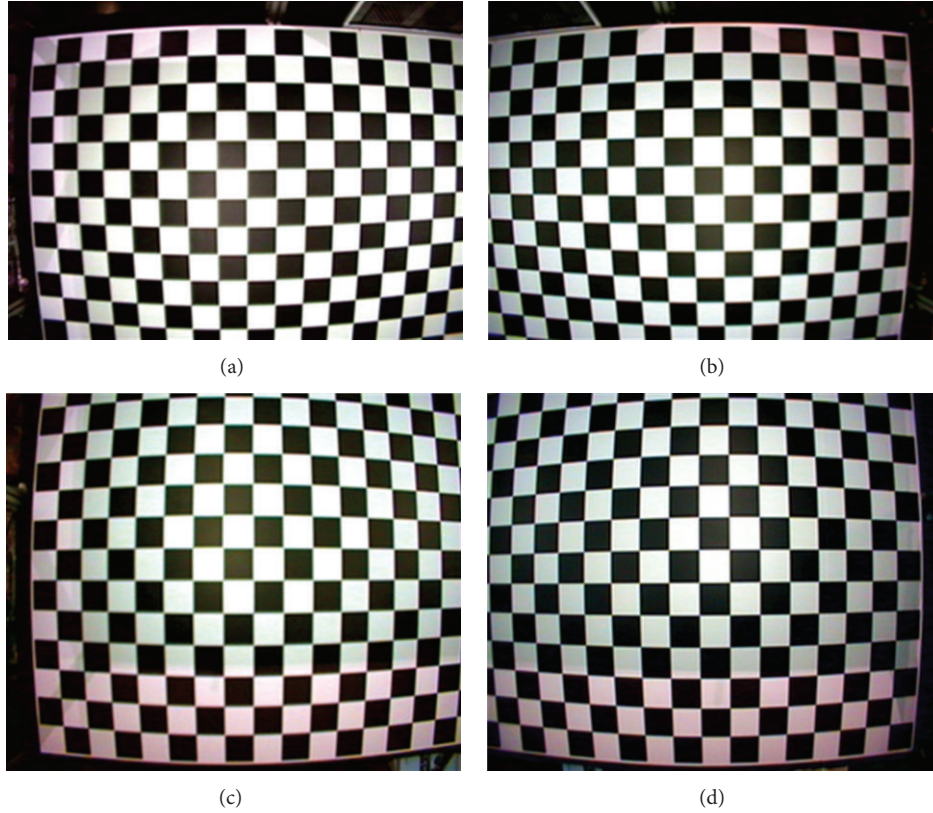
FIGURE 3: Raw images from the individual cameras: (a) C_{LT} (positioned at top left), (b) C_{RT} (positioned at top right), (c) C_{LB} (positioned at bottom left), and (d) C_{RB} (positioned at bottom right).

be recombined by joining the multiple images from the four cameras in the same coordinate system for better recognition. To stitch four images that are not aligned on the same coordinate plane as a result of camera placement, registered and aligned matrices have to be calculated to facilitate their matching, as shown in Figure 5. The homography matrix of the calibrated cameras can be calculated linearly with the help of one array that stores the coordinates of reference points chosen in the digital checkerboard images and another array that contains the corresponding points in the physical world. The collection of reference points is selected on the checker-patterned model plane for the four cameras used in this paper. The calibration methods used here also employ digital checkerboard-patterned images. A patterned board with 28×19 checkers and 100 mm edge length is placed on the working plane surface, as depicted in Figure 6.

Part of a planar checker pattern positioned in front of the four cameras is acquired by the four cameras, respectively. The transformation calculation comprises calculation of homography matrix H_{RB} between a partial checker pattern plane P and an image I_{RB}, calculation of homography matrix H_{RT} between partial checker pattern plane P and an image I_{RT}, calculation of homography matrix H_{LT} between partial checker pattern plane P and an image I_{LT}, and calculation of homography matrix H_{LB} between partial checker pattern plane P and an image I_{LB}. To express the homography H_{LB} mapping in terms of matrix multiplication, homogeneous

coordinates are used to express both the viewed point $\widetilde{O}$ and the point $\tilde{o}_{LB}$ on the image plane to which $\widetilde{O}$ is mapped. Suppose that $\widetilde{O} = \begin{bmatrix} X & Y & Z & 1 \end{bmatrix}^T$ and $\tilde{o}_{LB} = \begin{bmatrix} u & v & 1 \end{bmatrix}^T$ are the homogeneous coordinates of an arbitrary corner point in the checker pattern P and in image plane I_{LB}, respectively. The homography H_{LB} can be expressed as

$$\tilde{o}_{LB} = sH_{LB}\widetilde{O}, \tag{1}$$

where s is an arbitrary scale factor. After the checker pattern corner is located, the corresponding indices are stored for homography calculation. Homography transform operates on homogeneous coordinates. Without loss of generality, we can choose to define a planar scene that maps points on the plane so that final z-buffer depth is zero (i.e., $Z = 0$). Then, a coordinate $\widetilde{O}' = \begin{bmatrix} X & Y & 1 \end{bmatrix}^T$, which is defined on the plane, where

$$\tilde{o}_{LB} = sH_{LB}\widetilde{O}'. \tag{2}$$

The homography matrix that maps a planar object's points onto the image plane is a three-by-three matrix. On the basis of homography, four cameras in different locations and orientations are registered to recover the rigid rotation and translation of the planar pattern. For the homography
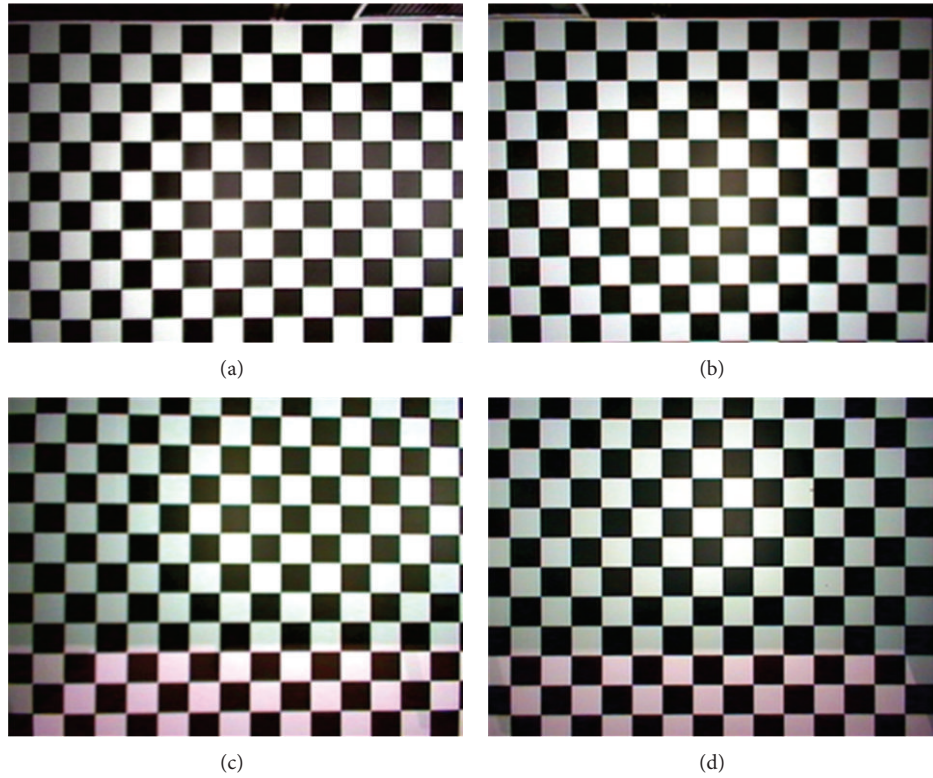
(a)

(b)

(c)

(d)

FIGURE 4: Undistorted images for the individual cameras, after distortion compensation: (a) C_{LT} (positioned at top left), (b) C_{RT} (positioned at top right), (c) C_{LB} (positioned at bottom left), and (d) C_{RB} (positioned at bottom right).
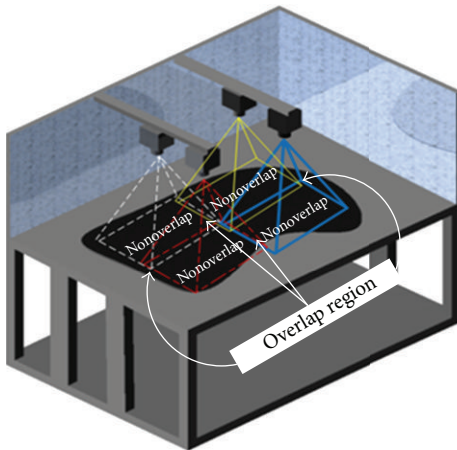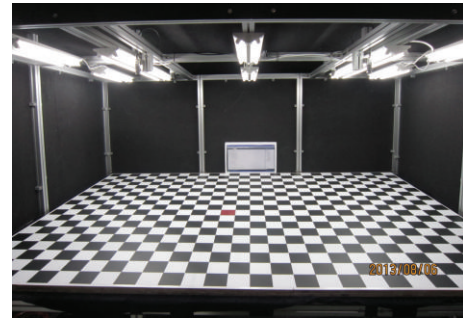

FIGURE 5: This large piece of leather is partially captured by four separate cameras and four images that are not aligned on the same coordinate plane as a result of camera placement.

FIGURE 6: A patterned board with 28×19 checkers and 100 mm edge length is placed on the working plane surface.

matrices of the other three cameras, homography can be expressed as

$$\tilde{o}_{RB} = sH_{RB}\tilde{O}',$$

$$\tilde{o}_{LT} = sH_{LT}\tilde{O}', \qquad (3)$$

$$\tilde{o}_{RT} = sH_{RT}\tilde{O}'.$$

Only reasonable overlapping of the planar pattern in the field of view among the four neighboring cameras is necessary, and therefore the images from the individual cameras are registered and aligned. The fused image is produced by stitching the registered and aligned images, then the overlapping areas between two adjacent regions are calculated, and a new pixel set is obtained on the basis of a weighted linear interpolation process between the two overlapped pixel sets. The seamless blended images based on homography matrices, that is, H_{LB}, H_{RB}, H_{LT}, and H_{RT}, provide a complete image map with a large field of view, as shown in Figure 7.
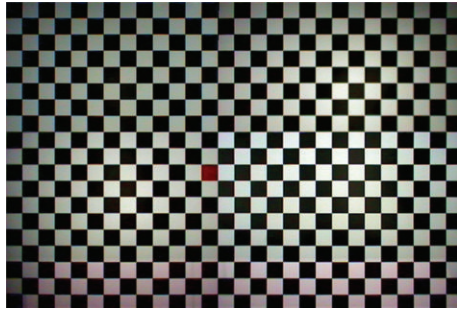
FIGURE 7: The images from the four cameras are fused together to provide a complete image map.
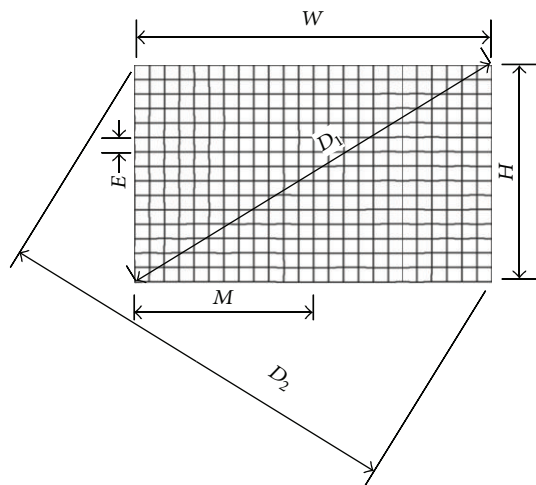

FIGURE 8: The digital checkerboard images are characterized by known geometric entities, that is, maximum width W, half of the width M, maximum height H, edge length E, and diagonal lengths D_1 and D_2, respectively.

3. Results and Discussion

We used the 400 checkers on the patterned board to verify our calibrated results. As shown in Figure 8, the digital checkerboard images are characterized by known geometric entities, that is, maximum width W, half of the width M, maximum height H, edge length E, and diagonal lengths D_1 and D_2, respectively. Conventional global alignment approaches that employ a manual fusion process, after hours of careful alignment along the vertical planes of the checkerboard, obtain a fused accuracy with a mean error of 17.28 mm and a standard deviation of 12.20. Further, their mean absolute percentage error is 1.1%. Our proposed automatic registration approach, which employs the homography based fusion process, results in a fused accuracy with a mean error of 0.37 mm and a standard deviation of 0.41. Further, our mean absolute percentage error is 0.1%. A comparison of our automatic registration approach to the manual fusion process is given in Table 1.

Following completion of the fused image map, the defect images are segmented and the areas with differing quality are
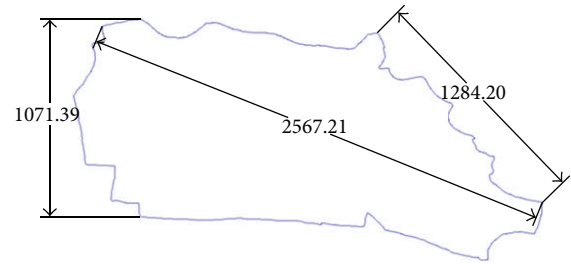

FIGURE 9: The proposed multicamera fused leather defects marking system is integrated with a CAD system in the leather industry.
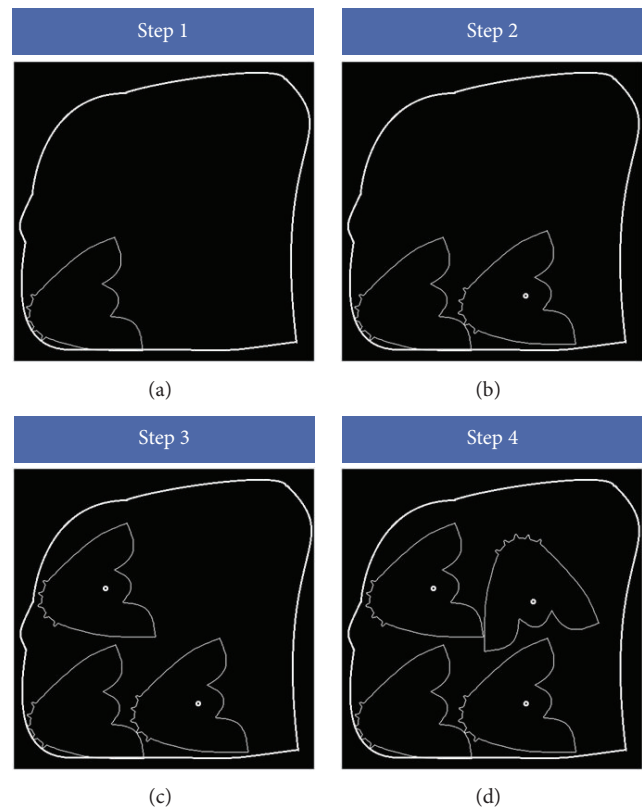

FIGURE 10: The nesting module developed by us for the leather production process.

marked manually by a defect marking pen. To track the marking pen in a complex environment and grab the marking dot are trivial for humans, even if the background is disordered and colorful. To determine the characteristics of the marking pen, image preprocessing is required in order to search for the marking dot. To simplify image analysis, the preprocessing steps use morphological subroutines (HSV color transfer, erosion, dilation, and majority of threshold) to reduce the disturbances, all of which are done prior to the determined motion. There are many other objects with various colors that complicate the identification process and it is difficult for a computer to understand the concept of each color. Therefore, we applied the HSV color model. In order to distinguish the target object from the background environment, information

TABLE 1: Comparison of the manual fusion process to our automatic registration approach.

Geometric entities	Standard value (mm)	Value obtained by manual process	Value obtained by automatic registration
W	2400.00	2437.24	2401.01
H	1500.00	1481.26	1499.92
E	100.00	101.64	100.74
M	1300.00	1313.47	1299.87
D_1	2830.19	2840.04	2830.21
D_2	2830.19	2852.90	2830.45
Mean error		17.28	0.37
Standard deviation		12.20	0.41

about the hue level of the marking pen must be obtained. After acquisition, each image is individually processed to determine the background and follow the path of the marking pen. At each acquisition, the dots marked by the marking pen are converted from pixel to millimeter and from the image reference system to the machine absolute system. Less than 20 ms is taken to process the fused image. As shown in Figure 9, our proposed machine vision system has been fully integrated into the commercial CAD program used in the leather industry via a DXF link. Demonstration videos of our experiments are available at http://youtu.be/z_TD8L9EH80 and http://youtu.be/Kfu8vyvd6-4. Following the marking of the defects by the marking system, the data are finally passed to the automated process of the extended nesting module created by us for the leather production process, as shown in Figure 10.

4. Conclusions

In this paper, we proposed an approach that solves the problem of real-time video fusion in a multicamera system for leather defect detection systems. We achieve complete multicamera calibration by applying homography transformation. We employ a homography matrix to calculate overlapping pixels and finally implement boundary resampling to blend images. Experimental results show that our proposed homography based registration and stitching method is effective for leather multi-camera fused leather defects marking and nesting systems. Our method improves the mean absolute percentage error from 1.1% obtained by manual processes to 0.1% with automatic registration.

Acknowledgments

References

[1] A. Lerch and D. Chetverikov, "Knowledge-based line-correction rules in a machine-vision system for the leather industry," *Engineering Applications of Artificial Intelligence*, vol. 4, no. 6, pp. 433–438, 1991.

[2] A. Lerch and D. Chetverikov, "Correction of line drawings for image segmentation in leather industry," in *Proceedings of the 11th IAPR International Conference on Computer Vision and Applications*, vol. 1, pp. 45–48, 1992.

[3] J. D. Aranda Penaranda, J. A. Ramos Alcazar, L. M. Tomas Balibrea, J. L. Munoz Lozano, and R. Torres Sanchez, "Inspection and measurement of leather system based on artificial vision techniques applied to the automation and waterjet cut direct application," in *Proceedings of the IEEE International Conference on Systems, Man and Cybernetics*, vol. 1, pp. 863–867, October 1994.

[4] S. Anand, C. McCord, R. Sharma, and T. Balachander, "An integrated machine vision based system for solving the nonconvex cutting stock problem using genetic algorithms," *Journal of Manufacturing Systems*, vol. 18, pp. 396–414, 1999.

[5] J. Paakkari, H. Ailisto, M. Niskala, M. Mäkäräinen, and K. Väinämö, "Machine vision guided waterjet cutting," in *Diagnostic Imaging Technologies and Industrial Applications*, vol. 3827 of *Proceedings of SPIE*, pp. 44–51, Munich, Germany, 1999.

[6] M. Lanzetta and G. Tantussi, "Design and development of a vision based leather trimming machine," in *Proceedings of the 6th International Conference on Advanced Manufacturing Systems and Technology*, pp. 561–568, 2002.

[7] C. Yeh and D.-B. Perng, "A reference standard of defect compensation for leather transactions," *The International Journal of Advanced Manufacturing Technology*, vol. 25, no. 11-12, pp. 1197–1204, 2005.

[8] K. Krastev and L. Georgieva, "Identification of leather surface defects using fuzzy logic," in *Proceedings of the International Conference on Computer Systems and Technologies*, Varna, Bulgaria, 2005.

[9] K. Krastev and L. Georgieva, "A method for leather quality determination using fuzzy neural networks," in *Proceedings of the International Conference on Computer Systems and Technologies*, Veliko Tarnovo, Bulgaria, 2006.

[10] L. Governi, Y. Volpe, M. Toccafondi, and M. Palai, "Automated dyeing of free-form leather patch edges: a machine vision based system," in *Proceedings of the International conference on Innovative Methods in Product Design*, Venice, Italy, 2011.

[11] F. Q. He, W. Wang, and Z. C. Chen, "Automatic visual inspection for leather manufacture," *Key Engineering Materials*, vol. 326–328, pp. 469–472, 2006.

[12] M. Lanzetta and G. Tantussi, "Design and development of a vision based leather trimming machine," in *Proceedings of the 6th International Conference on Advanced Manufacturing Systems and Technology*, pp. 561–568, 2002.

Research Article

A Sphere-Based Calibration Method for Line Structured Light Vision Sensor

Zhenzhong Wei, Mingwei Shao, Yali Wang, and Mengjie Hu

Key Laboratory of Precision Opto-Mechatronics Technology, Beihang University, Ministry of Education, Beijing 100191, China

Correspondence should be addressed to Mingwei Shao; smw1987@163.com

A major difficulty in calibrating line structured light vision sensor is how to obtain enough calibration feature points, due to the fact that known world points on the calibration target do not rightly fall onto the light stripe plane. This paper presents a calibration method using a target, consisting of one sphere and a reference board, to obtain feature points on the light stripe, which is the intersection of the structured-light plane and the reference board. By moving the sphere into several positions on the fixed reference board, we can get a plane in parallel with the reference one. From the acquired right-circular cone and known radius of the sphere, the function of the reference board can be deduced. Moving the target randomly into different positions, enough points lying on the structured-light plane can be obtained. Experiment results show that the accuracy of the proposed calibration method can reach 0.102 mm within the view field of 200 mm ∗ 200 mm; meanwhile, robustness and easy operation can be indicated.

1. Introduction

The Line Structured Light Vision Sensor (LSLVS) consisting of one camera and one projector is widely used in industrial measurement owing to its wide measurement range, high precision, real-time ability, easy information extracting, and so forth. Calibration, with the purpose of establishing expression of the structured-light plane under the camera coordinate system, is one of the basic measurement tasks of LSLVS [1].

Heretofore, the calibration methods of LSLVS can be classified into three categories: 3D target based method, planar target based method, and 1D target based method. Unsatisfactorily, the 3D target method [2–4] is not accurate enough because of less feature points and the problem of mutual occlusion between different planes of the target. Additionally, the target, normally a cube with some special accessories, is difficult to produce precisely and is cumbersome for onsite calibration.

The method using a planar target is more available in the LSLVS calibration than 3D target based method. Typically, the method based on the invariance of double cross-ratio uses a planar checkerboard-pattern target to realize the calibration of the LSLVS [5–7]. The intersections of the light stripe

plane and checkerboards with accurately known size can be obtained under the image coordinate system. Accordingly, feature points on the structured-light plane can be gained based on the invariance of double cross-ratio. Another calibration method represents the light stripe on a planar target with Plücker matrix [8]. Combining Plücker matrixes of the light stripes in different positions, the equation of the structured-light plane under the camera coordinate system can be solved. The method based on the vanishing point and vanishing line [9] is familiar. With a planar rectangle target, the normal vector of the structured-light plane can be calculated from its vanishing line. As the size of the target is known accurately, the representation of the structured-light plane can be deduced.

1D target based method [10, 11] is proposed as its convenient operation. One feature point, the intersection of the light stripe and the 1D target, can be got each time based on the invariance of double cross-ratio. By moving the target randomly into more positions, enough feature points can be obtained.

Xu et al. [12] use four spheres and a named standard board to get the expression of the plane through centers of the spheres and then attain the representation of the standard
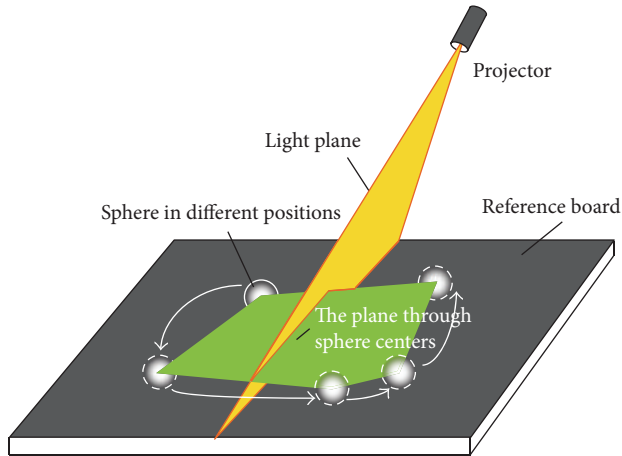
Figure 1: The principle of the calibration.

Figure 2: The measurement model of the LSLVS.

board as the known radius of each sphere. By moving the standard board into several positions, the height matrix, which gives the relationship between matching differences and height, can be deduced based on successive geometrical calculation. According to the model of calibration and the obtained height matrix, the structured light sensor of 3D measurement can be calibrated. Inspired by this method, a calibration method for line structured light vision sensor only using a white sphere and a black reference board is presented (see Figure 1).

By moving the sphere into several positions on the fixed reference board, we can get a plane through the centers of spheres in different positions. The center of each sphere under the camera coordinate system can be gained from its corresponding sphere projection on the image plane. Then the plane through the sphere centers (a virtual plane in order to express the reference board easily as illustrated in Figure 1) can be obtained by planar fitting easily. As the distance from the sphere center to the reference board is a known constant and the normal vector of the plane through sphere centers has been deduced, the representation of the reference board under camera coordinate system can be solved. Then a group of collinear feature points are obtained from the light stripe on the reference board.

Moving the target randomly into more than two different positions, we can get enough feature points of the structured-light plane easily. In this method, all feature points projected on the reference board can be used to fit the structured-light plane; meanwhile, the sphere projection is not concerned with the sphere orientation, which can make the calibration more accurate and robust.

2. Measurement Model of LSLVS

The location relationship between the camera in LSLVS and the structured-light plane projector remains unchangeable in the process of calibration and measurement. So the structured-light plane can be expressed as a fixed function,
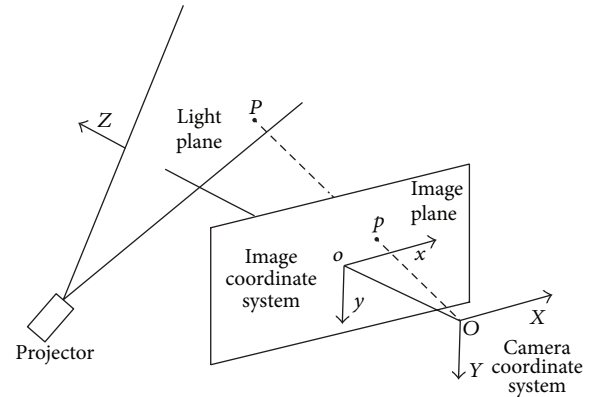
which is defined as (1), under the camera coordinate system. Consider

$$[A_L, B_L, C_L, D_L] [X, Y, Z, 1]^T = 0, \tag{1}$$

where A_L, B_L, C_L, and D_L are the parameters of the structured-light plane's expression.

The measurement model of LSLVS is illustrated in Figure 2. $O\text{-}XYZ$ is the Camera Coordinate System (CCS), while $o\text{-}xy$ is the Image Coordinate System (ICS). Under the CCS, the center of projection of the camera is at the origin and the optical axis points in the positive Z direction. A spatial point P is projected onto the plane with $Z = f_0$, referred to as the image plane under the CCS, where f_0 is the effective focal length (EFL). Suppose the point $p = (x, y, 1)^T$ is the projection of $P = (X, Y, Z)^T$ on the image plane. Under the undistorted model of the camera, namely the ideal pinhole imaging model, P, p and the center of projection O are collinear. The fact can be expressed by the following equation:

$$Z \begin{bmatrix} x \\ y \\ 1 \end{bmatrix} = \begin{bmatrix} f_0 & 0 & 0 & 0 \\ 0 & f_0 & 0 & 0 \\ 0 & 0 & 1 & 0 \end{bmatrix} \begin{bmatrix} X \\ Y \\ Z \\ 1 \end{bmatrix}. \tag{2}$$

Practically, the radial distortion and the tangential distortion of the lens are inevitable. When considering the radial distortion, we have the following equations:

$$\begin{aligned} \overline{x} &= x \left(1 + k_1 r^2 + k_2 r^4\right) \\ \overline{y} &= y \left(1 + k_1 r^2 + k_2 r^4\right), \end{aligned} \tag{3}$$

where $r^2 = x^2 + y^2$, $(x, y)^T$ is the distorted image coordinate, $(\overline{x}, \overline{y})^T$ is the idealized one, and k_1, k_2 are the radial distortion coefficients of the lens.

3. Calibration of the LSLVS

In our method, the calibration can be executed by the following three key points: (1) work out the coordinates of the sphere centers in different positions under the CCS,
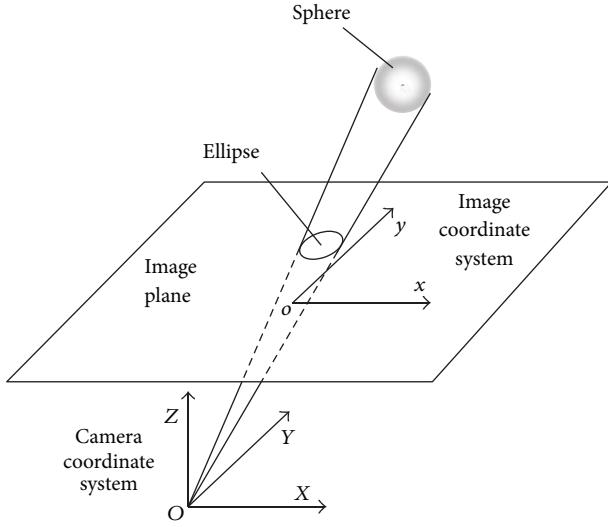
FIGURE 3: The projection relationship of a sphere.

(2) compute the function of the reference board from the coordinates of the sphere centers in different positions, (3) obtain enough feature points on the structured-light plane.

3.1. Calculation of the Sphere Center in 3D Space. The projection of a sphere on the image plane is an ellipse (see Figure 3), which can be expressed as a matrix form:

$$\begin{bmatrix} x \\ y \\ 1 \end{bmatrix}^T \begin{bmatrix} a & c/2 & d/2 \\ c/2 & b & e/2 \\ d/2 & e/2 & f \end{bmatrix} \begin{bmatrix} x \\ y \\ 1 \end{bmatrix} = 0, \quad (4)$$

where $(x, y, 1)^T$ is the homogeneous coordinate of the projective point on the image plane and a, b, c, d, e, f are the parameters of the elliptical expression. Fitting the ellipse on the image plane, the function of the ellipse under ICS can be obtained.

According to (2) and (4), we obtain the matrix representation of the right-circular cone under CCS as

$$[X \quad Y \quad Z] Q [X \quad Y \quad Z]^T = 0, \quad (5)$$

where the matrix Q is defined as

$$Q = \begin{bmatrix} A & C/2 & D/2 \\ C/2 & B & E/2 \\ D/2 & E/2 & F \end{bmatrix} \quad (6)$$

and the related definitions are shown as follows:

$$\begin{aligned} A = a f_0^2, \qquad B = b f_0^2, \qquad C = c f_0^2, \\ D = d f_0, \qquad E = e f_0, \qquad F = f. \end{aligned} \quad (7)$$

Defining

$$\bar{\lambda} = R \sqrt{\frac{|\lambda_1| \left(|\lambda_2| + |\lambda_3| \right)}{|\lambda_3| \left(|\lambda_1| + |\lambda_3| \right)}}, \quad (8)$$

the coordinate of the sphere center $[X_0 \quad Y_0 \quad Z_0]^T$ under CCS can be expressed by the following equation [13, 14]:

$$[X_0 \quad Y_0 \quad Z_0]^T = \bar{\lambda} [e_{3x} \quad e_{3y} \quad e_{3z}]^T, \quad (9)$$

where λ_1, λ_2, λ_3 are the eigenvalues of matrix Q, and λ_1 and λ_2 must have the same sign, while λ_3 must have the different one (when Q is a spherical matrix, we have $\lambda_1 = \lambda_2$), $[e_{3x} \quad e_{3y} \quad e_{3z}]^T$ is the eigenvector corresponding to λ_3, and R is the radius of the sphere.

3.2. Determination of the Reference Board. As the sphere with known radius R is moved on the reference board which is fixed in one position, we can get a plane through the centers of spheres located in different positions. Define the plane through the sphere centers as

$$[A_S, B_S, C_S, D_S] [X, Y, Z, 1]^T = 0. \quad (10)$$

When sphere centers located in more than three different positions have been gained, the unit normal vector of the plane through sphere centers under the CCS, which is expressed as $\vec{N} = [A_S, B_S, C_S]^T$ and the parameter D_S, can be solved.

As the plane through the sphere centers is in parallel with the reference board and the distance of the two planes is known as the radius R, according to (10), the reference board can be expressed as

$$[A_S, B_S, C_S, D_S + E_S] [X, Y, Z, 1]^T = 0. \quad (11)$$

The parameter E_S can be calculated as follows: defining the coordinate of the sphere center under the CCS as $(X_0, Y_0, Z_0)^T$, the direction vector from the origin to the sphere center is $\vec{n} = [X_0, Y_0, Z_0]^T$. As the target should locate in the positive Z direction under the CCS, the location relationship is illustrated in Figure 4. E_S can be deduced from the following equations:

$$E_S = \begin{cases} R, & \text{dot} \left(\vec{N}, \vec{n} \right) < 0 \\ -R, & \text{dot} \left(\vec{N}, \vec{n} \right) \geq 0. \end{cases} \quad (12)$$

3.3. The Structured-Light Plane. Combining (2) and (11), the light stripe on the reference board under CCS can be worked out. Moving the reference board randomly into different positions and repeating as mentioned in Section 3.2, we can get enough feature points on the structured-light plane. Fitting the structured-light plane by the linear least square method, the representation under the CCS (1) can be solved.

4. Simulations and Discussions

In this section, simulations have been conducted to evaluate the impacts of some factors on the proposed calibration method. The intrinsic parameters of the camera used in simulations are listed in Table 1.
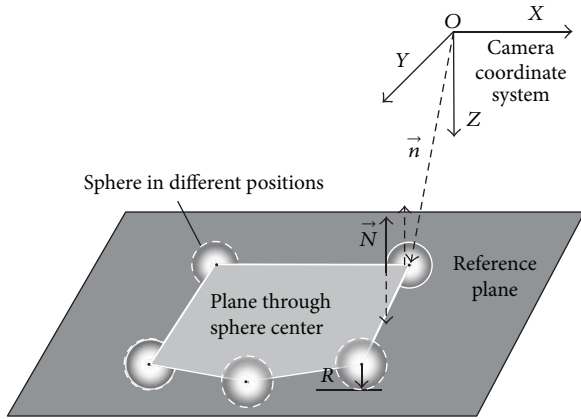
FIGURE 4: The sphere in different positions and the reference board under CCS.

TABLE 1: The intrinsic parameters of the camera.

f_0 (mm)	f_x (pixels)	f_y (pixels)	u_0 (pixels)	v_0 (pixels)
16	3953.4	3949.3	863.7	515.7

Where f_x is the scale factor in the x-coordinate direction, f_y is the scale factor in the y-coordinate direction, and $(u_0, v_0)^T$ are the coordinates of the principal point.

The simulation results are detailed below.

4.1. The Influence of the Projection and Light Stripe. In this method, feature points of the structured-light plane are obtained from the intersection of the reference board and the structured-light plane. Gaussian noise with means 0 is added to perturb both the sphere projection, which determined the precision of the reference board, and the light stripe on the image plane to evaluate the proposed method.

(1) The assumed radius of the sphere is 20 mm. Gaussian noise with standard deviations varying from 0 to 0.5 pixels is added to both coordinates of the image points to generate the perturbed image points of the sphere projections in different positions. In Figure 5, the Root-Mean-Square (RMS) error and the mean absolute error (MAE) are illustrated. These errors are solved from the intersection angle of two normal vectors, the idealized structured-light plane's and the perturbed one's. Each point in Figure 5 represents result averaged 100 uniformly distributed rotations.

(2) Gaussian noise with standard deviations varying from 0 to 1.0 pixel is added to both coordinates of the image points to generate the perturbed image points of the light stripe on the reference board. The Root-Mean-Square (RMS) error and the mean absolute error (MAE) are illustrated in Figure 6 with the same calculation method as mentioned in Figure 5. And each point in Figure 6 represents result averaged 100 uniformly distributed rotations.

From Figures 5 and 6 we can see that the calibration error, including the RMS error and the MAE, increases due to the
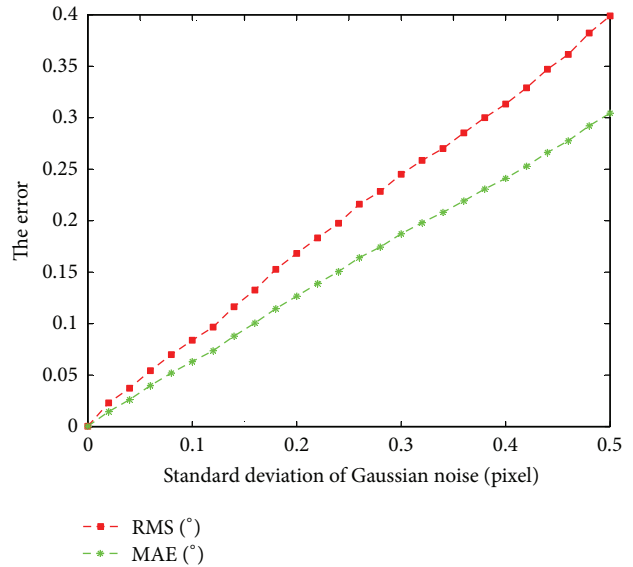

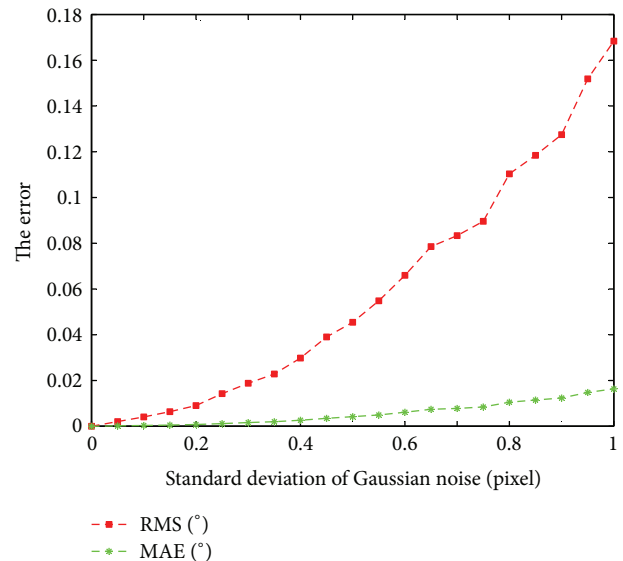FIGURE 5: The error as the function of the added Gaussian noise to sphere projections.

FIGURE 6: The error as the function of the added Gaussian noise to the light stripe.

bias of the image points on the sphere projections and the light stripe.

As we have only moved the sphere into 4 positions and the light stripe is fitted just by 1000 image points, the proposed method is significantly affected by the bias of the sphere projections.

4.2. The Influence of Other Factors. As the reference board is deduced from the plane through the sphere centers, the indirect factors to the calibration method include the radius, the number of movement, and localization of the sphere. The
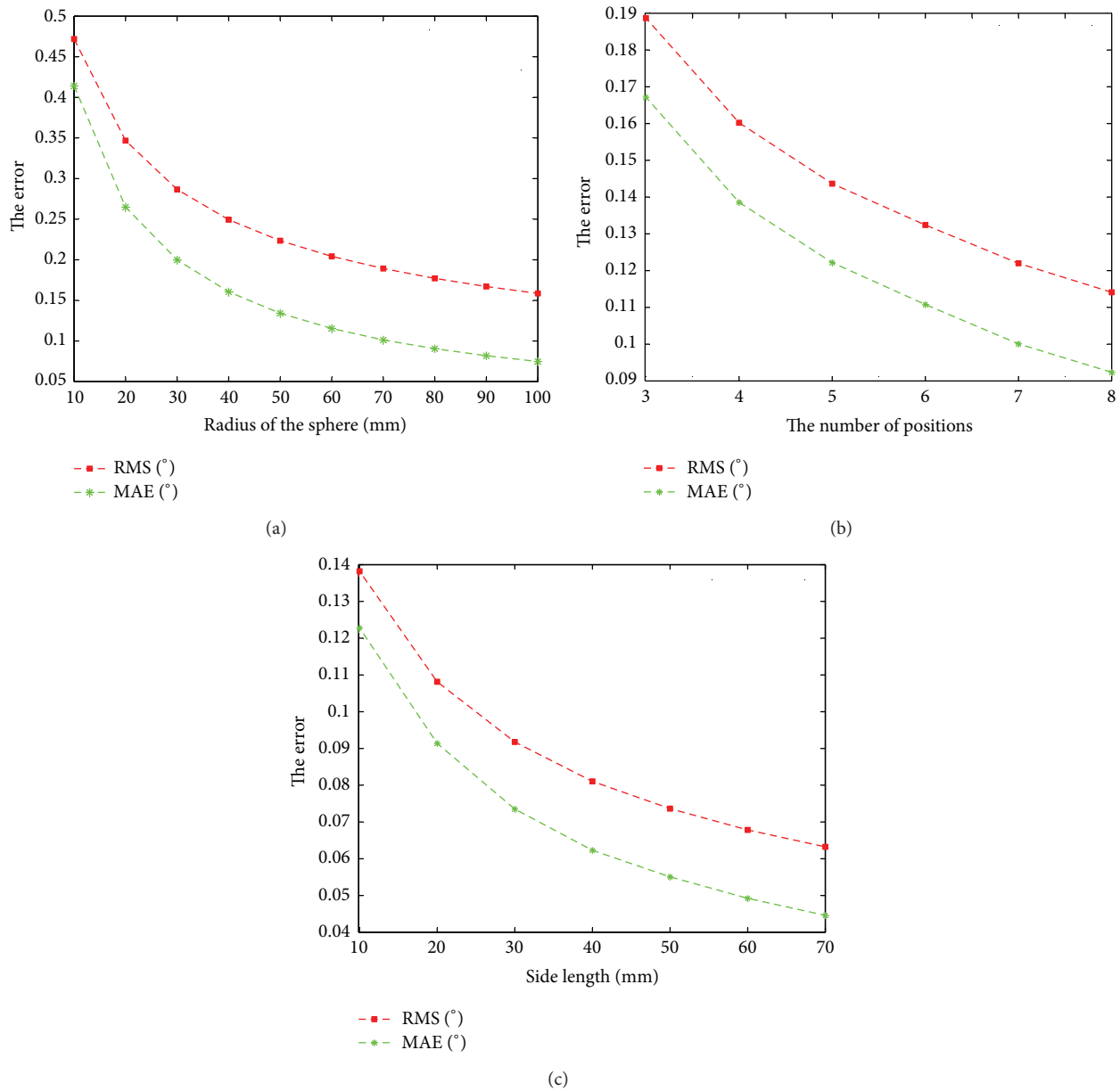
(a)

(b)

(c)

Figure 7: (a) The error as the function of radius of the sphere. (b) The error as the function of the number of positions. (c) The error as the function of the localizations of positions.

following simulations have been conducted to evaluate the impacts of the three factors.

(1) The sphere with radius varying from 10 mm to 100 mm has been assumed in our simulations. Four different positions are moved into in each simulation. Gaussian noise with means 0 and standard deviation 0.1 pixels is added to perturb the projections of the sphere in different positions on the image plane. The influence of the noise is illustrated in Figure 7(a).

(2) The sphere with a constant radius is moved into 3–8 different positions separately to fit the plane through the sphere centers in the simulations. Gaussian noise with means 0 and standard deviation 0.1 pixels is

added to both coordinates of the image points to generate the perturbed image points of the sphere projections. The effect of the noise to the calibration result, when different numbers of positions the sphere is moved into, is shown in Figure 7(b).

(3) The sphere with a constant radius is controlled to move into 4 different positions in the simulations. The four positions separately locate in the four vertices of a square with length of side varying from 10 mm to 70 mm. Gaussian noise with means 0 and a standard deviation 0.1 pixels is added to perturb the projections of the sphere in different positions. We get the effect as illustrated in Figure 7(c).
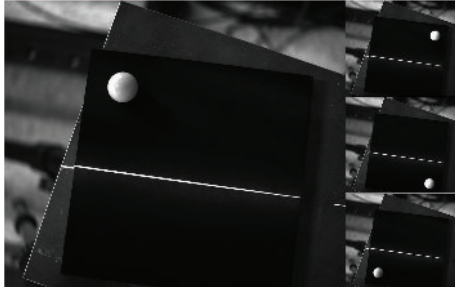
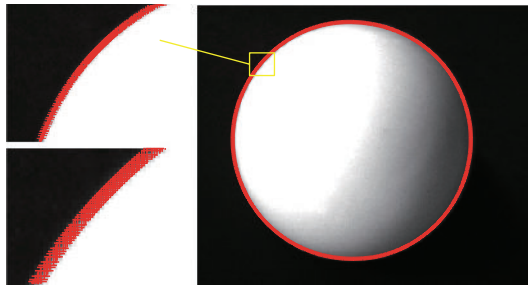FIGURE 8: The images of the real target.

FIGURE 9: The extraction of a sphere projection.

TABLE 2: The intrinsic parameters of the camera.

f_x (pixels)	f_y (pixels)	u_0 (pixels)	v_0 (pixels)	k_1	k_2
5125.2	5124.9	1270.7	1037.7	−0.2531	0.3777

In these figures, both the Root-Mean-Square (RMS) error and the mean absolute error (MAE) are illustrated. These errors are solved from the intersection angle of two normal vectors, the idealized structured-light plane's and the perturbed one's, which is the same as mentioned in Section 4.1. Each point in Figure 7 represents result averaged 100 uniformly distributed rotations.

From Figures 7(a) and 7(b), we can see that, when the radius is greater or there are more positions the sphere is moved into, the calibration result will be better. It also significantly shows that the result of the proposed calibration method will be better when the relative distance of the positions increases, as illustrated in Figure 7(c).

5. Experiments and Discussions

The camera used in our calibration experiment is AVT Stingray F-504B with a resolution of 2452∗2056 pixels and the view field is about 200 mm ∗ 200 mm. Intrinsic parameters of the camera are listed in Table 2. f_x, f_y, u_0, v_0 are defined as mentioned in Table 1, while k_1, k_2 are the radial distortion coefficients of the lens.

The radius of the sphere used in our experiment is 10 mm, with the accuracy of 10 μm, while the size of the black reference board is 150 mm ∗ 150 mm, with the machining accuracy of 30 μm (see Figure 8). The white sphere is moved into
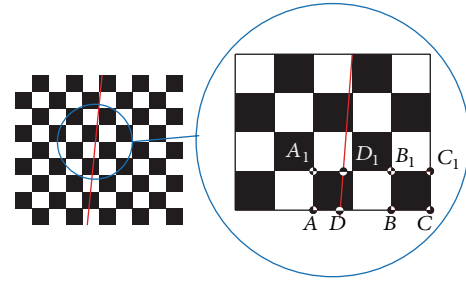

FIGURE 10: The obtainment of the real distance.

four positions on the black reference board. The structured-light plane projects on the reference board clearly, which is illustrated in Figure 8.

We first compensated for camera distortion by rectifying all real images. In order to improve the accuracy of the extraction of image points, including the contour of sphere projection and the light stripe on the image plane, the Hessian matrix algorithm is applied, which can make extracting of the image points at subpixel accuracy [15] (Figure 9).

5.1. Accuracy Evaluation. A checkerboard-pattern target is used to evaluate the accuracy of the proposed calibration method.

Real distance (R-dist.): the grid pitch of the target is known accurately as l, while the length of AD can be defined as l_0 (see Figure 10). Based on the invariance of cross-ratio, the following equation can be obtained:

$$\frac{AB/BD}{AC/DC} = \frac{2l/(2l - l_0)}{3l/(3l - l_0)}. \tag{13}$$

The real length of AD can be solved, so can A_1D_1. Then the distance between point D and point D_1 can be worked out.

Calculated distance (C-dist.): combining (1) with (2), bring point D and point D_1 under ICS into them, we can work out the coordinates under the CCS, and then the distance of the two points can be solved. Repeat until enough distances have been obtained. The results are shown in Table 3.

As the radius of the sphere used in our experiment is 10 mm and the positions of the reference board in the process of calibrating the line structured light vision sensor is 5, when we just move the sphere into four different positions on the reference board, the result with the accuracy of 0.102 mm is well enough. The calibration method will be more accurate and stable if the conditions are improved in the experiment as mentioned in Section 4.

5.2. The Number of Located Positions of the Reference Board. In our method, all the image points of the light stripe projected on the reference board are used to fit the structured-light plane. More feature points will be obtained when more calibration images are used in the experiment, and the result will be more stable. For the purpose of determination, the reference board is moved to 2–6 different positions, and the same number of images can be used to obtain the light stripe

Table 3: The result of our experiment (mm).

No.	R-dist.	C-dist.	Error	RMS
1	17.003	16.961	0.043	
2	17.003	16.959	0.045	
3	17.003	16.957	0.047	
4	17.003	16.955	0.049	
5	17.003	16.951	0.053	
6	17.001	16.997	0.004	
7	17.001	16.973	0.028	
8	17.001	16.961	0.040	
9	17.001	16.949	0.052	
10	17.001	16.985	0.016	0.102
11	17.000	17.195	−0.195	
12	17.000	17.135	−0.135	
13	17.000	17.074	−0.074	
14	17.000	17.014	−0.014	
15	17.000	16.955	0.045	
16	17.001	17.201	−0.200	
17	17.001	17.179	−0.178	
18	17.001	17.157	−0.156	
19	17.001	17.112	−0.112	
20	17.001	17.134	−0.134	

Table 4: The relation between the number of positions and the RMS error.

Amount	2	3	4	5	6
RMS (mm)	0.107	0.109	0.107	0.102	0.096

Table 5: The comparison with other methods.

Method	2D method	1D method	Sphere method
RMS (mm)	0.095	0.102	0.096

in the calibration experiment. The accuracy is evaluated by the method mentioned in Section 5.1, which is shown in Table 4.

5.3. The Comparison with Other Methods. Our proposed method is compared with two typical calibration methods which are suited for onsite calibration, the method based on the invariance of double cross-ratio (2D target based method) [7] and the method based on 1D target [11]. As listed in Table 5, we can see that the three calibration methods have nearly the same accuracy obtained from experiments.

Nevertheless, in the two typical calibration methods, only a few feature points on the light stripe are used to obtain the structure-light plane, which is improved in our proposed method as all feature points projected on the reference board are used to fit the structured-light plane. This feature makes the calibration stable and robust. Meanwhile, the traditional calibration methods have the problem of visual angle. When observed from different angles, different images of light stripe will be obtained, which can affect the accuracy of the calibration and restrict the movement of the

target. However, the sphere-based method can prevent it, as the sphere projection is not concerned with the sphere orientation.

6. Conclusion

The method presented in this paper utilizes a sphere target to finish the calibration of line structured light vision sensor. As the function of the reference board can be deduced from the projections of the spheres in different positions under the camera coordinate system, enough feature points on the structured-light plane can be obtained by moving the target into several different positions. In this paper, we have conducted enough simulations and experiments to evaluate the proposed calibration method. As all feature points projected on the reference board can be used to fit the structured-light plane and the sphere projection is not relative of the sphere orientation, the calibration is improved more accurately and robustly. Experimental results show the accuracy of the method can reach 0.102 mm within the view field of about 200 mm ∗ 200 mm, which can be improved if the experiment conditions are better. Additionally, efficiency and convenience can be deduced from the free combination of one sphere and a reference board. So this method is generally efficient for on-site calibration and no less accurate than other classical calibration methods.

Acknowledgments

References

[1] G. Zhang, *Vision Measurement*, Science Press, 2008.

[2] R. Dewar, "Self-generated targets for spatial calibration of structured light optical sectioning sensors with respect to an external coordinate system," in *Proceedings of the Robots and Vision Conference*, pp. 5–13, Detroit, Mich, USA, 1988.

[3] K. W. James, "Noncontact machine vision metrology with a CAD coordinate system," *Autofact'88 Conference Proceedings*, pp. 9–17, 1988.

[4] F. Duan, F. Liu, and S. Ye, "A new accurate method for the calibration of line structured light sensor," *Chinese Journal of Scientific Instrument*, vol. 211, pp. 108–110, 2000.

[5] G. Xu, L. Liu, and J. Zeng, "A new method of calibration in 3D vision system based on structure-light," *Chinese Journal of Computers*, vol. 18, no. 6, pp. 450–456, 1995.

[6] D. Q. Huynh, R. A. Owens, and P. E. Hartmann, "Calibrating a structured light stripe system: a novel approach," *International Journal of Computer Vision*, vol. 33, no. 1, pp. 73–86, 1999.

[7] Z. Wei, G. Zhang, and Y. Xu, "Calibration approach for structured-light-stripe vision sensor based on the invariance of double cross-ratio," *Optical Engineering*, vol. 42, no. 10, pp. 2956–2966, 2003.

[8] Z. Liu, G. Zhang, Z. Wei, and J. Jiang, "An accurate calibration method for line structured light vision sensor," *Acta Optica Sinica*, vol. 29, no. 11, pp. 3124–3128, 2009.

[9] Z. Wei, M. Xie, and G. Zhang, "Calibration method for line structured light vision sensor based on vanish points and lines," in *Proceedings of the 20th International Conference on Pattern Recognition (ICPR '10)*, pp. 794–797, August 2010.

[10] Z. Wei, L. Cao, and G. Zhang, "A novel 1D target-based calibration method with unknown orientation for structured light vision sensor," *Optics and Laser Technology*, vol. 42, no. 4, pp. 570–574, 2010.

[11] F. Zhou and F. Cai, "Calibrating structured-light vision sensor with one-dimensional target," *Journal of Mechanical Engineering*, vol. 46, no. 18, pp. 7–12, 2010.

[12] J. Xu, J. Douet, J. Zhao, L. Song, and K. Chen, "A simple calibration method for structured light-based 3D profile measurement," *Optics and Laser Technology*, vol. 48, pp. 187–193, 2013.

[13] Y. Shiu and S. Ahmad, "3D location of circular spherical features by monocular model-based vision," in *Proceedings of the IEEE Conference on System, Man and Cybernetics*, pp. 576–581, Cambridge, Mass, USA, 1989.

[14] R. Safaee-Rad, I. Tchoukanov, K. C. Smith, and B. Benhabib, "Three-dimensional location estimation of circular features for machine vision," *IEEE Transactions on Robotics and Automation*, vol. 8, no. 5, pp. 624–640, 1992.

[15] C. Steger, *Unbiased extraction of curvilinear structures from 2D and 3D image [Ph.D. Dissertation]*, Technische Universitaet Muenchen, 1998.

Research Article

Marker Identification Technique for Deformation Measurement

Huaiwen Wang[1,2]

[1] *Tianjin Key Laboratory of Refrigeration Technology, Tianjin University of Commerce, Tianjin 300134, China*
[2] *School of Mechanical Engineering, Tianjin University of Commerce, Tianjin 300134, China*

Correspondence should be addressed to Huaiwen Wang; wanghw@tjcu.edu.cn

A technique for noncontact optical measurement of in-plane displacement based on correlation analysis is presented. This approach can be used to identify the position of a marker before and after deformation of a specimen or plane test object. Some mechanical parameters of materials and strains can be calculated using information from several markers' displacement. The method is simpler than other optical techniques in experimental processing and can be efficiently used to measure large deformations. Two applications of this method are illustrated. One application of this method is to test the mechanical behavior of polymer film material. Another application of this method is to measure the displacement field in a strata movement simulation experiment.

1. Introduction

Surface deformation measurement is one of the key factors in the experimental mechanics. Many optical methods have been developed for this aim, such as Moiré interferometry [1–3], shearography [4], electronic speckle pattern interferometry (ESPI) [5], and digital speckle correlation method (DSCM) [6–9]. Each method has its advantages and disadvantages in different fields of application. The DSCM enables direct measurement of the surface deformation field to subpixel accuracy. Due to its advantages of noncontact, whole field, wide measuring range, and so forth, some of its applications in the field of experimental mechanics have been achieved in recent years [10–12]. Publications in a wide range of journals have attracted the attention of both researchers and practitioners with backgrounds in the mechanics of solids, applied physics, mechanical engineering, and materials science [13–16].

In this paper, a marker identification technique is developed, which can be used to recognize the position of a marker before and after deformation. The method is based on the correlation theory and has some special assets. Its experimental procedure is simpler than that of the DSCM. For illustration the marker identification method (MIM) is used to test some material parameters of polymer film and measure the displacement fields in a strata movement simulation experiment.

2. Marker Identification Method (MIM)

Correlation theory has been widely used in the fields of physics, chemistry, mathematics, mechanics, image processing, and so forth. A correlation coefficient is a quantitative assessment of the strength of relationship between two variables in a set of (x, y) pairs [8, 17, 18]. In experimental mechanics field, correlation coefficient is an important tool in particle image velocimetry (PIV) techniques [19] and digital speckle correlation method [20, 21]. For this method, an image of a plane specimen surface is recorded before loading and defined as an undeformed pattern. Other images of the deformed pattern are taken during loading the specimen. These images show a deformed pattern relative to the undeformed pattern. From the difference between both these patterns the deformations can be calculated. Then the experimental measurement becomes a process of mathematical calculation, in which the correlation criterion plays the function of bridge [22–24].

In the marker identification process the information carriers are dots marked on the surface of the specimen or the object, respectively. Several dots were marked on the

specimen and sometimes the natural texture on the specimen surface also can be used as those dots. Before and after loading, two patterns of the specimen were recorded by a charge coupled device (CCD) camera and stored in computer as data files. The measurement system used in the tests is shown in Figure 1.

A subset, whose center is one marked dot, is selected as the reference subset in the undeformed image. The next step is to find the target subset, that is, finding the location where the reference subset moves to. The coordinate system and deformation of the markers are illustrated in Figure 2. In order to find the best possible estimation of the deformation values a criterion must be established mathematically. Here we use a cross-correlation coefficient for the two subsets that can be written as [12]

$$C = \frac{\sum \left(f_i\left(x,y\right) - \overline{f} \right) \cdot \left(g_i\left(x^*, y^*\right) - \overline{g} \right)}{\sqrt{\sum \left(f_i\left(x,y\right) - \overline{f} \right)^2 \cdot \sum \left(g_i\left(x^*, y^*\right) - \overline{g} \right)^2}}, \quad (1)$$

where (x, y) and (x^*, y^*) are Cartesian coordinates of a material point in the two subsets. $f_i(x, y)$ and $g_i(x^*, y^*)$ are gray levels of that point in the corresponding subsets, and $\overline{f}$ and $\overline{g}$ are the average values of $f_i(x, y)$ and $g_i(x^*, y^*)$, respectively. Each of these subset points (x, y) is mapped on to (x^*, y^*) using

$$x^* = x + u,$$
$$y^* = y + v, \quad (2)$$

where u and v are the in-plane displacement components of each subset's center point.

The correlation coefficient C represents how close the related two subsets are, with $C = 1$ corresponding to perfect correlation. Owing to the systematic errors, random errors, and the distortion of image, the correlation coefficient C cannot equal 1 in practice generally. The maximum of C is considered as the coincidence of the assumed displacement with the actual deformation components.

The digital pattern obtained by a digitizer is given as discrete data. To accurately determine the deformation at arbitrary locations, an interpolation method should be used. In this present work, a bicubic polynomial interpolation method is used which can be expressed as a convolution operator with the kernel function

$$\text{Cubic}\left(d\right) = \begin{cases} (d-2)\,dd + 1, & (d \le 1), \\ [(5-d)\,d - 8.0]\,d + 4.0, & (1 < d \le 2), \end{cases} \quad (3)$$

where d is the x or y component of the distance between the sampled pixels and the subpixel location. With this method, the gray value of an arbitrary location (x, y) is calculated by the formula

$$g\left(x,y\right) = \sum_{i=1}^{4}\sum_{j=1}^{4} g\left(x_i, y_j\right)\text{Cubic}\left(dx_i\right)\text{Cubic}\left(dy_j\right), \quad (4)$$

where $g(x_i, y_j)$ is the gray value of the nearest 4×4 sampled pixels around the subpixel location and dx_i and dy_j are the x

and y components of the distance between the sampled pixels (x_i, y_j) and the subpixel location, respectively. The flow chart for the marker identification routine is shown in Figure 3.

Considering a point P on the object surface and two small segments PA and PB along x-axis and y-axis, as shown in Figure 2, the normal strain and the shear strain can be determined according to the theory of linear elasticity. Linear elastic material response and small deformations provided

$$\varepsilon_x = \frac{\left(u_A - u_P\right)}{\overline{PA}},$$

$$\varepsilon_y = \frac{\left(v_B - v_P\right)}{\overline{PB}},$$

$$\gamma_{xy} = \alpha + \beta \approx \tan\alpha + \tan\beta = \frac{\left(v_A - v_P\right)}{\overline{PA}} + \frac{\left(u_B - u_P\right)}{\overline{PB}}, \quad (5)$$

where $u_i = x_i' - x_i,\ v_i = y_i' - y_i\ (i = P, A, B),\ \overline{PA} = x_A - x_P,$ and $\overline{PB} = y_B - y_P.$

The aim of material testing is to determine the characteristic material parameters, that is, Young's modulus E and Poisson's ratio ν or the shear-modulus G, respectively. As the three quantities are depending on each other, if the loading force F_x and the cross-section area A_0 in the unloaded state are given, assuming linear elastic material response, the stress state is known; then (6) yields Young's modulus E and either Poisson's ratio ν or the shear-modulus G:

$$\nu = -\frac{\varepsilon_y}{\varepsilon_x},$$

$$A\left(\varepsilon\right) = A_0\left(1 - \nu \cdot \varepsilon_x\right)^2 = A_0\left(1 + \varepsilon_y\right)^2,$$

$$\sigma_x = \frac{F_x}{A\left(\varepsilon\right)} = \frac{F_x}{A_0}\left(1 + \varepsilon_y\right)^{-2},$$

$$E = \frac{F_x}{A_0} \times \varepsilon_x^{-1} \times \left(1 + \varepsilon_y\right)^{-2},$$

$$\left(G = \frac{E}{2\left(1 + \nu\right)}\right). \quad (6)$$

3. Analysis and Discussion of Marker Identification Method

The precision of displacement measurement of the marker identification method is similar to that of the DSCM in small deformation region, that is, accuracy up to ±0.01 pixels in theory (it may be up to ±0.05 pixels or even more in practice owing to the effect of systematic errors, random errors, and the quality of the computer vision system). And in large deformation region, the error will be higher than that in small deformation. The precision of the strain measurement is directly related to the displacement identification of the marker and the distance between markers, so it can be improved by increasing the distance between markers and employing high quality CCD camera and digitizing board.
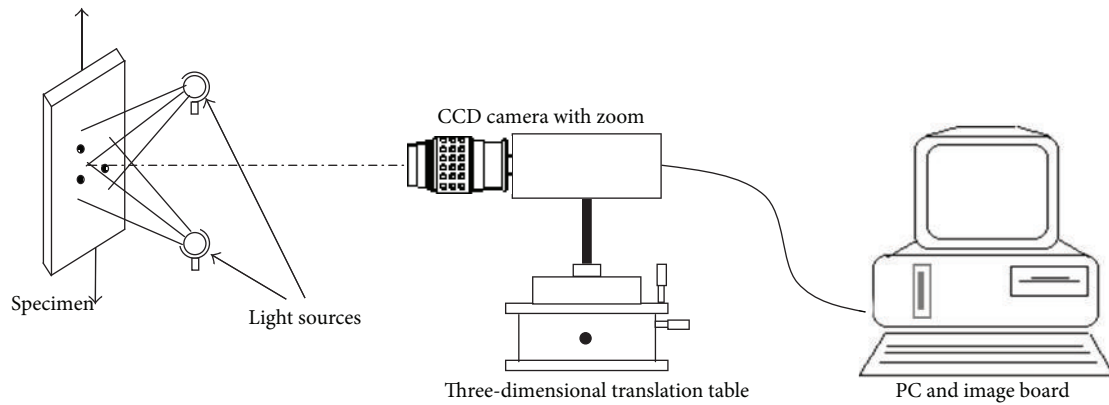
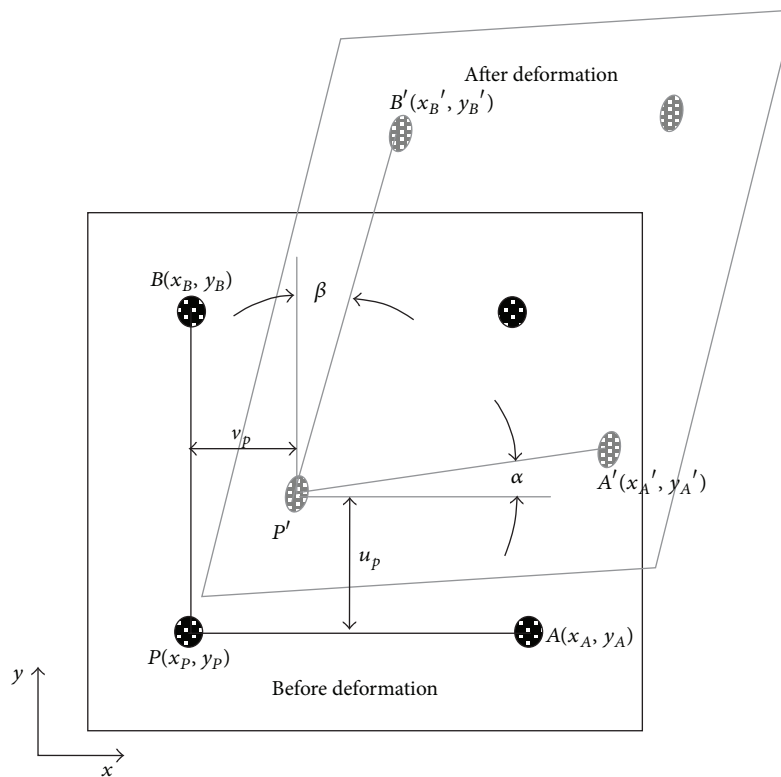FIGURE 1: Schematic of computer vision system.

FIGURE 2: Markers and their deformation kinematics.

The MIM has some special advantages than other optical techniques in experimental mechanics. Firstly, the preparative procedure of the experiment is simpler than that of the DSCM. No speckle field is needed on the specimen surface and the information carrier of deformation is marked by dots. Making several artificial markers or selecting several natural markers on the specimen's surface will be easy to realize. Secondly, the distribution of correlation coefficient is unimodal, as shown in Figure 4(a). In digital speckle correlation method the correlation coefficient distribution in an area of calculation is single-peaked in a small area with some small peaks in the surrounding area, as shown in Figure 4(b). The unimodality of correlation coefficient broadens the

measuring region and the proposed method can be used to measure small deformation as well as large deformation. Thirdly, owing to the unimodality of correlation coefficients, the chance of misidentification is reduced in the progress of calculation, and the conditions and environment of the testing are not stringent. Fourthly, this method can be used from microscale to macroscale. The size and color of the markers can be chosen for different testing objects. The actual size of the marker relies on the enlargement factor of the image capture system. This size of the marker on the captured pictures must be smaller than the subset for correlation calculation. The color of the marker should have high-contrast to the specimen's surface. MIM can be used
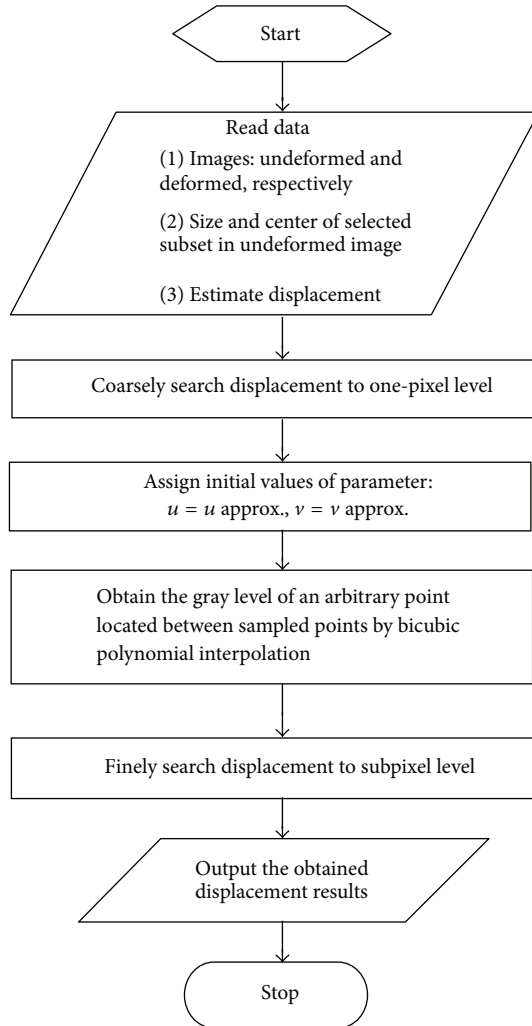
Figure 3: Flow chart for the marker identification routine.

Table 1: Results of the simulated strain.

	Exact values	Measured values	Difference	Error (%)
Case 1				
ε_x	0	0	0	
ε_y	0	0	0	
Case 2				
ε_x	0.25	0.2510	0.0010	0.4%
ε_y	−0.1	−0.1005	−0.0005	0.5%
Case 3				
ε_x	0.5	0.5119	0.0119	2.38%
ε_y	−0.2	−0.1965	0.0035	−1.75%

were all compared with the reference image by the marker identification method. The exact strain for case 1 should be $\varepsilon_{1x} = 0$, $\varepsilon_{1y} = 0$, for case 2 should be $\varepsilon_{1x} = 0.25$, $\varepsilon_{1y} = −0.1$, and for case 3 should be $\varepsilon_{1x} = 0.5$, $\varepsilon_{1y} = −0.2$, respectively. The corresponding strains were calculated to be $\varepsilon_{1x} = 0$, $\varepsilon_{1y} = 0$ for case 1, $\varepsilon_{1x} = 0.2510$, $\varepsilon_{1y} = −0.1005$ for case 2, and $\varepsilon_{1x} = 0.5119$, $\varepsilon_{1y} = −0.1965$ for case 3. Here the distance between the selected makers is 276 pixels and 268 pixels in x and y direction, respectively.

The results are summarized in Table 1. It is shown that the marker identification method is precise and can be effactually used to measure the strain in wide measurement range.

4.2. Uniaxial Tension Test. The experiment involved a uniaxial tension test of Nylon 6 polymer film material. The specimen's shape and dimensions are shown in Figure 6. Dots are marked on its surface as shown in Figure 7. During the measurement the ambient temperature has been kept constant at 20°C. The experiment has been performed on a CSS-44100 electronic universal testing machine. The crossbeam speed has been set to 1 mm/min.

The load-time curve is shown in Figure 8(a). The computer vision system was working parallel to the loading process and the images were taken every 15 seconds. The image board digitizes each video line into 768 pixels while counting 576 video lines through each frame, and the discrete intensity values are recorded in 256 gray levels in the vision system.

By calculating the elongation between points 1 and 3, 4 and 6, and 7 and 9, respectively (see Figure 6), three values ε_{x1}, ε_{x2}, and ε_{x3} at time t_i were obtained, the mean value of which $\overline{\varepsilon_x} = (1/3)(\varepsilon_{x1}, \varepsilon_{x2}, \varepsilon_{x3})$ yields the longitudinal strains of the specimen. So the strain-time curve can be obtained by calculating the longitudinal strains at different times, as shown in Figure 8(b).

The load-time curve and the strain-time curves are connected over the time. Regarding (5) the stress-strain curve in longitudinal direction can be achieved as shown in Figure 8(c). The transversal strains are calculated in the same way and the stress-strain curve in cross-direction was also obtained as shown in Figure 8(d).
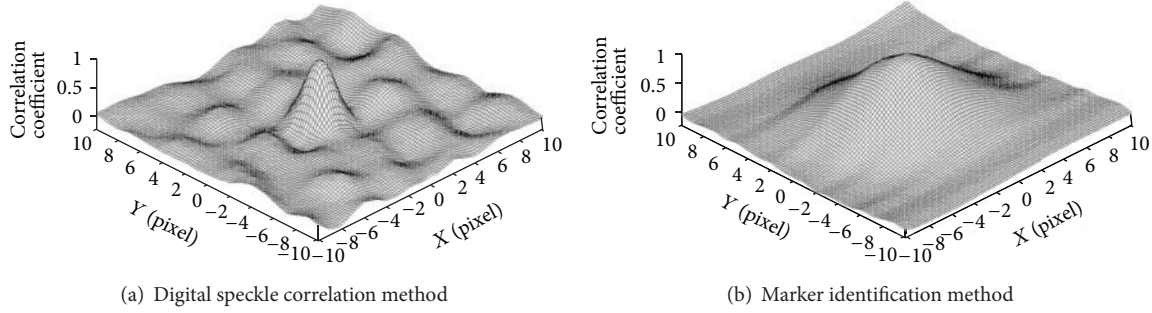
in some special testing and environment conditions, such as engineering testing, long-term testing, temperature, moist, and humid environment.

4. Application of Marker Identification Method in Mesoscale

In this section, the measurement range and the precision of the method have been discussed by a simulated test. And then a uniaxial tension test and a creep test of polymer film material also have been performed to demonstrate the application of the MIM.

4.1. Discussion for the Measurement Range and the Precision. The measurement range and the precision of the method are discussed by a simulated test. In this test, first, an image was captured as the reference image. And deformed images with 0%, 25%, and 50% actual deformations were created, as shown in Figure 5, by an image processing software. Here we assumed that the Poisson ratio was a constant and was equal to 0.4. Then the deformed images including reference image

(a) Digital speckle correlation method

(b) Marker identification method

FIGURE 4: Distribution of the correlation coefficient.
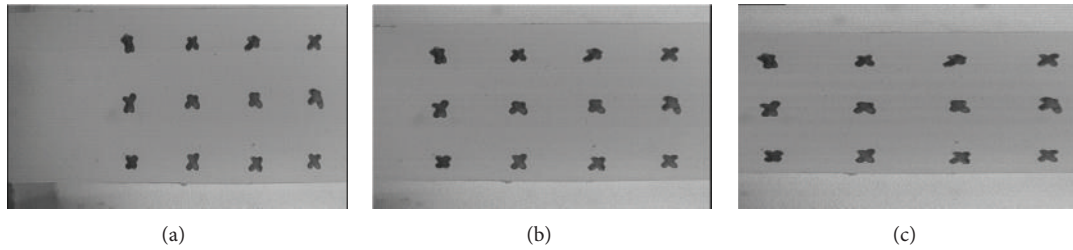

(a)

(b)

(c)

FIGURE 5: Images for simulated test: (a) undeformed image, (b) deformed image with 20% actual deformation, and (c) deformed image with 50% actual deformation.
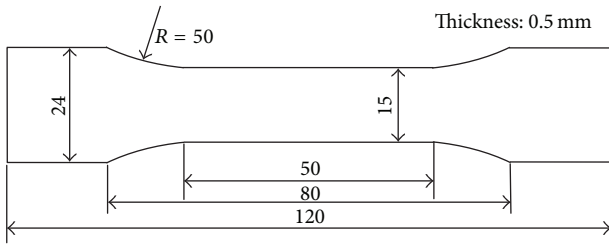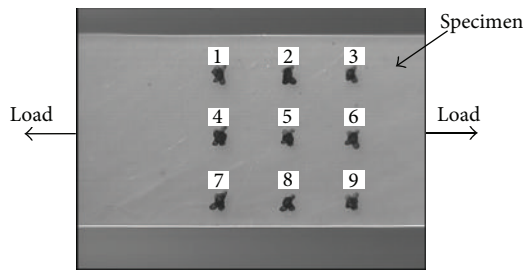

FIGURE 6: Dimension of the specimen.

FIGURE 7: Marked dots on the specimen (i stands for the ith dot, $i = 1, 2, \ldots, 9$).

In the elastic deformation state Young's modulus $\overline{E} = 1.04$ GPa and Poisson's ratio $\overline{\nu} = 0.406$ are calculated according to (6).

4.3. Creep Test. The third experiment is related to testing the time-depending response of macromolecular film material. The strain state was determined by measuring the deformations over time by means of the MIM. Based on the obtained data the material response, that is, the bulk-modulus $K(t)$ as a function of time, and Poisson's ration were calculated. The specimen of size $60 \times 3.83 \times 0.5$ mm was loaded by constant load $F = 40$ N. The measurements were performed in time intervals $\Delta T = 60$ min. Taking into account the lateral contraction of the cross-section, the stress $\sigma(x)$ as a function of time holds

$$\sigma_x(t) = \frac{F}{b \cdot d}\left[1 - \nu(t) \cdot \varepsilon_x(t)\right]^{-2}. \tag{7}$$

At time $t(0^+) = 2$ min. ε_x and ε_y were determined, yielding a mean value of Poisson's ratio of $\nu(0^+) = 0.406$. Further measurements had proven that the changes of Poisson's ratio over time could be neglected:

$$\nu(t) \approx \nu(0^+) \approx \text{const.} \tag{8}$$

Based on Boltzmann's superposition principle [14] the relation between the uniaxial stress state and the strain state runs in discrete formulation [15, 16], and linear viscoelastic material response provided

$$\sigma_x(t) = 3(1 - 2\nu)$$
$$\times \left\{ K(0^+) \cdot \varepsilon_x(t_n) \right.$$
$$\left. - \frac{1}{2}\sum_{\nu=1}^{n}\left[K(t_n - t_\nu) - K(t_n - t_{\nu-1})\right] \right. \tag{9}$$
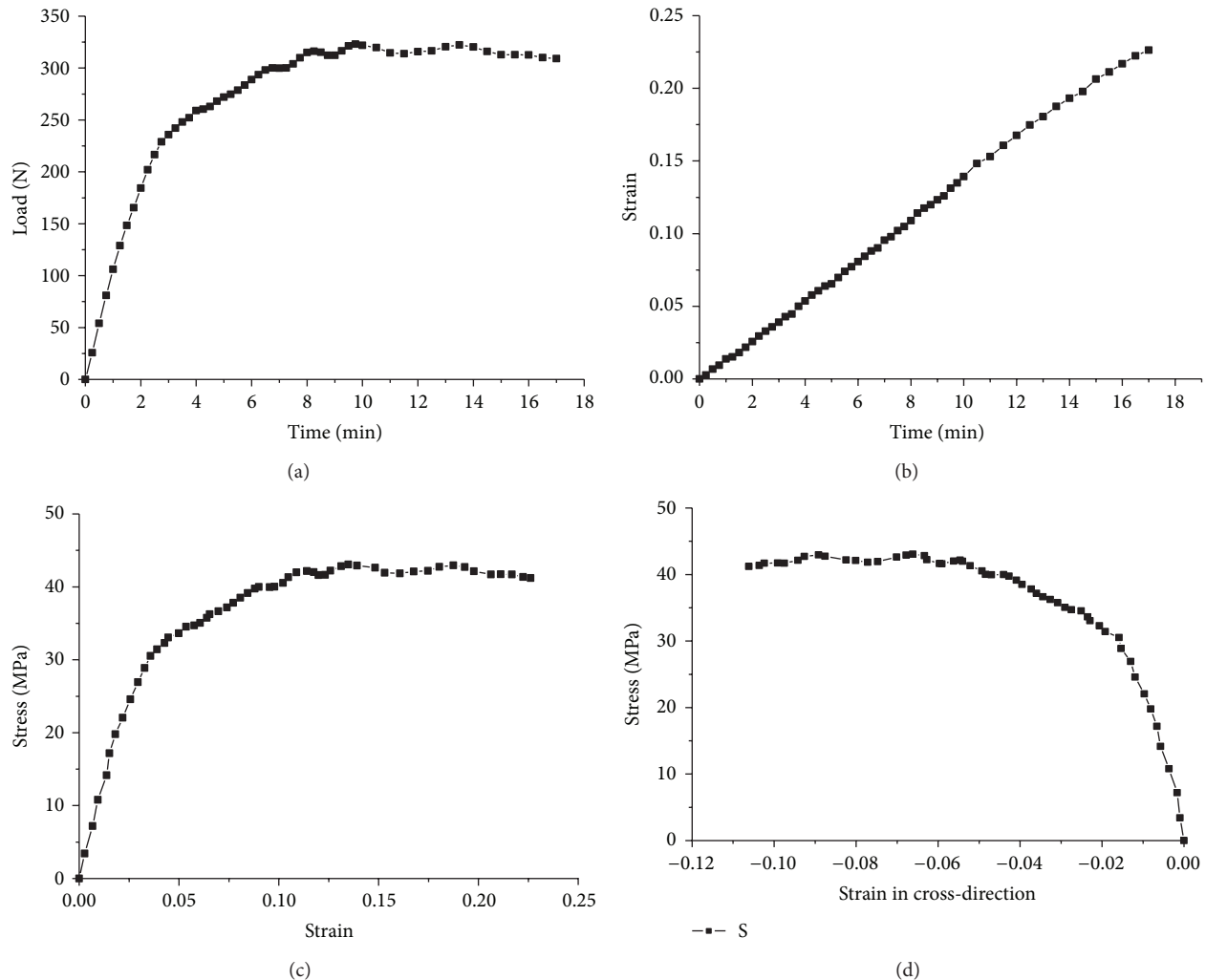$$\left. \times \left[\varepsilon_x(t_{\nu-1}) + \varepsilon_x(t_\nu)\right] \right\},$$

FIGURE 8: Experimental results of the marker identification method for Nylon 6 polymer film material. (a) Load versus time curve, (b) strain versus time curve, (c) stress versus strain curve of the material, and (d) stress versus strain curve in cross-direction.

where $K(t)$ denotes the bulk-modulus. The result of the evaluation according to (9) is given in Table 2 and Figure 9, respectively.

5. Application of Marker Identification Method in Macroscale

To carry out simulative experiment of similar materials is a common way to investigate the law of movement of the mined rock under the condition of mining in depth [25–27]. In this section, the MIM is used to measure the strata movement displacement fields.

5.1. Simulative Experiment of Similar Materials in Mining Progress. According to the actual status of a working face in Huainan Coal Group Co., Ltd., we made a similar material model. The different strata were simulated by similar materials with different proportioning of sand, gypsum, and white

lime. An artificial faultage was made by mica powder. In order to measure the deformation of the model, some markers ($15 \times 17 = 255$) were made on the surface of the model, as shown in Figure 10. The model and the actual status of the working face must meet geometric similarity, kinematics similarity, and boundary condition similarity.

In order to capture the patterns of the model under different deformation states, an optical image capture system was employed. The image capture device used here was a digital camera, instead of CCD camera with image board. Before exploitation, a pattern was captured as the undeformed pattern. Then, with the process of exploitation, patterns under different advances were captured as deformed patterns.

The deformation fields of the model under different advances can be obtained by the MIM. For example, the displacement fields in vertical direction with advance length equal to 1.836 m and 2.232 m are shown in Figure 11. The stability and subsidence rule of strata can be achieved by the analysis of these deformation fields.

TABLE 2: Results of the strain and bulk-modulus in creep test.

	1	2	3	4	5	6	7	8	9	10	11	12	13	14	15
Time (min)	2	60	120	180	240	300	360	420	480	540	600	660	720	780	840
$\varepsilon_x(t)$ (%)	2.37	4.0	4.95	5.50	5.75	5.9	6.0	6.1	6.2	6.27	6.35	6.41	6.47	6.53	6.60
$K(t)$ (N/mm^2)	1500.6	745	612	607	605	599	595	581	571	563	561	558	554	548	543
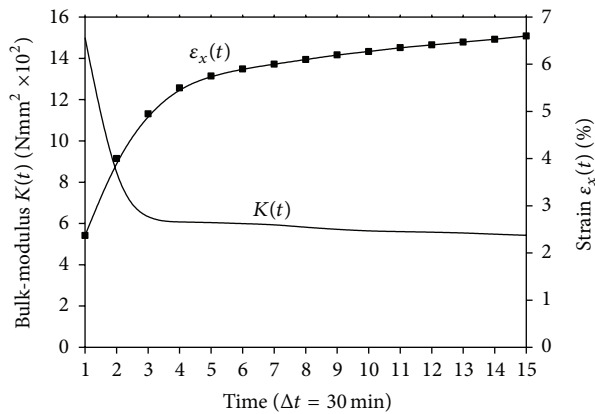
FIGURE 9: Results of the strain and bulk-modulus in creep test.
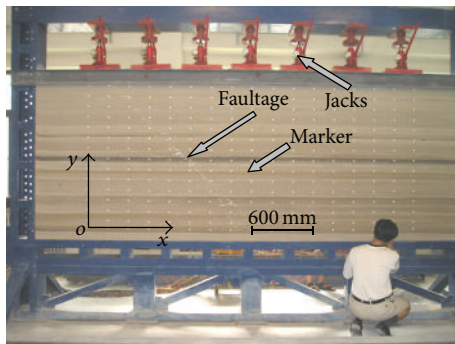
FIGURE 10: General picture of the experimental model.

(a) Advance length equal to 1.836 m

(b) Advance length equal to 2.232 m

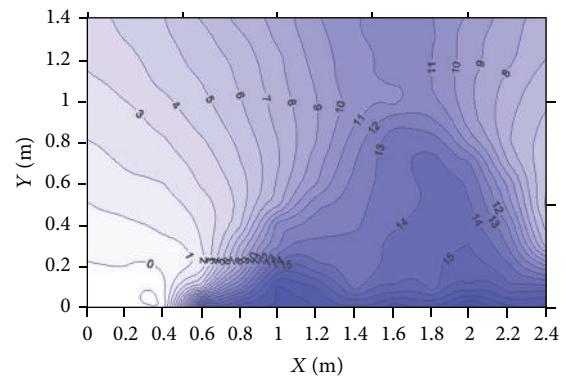FIGURE 11: Displacement contour map in vertical direction with different advances (unit: mm).

5.2. Precision Analysis in This Experiment. As a noncontacted optical measurement technique, the precision of the MIM may reach subpixel level. The magnification factor used here is 1 mm = 0.75 pixels. Thus, the error of method is less than 1 mm. To quantitatively evaluate the error of the MIM in this paper, a comparison between the MIM and the theodolite was made, as shown in Figure 12. We can see that the measurement results by the MIM agree well with the results by the theodolite.

6. Conclusion

An optical experimental technique, the "marker identification method" (MIM), has been presented, which shows special advantages. The measurement setup is quite simple and does not need special equipment, so MIM can be regarded as a low-cost method, which is easy to handle in practice. The
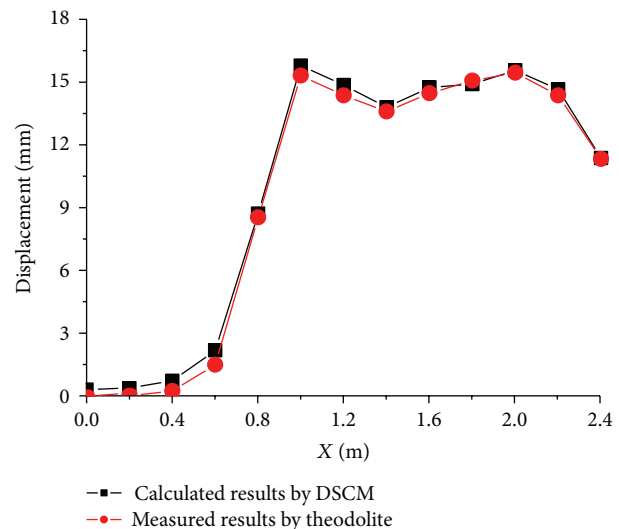

FIGURE 12: Results of comparison between MIM and theodolite.

accuracy of the method is enough to practical applications, material properties' test, and structural analyses. It has been shown that the method can be used effectively not only in the range of linear elasticity but also in the analysis of viscoelastic problems. Further on it is possible to measure finite displacement as well as to take into account nonlinear and elastic-plastic material response. Illustrations indicate that this method not only can be used in mesoscale but also can be used in macroscale.

Acknowledgments

References

[1] K. Yilan and L. Hua, "Investigation of near-tip displacement fields of a crack normal to and terminating at a bimaterial interface under mixed-mode loading," *Engineering Fracture Mechanics*, vol. 69, no. 18, pp. 2199–2208, 2002.

[2] W. Qiu, Y. L. Kang, Q. H. Qin, and W. T. Li, "Regional identification, partition, and integral phase unwrapping method for processing Moiré interferometry images," *Applied Optics*, vol. 45, no. 25, pp. 6551–6559, 2006.

[3] W. Qiu, Y. L. Kang, Q. H. Qin, Q. C. Sun, and F. Y. Xu, "Study for multilayer piezoelectric composite structure as displacement actuator by Moiré interferometry and infrared thermography experiments," *Materials Science and Engineering A*, vol. 452-453, pp. 228–234, 2007.

[4] X. Xie, N. Xu, J. F. Sun, Y. H. Wang, and L. X. Yang, "Simultaneous measurement of deformation and the first derivative with spatial phase-shift digital shearography," *Optics Communications*, vol. 286, pp. 277–281, 2013.

[5] Y. W. Qin, J. Chen, and H. B. Fan, "The study and application of a new filtering method on electronic speckle pattern interferometric fringe," *Optics and Lasers in Engineering*, vol. 39, no. 4, pp. 449–456, 2003.

[6] H. W. Wang and Y. L. Kang, "Improved digital speckle correlation method and its application in fracture analysis of metallic foil," *Optical Engineering*, vol. 41, no. 11, pp. 2793–2798, 2002.

[7] Z. F. Zhang, Y. L. Kang, H. W. Wang, Q. H. Qin, Y. Qiu, and X. Q. Li, "A novel coarse-fine search scheme for digital image correlation method," *Measurement*, vol. 39, no. 8, pp. 710–718, 2006.

[8] Q. Li, Y. L. Kang, W. Qiu et al., "Deformation mechanisms of carbon nanotube fibres under tensile loading by insitu Raman spectroscopy analysis," *Nanotechnology*, vol. 22, no. 22, Article ID 225704, 2011.

[9] W. Qiu, Q. Li, Z. K. Lei, Q. H. Qin, W. L. Deng, and Y. L. Kang, "The use of a carbon nanotube sensor for measuring strain by micro-Raman spectroscopy," *Carbon*, vol. 53, pp. 161–168, 2013.

[10] B. Pan, K. M. Qian, H. M. Xie, and A. Asundi, "Two-dimensional digital image correlation for in-plane displacement and strain measurement: a review," *Measurement Science and Technology*, vol. 20, no. 6, Article ID 062001, 2009.

[11] B. Pan, D. F. Wu, and L. P. Yu, "Optimization of a three-dimensional digital image correlation system for deformation measurements in extreme environments," *Applied Optics*, vol. 51, no. 19, pp. 4409–4419, 2012.

[12] B. Pan, L. P. Yu, D. F. Wu, and L. Q. Tang, "Systematic errors in two-dimensional digital image correlation due to lens distortion," *Optics and Lasers in Engineering*, vol. 51, no. 2, pp. 140–147, 2013.

[13] S. P. Ma, J. Z. Pang, Q. W. Ma, X. Wang, and H. T. Wang, "Experimental investigation of the yielding process of a ductile polycarbonate cylinder subjected to line loading using digital image correlation," *Polymer Testing*, vol. 32, no. 3, pp. 461–467, 2013.

[14] S. P. Ma, Z. L. Zhao, and X. Wang, "Mesh-based digital image correlation method using higher order isoparametric elements," *Journal of Strain Analysis for Engineering Design*, vol. 47, no. 3, pp. 163–175, 2012.

[15] Z. Jian-ping, X. He-ping, Z. Hong-wei, and P. Su-ping, "SEM in situ investigation on thermal cracking behaviour of Pingdingshan sandstone at elevated temperatures," *Geophysical Journal International*, vol. 181, no. 2, pp. 593–603, 2010.

[16] J. P. Zuo, Y. Zhao, N. B. Chai, and H. W. Wang, "Measuring micro/meso deformation field of geo-materials with SEM and digital image correlation method," *Advanced Science Letters*, vol. 4, no. 4-5, pp. 1556–1560, 2011.

[17] H. Cen, Y. L. Kang, Z. K. Lei, Q. H. Qin, and W. Qiu, "Micromechanics analysis of Kevlar-29 aramid fiber and epoxy resin microdroplet composite by micro-Raman spectroscopy," *Composite Structures*, vol. 75, no. 1–4, pp. 532–538, 2006.

[18] Y. L. Kang, X. H. Lin, and Q. H. Qin, "Inverse/genetic method and its application in identification of mechanical parameters of interface in composite," *Composite Structures*, vol. 66, no. 1–4, pp. 449–458, 2004.

[19] D. Dabiri, "Digital particle image thermometry/velocimetry: a review," *Experiments in Fluids*, vol. 46, no. 2, pp. 191–241, 2009.

[20] J. P. Zuo, X. S. Wang, and M. Zuo, "Micro deformation testing of cast AM60B Mg alloy based on scanning electron microscope and digital image correlation method," *Materials Evaluation*, vol. 68, no. 9, pp. 1030–1036, 2010.

[21] J. P. Zuo, H. P. Xie, and H. W. Zhou, "Investigation of meso-failure behavior of rock under thermal-mechanical coupled effects based on high temperature SEM," *Science China Physics, Mechanics and Astronomy*, vol. 55, no. 10, pp. 1855–1862, 2012.

[22] L. C. Dai, X. Feng, B. Liu, and D. N. Fang, "Interfacial slippage of inorganic electronic materials on plastic substrates," *Applied Physics Letters*, vol. 97, no. 22, Article ID 221903, 2010.

[23] Y. Huang, X. Feng, and B. Qu, "Slippage toughness measurement of soft interface between stiff thin films and elastomeric substrate," *Review of Scientific Instruments*, vol. 82, no. 10, Article ID 104704, 2011.

[24] D. J. Jiang, X. Feng, B. R. Qu, Y. Wang, and D. N. Fang, "Rate-dependent interaction between thin films and interfaces during micro/nanoscale transfer printing," *Soft Matter*, vol. 8, no. 2, pp. 418–423, 2012.

[25] H. W. Zhou, C. P. Wang, B. B. Han, and Z. Q. Duan, "A creep constitutive model for salt rock based on fractional derivatives," *International Journal of Rock Mechanics and Mining Sciences*, vol. 48, no. 1, pp. 116–121, 2011.

[26] H. W. Zhou and H. Xie, "Anisotropic characterization of rock fracture surfaces subjected to profile analysis," *Physics Letters A*, vol. 325, no. 5-6, pp. 355–362, 2004.

[27] H. W. Zhou, Y. H. Zhang, A. M. Li, and D. Y. Qiu, "Experimental study on moving boundaries of fluid flow in porous media," *Chinese Science Bulletin*, vol. 53, no. 16, pp. 2438–2445, 2008.

Research Article

Automatic Measurement in Large-Scale Space with the Laser Theodolite and Vision Guiding Technology

Bin Wu and Bing Wang

State Key Laboratory of Precision Measuring Technology & Instrument, Tianjin University, Tianjin 300072, China

Correspondence should be addressed to Bin Wu; wubin@tju.edu.cn

The multitheodolite intersection measurement is a traditional approach to the coordinate measurement in large-scale space. However, the procedure of manual labeling and aiming results in the low automation level and the low measuring efficiency, and the measurement accuracy is affected easily by the manual aiming error. Based on the traditional theodolite measuring methods, this paper introduces the mechanism of vision measurement principle and presents a novel automatic measurement method for large-scale space and large workpieces (equipment) combined with the laser theodolite measuring and vision guiding technologies. The measuring mark is established on the surface of the measured workpiece by the collimating laser which is coaxial with the sight-axis of theodolite, so the cooperation targets or manual marks are no longer needed. With the theoretical model data and the multiresolution visual imaging and tracking technology, it can realize the automatic, quick, and accurate measurement of large workpieces in large-scale space. Meanwhile, the impact of artificial error is reduced and the measuring efficiency is improved. Therefore, this method has significant ramification for the measurement of large workpieces, such as the geometry appearance characteristics measuring of ships, large aircraft, and spacecraft, and deformation monitoring for large building, dams.

1. Introduction

With the development of the large-scale equipment manufacturing, the precise measurement of point, length, and surface characteristics in large-scale space becomes a hot and knotty issue for industrial production. Due to the wide measuring range and high accuracy, the theodolite, total station, and laser tracker have been the mainstream measuring systems in the field of precise industrial measurement [1–5]. Both total station and laser tracker need cooperation targets in the measurement process; therefore the realization and application of such contact measurement methods are greatly limited by measuring range and conditions in the field of industrial measurement. The theodolite measurement system needs two or more high precision electronic theodolites to realize the spatial angle intersection measurement without cooperation targets and also has high measurement accuracy and flexibility in application. However, traditional theodolites measurement needs the human eye to collimate measured features, which inevitably brings about the obvious artificial error and low measurement efficiency.

With the development of electronic technology, information processing technology, and measurement theory, the industrial photogrammetry system represented by V-STARS of Geodetic Services Inc. and indoor space positioning measurement system represented by iGPS of the Nikon Inc. are developed for largescale space measurement [6–10]. Based on multidirectional imaging for the coding and noncoding marks by high-precision digital camera and the image processing algorithms, the photogrammetry system achieves the coordinates' measurement of the space characteristics (the light reflecting symbols attached on the surface of the measured object or optical projection marks) [11–15]. This method requires the measured object to be imaged at different positions and directions. Simultaneously, it also needs to paste marks on the object surface or carry on regional optical projections with projector. In addition, aerial platform or other auxiliary lifting device is required in the measurement of large-scale objects. With the complicated process and low efficiency, this method tends to be adopted in the measurement of the single sample. Similar with the operation model of the Global Positioning System (GPS),

several transmitters as the positioning satellites in GPS are placed in the measuring space and their relationships are calibrated accurately to build the global measurement and control network of the iGPS. Then the receivers similar to the positioning terminals in GPS, handheld or fixed on a workpiece, can be located [16]. With the advantage of extended measuring range without loss of accuracy, the ability of multiobjective real-time measurement, iGPS has been used in the precise assembly and adjustment of large aircraft, antenna, and so on [10]. However, it is not suitable for the automatic measurement of the large-scale workpieces with quantities of characteristic points or geometric dimensions.

Based on the traditional forward intersection measuring principle of theodolite, this paper presents a novel automatic measurement method with laser theodolites which can project a collimated laser beam along its sight-axis, as the Leica DL2 laser pointer, and the vision tracking technology for volume workpiece (equipment) in large space. Supported by the theoretical model data and the multiresolution vision imaging and guiding technology, it can realize the automatic, quick, and accurate measurement of large workpiece. In the measuring system, the measured marks on the surface of the workpieces are spotted by the collimating laser, and cooperation targets or artificial markers are not required. In addition, the collimated laser beam is coaxial with the sight-axis of the theodolite, so the projected light spot on the object indicates the aiming direction of the theodolite. The projected light spot can be captured by camera and used to evaluate the intersection of multitheodolite. And then automatic tracking the light spot instead of aiming with human eye and guiding the exact intersection of multitheodolite can be achieved. Obviously, it can reduce the artificial error and improve the measuring efficiency. Therefore, this method is of great significance for the measurement of large-scale space and large workpieces (equipment), such as the geometry appearance characteristics measuring of ships, large aircraft, spacecraft, and high-speed trains and deformation monitoring for large buildings or dams and so on.

2. Operating Principle and Its Workflow

The automatic measurement system based on vision tracking and guiding laser theodolite consists of the laser theodolite measurement subsystem and the vision tracking and guiding subsystem, which is shown as in Figure 1. The laser theodolite measurement subsystem is composed of two Leica TM5100A (or TM6100A) electric theodolites with DL2 laser pointer and servomotor. After precise orientation, the subsystem obtains three-dimensional (3D) coordinates of target point by the spatial forward angular intersection method or the sophisticated bundle adjustment method. The vision tracking and guiding subsystem contains a two-dimensional (2D) precise turntable and a CCD camera with 30x optical zoom lens. The CCD camera rotates with the precise turntable to track the measured characteristics and the projected spot of laser pointer, and then guides two theodolites to intersect automatically and accurately.

The laser beam from the laser pointer, coaxial with the theodolite sight-axis, not only provides measuring marks on the measured workpiece but also supports the vision tracking and guiding by realizing visualization of theodolite aiming direction. When initially searching and tracking the measured characteristics, the tracking camera, with the ability of multilevel zoom and multiresolution imaging, works on the mode of short focal length, large field of view, and low resolution to track the measured characteristic in specific areas. Then the focal length is increased and the field of view is decreased to increase the imaging resolution. The camera guides two theodolites to intersect accurately and identifies the result, thus ensuring the automatic precise coordinate measurement.

Referring to the schematic diagram shown as in Figure 1, the workflow of the measurement system is as follows. (1) Establish the coordinates system of double-theodolite measurement system (DMS) and the mathematical model of multiresolution vision tracking measurement system (MMS). (2) Measure the designed or machining datum points on the measured workpiece, and establish the relationship between the real workpiece and DMS. (3) Input the theoretical designed data of the workpiece, and transform theoretical designed data into the coordinate system of DMS. (4) With the guidance of transformed designed data and MMS, the CCD camera rotates with the precise turntable to track the characteristic area. (5) Drive the primary (left) theodolite to aim at the measured characteristics of the workpiece according to MMS and certain control strategy, and then guide the secondary (right) theodolite to intersect with the primary theodolite accurately, and obtain the 3D coordinates of the measured characteristic. (6) Repeat step 4 and step 5 until all the characteristics are measured.

In the measuring process above, the key technologies mentioned such as the theodolite precise mutual aiming, measurement model of forward intersection, sophisticated bundle adjustment method, and the control strategy of theodolite and precise turntable are comparatively mature. However, there are few researches on the technologies of vision tracking and guiding measurement based on theodolite system.

3. Mathematical Model of Vision Tracking and Guiding System

Automatic tracking and superposition recognition of laser marks (equivalent to the intersection of two theodolites) are crucial steps in theodolite automatic measurement, which can be achieved by multiresolution camera with the cooperation of precise turntable. Firstly, the DMS should be orientated precisely and the coordinate transformation relationship between the real workpiece and DMS is established. Then, the camera tracks the measured characteristic according to the model data of workpiece. Synchronously, the theodolites are automatically guided to the nearby area of theoretical measured characteristics via the model data of workpiece and the inverse model of theodolite intersection measurement. The guidance of mathematical model data to
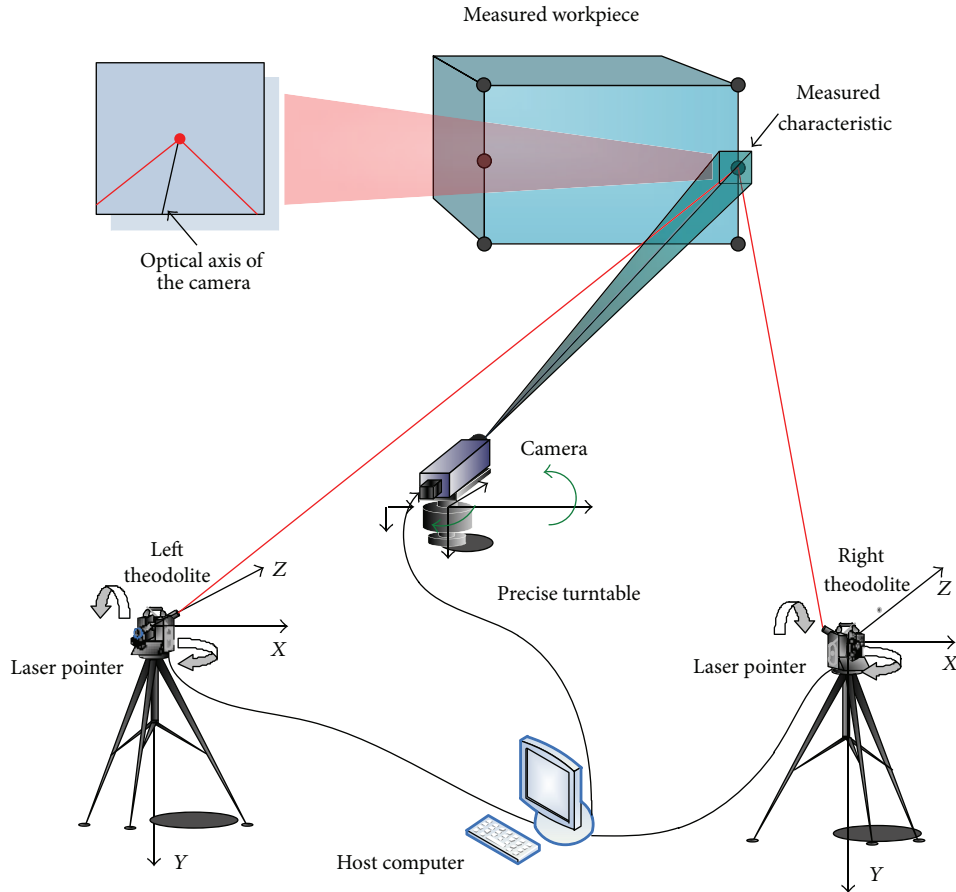
FIGURE 1: Schematic diagram of the measurement system.

the theodolite can be realized by the relationship between the measured workpiece and DMS. However, the guidance of mathematical model data to the tracking camera and the tracking outcome of camera to theodolites are achieved by the relationship above and the calibration of the relationship of DMS and the vision tracking subsystem in advance, namely, the establishment of MMS.

MMS and relationships between coordinate systems are shown in Figure 2. The 2D precise turntable is composed of the horizontal turntable and the vertical rotating end platform. The end platform, which the tracking camera is mounted on, is fixed on the horizontal turntable and rotates with the horizontal turntable. The relative position relationship between the camera coordinate system and the end platform coordinate system remains unchanged during the guidance. Three steps are required to establish the transformed relation from double-theodolite coordinate system (DCS) to the camera coordinate system. (1) Build the initial precise turntable coordinate system under DCS. (2) Set up the real-time precise turntable coordinate system. (3) Establish the relationship between the real-time precise turntable coordinate system and the camera coordinate system.

Define DCS as $X_w Y_w Z_w$, the initial precise turntable coordinate system as $X_{yt0} Y_{yt0} Z_{yt0}$, and the real-time precise turntable coordinate system as $X_{ytm} Y_{ytm} Z_{ytm}$.

3.1. Initial Precise Turntable Coordinate System under the Double-Theodolite Coordinate System.
Fix ZrO_2 ceramic balls (2 mm in diameter, precision class G10, GB308-2002/ISO3290-1998) on the end platform of the precise turntable. The precise turntable rotates horizontally several steps, and then the center coordinates of ceramic balls in each position can be measured and recorded via DMS. Since the trajectory of ceramic ball is an arc, which can be fitted by the center coordinates of the ceramic balls, the coordinates of arc center and the normal vector of fitting arc plane can be obtained to determine the vertical rotation axis of the precise turntable, that is the z'-axis. Similarly, keep the horizontal rotating position of the turntable unchanged while it rotates vertically; the horizontal rotation axis, the x-axis, is obtained.

Due to the turntable machining and assembling error, the horizontal rotation axis and the vertical rotation axis are not intersecting but are vertical in different planes. The relative offset Δy between x-axis and z'-axis can be calculated via the parameters of the x-axis and z'-axis. Build z-axis, parallel with z'-axis and intersecting with x-axis, and the initial precise turntable coordinate system $X_{yt0} Y_{yt0} Z_{yt0}$ in DCS can be constructed according to the right-hand rule.

3.2. Real-Time Precise Turntable Coordinate System.
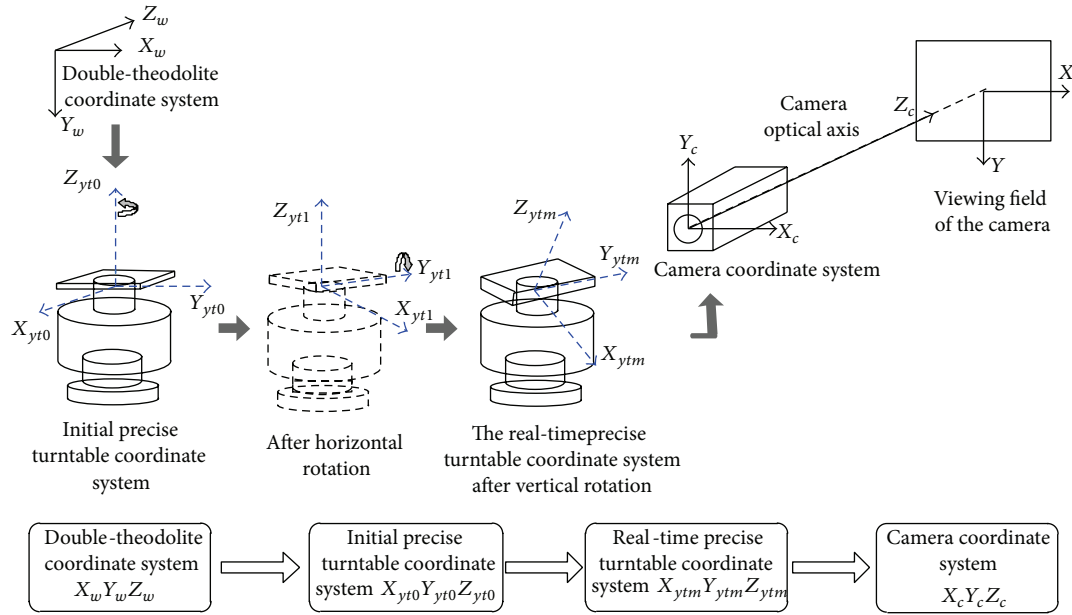Assume that the real-time precise turntable coordinate system is

FIGURE 2: The mathematical model of vision tracking measurement system and the transformation relationship between coordinate systems.

$X_{ytm}Y_{ytm}Z_{ytm}$ and the angles of the precise turntable rotating around the vertical and horizontal axes are θ and α, respectively. Then, the relationship between the initial precise turntable coordinate system and the real-time precise turntable coordinate system can be written as

$$\begin{bmatrix} x_{yt0} & y_{yt0} & z_{yt0} & 1 \end{bmatrix}^T = \mathbf{M}_{\text{rotate}} \cdot \begin{bmatrix} x_{ytm} & y_{ytm} & z_{ytm} & 1 \end{bmatrix}^T. \quad (1)$$

Thereinto,

$$\mathbf{M}_{\text{rotate}} = \begin{bmatrix} \cos\theta & -\sin\theta & 0 & 0 \\ \sin\theta & \cos\theta & 0 & 0 \\ 0 & 0 & 1 & 0 \\ 0 & 0 & 0 & 1 \end{bmatrix}$$

$$\cdot \begin{bmatrix} 1 & 0 & 0 & 0 \\ 0 & 1 & 0 & \Delta y \\ 0 & 0 & 1 & 0 \\ 0 & 0 & 0 & 1 \end{bmatrix} \quad (2)$$

$$\cdot \begin{bmatrix} 1 & 0 & 0 & 0 \\ 0 & \cos\alpha & -\sin\alpha & 0 \\ 0 & \sin\alpha & \cos\alpha & 0 \\ 0 & 0 & 0 & 1 \end{bmatrix}.$$

Set the coordinate of a spatial point X in DCS as (x_w, y_w, z_w) and that in initial precise turntable coordinate system as $(x_{yt0}, y_{yt0}, z_{yt0})$. So the relationship between two coordinates can be expressed as

$$\begin{bmatrix} x_w & y_w & z_w & 1 \end{bmatrix}^T = \mathbf{M}_a \cdot \begin{bmatrix} x_{yt0} & y_{yt0} & z_{yt0} & 1 \end{bmatrix}^T, \quad (3)$$

with

$$\mathbf{M}_a = \begin{bmatrix} i_x & i_y & i_z & x_0 \\ j_x & j_y & j_z & y_0 \\ k_x & k_y & k_z & z_0 \\ 0 & 0 & 0 & 1 \end{bmatrix}, \quad (4)$$

where (i_x, j_x, k_x) and (i_y, j_y, k_y) are the direction vectors of horizontal axis and vertical axis, respectively; (x_0, y_0, z_0) is the initial orientation parameter of the horizontal axis and vertical axis. $\mathbf{M}_a$ can be obtained according to the calibration algorithm in Section 3.1. Combining (1) and (3), the relationship between DCS and real-time precise turntable coordinate system is as follows:

$$\begin{bmatrix} x_w & y_w & z_w & 1 \end{bmatrix}^T = \mathbf{M}_a \cdot \mathbf{M}_{\text{rotate}} \cdot \begin{bmatrix} x_{ytm} & y_{ytm} & z_{ytm} & 1 \end{bmatrix}^T. \quad (5)$$

3.3. Relationship between the Real-Time Precise Turntable Coordinate System and Camera Coordinate System. Place a planar target (7×10 dots matrix, and 30 mm distance between adjacent features in row and column, as shown in Figure 3) in several positions, and lock the pose and focal length of tracking camera. Capture images of planar target and use calibration algorithm of Zhang [17] to obtain the external parameters of the tracking camera, which indicates the relationship between the camera coordinate system and the target coordinate system. Meanwhile, with the "+" features measurement of the planar target via double theodolites, the relationship between DCS and the target coordinate system can be established. Take DCS as a medium and obtain the relationship between DCS and the camera coordinate system. Then, combined with the aforementioned relationship between the DCS and the precise turntable coordinate system, it realizes the calibration of the relationship between the precise turntable coordinate system and the camera coordinate system.

Assume that a feature point of the planner target in the target coordinate system is $(x, y, 0)$ and (x_c, y_c, z_c) in the camera coordinate (x_w, y_w, z_w) in DCS respectively. Define the
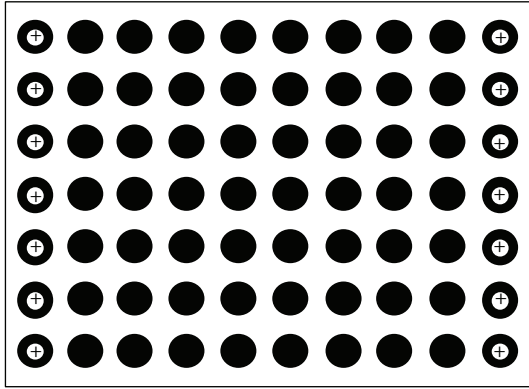
FIGURE 3: The planar target.

transformation matrix from the camera coordinate system to the target coordinate system to be $\mathbf{M}_b$; then we can get

$$[x_c \quad y_c \quad z_c \quad 1]^T = \mathbf{M}_b \cdot [x \quad y \quad 0 \quad 1]^T, \tag{6}$$

$$\mathbf{M}_b = \begin{bmatrix} r_{11} & r_{12} & r_{13} & t_x \\ r_{21} & r_{22} & r_{23} & t_y \\ r_{31} & r_{32} & r_{33} & t_z \\ 0 & 0 & 0 & 1 \end{bmatrix}. \tag{7}$$

Set the transformation matrix from DCS to the target coordinate system as $\mathbf{M}_{RT}$; then we get

$$[x \quad y \quad 0 \quad 1]^T = \mathbf{M}_{RT} \cdot [x_w \quad y_w \quad z_w \quad 1]^T. \tag{8}$$

From (6) and (8), the transforming relationship between the camera coordinate system and DCS can be expressed as

$$[x_c \quad y_c \quad z_c \quad 1]^T = \mathbf{M}_b \cdot \mathbf{M}_{RT} \cdot [x_w \quad y_w \quad z_w \quad 1]^T. \tag{9}$$

From (5) and (9), the relationship of precise turntable coordinate system and camera coordinate system can be written as

$$[x_c \quad y_c \quad z_c \quad 1]^T = \mathbf{M}_{yc} \cdot [x_{ytm} \quad y_{ytm} \quad z_{ytm} \quad 1]^T, \tag{10}$$

$$\mathbf{M}_{yc} = \mathbf{M}_b \cdot \mathbf{M}_{RT} \cdot \mathbf{M}_a \cdot \mathbf{M}_{\text{rotate}}. \tag{11}$$

The camera is fixed on the end platform of the precise turntable, so $\mathbf{M}_{yc}$ can be calibrated in advance.

Combining (5) with (10), we can get the transforming relationship between DCS and the real-time camera coordinate system, namely, the MMS as

$$[x_w \quad y_w \quad z_w \quad 1]^T = \mathbf{M}_a \cdot \mathbf{M}_{\text{rotate}} \cdot \mathbf{M}_{yc}^{-1} \cdot [x_c \quad y_c \quad z_c \quad 1]^T. \tag{12}$$

The camera detects the measured characteristic; then the camera optical axis points to the characteristic automatically. Therefore, from (12) and the angles of precise turntable's horizontal and vertical rotation, the horizontal and vertical angles when both the theodolites point to the same measured characteristic can be obtained. Conversely, if the coordinates of measured characteristics in DCS are known, the tracking camera can also be guided to the measured area.

4. Realization of the Vision Tracking and Guiding Measurement

According to the analysis above, the process of vision tracking and guiding measurement can be realized by two procedures. (1) On the basis of the relationship between real workpiece and the DMS, theodolites and tracking camera are initially guided by the theoretical designed data of workpiece (the mathematical model data of workpiece). (2) The tracking camera guides theodolites to complete the intersecting measurement.

4.1. Initial Guidance of the Theodolites and Tracking Camera Based on Theoretical Designed Data. After orientation of DMS and construction of MMS, the designed or machining reference points are measured via DMS. Then, the theoretical designed data of workpiece is transformed to the coordinate system of DMS. According to the MMS, the camera rotates with the precise turntable to track the characteristic area. After that, the horizontal and vertical angles at which theodolites point to the theoretical characteristic can be determined, respectively, and thus the initial guidance to the tracking camera and theodolites is realized.

4.2. Guidance of Tracking Camera to the Scanning Measurement of Theodolite. After the initial guidance of the designed model data, the sight-axis of theodolite and the optical axis of tracking camera have already pointed to the neighboring area of measured characteristic, with the visible laser mark located in the field of view of camera. Adjust the pose of tracking camera and ensure that the camera can detect the theoretical characteristic mark. Theoretically, when combining the image processing technologies like feature recognition and positioning, with MMS, the tracking camera can guide the theodolites to intersect precisely in the area of measured characteristic, and the precise measurement can be realized. Since the theodolite is driven by stepping motors, a scanning step angle exists in the automatic measurement. Take Leica TM5100A theodolite as an example. Figure 4 shows the changing curve of horizontal angles that the theodolite continuously receives 200 instructions of $0.0005°$ $(1.8'')$ horizontal rotation. According to the changing curve, there is no valid movement in the horizontal direction of theodolite besides the stochastic disturbance, and further tests confirmed that the minimum scanning step angle is $3.6''$. Therefore, the collimation of theodolite sight-axis to the measured characteristic and the precise intersection of double theodolites cannot be truly realized in the strict sense. Aimed at the realization of the automatic and high-precision vision guiding measurement, neighborhood scanning of measured characteristic and discrete linear interpolation is necessary.

4.2.1. Neighborhood Scanning of Measured Characteristic. In order to realize the measurement of the characteristic points, the theodolites are controlled to complete the ergodic neighborhood scanning. The scanning process involves the horizontal linear scanning and vertical linear scanning of
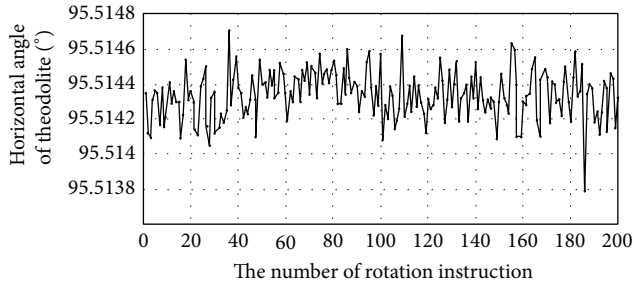
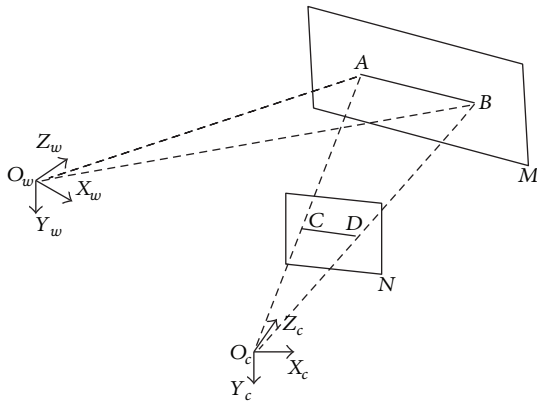FIGURE 4: Horizontal angle changing curve of the TM5100A theodolite continuous horizontal rotation.

FIGURE 5: The diagram of neighborhood scanning.

FIGURE 6: Grid model of the neighborhood scanning on image plane.

of theodolite, namely, $\theta \propto |AB|$. In addition, the distance between tracking camera and measured point is far outweigh the scanning range of laser mark, and $|AB| \propto |CD|$ can be obtained approximately, and thus $\theta \propto |CD|$.

4.2.2. Discrete Linear Interpolation Model of Laser Mark. Since the relationship between the DCS and the coordinate system of tracking camera is not just translation, the small-scope and uniaxial rotation of the theodolite may cause the image position changes of laser mark in both X and Y directions simultaneously. According to the analysis above, the translational distance of laser mark on image plane and the scanning angle of theodolite have an approximate linear relationship. Set the image plane position of laser mark as $P(u_N, v_N)$ and the horizontal angle and vertical angle as x and y, respectively; then we can get

$$
\begin{aligned}
u_N &= a_1 x + b_1 y + c_1, \\
v_N &= a_2 x + b_2 y + c_2.
\end{aligned}
\tag{13}
$$

Thereinto, (a_1, b_1, c_1) and (a_2, b_2, c_2) are coefficients of two linear equations. Slightly drive the theodolite at least three times positions in the range of neighborhood, and take the corresponding value of (u_{iN}, v_{iN}) and (x_i, y_i) as control points; then the coefficients of equations can be calculated via the least square method as

$$
\begin{aligned}
X_1 &= \left(A^T A\right)^{-1} A^T U, \\
X_2 &= \left(A^T A\right)^{-1} A^T V.
\end{aligned}
\tag{14}
$$

In the above equations,

$$
\begin{aligned}
X_1 &= \begin{bmatrix} a_1 & b_1 & c_1 \end{bmatrix}^T, \quad X_2 = \begin{bmatrix} a_2 & b_2 & c_2 \end{bmatrix}^T, \\
U &= \begin{bmatrix} u_1 & u_2 & \cdots & u_N \end{bmatrix}^T, \quad V = \begin{bmatrix} v_1 & v_2 & \cdots & v_N \end{bmatrix}^T, \\
A &= \begin{bmatrix} x_1 & y_1 & 1 \\ x_2 & y_2 & 1 \\ \vdots & \vdots & \vdots \\ x_N & y_N & 1 \end{bmatrix}.
\end{aligned}
\tag{15}
$$

theodolite. Take the horizontal linear scanning as an example; the horizontal dial plate of theodolite rotates at a small angle while the vertical dial plate is fixed. The neighborhood of measured characteristic is small enough to be regarded as a local plane approximately, named M. When theodolite scans horizontally, the trajectory of laser beam coaxial with the sight-axis of theodolite on plane M is approximatly a line segment, named AB and shown us in Figure 5. Lets set N as the image plane of tracking camera and O_C as the optical center of the camera. Referring to the ideal pin-hole imaging model of camera, the line segments $O_C A$ and $O_C B$ have two intersection points with plane N, respectively, named C and D, which are the corresponding image points of A and B on plane N. Then the line segment CD is the trajectory of laser mark on the image plane. According to the analysis, if the pose of tracking camera is fixed and the theodolite carries out a horizontal or vertical uniaxial scanning only, there is little change on the trajectory slope of laser mark in neighborhood area, and those trajectories on image plane can be approximately regarded as a parallel grid, shown in Figure 6.

Generally, the distance between the theodolite and characteristic points ranges from several meters to tens of meters, while the range of scanning neighborhood is a few centimeters, so $|AB| \ll L$. When the theodolite carries out a neighborhood scanning of measured characteristic, an approximate linear relationship can be indicated from the shift distance of laser mark on M and the scanning angle
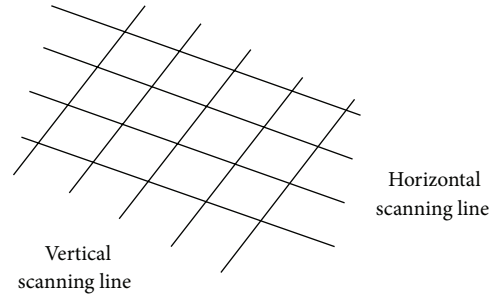
TABLE 1: Results and errors of the automatic measurement system (mm).

| Position no.	Manual measurement results			Automatic measurement results			Deviation		
	x	y	z	x	y	z	Δx	Δy	Δz
1	−279.462	−613.025	3681.021	−279.332	−612.938	3680.989	−0.130	−0.087	0.032
2	−278.368	−231.527	3686.651	−278.389	−231.572	3686.683	0.021	0.045	−0.032
3	−272.15	−0.764	3689.799	−272.162	−0.722	3689.905	0.012	−0.042	−0.106
4	264.774	−20.398	3683.483	264.798	−20.217	3682.297	−0.024	−0.181	0.186
5	275.166	1202.141	3699.063	275.156	1202.15	3699.124	0.010	−0.009	−0.061
6	735.179	−331.672	3673.456	735.208	−331.608	3673.467	−0.029	−0.064	−0.011
7	739.23	539.285	3682.702	739.205	539.301	3682.645	0.025	−0.016	0.057
8	1177.874	−624.384	3665.607	1177.886	−624.418	3665.559	−0.012	0.034	0.048
9	1176.059	20.859	3671.684	1175.991	20.874	3671.76	0.068	−0.015	−0.076
10	1178.963	970.478	3679.866	1178.982	970.428	3679.731	−0.019	0.050	0.135
11	1700.74	−661.313	3658.718	1700.645	−661.241	3658.761	0.095	−0.072	−0.043
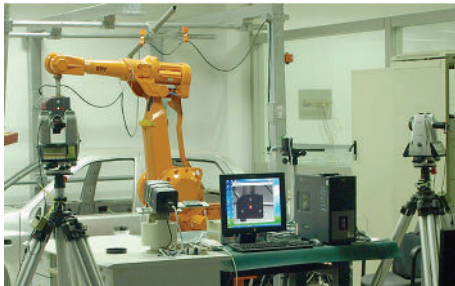
FIGURE 7: Experiment system.
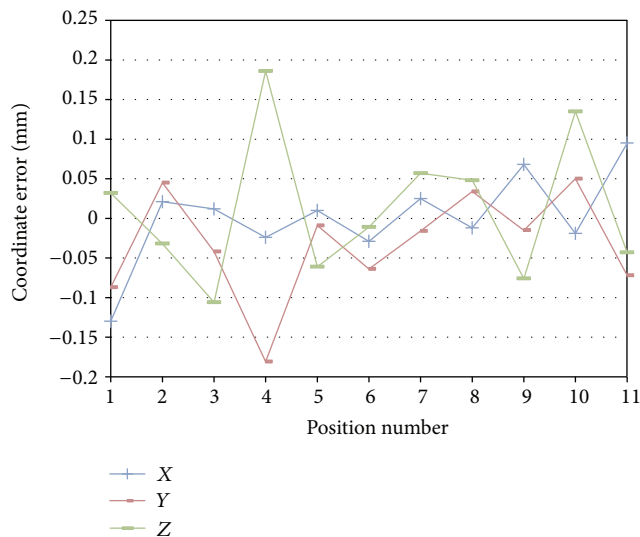
FIGURE 8: Errors of the automatic measurement.

Thus, (14) can be rewritten in matrix form as

$$
\begin{bmatrix} u_N \\ v_N \\ 1 \end{bmatrix} = \begin{bmatrix} a_1 & b_1 & c_1 \\ a_2 & b_2 & c_2 \\ 0 & 0 & 1 \end{bmatrix} \begin{bmatrix} x \\ y \\ 1 \end{bmatrix}. \tag{16}
$$

Then (16) can be further transformed as

$$
\begin{bmatrix} x \\ y \\ 1 \end{bmatrix} = \frac{1}{a_1 b_2 - a_2 b_1} \begin{bmatrix} b_2 & -b_1 & b_1 c_2 - b_2 c_1 \\ -a_2 & a_1 & c_1 a_2 - c_2 a_1 \\ 0 & 0 & a_1 b_2 - a_2 b_1 \end{bmatrix} \begin{bmatrix} u_N \\ v_N \\ 1 \end{bmatrix}. \tag{17}
$$

Substitute the centroid coordinate of measured characteristic (u_0, v_0) into (17), and then the angle when the theodolite aims at the measured characteristic can be obtained. Furthermore, the space coordinate of measured characteristic can be calculated referring to the measurement model of forward intersection.

5. Equipment Setup and Experiment Procedure

In this experiment system, the laser theodolite measurement subsystem is composed of two Leica TM5100A electric theodolites (with DL2 laser pointer), and the vision tracking and guiding measurement subsystem contains a precise turntable, a Toshiba CS8620Ci camera and a Tokina TM33Z1540NPN zoom lens, which are shown as in Figure 7.

Based on the above-mentioned method of vision tracking and guiding measurement, experiments of coordinate measurement of spatial points were conducted to verify the accuracy of the system. As regards small quantity of measured points, the accuracy of manual aiming measurement ranges from 0.01 mm to 0.05 mm. Due to the high precision, the result of manual aiming measurement was regarded as the true value and was compared with the results of automatic measurement.

11 points were measured automatically, and their three-dimensional coordinates can be calculated, respectively. Compared with the results of manual aiming measurement, the deviations of X, Y, and Z coordinate at each point are shown in Table 1 and Figure 8.

The errors of automatic measurement are within 0.3 mm and meet the requirement of large-scale measurement. The factors that affect the accuracy of the automatic measurement involve the extraction accuracy of laser mark, position accuracy of measured characteristic, and the coaxiality of laser

beam and the sight-axis of theodolite. On the basis of further optimization of extraction algorithm and improvement of the measuring conditions, the measurement accuracy can still be improved largely.

6. Conclusions and Future Work

Based on traditional theodolite measurement principle of forward intersection, this paper presents a new kind of laser theodolite automatic measurement method for large space and large workpiece (equipment), through the integration of collimating laser coaxial with the sight-axis of new type electronic theodolite and the vision tracking and guiding technology. This method needs no cooperation targets and avoids pasting manual marks on the large workpiece, thus realizing the automatic, quick, and accurate measurement. Therefore, it has significant ramification for the measurement of large-scale space and large workpiece (equipment), such as the geometry appearance characteristics measuring of ships, large aircraft, spacecraft, and high-speed trains and deformation monitoring for large building, dams. In the experiments the measurement errors are within 0.3 mm, and satisfy the requirement of large-scale measurement. By further optimization of extraction algorithm, the measurement accuracy can be improved to the scale of 10 μm, and the measurement system can apply to more measurement occasions and more complicated industrial environment.

Conflict of Interests

The authors declared that they have no conflict of interests in this work.

Acknowledgments

References

[1] W. Cuypers, N. van Gestel, A. Voet, J.-P. Kruth, J. Mingneau, and P. Bleys, "Optical measurement techniques for mobile and large-scale dimensional metrology," *Optics and Lasers in Engineering*, vol. 47, no. 3-4, pp. 292–300, 2009.

[2] Z. G. Liu, Y. Z. Xu, Z. Z. Liu, and J. W. Wu, "A large scale 3D positioning method based on a network of rotating laser automatic theodolites," in *Proceedings of the IEEE International Conference on Information and Automation (ICIA '10)*, pp. 513–518, June 2010.

[3] F. M. Zhang and X. H. Qu, "Large-scale shape measurement by a combined method based on three instruments," *Optical Engineering*, vol. 51, no. 8, Article ID 083603, 9 pages, 2012.

[4] Z. Wang, L. Mastrogiacomo, F. Franceschini, and P. Maropoulos, "Experimental comparison of dynamic tracking performance of iGPS and laser tracker," *International Journal of Advanced Manufacturing Technology*, vol. 56, no. 1–4, pp. 205–213, 2011.

[5] A. Kayani and J. Jamshidi, "Measurement assisted assembly for large volume aircraft wing structures," in *Proceedings of the 4th International Conference on Digital Enterprise Technology*, pp. 19–21, 2007.

[6] F. Q. Zhou, B. Peng, Y. Cui, Y. X. Wang, and H. S. Tan, "A novel laser vision sensor for omnidirectional 3D measurement," *Optics & Laser Technology*, vol. 45, no. 1, pp. 1–12, 2012.

[7] N. Kochi, T. Ito, K. Kitamura, and S. Kaneko, "Development of 3D image measurement system and stereo-matching method, and its archeological measurement," *IEEJ Transactions on Electronics, Information and Systems*, vol. 132, no. 3, pp. 391–400, 2012.

[8] T. Dodson, R. Ellis, C. Priniski, S. Raftopoulos, D. Stevens, and M. Viola, "Advantages of high tolerance measurements in fusion environments applying photogrammetry," in *Proceedings of the 23rd IEEE/NPSS Symposium on Fusion Engineering (SOFE '09)*, pp. 1–4, June 2009.

[9] T. Luhmann, "Close range photogrammetry for industrial applications," *ISPRS Journal of Photogrammetry and Remote Sensing*, vol. 65, no. 6, pp. 558–569, 2010.

[10] J. E. Muelaner, Z. Wang, J. Jamshidi et al., "iGPS-An initial assessment of technical and deployment capability," in *Proceedings of the 3rd International Conference on Manufacturing Engineering*, pp. 805–810, University of Bath, October 2008.

[11] W. Bösemann, "Advances in photogrammetric measurement solutions," *Computers in Industry*, vol. 56, no. 8-9, pp. 886–893, 2005.

[12] F. Q. Zhou, Y. X. Wang, B. Peng, and Y. Cui, "A novel way of understanding for calibrating stereo vision sensor constructed by a single camera and mirrors," *Measurement*, vol. 46, no. 3, pp. 1147–1160, 2012.

[13] W. Bösemann, "Online, offline, realtime—recent developments in industrial photogrammetry," in *Videometrics VII*, Proceedings of SPIE, pp. 87–94, January 2003.

[14] G. Ganci and H. Handley, "Automation in videogrammetry," *International Archives of Photogrammetry and Remote Sensing*, vol. 32, pp. 53–58, 1998.

[15] T. Xue, L. Q. Qu, Z. F. Cao, and T. Zhang, "Three-dimensional feature parameters measurement of bubbles in gas-liquid two-phase flow based on the virtual stereo vision," *Flow Measurement and Instrumentation*, vol. 27, pp. 29–36, 2012.

[16] D. A. Maisano, J. Jamshidi, F. Franceschini et al., "Indoor GPS: system functionality and initial performance evaluation," *International Journal of Manufacturing Research*, vol. 3, no. 3, pp. 335–349, 2008.

[17] Z. Y. Zhang, "A flexible new technique for camera calibration," *IEEE Transactions on Pattern Analysis and Machine Intelligence*, vol. 22, no. 11, pp. 1330–1334, 2000.

Research Article

Multibubbles Segmentation and Characteristic Measurement in Gas-Liquid Two-Phase Flow

Ting Xue,[1,2] Yanlong Chen,[1,2] and Penghui Ge[1,2]

[1] *College of Electrical Engineering and Automation, Tianjin University, Tianjin 300072, China*
[2] *Tianjin Key Laboratory of Process Measurement and Control, Tianjin 300072, China*

Correspondence should be addressed to Ting Xue; xueting@tju.edu.cn

Gas-liquid two-phase flow is a typical flow, and bubble characteristic measurement is of great importance to discover flow mechanism and guide the practical fluid mechanical engineering. In this paper, a virtual stereo vision measurement system mainly consists of a high-speed camera, and two optical reflector sets was established, and bubble images in gas-liquid two-phase flow were captured by the optimized virtual stereo vision sensor. Overlapping bubbles segmentation is indispensable for the images, and an effective multibubbles segmentation method was proposed. Firstly the convexities of the overlapped area were identified based on the chain code difference, and the pseudoconcave points were removed based on the concave length constraint. According to the matching principle of concave points, the segmentation area was clarified, and the overlapping bubbles were segmented effectively. Therefore, the modality and motion feature parameters of bubbles were estimated, and three-dimensional bubble trajectories and velocity vector field were reconstructed according to the measurement model of virtual stereo vision. The experimental results show that the segmentation and characteristic measurement method of multibubbles is valid and with high precision.

1. Introduction

Gas-liquid two-phase flow is a typical flow, and bubble characteristic measurement is of great importance to discover the flow mechanism and guide the practical fluid mechanical engineering [1]. With the development of computer and optoelectronic techniques, visual inspection [2, 3] based on photography has been widely used in multiphase flow measurement. However, the overlapping bubbles, which would decrease the reconstruction accuracy of modality and motion feature parameters of bubbles in gas-liquid two-phase, exist widely and cannot be recognized effectively. Many scholars have studied different methods to deal with overlapping objects in digital images, such as mathematical morphology [4], improved watershed algorithm [5], and active contour tracking algorithm [6]. However, there are some obvious disadvantages for these algorithms to detect overlapping bubbles. For example, the segmentation computation is huge, because the corrosion and expansion processes are tracked every time, which easily lead to oversegmentation. Other scholars have studied unique brightness information within

the overlapping region, but the brightness difference on the surface of bubbles is an indispensable factor. Searching the edge concave points for segmenting overlapping objects is widely used in particle segmentation [7], which is faster in processing speed than other methods. In the method, extracting and matching concave points are two key steps.

Qian et al. [8] used iterated searching method to find the candidate concavities and obtained optimal splitting conic based on minimum mean square error ellipse fitting with concavities constrains, which improved the calculation accuracy of overlapping area. Heavily overlapping bubbles recognition algorithm which needs to find the local negative curvature maximum of the perimeter as connecting points was utilized by Honkanen et al. [9]. But ellipse-like bubble images with smooth outline are unavoidable in actual images. Zhang et al. [10] proposed polygonal approximation method to find dominant points and segmented ellipse fitting bubbles based on average distance deviation criterion and two constraint conditions. Similarly, it was not accurate for ellipse-like bubbles shape, and false connection points could not be recognized and removed. Yu et al. [11] utilized Normal-line

Hough Transform method to detect the particle centers to segment overlapping solid particles in solid-liquid two-phase flow. But Normal-line Hough Transform is only proper for the arc detection and not effective for particles with complex outline. Moreover, the radius of solid particles must be given firstly, which limits the application considerably.

Considering the real outline of bubbles and taking the irregular bubble shapes into account, a multibubbles segmentation method based on virtual stereo vision and chain code information is proposed. It consists of three main steps, identification of candidate concave points referring to chain code difference, removal of the pseudoconcave points based on the concave length, and matching real concave points according to axial constraint. The method is fast and also suitable for more complex outline of overlapping bubbles, moreover, it can avoid oversegmentation and improve segmentation accuracy for removal of the pseudoconcave point. The proposed matching principle of concave points can improve the segmentation speed as well. Finally, three-dimensional bubble trajectories and velocity vector field are reconstructed according to the measurement model of the virtual stereo vision. The experimental results show that the segmentation and characteristic measurement method of multibubbles is valid and with high precision.

2. Multibubbles Segmentation

2.1. Selection of Candidate Concave Points. The chain code is a classical type which can be used to represent the outline of objects by the line and orientation in four or eight different directions [12], which often applied in the image to increase the computation speed and realize the segmentation more easily. Eight-direction chain code, which used in the method, can precisely describe the outline of objects because there are at most eight neighboring pixels around one pixel. The chain code value of one point refers that the previous point points to the current point, and the direction rotates anticlockwise. The relation between the two chain codes of two adjacent points, for example C_1 and C_2, is relative and is termed relative chain codes. C_1 and C_2 are original chain code, and the value range of C_1 and C_2 is 0~7 which represents eight different directions, respectively. When their directions are the same, the relative chain code value is 0. The absolute chain code $A(i)$ is the accumulation of the overall relative chain codes before the current point i, and $A(0)$ is defined as 0 initially. Therefore, the sum of three adjacent chain codes is

$$\text{Sum}(i) = A(i) + A(i-1) + A(i-2). \tag{1}$$

And the chain code difference Diff(i) is defined as

$$\text{Diff}(i) = \text{Sum}(i+3) - \text{Sum}(i). \tag{2}$$

The chain code difference Diff(i) represents the angle difference of point i, which is in proportion to the boundary curvature. The concave points of the outline can be easily tracked through Diff(i). Figure 1 shows the schematic diagram of chain code difference.

The value of Diff with different points in Figure 1 is as shown in Table 1.

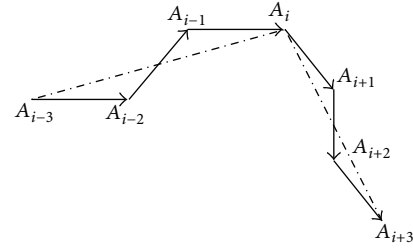FIGURE 1: Schematic diagram of chain code difference.

TABLE 1: Computation results of chain codes in Figure 1.

A_{i-2}	A_{i-1}	A_i	A_{i+1}	A_{i+2}	A_{i+3}	Sum_i	Sum_{i+3}	$\text{Diff}(i)$
0	1	0	−1	−2	−1	1	−4	−5

Obviously, the chain code difference Diff(i) is −5. The point i is noted as one convex point, and the direction changes clockwise due to Diff(i) = −5.

Therefore, the principle of selecting the candidate concave points can be described as follows. If value of Diff(i) is greater than 3, the current point is one of concave points. Otherwise, the current point is regarded as convex point. Firstly, the chain code differences of all points on the contour are calculated, and the current point is selected as candidate concave point if the value is greater than 3. That is, if some concave points are tracked on the bubble contour, these bubbles are served as candidate bubbles.

2.2. Removal of the Pseudoconcave Points. All overlapping bubbles have been selected through comparison of chain code differences. However not all of them are real overlapping bubbles. It is because of the various shapes of bubbles that some selection points maybe pseudoconcave points, which may result in oversegmentation. Some constraint conditions have to be added. A new function $\varphi(i)$ is defined as follows

$$\varphi(i) = \begin{cases} 1, & \text{Diff}(i) > 3, \\ 0, & \text{others}. \end{cases} \tag{3}$$

The neighborhood δ is defined as concave cluster if the point i satisfies the condition of Diff(i) > 3. Then the cluster length or concave length is figured out. If the concave length is larger than the given threshold value, the cluster is regarded as matching concave point. Otherwise the clusters are not real concave points and should be removed.

2.3. Matching Real Concave Points. Figure 2 shows the schematic diagram of overlapping bubbles. Figure 2(a) describes that only two bubbles are overlapped, and points A and B can be matched easily. But sometimes there are more than two bubbles overlapped together, as shown in Figure 2(b), there are 6 different matching combinations between A, B, C, and D. In order to increase the speed of calculation and improve the matching accuracy, a simple but effective method is proposed in the paper. It is based on the two principles: (1) the matching concave points must be located in the both sides
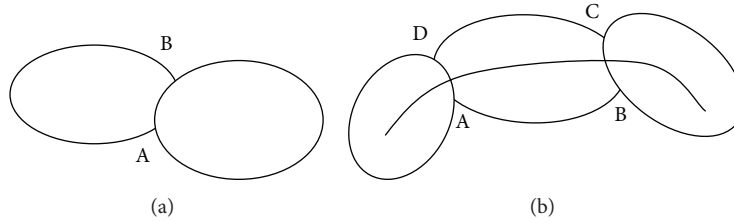
FIGURE 2: Schematic diagram of overlapping bubbles (a) two overlapping bubbles and (b) more overlapping bubbles.
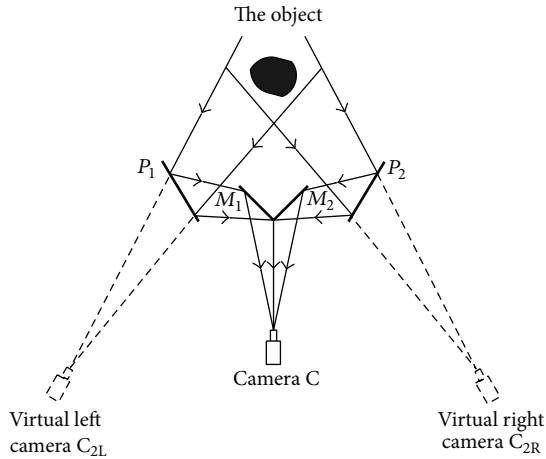

FIGURE 3: Measurement principle of virtual stereo vision.

FIGURE 4: Schematic diagram of bubble velocity measurement.

of medial axis, and (2) the line between the matching pairs has only one intersection point with the medial axis.

3. Three-Dimensional Reconstruction Principle

3.1. Experimental Setup. A Weinberger high-speed camera whose maximum resolution is 1280∗1024 @ 500 fps is used in the experiment. A laptop is used to drive the camera and acquire the RGB images. The LED panel light supplies the backlight source and the power can be adjusted discretely. In order to reconstruction the three-dimensional parameters of bubbles, virtual stereo vision measurement platform is established. The schematic diagram of measurement principle is described in **Figure 3**. The vision sensor consists of symmetrical reflector sets M_1, M_2 in the middle and symmetrical reflector sets P_1 and P_2 on both sides. When bubbles are quantitatively measured, the features are imaged by real camera from the view of left and right to form stereoscopic parallax. The virtual stereo vision measurement platform does not need two severely synchronous images, which decreases the system complexity effectively, and has lower cost and relatively high speed for the particular dynamic measurement of gas-liquid two-phase flow [13, 14].

3.2. Principles of Three-Dimensional Reconstruction. In order to identify the bubble pairs in the left and right half image accurately, epipolar constraint [15] based on the bubbles
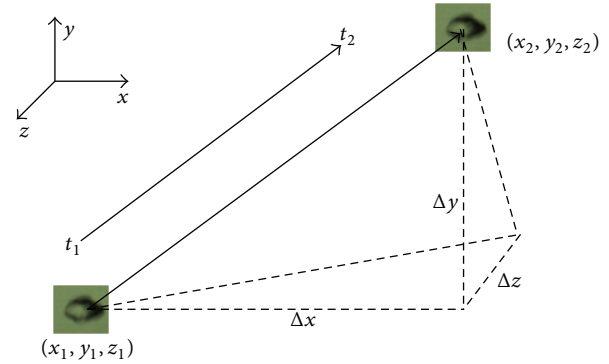
centroid, supplemented by the constraints of bubbles height and projection characteristics are adopted. The modality and motion parameters of bubbles can be extracted with subpixel precision. For example, the center coordinates $(\overline{x}, \overline{y})$ of one bubble are given by

$$
\begin{aligned}
\overline{x} &= \frac{M_{10}}{M_{00}}, \\
\overline{y} &= \frac{M_{01}}{M_{00}},
\end{aligned}
\tag{4}
$$

where M_{10} and M_{01} are the first moment and M_{00} denotes the bubble area.

Figure 4 shows the measurement scheme of three-dimensional velocity of bubbles. (x_1, y_1, z_1) and (x_2, y_2, z_2) refer to the center coordinates of the same bubble at time t_1 and t_2, while Δx, Δy, and Δz are the displacements in horizontal, vertical, and depth direction, respectively. The same operations are performed in the adjacent frames to extract the centroid coordinates of one bubble and calculate the three-dimensional position with stereo matching and reconstruct the velocity by motion matching of different frames. The bubble velocity is defined as the displacement per unit time, and given by

$$
\begin{aligned}
u &= \frac{x_2 - x_1}{\Delta t}, \\
v &= \frac{y_2 - y_1}{\Delta t}, \\
w &= \frac{z_2 - z_1}{\Delta t},
\end{aligned}
\tag{5}
$$

$t = 0\,s$ $t = 0.0321\,s$ $t = 0.0642\,s$

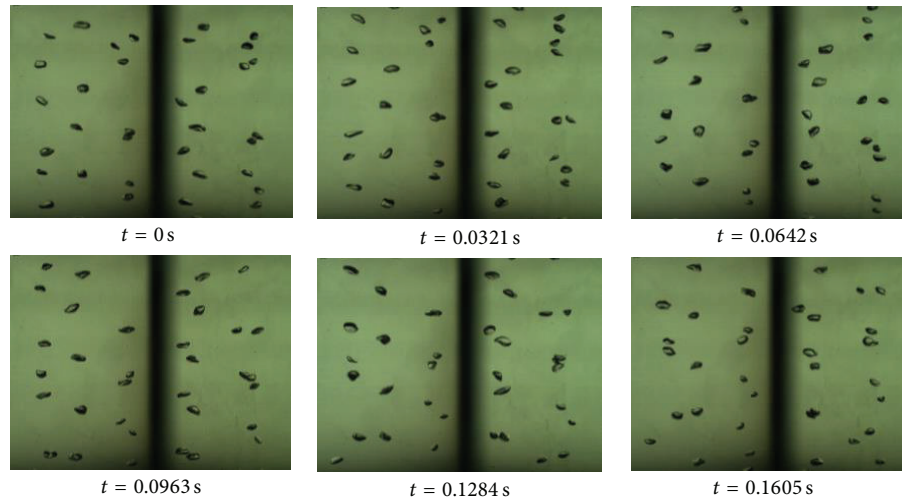$t = 0.0963\,s$ $t = 0.1284\,s$ $t = 0.1605\,s$

FIGURE 5: Original image sequences (at the intervals of 9 frames).

where u, v, and w are velocities in the x, y, and z direction, respectively, and time interval is $\Delta t = t_2 - t_1$.

According to the stereo and moving matching based on the motion characteristic of bubbles, the three-dimensional trajectories of bubble and velocity vector field can be accurately reconstructed based on the modality and motion feature parameters at different time.

4. Characteristic Measurements

RGB bubble images of the air-water two-phase flow are taken by the virtual stereo vision sensor. Figure 5 shows the original images taken at 280 fps. Image analysis and data processing are carried out with VC++ software. The automatic multibubbles segmentation method is described in the following sections.

4.1. Image Preprocessing. In order to extract the modality and motion features, such as the perimeter, area, circularity, and mass center coordinates of bubbles, several image preprocessing steps are necessary to be performed. Transformation from RGB images to gray images can reduce the computation data and increase the processing speed. Image difference and median filtering are intended to eliminate noises. According to the characteristics of bubble images, the improved Otsu method with dynamic threshold compression is used for image binarization subsequently. Then image morphological processing and the automatic recognition method are developed to eliminate the impurities and noise and identify the bubble feature regions [16]. The first image in Figure 5 is one typical image including overlapping bubbles. Figure 6 shows the preprocessing result for the first image in Figure 5. The image is divided into two parts, which are the left captured by the left virtual camera and the right captured by the right virtual camera. Then 8-connected area criterion is served as the rule of labeling the bubbles from the top to bottom in the two parts. There are two sets of overlapping bubbles obviously, labeled by number 10 and 26, respectively. The two
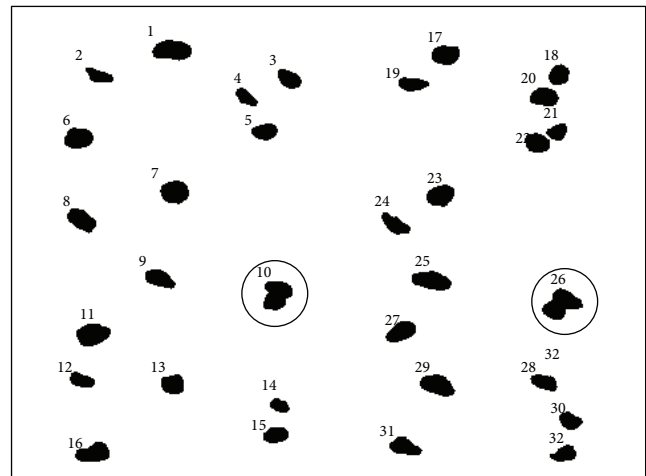

FIGURE 6: Result of image preprocessing.

sets of bubbles must be segmented first before extracting the modality parameters of bubbles.

4.2. Multibubbles Segmentation. The chain code differences of all points on the outline are calculated first. If the value of the chain code differences is greater than 3, the current point is selected as candidate concave point. Accordingly, overlapping bubbles are selected. Whether the candidate overlapping bubbles are real overlapping bubbles or not is judged by the concave length. If the concave length is greater than the given threshold, the cluster is the matching concave point. Otherwise the clusters are not real concave points and the pseudo-concave points are removed. Finally real concave points are matched according to axial constraint. Take number 26 bubble for example, the outline extracted based on 8-direction chain code is shown in Figure 7(a). There are 158 chain codes in total, and the chain code difference of all points is figured out according to the criterion in Section 2.1. The chain code
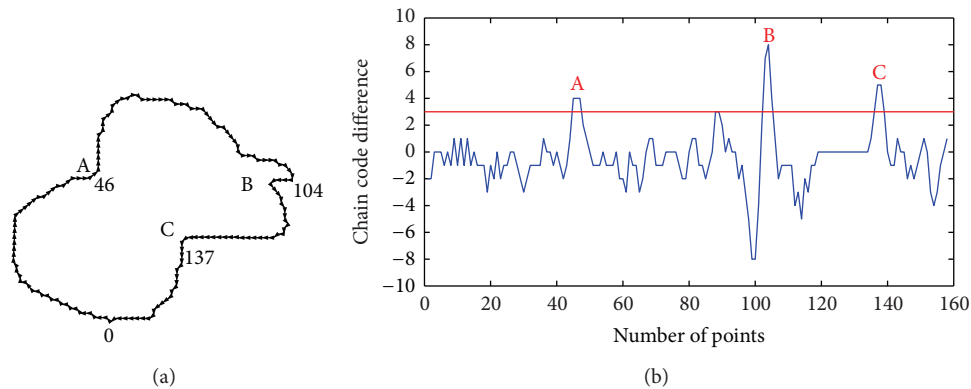
(a)

(b)

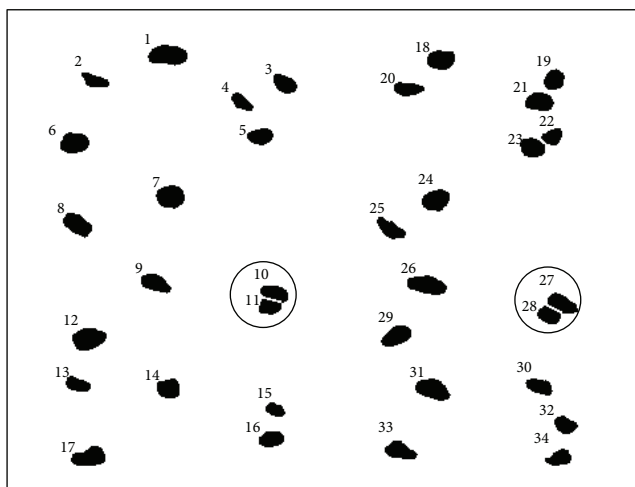FIGURE 7: Chain code of number 26 bubble (a) outline and (b) chain code difference.

FIGURE 8: Result of multibubbles segmentation.

FIGURE 9: Velocity vector after bubble segmentation.

difference is as shown in Figure 7(b). As can be seen from Figure 7(b), there are three positions where the value of chain code difference is greater than 3. The three points are labeled by A, B, and C, respectively. So the three points are selected as candidate concave points. Among them, point A and point C are real concave points, but point B is pseudoconcave point. According to the removal criterion of the pseudoconcave points, the lengths of concave cluster of three points A, B, and C are compared with the threshold and the pseudoconcave point B is removed. Finally, the segment line can be drawn based on medial axis described in Section 2.3.

Figure 8 shows the result of multibubbles segmentation. The overlapping bubbles 10 and 26 are segmented effectively.

4.3. Three-Dimensional Reconstruction of Motion Parameters. According to stereo and moving matching algorithm, three-dimensional center coordinates of each bubble in different frames are extracted. The three-dimensional trajectories of bubbles and velocity vector field can be reconstructed accurately according to three-dimensional center coordinates.

The velocity vector field is plotted in Figure 9, and arrow represents velocity vector direction, and the length of
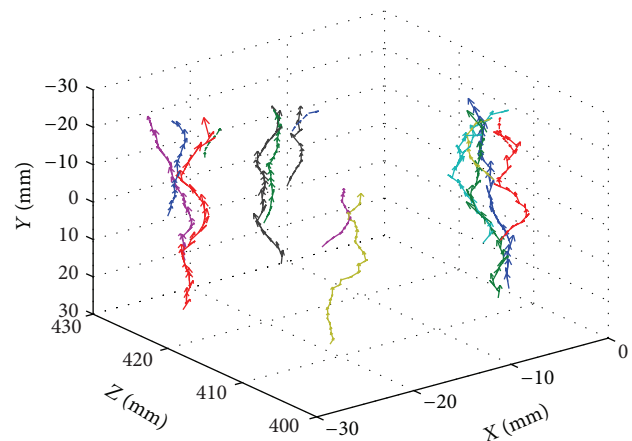
arrow lines represents the magnitude of bubble velocity. As shown in Figure 9, the maximum velocity of bubble rising is 0.235 m/s. The orientation and magnitude of bubble velocity varied continually during the rising period, resulting from combined effect of several forces such as buoyancy, surface tension, and atmospheric pressure.

The reconstruction precision can be estimated by target which is about 90 mm (length) × 80 mm (width) with μm-level accuracy [13]. The spatial distance between two adjacent spheres is known precisely to simulate the bubble distribution, and the target can occupy the full field of view basically. The measurement absolute error for three-dimensional bubble position and trajectory is smaller than 0.13 mm, and the relative error is smaller than 0.49%. Through comparing the measurement value and the real value, it shows the proposed segmentation method and three-dimensional reconstruction is valid and with high precision.

5. Conclusions

In this paper, a segmentation method for multibubbles in gas-liquid two-phase flow based on virtual stereo vision and chain code has been proposed, and characteristics of

three-dimensional trajectory of bubbles are measured accurately. A series of reconstruction steps including image preprocessing, multibubbles segmentation, parameters extraction, and reconstruction of three-dimensional velocity field are performed during the experiment, which can lay the foundation to study the bubble dynamics, behaviors, and gas holdup in gas-liquid two-phase flow. The segmentation method is faster, more effective, and also applicable for more complex outline of overlapping bubbles. Moreover, it can decrease oversegmentation and improve reconstruction accuracy. The experimental results show that the segmentation and characteristic measurement method of multibubbles is valid and with high precision.

Acknowledgment

References

[1] S.-Q. Zheng, Y. Yao, F.-F. Guo, R.-S. Bi, and J.-Y. Li, "Local bubble size distribution, gas-liquid interfacial areas and gas holdups in an up-flow ejector," *Chemical Engineering Science*, vol. 65, no. 18, pp. 5264–5271, 2010.

[2] M. Honkanen, H. Eloranta, and P. Saarenrinne, "Digital imaging measurement of dense multiphase flows in industrial processes," *Flow Measurement and Instrumentation*, vol. 21, no. 1, pp. 25–32, 2010.

[3] B. Wu, J. Kang, and W. Han, "Design of Dammann gratingbased on the parallel recombination simulated annealing algorithm," *Optik*, vol. 124, no. 17, pp. 2928–2931, 2013.

[4] M. A. Luengo-Oroz, E. Faure, and J. Angulo, "Robust iris segmentation on uncalibrated noisy images using mathematical morphology," *Image and Vision Computing*, vol. 28, no. 2, pp. 278–284, 2010.

[5] X. Zhang, Y. Shan, W. Wei, and Z. Zhu, "An image segmentation method based on improved watershed algorithm," in *Proceedings of the International Conference on Computational and Information Sciences (ICCIS '10)*, pp. 258–261, Chengdu, China, December 2010.

[6] N. Santhiyakumari, P. Rajendran, M. Madheswaran, and S. Suresh, "Detection of the intima and media layer thickness of ultrasound common carotid artery image using efficient active contour segmentation technique," *Medical and Biological Engineering and Computing*, vol. 49, no. 11, pp. 1299–1310, 2011.

[7] W. H. Liu and Q. M. Sui, "Automatic segmentation of overlapping powder particle based on searching concavity points," *Journal of Electronic Measurement and Instrument*, vol. 24, pp. 1095–1100, 2010.

[8] X.-M. Qian, H. Zhu, C.-L. Feng et al., "An overlapping bubbles partition method in aerated water flows," in *Proceedings of the International Conference on Machine Learning and Cybernetics (ICMLC '04)*, vol. 6, pp. 3746–3750, August 2004.

[9] M. Honkanen, P. Saarenrinne, T. Stoor, and J. Niinimäki, "Recognition of highly overlapping ellipse-like bubble images," *Measurement Science and Technology*, vol. 16, no. 9, pp. 1760–1770, 2005.

[10] W. H. Zhang, X. Jiang, and Y. M. Liu, "A method for recognizing overlapping elliptical bubbles in bubble image," *Pattern Recognition Letters*, vol. 33, pp. 1543–1548, 2012.

[11] X. R. Yu, K. Abe, Y. Hirose, and T. Hazuku, "Measurement technique for solid-liquid two-phase flow using a Normal-line Hough Transform method," *Journal of Physics*, vol. 147, pp. 301–306, 2009.

[12] A. Pflug, D. Hartung, and C. Busch, "Feature extraction from vein images using spatial information and chain codes," *Information Security Technical Report*, vol. 17, no. 1-2, pp. 26–35, 2012.

[13] T. Xue, L. Q. Qu, Z. F. Cao, and T. Zhang, "Three-dimensional feature parameters measurement of bubbles in gas-liquid two-phase flow based on the virtual stereo vision," *Flow Measurement and Instrumentation*, vol. 27, pp. 29–36, 2012.

[14] F. Q. Zhou, Y. X. Wang, and B. Peng, "A novel way of understanding for calibrating stereo vision sensor constructed by a single camera and mirrors," *Measurement*, vol. 46, no. 3, pp. 1147–1160, 2013.

[15] J. Lim, N. Barnes, and H. Li, "Estimating relative camera motion from the antipodal-epipolar constraint," *IEEE Transactions on Pattern Analysis and Machine Intelligence*, vol. 32, no. 10, pp. 1907–1914, 2010.

[16] T. Xue, X.-D. Meng, and T. Zhang, "Extraction of bubble shape and motion feature parameters in the gas-liquid two-phase flow," *Journal of Optoelectronics Laser*, vol. 21, no. 8, pp. 1218–1221, 2010.

Research Article

Reference Sphere Positioning Measurement Based on Line-Structured Light Vision Sensor

Bin Wu and Yuan Zhang

State Key Laboratory of Precision Measuring Technology & Instrument, Tianjin University, Tianjin 300072, China

Correspondence should be addressed to Bin Wu; wubin@tju.edu.cn

The line-structured light vision sensor has been used widely in industrial vision measuring fields due to its simple structure, small volume, light weight, low cost, convenient calibration, and high accuracy of measurement. To locate the reference sphere precisely with line-structured light vision sensor, a mathematical model based on the measuring principle of line-structured light vision sensor is established in the paper. Then, the positioning measurement error is analyzed in detail. The experimental results show that the method is valid and correct. In addition, an accurate measurement area which is from $R_0 \times \sin 45°$ to $R_0 \times \sin 75°$ away from the center of reference sphere is delimited through the statistical analysis of the experimental data. For the robot temperature compensation and calibration of flexible vision measurement system, this method effectively solves the positioning measurement problems about reference sphere with line-structured light vision sensor and has been applied in the industrial flexible online measurement systems successfully.

1. Introduction

The line-structured light vision sensor consists of a line structured light projector (linear laser) and a camera [1]. This type of sensor has many advantages, such as simple structure, small volume, light weight, low cost, convenient calibration, and high accuracy of measurement. Hence, it is widely used in the industrial vision measuring fields [2, 3]. In particular in the flexible measurement system based on industrial robots [4], the line-structured light vision sensor has more prominent advantages at the aspect of flexibility and spatial accessibility than the stereo visual sensor (binocular or multi-camera vision sensor).

In the flexible online vision measurement system, each robot is configured with one line-structured light vision sensor generally. In principle, just the point in the structured light plan can be a positioning measurement. However, there are various types of the measured characteristics, such as edge (inflection point) [5], round hole (or ellipse hole) [6, 7], square hole (or rectangular hole), and sphere. Liu et al. [8] studied seam tracking based on a line-structured light vision sensor. Wu et al. [7] proposed a two-step method for spatial circle orientation with a line-structured light vision sensor

and analyzed the orientation errors in detail. Theoretically, this method can also realize the spatial measurement of the symmetrical features, such as elliptical hole, square hole, and rectangular hole. However, few scholars have researched about the reference sphere positioning measurement with the line-structured light vision sensor.

Industrial robot is the motion platform in the flexible online measuring system. It is well known that industrial robot has high position repeatability but low absolute positioning accuracy [9]. In addition, every joint motor can generate a large amount of heat with the robot moving, which leads to the significant changes of robot joint length and other robot parameters [10]. Due to the extreme complexity of the joint temperature distribution, it is difficult to establish an accurate temperature distribution model for the calculation of parameters that change. The external auxiliary devices are generally introduced into the system for robot parameters calibration and temperature compensation [11]. The reference sphere is a spatial geometry symmetrical object. So there is no strict posture requirement for the vision sensor during the positioning measurement. During the robot parameters calibration and temperature compensation, the sphere is an ideal auxiliary object, and its center acts as the physical
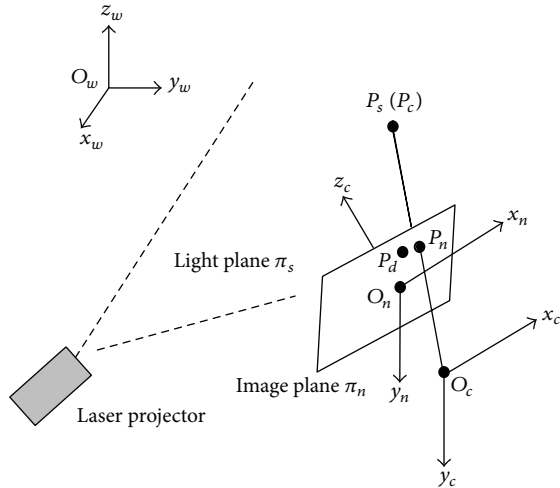
FIGURE 1: Measurement model of line-structured light vision sensor.

constraint of fixed point in the measurement space. Franke et al. [9] used four spheres with a known diameter and center points as the calibration objects for exterior orientation. Guo et al. [11] used the center of the sphere as the global control point in the measured field to compensate the positioning error of the robot. Therefore, the accurate positioning measurement method of the reference sphere with the line-structured light vision sensor is essential for the robot temperature compensation and parameters calibration.

To locate the reference sphere precisely, a mathematical model based on the measuring principle of the line-structured light vision sensor is established in the paper. Then, the positioning measurement error is analyzed in detail. Finally, experiments are carried out to verify the effectiveness of the mentioned measurement method and its measurement accuracy. Meanwhile, an accurate measurement area is delimited through the statistical analysis of the experimental data.

2. Measuring Principle of the Line-Structured Light Vision Sensor

The line-structured light vision sensor contains a line-structured laser and a camera. The line-structured laser projects a fan-shaped light plane in space, which intersects with the measured characteristics. The camera captures the light stripe image modulated by the characteristics, and 3D coordinates of points in the light stripe can be derived by image processing, triangulation measuring principle, and mathematical model of the line-structured light vision sensor.

As shown in Figure 1, $O_w - x_w y_w z_w$ is the 3D world coordinate frame, and $O_c - x_c y_c z_c$ is the camera coordinate frame. Note that O_c is the optical center of the camera, the x_c axis and the y_c axis are in keeping with the increasing direction of column and row on the image plane, respectively, and the z_c axis is the optical axis of the camera. In addition, the image plane π_n is perpendicular to the z_c axis and has a distance of 1 to O_c. $O_n - x_n y_n$ is assumed to be the 2D

image plane coordinate frame. O_n is the intersection of the image plane π_n and the optical axis z_c. The x_n axis and the y_n axis are parallel with the x_c axis and the y_c axis, respectively. Let the camera coordinate frame $O_c - x_c y_c z_c$ be the sensor coordinate frame, so the equation of the light plane π_s in $O_c - x_c y_c z_c$ can be used as the mathematical model of the line-structured light vision sensor. Assume that a point P_s is on the light plane π_s and its 3D coordinate in $O_c - x_c y_c z_c$ is $P_c = (x_c \ \ y_c \ \ z_c)^T$. The corresponding homogeneous coordinates of P_s are $\widetilde{P}_c = (x_c \ \ y_c \ \ z_c \ \ 1)^T$; then, the equation of light plane π_s in $O_c - x_c y_c z_c$ is given by

$$B \cdot \widetilde{P}_c = 0, \tag{1}$$

where $B = (a \ \ b \ \ c \ \ d)$ is the equation coefficient vector of light plane π_s, namely, the parameters of the sensor [12]. These parameters can be achieved precisely by the sensor calibration [13–15].

If P_n is the ideal projection of P_s on π_n, then P_s, O_c, and P_n are collinear [16]. Let homogeneous coordinate of P_n in $O_n - x_n y_n$ be $\widetilde{P}_n = (x_n \ \ y_n \ \ 1)^T$. The equation of the straight line can be represented as

$$P_c - k \cdot \widetilde{P}_n = 0, \tag{2}$$

where k is an arbitrary constant, except zero.

If $B = (a \ \ b \ \ c \ \ d)$ and $\widetilde{P}_n = (x_n \ \ y_n \ \ 1)^T$ are known, $P_c = (x_c \ \ y_c \ \ z_c)^T$ can be obtained by (1) and (2).

The relationship between $O_c - x_c y_c z_c$ and $O_w - x_w y_w z_w$ follows the rigid body coordinate transformation, which can be built by means of auxiliary target [17].

3. Mathematical Model of Reference Sphere Positioning Measurement

According to the measuring principle, the line-structured light vision sensor can measure the points on the light plane, but it cannot apply to the points out of the light plane [18]. When the light plane is projected on the reference sphere and the intersecting cross-section is the maximum circular cross-section π_0 in the sphere surface, 3D coordinates of points in the circumference of the largest cross-section can be obtained directly by the line-structured light vision sensor measuring model. If the 3D coordinate of a point in the cross-section circumference is $P_{ci} = (x_{ci} \ \ y_{ci} \ \ z_{ci})^T$, then

$$(x_{ci} - x_0)^2 + (y_{ci} - y_0)^2 + (z_{ci} - z_0)^2 = R_0^2, \tag{3}$$

where R_0 is the radius of the reference sphere and $O_0 = (x_0 \ \ y_0 \ \ z_0)^T$ is the center of the largest fitting circular cross-section, that is, the center of the reference sphere.

In the actual process of the reference sphere positioning measurement, it is difficult to meet the requirement that the light plane intersects with the maximum circular cross-section. As shown in Figure 2, O_0 is the center of the reference sphere. The actual intersecting cross-section of the light plane and the reference sphere is π_l. In the fitting circular cross-section, the center of the fitting circle is $O_l = (x_l \ \ y_l \ \ z_l)^T$, the

radius of the fitting circle is R_l, and the normal vector $\vec{V}$ of the plane π_l is the normal vector of the light plane:

$$(x_{ci} - x_l)^2 + (y_{ci} - y_l)^2 + (z_{ci} - z_l)^2 = R_l^2,$$
$$\vec{V} = (a \quad b \quad c). \tag{4}$$

The maximum circular cross-section π_0 is parallel with the actual intersecting cross-section π_l. l is defined as the distance between π_0 and π_l; then,

$$l = \|O_0 - O_l\| = \sqrt{R_0^2 - R_l^2}. \tag{5}$$

The normal vector $\vec{V}$ is consistent with the direction vector of the straight line O_lO_0; thus, line O_lO_0 can be expressed by

$$O_0 = O_l + \vec{V}^T \cdot t. \tag{6}$$

From (4) to (6), (7) can be derived as follows:

$$t = \frac{l}{\sqrt{a^2 + b^2 + c^2}}. \tag{7}$$

Combining (7) and (6), the coordinate of O_0 can be obtained.

4. Error Analysis of Reference Sphere Positioning Measurement

In Figure 3, the angle between light plane and the surface normal at the measured point is defined as the projected angle α.

As shown in Figure 4, the light plane intersects with the reference sphere. Assume that point A is an arbitrary point on the circular cross-section. O_0 is the center of the reference sphere. O_l is the center of the intersecting circle. The surface normal vector of the spherical surface at the point A is consistent with the direction vector of line O_0A. The direction vector of line O_0O_l is perpendicular to the plane π_l. According to the above definition, $\angle O_0AO_l$ is the projected angle at point A:

$$\cos\alpha = \frac{R_l}{R_0}. \tag{8}$$

According to (8), the projected angle α varies with the different R_l, which represents the different intersecting section of the light stripe and the spherical surface. However, all points on an intersecting sections have the same projected angle α. The curve that described the relationship between the projected angle and the radius of the circular cross-section is shown in Figure 5.

As shown in Figure 5, when the light plane is tangent with the reference sphere, namely, $R_l = 0$, there is $\alpha = 90°$. The projected angle α reduces gradually with the light plane approaching to the maximum circular cross-section. When the light plane intersects with the reference sphere on the maximum circular cross-section, namely, $R_l = R_0$, there is
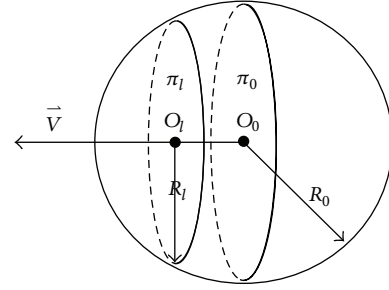

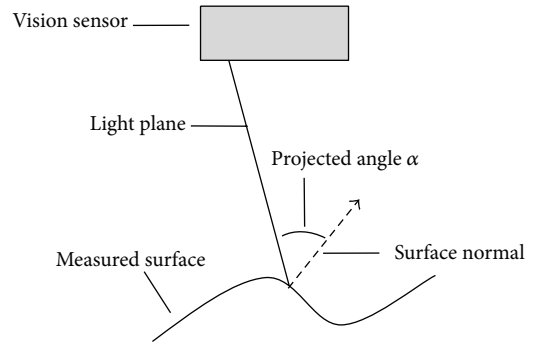
FIGURE 2: Actual reference sphere positioning measurement.

FIGURE 3: Definition of projected angle.

$\alpha = 0°$. The curve has approximate linear variation within a wide range. But when the light plane is near to the plane π_0, the projected angle α reduces quickly.

The actual light stripe which is produced by a semiconductor laser has the thickness, so the intersecting circular cross-section on the reference sphere surface has a certain width. Taking into account the factor of the projected angle, there will be a deviation between the geometric centers of light stripes which are in the measurement image and on the sphere surface, respectively. The larger the projected angle is, the much more deviation will be caused [19, 20]. Thus, a salient deviation can be yielded by a larger projected angle α when light plane is close to the edge of the sphere. The deviation will reduce the accuracy of the fitting result of R_l, the calculation of l, and the reference sphere positioning measurement finally.

The errors of R_l and l caused by the above deviation are defined as ΔR_l and Δl, respectively. The derivative of (5) is taken, and the relationship between Δl and ΔR_l is obtained:

$$\left|\frac{\Delta l}{\Delta R_l}\right| = \frac{1}{\sqrt{(R_0/R_l)^2 - 1}}. \tag{9}$$

In Figure 6, the curve indicates that $|\Delta l/\Delta R_l|$ increases gradually when the light plane intersects with the reference sphere from the edge to the center, along with $R_l/R_0 = 0$ to $R_l/R_0 = 1$. When the light plane and the reference sphere intersect near the edge of reference sphere, $|\Delta l/\Delta R_l|$ is very small, but the projected angle α is large. There are larger ΔR_l and Δl, and it will bring about the considerable positioning error of the sphere center. When the light plane is close to the
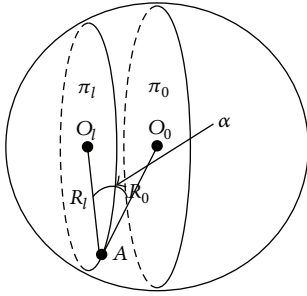
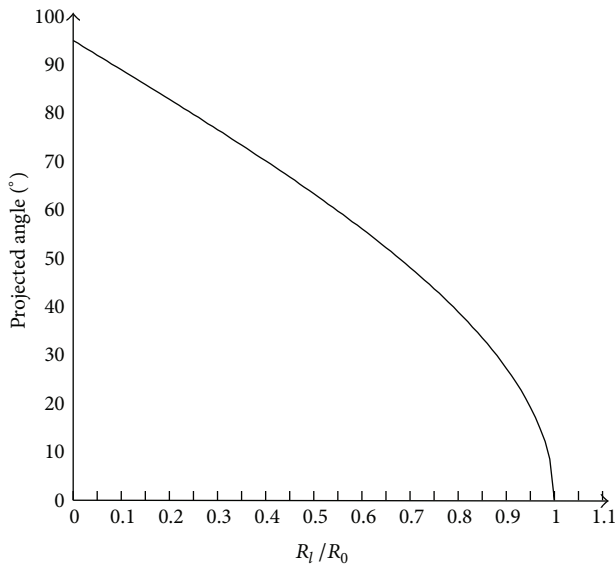FIGURE 4: Projected angle in sphere.

FIGURE 6: $|\Delta l / \Delta R_l|$ in different spherical positions.

FIGURE 5: Relation curve between the projected angle and the radius of the circular cross-section.

FIGURE 7: Experiment setup.

maximum circular cross-section, the projected angle α, the deviation, and ΔR_l are very small. But $|\Delta l / \Delta R_l|$ is very large; Δl and the positioning error of the sphere center will be also intolerable. So there is an accurate measurement area where the line-structured light vision sensor can project light stripe on it.

5. Experiments

Experiment setup is shown in Figure 7. The line-structured light vision sensor is mounted at the end effector of the robot. The reference sphere is fixed at a one-dimensional electric displacement rail whose repetitive positioning accuracy is less than $3\,\mu$m, and the resolution of its grating ruler is $1\,\mu$m. The reference sphere is ZrO$_2$ ceramic ball (level G10, GB308-2002/ISO3290-1998) attached with developer, with a diameter of Ø25.4 mm. The line-structured light vision sensor is composed of a TELI CS8620BCi camera made by Toshiba, a customized lens, and a linear semiconductor laser LH650-4-5 made by Huanic. The spatial resolution of the camera is 768×576 (pixel), and the pixel size is 8.6×8.3 (μm). The customized lens contains a piece of narrow-band pass

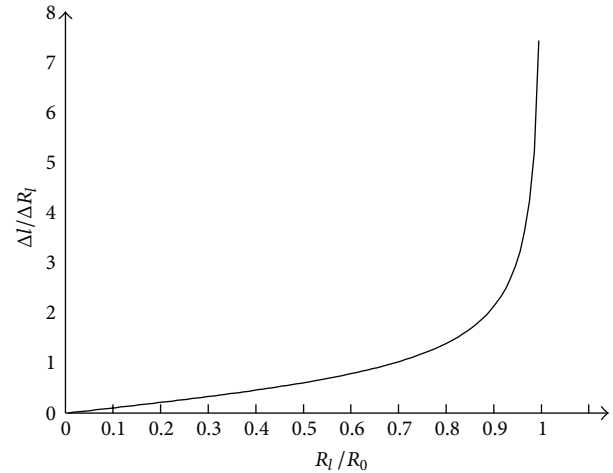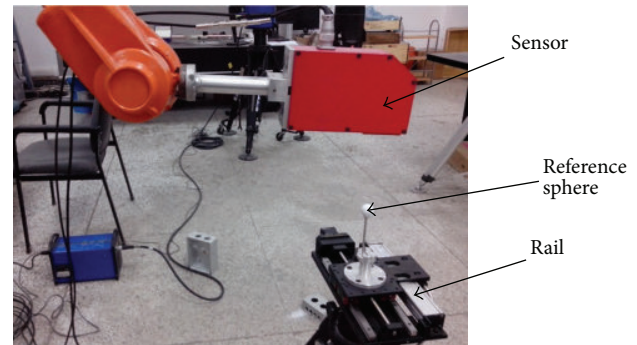filter that the central wavelength is 650 nm, and the half-width of the bandpass wave is 10 nm. The central wavelength of the semiconductor laser is 650 nm and the line width is less than 1 mm at the working distance of sensor. The parameters of the camera are calibrated precisely as follows:

$$
\begin{aligned}
f_x &= 3344.5766 \text{ pixel}, \qquad f_y = 3334.4450 \text{ pixel} \\
C_x &= 353.4754 \text{ pixel}, \qquad C_y = 311.0788 \text{ pixel} \\
k_1 &= 0.090209, \qquad k_2 = -1.465847 \\
p_1 &= -0.003622, \qquad p_2 = -0.004359.
\end{aligned} \tag{10}
$$

The structure parameters of the line-structured light vision sensor are expressed as

$$
\begin{pmatrix} a & b & c & d \end{pmatrix} = \begin{pmatrix} 1.0 & 0.001810 & 0.557520 & -139.376041 \end{pmatrix}. \tag{11}
$$

Above all, adjust the robot pose to meet the following requirements. The reference sphere is in the sensor's field of view and also at its working distance. The image plane of the camera is parallel with the plane of the guide rail roughly, and its horizontal direction is consistent with the moving direction of the guide rail. Then, stop the industrial robot
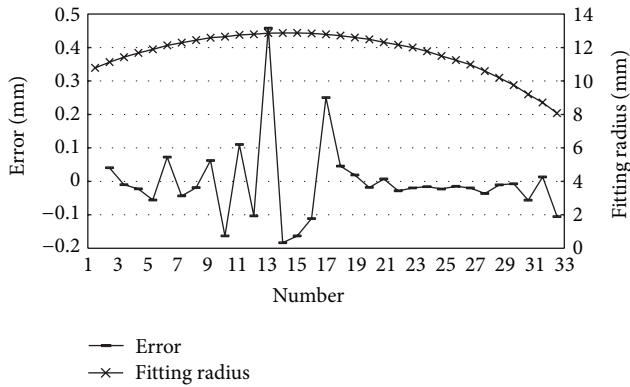
Figure 8: Fitting radius of the circular cross-section and distance error of the adjacent spheres.

to ensure the sensor is still. The reference sphere moves at several positions (1 mm interval) along with the guide rail and is measured simultaneously. The distances calculated by the positioning measurement results of the adjacent moving spheres are compared with the feedback data of the grating ruler. In the experiment, the start position of the light plane is on the middle of the right hemisphere. The sphere moves at 33 positions which passes through the maximum circular cross-section and terminates at the edge of the left hemisphere.

The fitting radius of the circular cross-section at different measuring positions and the distance error between the adjacent spheres are shown in Figure 8.

In Figure 8, the curve of the fitting circle's radius indicates that the light stripe goes from the middle position of one half sphere to the edge of the other half sphere. The distance error curve shows that the positioning measurement errors are larger at the center and at the edge of the reference sphere (at the edge of the left hemisphere in experiment). The conclusion is consistent with the foregoing error analysis. Further statistical analysis shows that the measurement accuracy is higher around the middle of the half ball, which is shown between positions no. 18 and no. 32 in Figure 8. With experiments and statistical analysis, we get that the accurate measurement area is from $R_0 \times \sin 45°$ to $R_0 \times \sin 75°$ away from the center of reference sphere.

6. Conclusions

Based on the measuring principle of the line-structured light vision sensor, a mathematical model of the reference sphere positioning measurement has been established in the paper, and the positioning measurement error has been analyzed in detail. The experimental results show that the method is valid and correct. In addition, an accurate measurement area which is from $R_0 \times \sin 45°$ to $R_0 \times \sin 75°$ away from the center of reference sphere is delimited through the statistical analysis of the experimental data. For the robot temperature compensation and calibration of flexible vision measurement system, this method effectively solves the positioning measurement problems about reference sphere with line-structured light vision sensor and has been applied in the industrial flexible online measurement systems successfully.

References

[1] F. Zhou and G. Zhang, "Complete calibration of a structured light stripe vision sensor through planar target of unknown orientations," *Image and Vision Computing*, vol. 23, no. 1, pp. 59–67, 2005.

[2] J. B. Park, S. H. Lee, and J. Lee, "Precise 3D lug pose detection sensor for automatic robot welding using a structured-light vision system," *Sensors*, vol. 9, no. 9, pp. 7550–7565, 2009.

[3] B. Wu, T. Xue, T. Zhang, and S. Ye, "A novel method for round steel measurement with a multi-line structured light vision sensor," *Measurement Science and Technology*, vol. 21, no. 2, Article ID 025204, 5 pages, 2010.

[4] F. J. Brosed, J. J. Aguilar, D. Guillomïa, and J. Santolaria, "3D geometrical inspection of complex geometry parts using a novel laser triangulation sensor and a robot," *Sensors*, vol. 11, no. 1, pp. 90–110, 2011.

[5] Y. Bian, T. Guo, and G. X. Zhang, "Measuring method of the workpieces' shoulder characteristic size based on structured light," in *7th International Symposium on Instrumentation and Control Technology*, vol. 7129 of *Proceedings of SPIE*, October 2008.

[6] F. Zhou, G. Zhang, and J. Jiang, "High accurate non-contact method for measuring geometric parameters of spatial circle," *Chinese Journal of Scientific Instrument*, vol. 25, no. 5, pp. 604–607, 2004.

[7] B. Wu, T. Xue, and S. Ye, "A two-step method for spatial circle orientation with a structured light vision sensor and error analysis," *Measurement Science and Technology*, vol. 21, no. 7, Article ID 075105, 2010.

[8] S. Y. Liu, G. R. Wang, and J. G. Zhong, "Application and prospect of vision sensing system in robot welding," *Mechanical Science and Technology*, vol. 24, no. 11, pp. 1276–1300, 2005.

[9] R. Franke, T. Bertram, M. Schulte, and C. Von Kopylow, "Development of a high accuracy automatic measurement system utilizing an industrial robot and a fringe projection system," in *Proceedings of the IEEE International Conference on Technologies for Practical Robot Applications (TePRA '09)*, pp. 141–148, November 2009.

[10] S. Eastwood and P. Webb, "Compensation of thermal deformation of a hybrid parallel kinematic machine," *Robotics and Computer-Integrated Manufacturing*, vol. 25, no. 1, pp. 81–90, 2009.

[11] L. Guo, Y. J. Liang, J. C. Song, Z. Y. Sun, and J. G. Zhu, "Compensation for positioning error of industrial robot for flexible vision measuring system," in *8th International Symposium on Precision Engineering Measurement and Instrumentation*, vol. 8759 of *Proceedings of SPIE*, 2013.

[12] F. Zhou, Y. Cui, B. Peng, and Y. Wang, "A novel optimization method of camera parameters used for vision measurement," *Optics and Laser Technology*, vol. 44, no. 6, pp. 1840–1849, 2012.

[13] F. Q. Zhou, Y. Cui, G. He, and Y. X. Wang, "Line-based camera calibration with lens distortion correction from a single image," *Optics and Lasers in Engineering*, vol. 51, no. 12, pp. 1332–1343, 2013.

[14] F. Q. Zhou, Y. Cui, Y. X. Wang, L. Liu, and H. Gao, "Accurate and robust estimation of camera parameters using RANSAC," *Optics and Lasers in Engineering*, vol. 51, no. 3, pp. 197–212, 2013.

[15] B. Zhang, Y. F. Li, and Y. H. Wu, "Self-recalibration of a structured light system via plane-based homography," *Pattern Recognition*, vol. 40, no. 4, pp. 1368–1377, 2007.

[16] T. Xue, L. Q. Qu, Z. F. Cao, and T. Zhang, "Three-dimensional feature parameters measurement of bubbles in gas-liquid two-phase flow based on the virtual stereo vision," *Flow Measurement and Instrumentation*, vol. 27, pp. 29–36, 2012.

[17] N. Geng, J. Zhu, D. Lao, and S. Ye, "Theory and algorithm of coordinate system registration based on rigid body kinematics," *Chinese Journal of Sensors and Actuators*, vol. 23, no. 8, pp. 1088–1092, 2010.

[18] Z. Xie, Q. Zhang, and G. Zhang, "Modeling and calibration of a structured-light-sensor-based five-axis scanning system," *Measurement*, vol. 36, no. 2, pp. 185–194, 2004.

[19] H. Y. Feng, Y. Liu, and F. Xi, "Analysis of digitizing errors of a laser scanning system," *Precision Engineering*, vol. 25, no. 3, pp. 185–191, 2001.

[20] Z. Xie, C. Zhang, and G. Zhang, "Error compensation for structured light sensors," *Chinese Journal of Scientific Instrument*, vol. 26, no. 7, pp. 667–725, 2005.